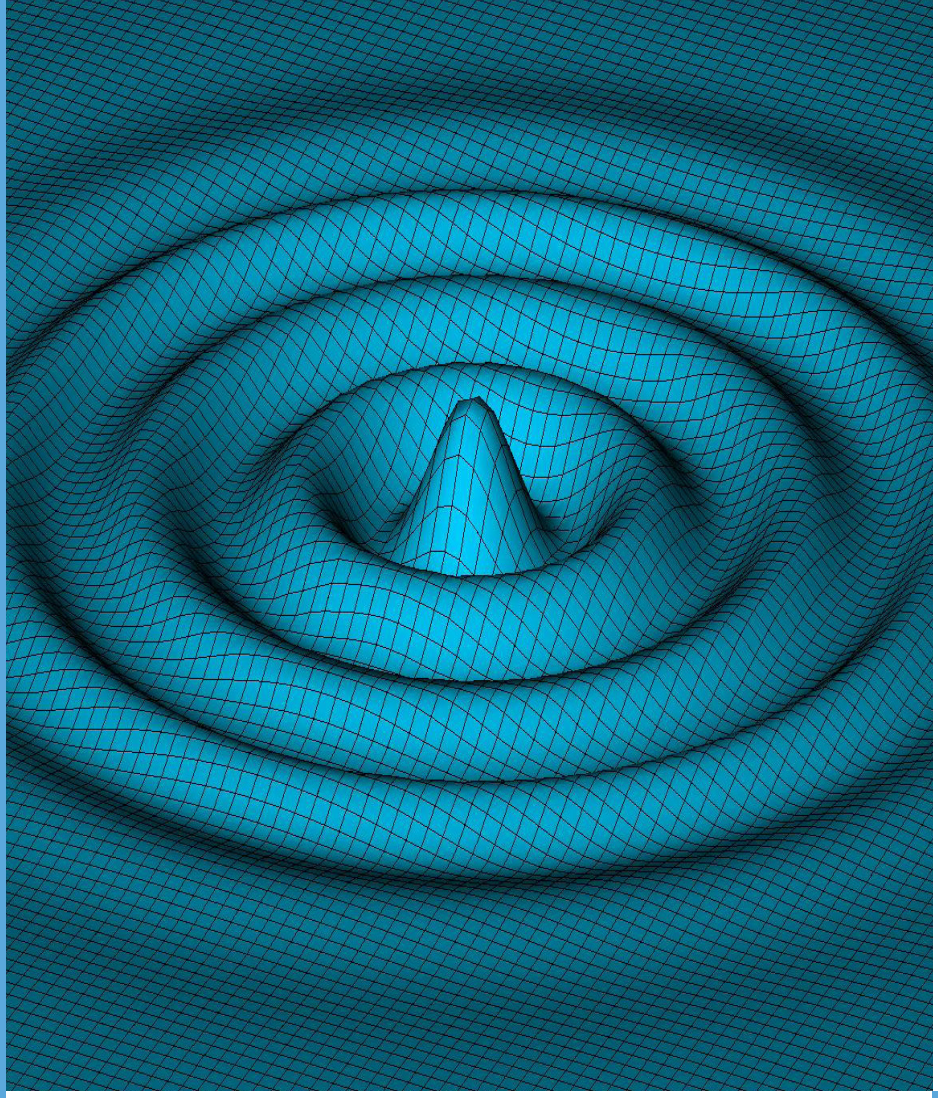

SCIENCE • TECHNOLOGY • RESEARCH HIGHLIGHTS • VISIONS

Dissertation
15

Numerical and experimental studies of nonlinear wave loads of ships

Timo Kukkanen

VTT

VTT SCIENCE 15

Numerical and experimental studies of nonlinear wave loads of ships

Timo Kukkanen

VTT Technical Research Centre of Finland

Doctoral dissertation for the degree of Doctor of Science in Technology (Doctor of Philosophy) to be presented with due permission of the School of Engineering for public examination and debate in Auditorium K216 at the Aalto University School of Engineering (Espoo, Finland) on the 26th of October 2012 at 12 noon.

ISBN 978-951-38-7932-7 (soft back ed.)
ISSN 2242-119X (soft back ed.)

ISBN 978-951-38-7933-4 (URL: http://www.vtt.fi/publications/index.jsp)
ISSN 2242-1203 (URL: http://www.vtt.fi/publications/index.jsp)

JULKAISIJA – UTGIVARE – PUBLISHER

VTT
PL 1000 (Tekniikantie 4 A, Espoo)
02044 VTT
Puh. 020 722 111, faksi 020 722 7001

VTT
PB 1000 (Teknikvägen 4 A, Esbo)
FI-02044 VTT
Tfn +358 20 722 111, telefax +358 20 722 7001

VTT Technical Research Centre of Finland
P.O. Box 1000 (Tekniikantie 4 A, Espoo)
FI-02044 VTT, Finland
Tel. +358 20 722 111, fax + 358 20 722 700

Kopijyvä Oy, Kuopio 2012

Numerical and experimental studies of nonlinear wave loads of ships

Laskennallinen ja kokeellinen tutkimus laivojen epälineaarisista aaltokuormista.
Timo Kukkanen. Espoo 2012. VTT Science 15. 219 p.

Abstract

Extreme wave loads have to be defined in the ultimate strength assessment of ship structures. Nonlinearities in extreme wave loads can be significant in high waves. Numerical and experimental studies of nonlinear wave loads are presented in this work. A nonlinear time domain method has been developed and the fundamentals of the method are given. The method is based on the source formulation expressed by means of the transient three-dimensional Green function. The exact body boundary condition is satisfied on the instantaneous floating position of the body. The free surface boundary condition is linear. The time derivative of the velocity potential in Bernoulli's equation is solved with a similar source formulation to that of the perturbation velocity potential.

The verification of the method is presented for a hemisphere and cones. Wigley hull forms are used to validate the calculation method in regular head waves and calm water.

Model tests of a roll-on roll-off passenger ship with a flat bottom stern have been carried out. Model test results of ship motions, vertical shear forces and bending moments in regular and irregular head waves and calm water are given.

The nonlinearities in ship motions and hull girder loads are investigated using the calculation method and the model test results. The nonlinearities in the hull girder loads have been found to be significant. The calculation method is used to predict rigid hull girder loads for the model test ship. It is shown that the time domain calculation method can be applied to ship-wave interaction problems to predict the nonlinear wave loads.

Keywords wave loads, nonlinear loads, numerical methods, model tests, ship strength

Laskennallinen ja kokeellinen tutkimus laivojen epälineaarisista aaltokuormista

Numerical and experimental studies of nonlinear wave loads of ships.
Timo Kukkanen. Espoo 2012. VTT Science 15. 219 s.

Tiivistelmä

Aaltokuormat on määritettävä arvioitaessa laivojen äärilujuutta. Epälineaarisuudet aaltokuormissa voivat olla merkittäviä kovassa merenkäynnissä. Työssä on tutkittu numeerisesti ja kokeellisesti epälineaarisia aaltokuormia. Työssä on kehitetty aikatason laskentamenetelmä vasteiden määrittämiseksi aallokossa. Menetelmä perustuu nopeuspotentiaalien ratkaisuun lähdejakautumien avulla rungon pinnalla. Lähdejakautumat on esitetty kolmiulotteisen ajasta riippuvan Greenin funktion avulla. Rungon pinnalla toteutetaan tarkka runkopinnanreunaehto. Vapaanpinnanreunaehto on linearisoitu. Paineen Bernoullin yhtälössä esiintyvä nopeuspotentiaalin aikaderivaatta ratkaistaan samalla lähdejakautumien ratkaisumenetelmällä kuin häiriönopeuspotentiaalin ratkaisu.

Laskentamenetelmä on verifioitu puolipallon ja kartion avulla. Wigley-runkomuotoja on käytetty laskentamenetelmän validoinnissa tyynessä vedessä sekä säännöllisessä vasta-aallokossa eri nopeuksilla.

Työssä esitetään mallikoetulokset tasapohjaperän omaavalle ro-pax-alukselle. Mallikokeissa mitattiin aluksen liikkeet ja kiihtyvyydet sekä laivapalkin leikkausvoimat ja taivutusmomentit. Kokeet tehtiin tyynessä vedessä eri nopeuksilla sekä säännöllisessä ja epäsäännöllisessä vasta-aallokossa nollanopeudella ja nopeudella eteenpäin.

Epälineaarisuuksia liikkeissä ja kuormissa tutkittiin kehitetyn laskentamenetelmän avulla sekä mallikokeiden tuloksiin perustuen. Tulosten perusteella havaittiin, että epälineaarisuudet ovat merkittäviä mallikoelaivalla. Laskentamenetelmän avulla määritettiin mallikoelaivalle laivapalkin voimat ja momentit. Laskentamenetelmän todetaan soveltuvan hyvin nesterakenne-vuorovaikutusongelmiin ennustettaessa laivojen aaltokuormia.

Avainsanat wave loads, nonlinear loads, numerical methods, model tests, ship strength

Preface

I am grateful to my supervisor professor Jerzy Matusiak for his encouragement and valuable advices during the studies in this thesis.

I owe my sincere gratitude to the reviewers professor Volker Bertram and professor Hidetsugu Iwashita for their excellent criticisms and comments.

I am obliged to Seppo Kivimaa, Technology Manager of the Vehicle Engineering and Ilkka Saisto, Team leader of the Ship hydrodynamics for the opportunity to carry out the research work at VTT and their faithful support.

My warmest appreciation to my colleagues for the discussions and the inspiring atmosphere to carry out the research work. I had opportunity to get excellent advices and fruitful discussions with Heikki Helasharju, Jussi Martio, Antonio Sanchez-Caja and Tuomas Sipilä. Especially, I was assisted in the model tests by the skilful experts Timo Lehti, Timo Lindroos and Sakari Merinen.

The model tests and part of the theoretical studies were carried out in the research project Laine during the years 2006…2009. The research project was funded by the Finnish Funding Agency for Technology and Innovation (Tekes), Finnish Navy, STX Finland, SWECO and Technip Finland Offshore. This financial support is gratefully acknowledged. Finally, I am sincerely grateful to the Finnish Seafaring Foundation (Merenkulun säätiö) for the funding which made it possible that I had finally time to get ready this thesis.

Helsinki, August 2012
Timo Kukkanen

Academic dissertation

Supervisor	Professor Jerzy Matusiak Aalto University School of Engineering
Reviewers	Professor Volker Bertram FutureShip GmbH-A GL company, Germany
	Professor Hidetsugu Iwashita Hiroshima University, Japan
Opponent	Professor Pandeli Temarel University of Southampton, UK

Contents

List of symbols

a	Wave amplitude
a_j	Wave amplitude of jth irregular wave component
a_k	Accelerations in time integration at time step k
a_{mi}	Accelerations of mass dm in hull girder loads, i = 1,2,…,6
a_z	Vertical accelerations in body-fixed coordinate system
f	Function
g	Gravity acceleration
h_c	Height of cone
i	Imaginary unit, $i = \sqrt{-1}$
k	Wave number, $k = 2\pi/\lambda_w$
m	Mass
m_L	Weight distribution
n	Symbol for normal in normal derivative, $\partial/\partial n$
n_{0i}	Components of generalized normal vector, i = 1,2,…,6
n_{pi}	Components of generalized normal vector for hull girder loads, i = 1,2,…,6
p, q, r	Roll, pitch and yaw velocities in body-fixed coordinate system
p_1	Pressure
p_a	Atmospheric pressure
r	Cylinder coordinate
r_c	Radius of cone
t	Time
Δt	Time step size
u, v, w	Surge, sway and heave velocities in body-fixed coordinate system

u_n	Velocity of body boundary at waterline
u_k	Velocities in time integration at time step k
v_1, v_2, v_3	Fluid velocity components in x-, y-, z-directions
x, y, z	Cartesian coordinates in space-fixed coordinate system
x_0 , y_0 , z_0	Cartesian coordinates in body-fixed coordinate system
x' , y' , z'	Coordinates of source points in space-fixed coordinate system
x_k	Motions in time integration at time step k
x_p	Cross section x coordinate of body for hull girder loads
$\hat{x}$	Extreme value
$\bar{x}$	Mean value
z_r	Relative motion between the ship's vertical motion and the incoming wave
z_{FP}, z_{AP}	Sinkage at fore and aft perpendiculars
A_{ij}	Added mass coefficients, i and j = 1,2, …, 6
B	Breadth of the ship
B_{ij}	Damping coefficients, i and j = 1,2, …, 6
C	Constant
C_B	Block coefficient
C_w	Wave resistance coefficient
Fn	Froude number, $Fn = U_0 / \sqrt{gL}$
F_i	Forces and moments in body-fixed coordinate system, i = 1,2,...,6
F_{Gi}	Gravity force components in body-fixed coordinate system, i = 1,2,3
F_{Ri}	Radiation force components, i = 1,2,...,6
F_{Pi}	Radiation-diffraction force components, i = 1,2,...,6
G	Green function
$G^{(t)}$	Memory part of the Green function
$\hat{G}^{(t)}$	Non-dimensional memory part
$G^{(0)}$	Impulsive part of the Green function
$\hat{G}^{(xy)}$	Non-dimensional derivative of the Green function with respect to x and y

$\hat{G}^{(z)}$	Non-dimensional derivative of the Green function with respect to z
$\widetilde{G}$	Finite element approximation
$\hat{G}^{e}$	Green function at nodes in finite element approximation
H_s	Significant wave height
I	Integral function
I_{ij}	Mass moment of inertia, i and j = 4,5,6
I_G	Estimated integral with Gauss quadratures
I_K	Estimated integral with Gauss-Kronrod quadratures
J	Jacobian
J_ν	Bessel function of the first kind of order ν
L	Characteristic length; for ship, $L = L_{pp}$
L_{pp}	Length between perpendiculars
L_{ij}	Impulse response function, i and j = 1,2,…,6
M_{sw}	Still water bending moment
N	Number of response cycles
N_i	Finite element shape functions, i = 1,2,...,9
N_G	Number of points in Gauss quadratures
N_P	Number of panels
N_T	Number of time steps
N_τ	Number of time steps in convolution integral
P	Field point coordinates (x, y, z); point on body in space-fixed coordinates
P_0	Point on body (x_0, y_0, z_0) in body-fixed coordinates
Q	Source point coordinates (x' , y' , z')
Q'	Image source point coordinates (x' , y' , $-z'$)
Q_{sw}	Still water shear force
R	Coordinate of singularities in the impulsive part of the Green function
R'	Coordinate of image singularities in the impulsive part of the Green function
S	Area or surface
S_0	Mean wetted surface

S_B	Body surface
S_F	Free surface
S_P	Area of panel
S_w	Wave spectrum
S_{wsa}	Wetted surface area
$S(\omega)$	Spectrum
T	Time delay $t-\tau$ in non-dimensional Green function; draught of the ship
T_1	Mean wave period
T_e	Encounter period
T_z	Zero crossing wave period
T_p	Peak wave period, modal period
U_0	Forward speed of the body in x-direction
U_k	Body velocities in time integration
U_{N}	Velocity of intersection of body and free surface at $z = 0$
V	Volume
V_{i}	Global hull girder forces and moments, $i = 1,2,...,6$
W_{i}	Weights in Gauss quadratures, $i = 1,2,...,\ N_G$
X, Y, Z	Space variables in non-dimensional Green function
$X^{(i)}$	Harmonic components of response, $i = 0,1,2,3,\ldots,\infty$

Greek symbols

α_w	Scale parameter of Weibull distribution
α_r	Exceedance probability level
β	Non-dimensional time term in the Green function
β_c	Deadrise angle of the cone
β_w	Shape parameter of Weibull distribution
γ_w	Location parameter of Weibull distribution
χ	Heading angle
$\varepsilon^{(i)}$	Phase of ith harmonic component
ε_j	Phase of jth irregular wave component
ε_{wet}	Criterion of wet panels
δ_k	Estimate of the error in time integration at time step k

ϕ	Perturbation velocity potential
ϕ_I	Velocity potential of incoming wave
ϕ_t	Acceleration potential or time derivative of velocity potential, $\phi_t = \partial\phi/\partial t$
η_i	Ship motions: surge, sway, heave, roll, pitch and yaw, i = 1,2,...,6
φ	Potential function to solve acceleration potential
κ	Frequency parameter, $\kappa = \omega U/g$
λ	Integration variable in Green function
λ_w	Wave length
μ	Coordinate parameter in Green function
ρ	Density of water
σ	Source strength
σ_x	Standard deviation
τ	Time
ω	Wave frequency
ω_c	Cut-off frequency of low pass filter
ω_e	Encounter frequency, $\omega_e = \omega - kU_0 \cos\chi$
ω_{n3}	Heave natural frequency
ξ_i	Local coordinates of panel or element
Φ	Total velocity potential
Γ_F	Intersection of free surface and body
ψ_i	Impulsive radiation potential of ith mode of motion
ζ	Wave elevation
∇	Displacement

Matrix and vector notations

a	Acceleration vector
$\mathbf{a}_m$	Acceleration of mass dm
f	Vector to solve unknown source strengths
g	Vector of gravity acceleration in body-fixed coordinates
n	Normal vector pointing out of the fluid
r	Position vector from the centre of gravity of the body

$\mathbf{r}_m$	Position vector of mass *dm* from the centre of gravity
$\mathbf{r}_p$	Position vector of the hull girder loads from the centre of gravity
$\mathbf{u}$	Body velocity vector in body-fixed coordinate system (u, v, w)
$\mathbf{v}$	Fluid velocity vector (v_1, v_2, v_3)
$\dot{\mathbf{u}}$	Translation acceleration vector
$\mathbf{x}$	Position vector in space-fixed coordinate system
$\mathbf{x}_G$	Position vector of the centre of gravity of body (η_1, η_2, η_3)
$\dot{\mathbf{x}}_G$	Velocity vector of the centre of gravity of body $(\dot{\eta}_1, \dot{\eta}_2, \dot{\eta}_3)$
[**A**]	Coefficient matrix of unknown source strengths
[**B**]	Transformation matrix of rotation velocities
[**I**]	Mass moment of inertia matrix
[**L**]	Transformation matrix of translational quantities
$\mathbf{F}$	Force vector in equations of motion
$\mathbf{F}_G$	Vector of gravity forces in equations of motion
$\mathbf{M}$	Moment vector in equations of motion
$\mathbf{N}$	Two-dimensional normal vector at waterline
$\mathbf{U}$	Velocity vector of body point, $\mathbf{U} = \mathbf{u} + \boldsymbol{\omega} \times \mathbf{r}$
$\mathbf{U}_\Gamma$	Velocity vector of intersection of body and free surface
$\boldsymbol{\sigma}$	Vector of source strengths
$\boldsymbol{\omega}$	Angular velocity vector in body-fixed coordinate system (p, q, r)
$\dot{\boldsymbol{\omega}}$	Angular acceleration vector in body-fixed coordinate system
$\boldsymbol{\Omega}$	Angular velocity vector in space-fixed coordinate system $(\dot{\eta}_4, \dot{\eta}_5, \dot{\eta}_6)$

1. Introduction

1.1 Background

Seaworthiness is an important subject concerning the safety of ships in waves. The ship shall be capable of operating safely in high waves, and it has to be designed to withstand wave loads. The mission of the ship and the environmental conditions define one of the design bases of ships. The predictions of wave loads are based on these environmental and operating conditions. The wave loads can range from slowly varying drift loads to slamming loads, and the importance of the different wave loads can change between ship types.

The wave-induced loads can be divided into frequency ranges depending on the dynamic behaviour of the ship and the structure. For example, the wave-induced responses can be divided into low, wave and high frequency ranges. In the low frequency range, the second-order wave-exciting forces induce slowly varying rigid body motions. Typical responses are large motions in the horizontal plane of moored offshore structures such as drift motions. The period of the low frequency responses is in the order of 20 seconds and above. Conventional wave frequency responses are rigid body motions and accelerations that occur at the same frequencies as the ocean surface waves. The wave periods of the ocean surface waves vary from about 3 to 15 seconds. In the high frequency range, typical responses are, for example, springing and whipping responses that induce dynamic responses on hull structures. In the high frequency range, the structural dynamic is important. Whipping is defined as a hull girder vibration in the lowest natural frequencies due to wave impact. Springing is continuous vibration of the hull girder due to encountered wave excitation. The duration of the slamming impact can be in the order of one second, and the duration of pressure peaks can clearly be shorter. The periods of dynamic responses of structures in the high frequency range are in the order of magnitude of one second for a hull girder and lower for local structures.

The ship structure's stresses can be divided into global hull girder stresses and local structural detail stresses. The global and local stresses are usually called primary and secondary stresses or, in more detail, primary, secondary and tertiary stresses. For example, the primary stresses affect a hull girder and the secondary stresses a whole double bottom. Tertiary stresses affect double bottom longitudinal stiffeners or a bottom plate. Hull girder primary stresses are an important part of the total stresses in the structures, and the allowable primary stress level also defines the sensitiveness of a structure to fatigue. One of the starting points for the structural design and analysis of the ships and marine structures is to define environmental and operating conditions. For ultimate strength analyses, extreme environmental conditions have to be defined in order to obtain the design loads for structural analyses. The extreme condition is typically the most severe sea state in the ship's lifetime that induces the largest stresses in the structural details. As different wave conditions and different types of loads may induce large stresses, several different conditions have to be considered. In a fatigue analysis, the whole operating profile of a ship is needed to obtain all the stress cycles that the ship will encounter during her service life. This means that all of the different environmental and operating conditions in the ship's lifetime have to be considered in analyses.

It is common practice in ship design to determine the wave loads by applying rules and standards. However, general standards and rules can sometimes be difficult to apply to unconventional ships. For example, the size of ships is increasing and new structural designs have been introduced. For complex structures and designs, direct calculation procedures are necessary. The direct calculation of wave loads in the structural analysis is now common practice for offshore structures. However, the direct calculation procedures, especially the calculation of the wave loads, are seldom applied to ships. One reason can be the rather great uncertainties in the wave load predictions for ships and the theoretical backgrounds of the calculation methods are not necessarily sufficient to obtain reliable predictions. For example, the forward speed of the ship is not properly taken into account in the methods or the methods are based on linear theory so that the extreme load predictions of the nonlinear responses are not possible. In the rules of classification societies, the wave loads and structural responses can be determined separately, for example, the external pressures and wave bending moments can be determined first, followed by the structural responses to determine structural scantlings. In principle, the rule loads can be compared with the loads calculated by direct methods. However, rule requirements for loads and structural responses can depend on each other to fulfil defined strength criteria for structural scantlings.

Direct calculations of wave loads in structural analyses of ships are generally based on linear theories expressed in the frequency domain. Responses can be assumed to be linear with respect to excitation if a change in the magnitude of excitation induces the same magnitude change in the responses. In the linear methods, the ship motions and wave amplitudes are assumed to be small and the body and free surface boundary conditions can be linearized. The linear methods cannot take into account the body geometry above the mean water level. However, the most frequent waves are relatively low and the linear theory is sufficient to predict the frequent load cycles that are important in fatigue analyses of ship structures. In high waves, the linearity assumption of wave loads with respect to wave height is not usually valid. Recently, several different approaches have been developed to take into account nonlinearities in wave load predictions. In the nonlinear calculation methods, the hydrodynamic boundary value problem is often expressed in the time domain. In nonlinear methods, the exact body boundary condition is used and the free surface condition is usually linearized.

The predictions of the wave-induced primary stresses are important in the ultimate strength assessment of the hull girder. If the hull girder has compression on deck it is called a sagging condition and a hogging condition if a compression is on a bottom. The sagging condition occurs if wave crests are at the bow and stern and hogging if a wave crest is at midship. The sagging increases if the ship has a large bow flare and the ship motions are large with respect to waves. The stern form of the ship can have the same effect if the ship has a flat bottom stern close to the water level. In the structural design of ships, it is common practice to express the extreme design wave loads by means of the sagging and hogging bending moments and shear forces. The sagging and hogging bending moments and shear forces are hull girder loads. The hull girder loads are internal forces and moments affecting the cross section of the ship hull. Accurate prediction of extreme wave loads is important in the ultimate strength assessment of the hull girder. For ships in heavy seas, the sagging loads are greater than the hogging loads. The linear theories cannot predict the differences between sagging and hogging loads.

1.2 Objective

The objective of this work is to study hydrodynamic loads of ships in waves, with the emphasis on nonlinear wave loads. The aim of the work is to increase understanding of wave loads for modern ship types by applying a numerical method and experimental results and to develop a reliable and practical calculation method of wave loads in regular and irregular waves that can be applied to ship-wave interaction problems in structural analyses.

1.3 Previous work

Direct calculations of wave loads in structural analyses are generally based on linear theories, but recently several different approaches have been developed to take into account nonlinearities in wave load predictions. A summary of different methods in seakeeping computations is given by Beck and Reed (2000).

Linearization of the free surface and the body boundary conditions with respect to the wave amplitude means that the wave amplitude is assumed to be small. In linear frequency domain methods, the body and free surface boundary conditions are linearized. The solution of the linear problem is typically carried out in the frequency domain using a frequency domain representation of the Green functions (see, e.g., Chang, 1977; Inglis and Price, 1982; Iwashita and Ohkusu, 1989; Iwashita, 1997). When a linear theory is used, all the hydrodynamic quantities are calculated up to the undisturbed mean water level. Hence, applying panel methods, it is sufficient that only the mean wetted surface of the hull is discretized by panels.

A two-dimensional method for large-amplitude ship motions and wave loads was presented by Fonesca and Guedes Soares (1998). The method was based on a strip-theory approach, and the radiation and diffraction forces and moments were linear. Nonlinear effects were included in hydrostatic restoring and Froude-Krylov forces and moments. A quadratic strip theory was applied by Jensen et al. (2008) to determine extreme hull girder loads on container ships. The method included the flexibility of the hull girder. A simplified procedure was also developed to analyse the hull girder loads and determine a long-term probability distribution for responses. Matusiak (2000) presented a two-stage approach to ship simulation in the time domain. This method included nonlinear effects in hydrostatic restoring and Froude-Krylov forces and moments.

A nonlinear hydroelastic method based on a two-dimensional strip theory was presented by Wu and Moan (1996, 2005). Furthermore, a stochastic method was described by Wu and Moan (2006) to predict extreme hull girder loads in irregular waves. Model test results for a container ship in regular and irregular oblique waves as well as calculated results were presented by Drummen et al. (2009) and Zhu et al. (2011).

Time domain three-dimensional linear and nonlinear methods based on a transient Green function were presented by Ferrant (1991), Lin and Yue (1991), Kataoka et al. (2002) and Sen (2002). The time domain representation of the Green function allows the exact body boundary condition to be applied. This means that pres-

sures can be solved in the actual floating position of the body and not only on the mean wetted surface. For example, Lin and Yue (1991) applied the exact body boundary condition in their seakeeping program LAMP (large amplitude motion program). The transient Green function can also be solved beforehand to reduce the computational time. Ferrant (1991) applied pre-calculated Green function values using a bilinear interpolation in the time domain calculation. The transient Green function was also applied to impulse response function approaches to solve hydrodynamic forces and moments. Bingham et al. (1994) and King et al. (1989) used an impulse response function method to solve a linearized boundary value problem calculating ship motions at forward speed.

A Rankine source method was applied to the ship motions and wave loads computation by Sclavounos et al. (1993). In the Rankine source methods, the free surface is discretized by panels as well as the body surface. A nonlinear Rankine source method was presented by Huang and Sclavounos (1998) and a weak-scatterer hypothesis (Pawlowski, 1992) applied. In the weak-scatterer hypothesis, the disturbance due to the ship motions in the wave flow is assumed to be small compared with the wave flow due to the incoming wave. Model tests and computations by the Rankine source method for the motions and loads of the container ship were given by Song et al. (2011). Koo and Kim (2004) presented a two-dimensional non-linear method in which the fluid flow was solved with two-dimensional Rankine sources. The boundary condition at the free surface was nonlinear and the exact body boundary condition was satisfied on the body surface. They applied an acceleration-potential formulation to solve the time derivative of the velocity potential in Bernoulli's equation (Tanizawa, 1995). Two- and three-dimensional methods based on the Rankine sources were presented by Zhang et al. (2010). The exact body boundary condition was used and the free surface boundary condition was linear.

A hybrid formulation was presented by Dai and Wu (2008) and Weems et al. (2000). They used the transient Green function on the outer domain and Rankine sources in the inner domain to solve the velocity potential. Applying the hybrid formulation, the possible instabilities in the transient Green function solution can be avoided. Kataoka and Iwashita (2004) presented a hybrid method in which the artificial boundary between the outer and inner domain was expressed in the space-fixed co-ordinate system. The use of the space-fixed co-ordinate system makes the method free from the line integral that appears typically when the moving artificial boundary is used.

Applying the Reynolds averaged Navier-Stokes (RANS) solver, Weymouth et al. (2005) calculated heave and pitch motions for a Wigley hull form in head seas. At the free surface, a surface-tracking approach was employed.

1.4 Present work

This work consists of numerical and experimental investigations. Model tests have been carried out to gain an insight into the nonlinear effects on ship motions and hull girder loads. A theory for a nonlinear method is presented and a calculation method has been developed for ship-wave interaction problems.

In particular, the scientific contribution and original features involve the following items:

1. The development of a time domain computer program for ship responses in regular and irregular waves has been carried out and the calculation method is presented in detail.

2. An application of the acceleration potential method to solve the time derivative of the velocity potential in Bernoulli's equation is presented. A body boundary condition is derived for the acceleration potential. The aim was to come up with a reliable solution for hydrodynamic pressures on the hull surface, especially if a ship has a flat bottom stern close to the free surface.

3. A transient Green function is solved using a numerical integration formula. The transient Green function is evaluated beforehand, and a finite element approximation has been adopted to interpolate the Green function values at each time step.

4. A verification of the calculation method is presented for a hemisphere and cones, and Wigley hull forms are used in validation. Simple linear and nonlinear solutions for cones are applied to the verifications of the calculation method and to the investigations of nonlinear effects.

5. Model tests have been carried out to obtain experimental data on nonlinear wave loads for modern ship hull forms, especially for hull forms that have a flat bottom stern. The model test results for motions, accelerations and hull girder loads are presented in regular and irregular head waves at zero and forward speeds and in calm water at different forward speeds.

6. Nonlinearities in responses are studied using calculated and model test results. The calculation method is used to predict motions and hull girder loads for the model test ship in regular and irregular head waves at zero and forward speeds. Moreover, steady hull girder loads in calm water at forward speeds are studied. The calculated motions and hull girder loads are compared with the model test results. A stochastic method is also applied to predict extreme values for the hull girder loads in short-term sea states for the model test ship.

This work focuses on wave-induced loads, and the investigations concentrate on nonlinear wave loads. The wave loads of the model test ship are studied with integrated external pressure loads and inertia loads, i.e. vertical bending moments and shear forces. The vertical bending moments and shear forces are internal loads at the cross sections of the hull girder. The hull girder is assumed to be rigid and the structural dynamics of the hull girder are not taken into account. This study concentrates on the wave loads in the wave frequency range.

In Chapter 2, the theory and numerical procedures of the time domain computer program are presented. First, the used coordinate systems are defined, and definitions of the transformation of the vectors between different coordinate systems are given. The frequently used notations in this work are also explained. Next, the governing equations and the hydrodynamic boundary and initial value problems are presented. The boundary and initial value problems for the perturbation velocity potential are similar to those given by Ferrant (1991), Lin and Yue (1991), and Sen (2002). The solution of the boundary value problem is based on source distributions on the body surface. The source distributions are represented with a transient three-dimensional Green function. The solution of the boundary value problem is expressed in the space-fixed coordinate system. The time domain computer program includes the solutions of the exact and linear body boundary conditions. The free surface boundary condition is linear. In the nonlinear calculation, the instantaneous position of the ship with respect to the mean water level is updated at every time step. Constant panel sizes and panel mesh are applied in the calculation method.

A method to solve the time derivative of the velocity potential in Bernoulli's equation is presented in this work. The solution is based on the same source formulation and transient Green function as the boundary value problem for the perturbation velocity potential but with a different body boundary condition. The acceleration potential method has been implemented in the calculation method. The acceleration potential method is verified using a hemisphere and cones in

harmonic heave motions at free surface. The acceleration-potential method is used to solve responses for Wigley hull forms and the model test ship.

A numerical integration of the memory part of the transient Green function is presented in this work. The numerical integration of the memory part is based on an adaptive Gauss-Kronrod quadrature formula. In order to reduce the computational time, the memory part is solved beforehand and the results are stored in the file. In the beginning of the time domain calculation, the table of the Green function values is read into the computer's memory and the Green function values are interpolated applying a finite element approximation.

Simple body geometries are used in verifications and validations of the time domain computer program. An analytical solution of the hydrodynamic added mass and damping coefficients for a hemisphere are used in the verification. Simple solutions of hydrodynamic forces for cones in a forced heave motion at free surface are also applied to verify the calculation method. Moreover, nonlinear heave radiation forces are approximated using the geometrical similarity of the cones. The aim was to obtain an insight into the nonlinearities in radiation and the hydrostatic restoring forces. Furthermore, experimental results of Wigley hull forms are used to validate the calculation method in regular waves and calm water. The analytical solution for the hemisphere and the experimental results for the Wigley hull forms have been commonly used in developing seakeeping calculation methods.

Model tests of a roll-on roll-off passenger (RoPax) ship are presented. The ship model has a flat bottom stern at the waterline (counter stern). Model test results of ship motions and vertical shear forces, and bending moments in regular and irregular head waves are given. In addition, model test results in calm water at different forward speeds are presented for sinkage of the ship and for steady vertical shear forces and bending moments.

The nonlinear effects on ship motions and hull girder loads are investigated using calculated and model test results. The investigations focused on sagging and hogging bending moments at midship and shear forces at the fore ship. The calculation method is applied to solve motions and hull girder loads for the model test ship. The calculated responses are compared with the model test results. Procedures to predict the extreme values of wave loads in design sea states are also reviewed. A procedure is applied to determine extreme hull girder loads for the model test ship. The RoPax model test ship used in this work is the same as that used in the earlier investigations in Kukkanen (2009, 2010). However, the earlier

calculated results were based on different solutions and numerical algorithms to those presented in this work.

Finally, the discussion and conclusions of the results and recommendations for further studies are given in the last two chapters.

2. Time domain calculation method

2.1 Definitions

In the time domain method, two coordinate systems are used: a space-fixed coordinate system $Oxyz$ and a body-fixed coordinate system $Ox_0y_0z_0$. The coordinate systems are shown in Figure 2.1. The space-fixed coordinate system is the inertial reference frame. The origin of the space-fixed coordinate system is at the calm water plane with the z-axis pointing vertically upwards. The forward speed of the body is U_0. The forward speed is defined as the speed of the centre of gravity of the body and the body moving at speed U_0 parallel to the direction of the x-axis if the other motions in the y- and z-directions are zero. The longitudinal coordinate x_0 of the body-fixed coordinate system is pointing to the bow of the body and the z_0-axis is pointing vertically upwards. The origin of the body-fixed coordinate system is at the centre of gravity of the body. The incoming waves are travelling with angle χ with respect to the x-axis and the heading angle of $\chi = 180$ degrees corresponds to head sea. The six degrees of freedom body motions are surge (η_1), sway (η_2), heave (η_3), roll (η_4), pitch (η_5) and yaw (η_6), defined with respect to the space-fixed coordinate system. The translational motions surge, sway and heave define the position of the centre of gravity of the body in the space-fixed coordinate system. The surge velocity $\dot{\eta}_1$ includes the forward speed U_0. Normal vectors are defined as positive, pointing out of the fluid.

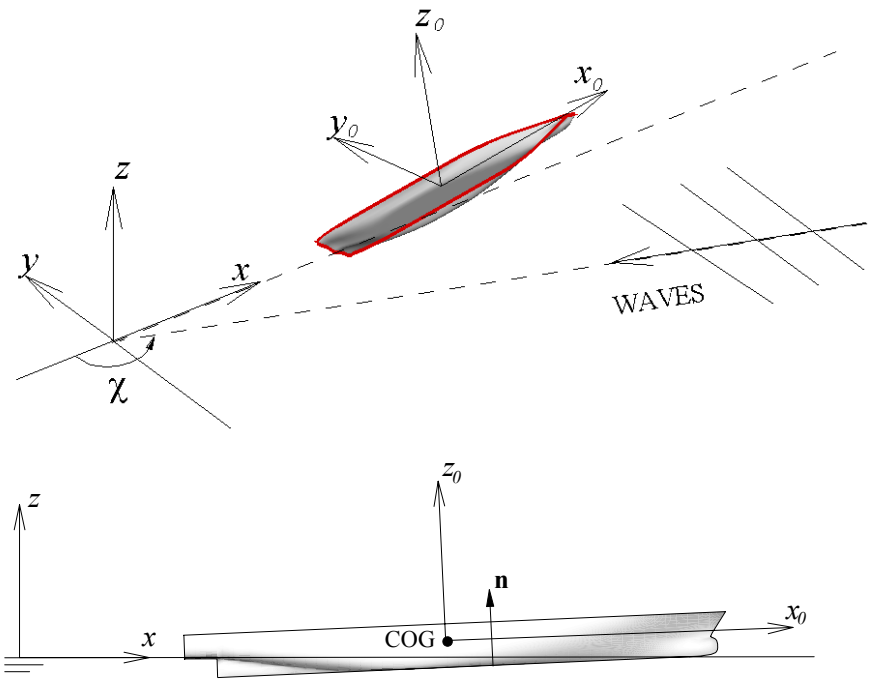

Figure 2.1. Coordinate systems used in the time domain method.

The relations between the body and space-fixed coordinate systems are given by the Eulerian angles roll, pitch and yaw (see, e.g., Salonen, 1999). All of the vector operations are evaluated for the vectors that are expressed in the same reference frame. The relation between the space-fixed and body-fixed coordinate systems is determined by vector transformations, applying the sequence of rotations yaw, pitch and roll. The orientation of the body velocities from the body-fixed coordinate system to the space-fixed coordinate system is obtained using the following transformation matrices:

$$\dot{\mathbf{x}}_G = [\mathbf{L}]\mathbf{u} \quad \text{or as} \quad \begin{Bmatrix} \dot{\eta}_1 \\ \dot{\eta}_2 \\ \dot{\eta}_3 \end{Bmatrix} = [\mathbf{L}] \begin{Bmatrix} u \\ v \\ w \end{Bmatrix} \tag{2.1}$$

$$\boldsymbol{\Omega} = [\mathbf{B}]\boldsymbol{\omega} \quad \text{or as} \quad \begin{Bmatrix} \dot{\eta}_4 \\ \dot{\eta}_5 \\ \dot{\eta}_6 \end{Bmatrix} = [\mathbf{B}] \begin{Bmatrix} p \\ q \\ r \end{Bmatrix} \tag{2.2}$$

Here, $\mathbf{u} = (u, v, w)$ is the vector of translational velocities and $\boldsymbol{\omega} = (p, q, r)$ is the vector of the angular velocities expressed in the body-fixed coordinate system. In the space-fixed coordinate system, the same velocities are the translational velocities $\dot{\mathbf{x}}_G = (\dot{\eta}_1, \dot{\eta}_2, \dot{\eta}_3)$ and the rotational velocities $\boldsymbol{\Omega} = (\dot{\eta}_4, \dot{\eta}_5, \dot{\eta}_6)$. The transformation matrix is [**L**] for the translational velocities and [**B**] for the angular velocities. The matrices are given as follows:

$$[\mathbf{L}] = \begin{bmatrix} c5c6 & -c4s6 + s4s5c6 & s4s6 + c4s5c6 \\ c5s6 & c4c6 + s4s5s6 & -s4c6 + c4s5s6 \\ -s5 & s4c5 & c4c5 \end{bmatrix} \tag{2.3}$$

$$[\mathbf{B}] = \begin{bmatrix} 1 & s4t5 & c4t5 \\ 0 & c4 & -s4 \\ 0 & s4/c5 & c4/c5 \end{bmatrix} \tag{2.4}$$

where $c\mathrm{i} = \cos\eta_i$, $s\mathrm{i} = \sin\eta_i$ and $t5 = \tan\eta_5$. From the space-fixed to body-fixed coordinate system, the transformation formulae are given by

$$\mathbf{u} = [\mathbf{L}]^{-1}\dot{\mathbf{x}}_G \tag{2.5}$$

$$\boldsymbol{\omega} = [\mathbf{B}]^{-1}\boldsymbol{\Omega} \tag{2.6}$$

The inverse of the transformation matrices is as follows:

$$[\mathbf{L}]^{-1} = [\mathbf{L}]^{\mathrm{T}} = \begin{bmatrix} c5c6 & c5s6 & -s5 \\ -c4s6 + s4s5c6 & c4c6 + s4s5s6 & s4c5 \\ s4s6 + c4s5c6 & -s4c6 + c4s5s6 & c4c5 \end{bmatrix} \tag{2.7}$$

$$[\mathbf{B}]^{-1} = \begin{bmatrix} 1 & 0 & -s5 \\ 0 & c4 & s4c5 \\ 0 & -s4 & c4c5 \end{bmatrix} \tag{2.8}$$

The transformation matrix [**L**] is used to transform directional vectors between the body-fixed and space-fixed coordinate systems. The position vector $\mathbf{r} = (x_0, y_0, z_0)$ from the centre of gravity of the body to the point at (x_0, y_0, z_0) in the body-fixed coordinate system can be expressed in the space-fixed coordinate system using the following transformation

$$\mathbf{x} = [\mathbf{L}]\mathbf{r} + \mathbf{x}_G\ , \tag{2.9}$$

where $\mathbf{x}_G = (\eta_1, \eta_2, \eta_3)$ is the position of the centre of gravity of the body expressed in the space-fixed coordinate system. The position vector from the space-fixed coordinate system to the body-fixed coordinate system is given as

$$\mathbf{r} = \left[\mathbf{L}\right]^{-1}\left(\mathbf{x} - \mathbf{x}_G\right) . \tag{2.10}$$

The orientation of the normal vector can be defined in a body-fixed or space-fixed coordinate system. From the body-fixed coordinate system to the space-fixed coordinate system the transformation is given by

$$\mathbf{n}(x, y, z) = \left[\mathbf{L}\right]\mathbf{n}(x_0, y_0, z_0) . \tag{2.11}$$

Definitions of frequently used notations in this work are given below.

Body linear solution: The body position is not updated during the calculation and the wetted surface of the body remains the same as at $t = 0$. The pressure is solved for the mean wetted surface below the mean waterline $z = 0$.

Body nonlinear solution: The instantaneous position of the body is updated during the calculation. The pressure is solved for the instantaneous wetted surface of the body below $z = 0$.

Body-wave nonlinear solution: The solution is the same as the body nonlinear solution but includes additional nonlinear effects in Froude-Krylov and hydrostatic restoring forces and moments; see Section 2.4.5. The Froude-Krylov and hydrostatic restoring pressures are solved up to the incoming wave elevation $z = \zeta$.

Constant panel mesh: The panel mesh is not updated during the time domain calculation. The geometry and size of the panels remain the same in the calculation and the panel mesh is the same as at time $t = 0$. Alternatively, the body surface can be re-panelized at every time step applying *spline-fitted mesh* to represent the body surface. The term *constant panel mesh* shall be distinguished from the *constant panel method* that is used in the numerical solution of the velocity potential.

Acceleration potential method: The time derivative of the velocity potential is solved using the source formulation. The solution is based on the Green function and the body boundary condition defined for the acceleration potential. Details are given in Section 2.3.2. Alternatively, the *backward difference method* can be applied to approximate the time derivative of the velocity potential. In the back-

ward difference method, the velocity potentials at the present and previous time steps are used.

2.2 Governing equations

The governing equations to describe the fluid flow are given in this section. Throughout this work, it is assumed that the fluid is inviscid and the fluid density ρ is constant. The fundamental conservation laws are the conservation of mass and momentum to describe the fluid velocity components v_1, v_2, v_3 and the pressure p_1. The governing equations presented in this section are given in, for example, Stoker (1958), Newman (1977) and Mei (1992). As the fluid density ρ is constant, the fluid is incompressible and the conservation of mass is given by the continuity equation as follows:

$$\nabla \cdot \mathbf{v} = 0 , \tag{2.12}$$

where $\mathbf{v}$ is the velocity vector of the fluid, $\mathbf{v} = (v_1, v_2, v_3)$. As the fluid is inviscid, the conservation of momentum can be given by Euler's equations as follows:

$$\left(\frac{\partial}{\partial t} + \mathbf{v} \cdot \nabla \right) \mathbf{v} = -\frac{1}{\rho} \nabla \left(p_1 + gz \right), \tag{2.13}$$

where g is the gravity acceleration and p_1 is the pressure, $p_1 = p_1(x, y, z, t)$. These equations can be further simplified assuming that the flow is irrotational. For inviscid fluid, the flow remains irrotational for all times if there is no vorticity at the initial time. The vorticity vector is defined as $\nabla \times \mathbf{v}$ and the irrotational flow as $\nabla \times \mathbf{v} = 0$. For the irrotational flow, the fluid velocity is given by the gradient of the scalar potential function

$$\mathbf{v} = \nabla \Phi , \tag{2.14}$$

where Φ is the velocity potential. Hence, it follows from the continuity equation Laplace's equation:

$$\nabla^2 \Phi = 0 . \tag{2.15}$$

Expressing the fluid velocities with the velocity potential in Euler's equations and integrating them with respect to the space variables, Bernoulli's equation for the pressure is obtained:

$$-\frac{p_1}{\rho} = \frac{\partial \Phi}{\partial t} + \frac{1}{2}\left|\nabla \Phi\right|^2 + gz + C\,. \tag{2.16}$$

The integration constant C depends on time but not on the space variables. The constant can be chosen arbitrarily or omitted and set to $C = 0$.

In addition to the conservation laws, the fluid has to satisfy boundary conditions on the fluid boundaries. A kinematic boundary condition has to be satisfied on fixed and moving surfaces. The kinematic boundary condition means that the velocity of the fluid particle has the same normal velocity as the boundary surface at the same point. The kinematic boundary condition on the moving surface is given by

$$\frac{\partial \Phi}{\partial n} = \mathbf{U} \cdot \mathbf{n}\,. \tag{2.17}$$

Here, $\mathbf{n}$ is the unit normal to surface pointing out of the fluid and $\mathbf{U}$ is the instantaneous velocity of the surface. If the surface is fixed, the right-hand side of the above equation is zero. The term $\partial\Phi/\partial n$ is the derivative in the normal direction and is given by $\partial\Phi/\partial n = \mathbf{n} \cdot \nabla\Phi$.

The kinematic free surface boundary condition can be expressed as follows

$$\frac{\partial \zeta}{\partial t} + \frac{\partial \Phi}{\partial x}\frac{\partial \zeta}{\partial x} + \frac{\partial \Phi}{\partial y}\frac{\partial \zeta}{\partial y} - \frac{\partial \Phi}{\partial z} = 0 \qquad \text{on } z = \zeta(x,y,t)\,, \tag{2.18}$$

where ζ is the free surface elevation. On the free surface, an additional boundary condition has to be included because the free surface itself is an unknown moving surface. The additional boundary condition is the dynamic free surface boundary condition:

$$g\zeta + \frac{\partial \Phi}{\partial t} + \frac{1}{2}\left|\nabla \Phi\right|^2 = -\frac{p_a}{\rho} \qquad \text{on } z = \zeta(x,y,t)\,, \tag{2.19}$$

where p_a is the atmospheric pressure that is assumed to be constant.

As the free surface boundary condition has to be solved at the instantaneous free surface elevation around the body and the body boundary conditions have to be solved on the instantaneous wetted surface, the boundary value problem is nonlinear. Linearization of the free surface boundary conditions with respect to the wave amplitude means that the wave amplitude is assumed to be small, only

linear terms are retained and higher order terms can be ignored. If the linear free surface boundary condition is used, the velocity potential can be solved up to the undisturbed mean water level $z = 0$ and not on the actual free surface $z = \zeta$. The linear free surface boundary conditions can be expressed as follows for the kinematic free surface condition:

$$\frac{\partial \zeta}{\partial t} - \frac{\partial \Phi}{\partial z} = 0 \qquad \text{on } z = 0, \tag{2.20}$$

and for the dynamic free surface condition

$$g\zeta + \frac{\partial \Phi}{\partial t} = -\frac{p_a}{\rho} \qquad \text{on } z = 0. \tag{2.21}$$

The kinematic and dynamic conditions can be combined to yield to the following free surface boundary condition

$$\frac{\partial^2 \Phi}{\partial t^2} + g\frac{\partial \Phi}{\partial z} = 0 \qquad \text{on } z = 0. \tag{2.22}$$

The time domain calculation method presented in this work is based on the inviscid and incompressible fluid, and the fluid flow is irrotational. The exact body boundary condition is satisfied and the free surface boundary condition is linear.

2.3 Theory of the method

2.3.1 Boundary value problem

The hydrodynamic forces and moments can be determined after the hydrodynamic boundary value problem has been solved for the body in waves. The hydrodynamic forces and moments can be calculated if the pressure on the body surface is known. The pressure is obtained from Bernoulli's equation and is expressed by means of the velocity potential. In the time domain method presented in this work, the velocity potential is expressed as a decomposition of the perturbation and incoming wave velocity potentials:

$$\Phi = \phi + \phi_I, \tag{2.23}$$

where the perturbation velocity potential is ϕ and the velocity potential of the incoming wave is ϕ_I.

The velocity potential of the incoming wave ϕ_I is given by an analytical formula. The perturbation velocity potential describes the fluid flow due to the radiation and diffraction by a floating body. The perturbation velocity potential ϕ is represented by means of source distributions and using Green's theorem. Green's theorem gives integral equations for the velocity potential where the source distributions over the body surface are represented using a three-dimensional transient Green function. The unknown source strengths are obtained satisfying the body boundary condition on the hull surface. Once the velocity potentials are known, the pressure on the body surface is obtained from Bernoulli's equation. The forces and moments acting on the body can be calculated by integrating the pressure over the wetted surface of the body. The accelerations of the body are solved from the equations of motion. The motions of the body can be determined when the accelerations are known.

In this work, the time derivative of the perturbation velocity potential $\partial\phi/\partial t$ in Bernoulli's equation is solved using an acceleration-potential method. The boundary value problem for $\partial\phi/\partial t$ is otherwise the same as for ϕ but the body boundary condition is different. The body boundary condition in the acceleration potential method is presented in Section 2.3.2. The time derivative of the velocity potential is the first term on the right-hand side in Bernoulli's equation (2.16).

Here, the boundary value problem is given for the perturbation velocity potential ϕ. The formula for the incoming wave velocity potential ϕ_I is also given. The boundary value problem is expressed in the space-fixed coordinate system.

The velocity potential ϕ has to satisfy Laplace's equation:

$$\nabla^2\phi = 0\,, \tag{2.24}$$

everywhere in the fluid. On the free surface S_F, the linear free surface boundary condition is given by

$$\frac{\partial^2\phi}{\partial t^2} + g\frac{\partial\phi}{\partial z} = 0\,, \qquad \text{on } S_F,\ z = 0. \tag{2.25}$$

The boundary condition on the body surface S_B is given as follows:

$$\frac{\partial\phi}{\partial n} = \mathbf{U}\cdot\mathbf{n} - \frac{\partial\phi_I}{\partial n}\,, \qquad \text{on } S_B, \tag{2.26}$$

where **n** is the unit normal to the body pointing out of the fluid and **U** is the velocity of the point on the body surface.

In addition, the boundary condition on the sea bottom is given by the condition:

$$\frac{\partial \phi}{\partial n} = 0, \qquad z \to -\infty. \tag{2.27}$$

Hence, an infinite water depth is assumed. The radiation condition takes into account that the body-generated waves are progressing outwards and vanishing at infinity:

$$\frac{\partial \phi}{\partial n} \to 0, \qquad r \to \infty, \tag{2.28}$$

where $r = \sqrt{x^2 + y^2}$.

In addition to the boundary conditions, the boundary value problem has to satisfy the following initial conditions:

$$\phi = 0 \text{ and } \frac{\partial \phi}{\partial t} = 0 \qquad \text{at } t = 0, \tag{2.29}$$

i.e. the fluid flow is not disturbed by the body at $t = 0$.

The velocity potential of the incoming wave satisfies Laplace's equation, the linear boundary condition at the free-surface and the bottom boundary condition. The velocity potential of the deep water linear wave can be given in the following form:

$$\phi_I = \mathrm{Re}\left\{ i \frac{ga}{\omega} \mathrm{e}^{-i(kx\cos\chi + ky\sin\chi)} \mathrm{e}^{kz} \mathrm{e}^{i\omega t} \right\}, \tag{2.30}$$

where a is the wave amplitude, ω is the wave frequency, and k is the wave number, $k = 2\pi/\lambda_w = \omega^2/g$. The imaginary unit is i.

In the body nonlinear solution, the exact body boundary condition is used and the perturbation potential is solved at the actual floating position of the body. The body boundary condition is applied to the instantaneous wetted surface $S_B(t)$ on $z < 0$. In the body boundary condition (2.26), the instantaneous normal component of the velocity of the point on the body surface is given by

$$\mathbf{U} \cdot \mathbf{n} = \left(\mathbf{u} + \boldsymbol{\omega} \times \mathbf{r}\right) \cdot \mathbf{n} \,, \tag{2.31}$$

where the position vector **r** and the velocities **u** and **ω** are given in the body-fixed coordinate system and hence the normal vector **n** is also expressed in the body-fixed coordinate system. Thus, all the vector operations are performed in the same coordinate system. In the body boundary condition (2.26), the fluid velocities of the incoming wave $\nabla\phi_I$ are expressed in the space-fixed coordinate system. Thus, the normal derivative of the velocity potential of the incoming wave $\partial\phi_I/\partial n = \mathbf{n} \cdot \nabla\phi_I$ is expressed in the space-fixed coordinate system. The orientation of the normal vector from the body-fixed to the space-fixed coordinate system is given by the relation (2.11).

In the body linear solution, the wetted surface of the body S_B is independent of time and remains the same as at time $t = 0$. Hence, the body boundary condition is applied to the mean wetted surface of the body. However, the motions of the body-fixed coordinate system with respect to the space-fixed coordinate system are taken into account in the linear sense. In the body boundary condition, the velocities of the body in the body-fixed coordinate system are expressed using linear forms of the transformation equations (2.5) and (2.6). The linear form of the transformation matrix [**B**] for the angular velocities is the unit matrix, and the linear form of the transformation matrix $\left[\mathbf{L}\right]^{-1}$ for the translational velocities **u** is given by

$$\left[\mathbf{L}\right]^{-1} = \begin{bmatrix} 1 & \eta_6 & -\eta_5 \\ -\eta_6 & 1 & \eta_4 \\ \eta_5 & -\eta_4 & 1 \end{bmatrix}. \tag{2.32}$$

2.3.2 Boundary condition of the acceleration potential

The time derivative of the velocity potential $\phi_t = \partial\phi/\partial t$ appears in Bernoulli's equation. The term acceleration potential is also used for the time derivative of the velocity potential. The boundary value problem for the velocity potential given in the previous section does not give a direct solution for the acceleration potential. In the time domain methods, the acceleration potential is often solved using numerical methods such as a backward difference method (see, e.g., Lin and Yue, 1991; Sen, 2002). In the backward difference method, the acceleration potential is approximated by applying the substantial derivative of the velocity potential as follows:

$$\frac{\partial \phi_k}{\partial t} \approx \frac{\phi_k - \phi_{k-1}}{\Delta t} - \mathbf{U}_k \cdot \nabla \phi_k \,, \tag{2.33}$$

where ϕ_k is the velocity potential at time step k and Δt is the time step size. Hence, the solution includes the velocity potentials from present and previous time steps.

The solution of the time derivative of the velocity potential can also be determined by solving a boundary value problem defined for the acceleration potential. Different methods have been developed to solve ϕ_t and the differences in the methods depend on the applied boundary conditions and the solution methods, for example, Rankine source methods have been used. One method is to solve $\phi_t + \mathbf{U} \cdot \nabla \phi$, i.e. solving the substantial derivative of ϕ instead of solving ϕ_t directly. Vinje and Brevig (1981) applied this method to calculate motions of two-dimensional bodies, and Kang and Gong (1990) gave a solution for three-dimensional free surface problems. Greco (2001) applied a similar approach, studying a two-dimensional green water loading. Tanizawa (1995) developed a solution for the acceleration potential starting from the fluid acceleration. The boundary condition was determined for the acceleration of the fluid particle, which has to be the same as the acceleration on the point of the body surface. Hence, the fluid particle is followed and not the fluid on a fixed point on the body. The fluid acceleration is a nonlinear function of the velocity potential, and the potential for the fluid acceleration does not satisfy Laplace's equation. The nonlinear part can be subtracted to obtain a linear function that can be solved using the same methods as those used to solve the velocity potential. However, higher order derivatives of the velocity potentials have to be solved. The boundary condition also includes terms for which the curvature of the body is needed. Wu (1998) derived a boundary condition for the acceleration potential starting from the body boundary condition of the velocity potential. The derived boundary condition includes higher order derivatives of the velocity potential. A similar boundary condition for the acceleration potential was presented by Bandyk and Beck (2011). A review and comparison of different acceleration-potential methods applied to the fluid and body interaction problems were given by Bandyk and Beck (2011). They also showed calculation results for two-dimensional bodies for which the velocity and acceleration potentials were solved using Rankine sources.

In this work, a boundary condition for the acceleration potential is derived that can be used in the time domain method in the body nonlinear and linear solutions. The same approach was applied as Kang and Kong(1990) to represent the problem by the substantial derivative of ϕ instead of solving ϕ_t directly. However, the present boundary condition includes also terms due to the incident wave potential ϕ_I. The terms describing the body motions are the same as presented by

Wu(1998) and Kang and Kong(1990). Furthermore, the acceleration potential is also solved by applying the panel method for which source distributions are expressed by means of the transient Green function in integral equations.

The boundary condition for the acceleration potential is derived from the body boundary condition (2.26). Taking the absolute time derivative in the inertial reference frame from both sides of the body boundary condition for the velocity potential ϕ, it follows that

$$\frac{d}{dt}\left(\frac{\partial\phi}{\partial n}\right) = \frac{d}{dt}\left[\left(\mathbf{U} - \nabla\phi_I\right)\cdot\mathbf{n}\right] \qquad \text{on } S_B. \tag{2.34}$$

The left-hand side of the above equation can be written as

$$\frac{d}{dt}\left(\frac{\partial\phi}{\partial n}\right) = \frac{d}{dt}\left(\mathbf{n}\cdot\nabla\phi\right) = \mathbf{n}\cdot\frac{d}{dt}\left(\nabla\phi\right) + \frac{d\mathbf{n}}{dt}\cdot\nabla\phi\,. \tag{2.35}$$

The time derivative of the normal vector is $\frac{d\mathbf{n}}{dt} = \boldsymbol{\omega}\times\mathbf{n}$. For the fluid term, the time derivative is evaluated following the fluid on the fixed point on the body surface. Hence, the time derivative is given by the substantial derivative:

$$\frac{d}{dt} = \frac{\partial}{\partial t} + \mathbf{U}\cdot\nabla\,, \tag{2.36}$$

and Equation (2.35) can be written as follows:

$$\frac{d}{dt}\left(\frac{\partial\phi}{\partial n}\right) = \mathbf{n}\cdot\left[\frac{\partial\nabla\phi}{\partial t} + (\mathbf{U}\cdot\nabla)\cdot\nabla\phi\right] + \left(\boldsymbol{\omega}\times\mathbf{n}\right)\cdot\nabla\phi\,. \tag{2.37}$$

The term $(\mathbf{U}\cdot\nabla)\cdot\nabla\phi$ can be given in the following form using a vector identity (Milne-Thomson, 1968, p. 46, 2-34 III):

$$\left(\mathbf{U}\cdot\nabla\right)\nabla\phi = \nabla\left(\mathbf{U}\cdot\nabla\phi\right) - \nabla\phi\times\left(\nabla\times\mathbf{U}\right) - \left(\nabla\phi\cdot\nabla\right)\mathbf{U} - \mathbf{U}\times\left(\nabla\times\nabla\phi\right). \tag{2.38}$$

As the flow is irrotational $\mathbf{U}\times\left(\nabla\times\nabla\phi\right) = 0$, it follows that

$$\left(\mathbf{U}\cdot\nabla\right)\nabla\phi = \nabla\left(\mathbf{U}\cdot\nabla\phi\right) - \nabla\phi\times\left(\nabla\times\mathbf{U}\right) - \left(\nabla\phi\cdot\nabla\right)\mathbf{U}\,. \tag{2.39}$$

The terms $\nabla\phi\times\left(\nabla\times\mathbf{U}\right)$ and $\left(\nabla\phi\cdot\nabla\right)\mathbf{U}$ can be further simplified substituting $\mathbf{U} = \mathbf{u} + \boldsymbol{\omega}\times\mathbf{r}$ in the two terms in the above equation. This gives the following result:

$$(\mathbf{U}\cdot\nabla)\nabla\phi = \nabla(\mathbf{U}\cdot\nabla\phi) - 2\nabla\phi\times\boldsymbol{\omega} + (\nabla\phi\times\boldsymbol{\omega}). \tag{2.40}$$

Substituting this back into Equation (2.37) gives

$$\frac{d}{dt}\left(\frac{\partial\phi}{\partial n}\right) = \mathbf{n}\cdot\left[\frac{\partial\nabla\phi}{\partial t} + \nabla(\mathbf{U}\cdot\nabla\phi) + \boldsymbol{\omega}\times\nabla\phi\right] + (\boldsymbol{\omega}\times\mathbf{n})\cdot\nabla\phi, \tag{2.41}$$

and changing the order of the vector operations in the last term, $(\boldsymbol{\omega}\times\mathbf{n})\cdot\nabla\phi = -\mathbf{n}\cdot(\boldsymbol{\omega}\times\nabla\phi)$, the above equation is given as follows:

$$\begin{aligned}\frac{d}{dt}\left(\frac{\partial\phi}{\partial n}\right) &= \mathbf{n}\cdot\left(\frac{\partial\nabla\phi}{\partial t} + \nabla(\mathbf{U}\cdot\nabla\phi)\right) + \mathbf{n}\cdot(\boldsymbol{\omega}\times\nabla\phi) - \mathbf{n}\cdot(\boldsymbol{\omega}\times\nabla\phi)\\ &= \mathbf{n}\cdot\nabla\left(\frac{\partial\phi}{\partial t} + \mathbf{U}\cdot\nabla\phi\right) = \frac{\partial}{\partial n}\left(\frac{d\phi}{dt}\right).\end{aligned} \tag{2.42}$$

Furthermore, defining a potential function φ as follows:

$$\varphi = \frac{\partial\phi}{\partial t} + \mathbf{U}\cdot\nabla\phi = \frac{d\phi}{dt}, \tag{2.43}$$

then Equation (2.42) can also be given as follows:

$$\frac{d}{dt}\left(\frac{\partial\phi}{\partial n}\right) = \frac{\partial\varphi}{\partial n}. \tag{2.44}$$

Hence, the left-hand side of Equation (2.34) is the normal derivative of the potential function φ.

The right-hand side of Equation (2.34) is

$$\frac{d}{dt}\left(\frac{\partial\phi}{\partial n}\right) = \frac{d}{dt}\left[(\mathbf{U}-\nabla\phi_I)\cdot\mathbf{n}\right] = \frac{d}{dt}(\mathbf{U}\cdot\mathbf{n}) - \frac{d}{dt}(\nabla\phi_I\cdot\mathbf{n}). \tag{2.45}$$

The velocity of the point on the body surface in the normal direction can be written as follows:

$$\frac{d}{dt}(\mathbf{U}\cdot\mathbf{n}) = \frac{d}{dt}\left[(\mathbf{u}+\boldsymbol{\omega}\times\mathbf{r})\cdot\mathbf{n}\right]$$

$$= \left(\dot{\mathbf{u}} + \dot{\boldsymbol{\omega}} \times \mathbf{r} + \boldsymbol{\omega} \times \left(\boldsymbol{\omega} \times \mathbf{r}\right)\right) \cdot \mathbf{n} + \left(\mathbf{u} + \boldsymbol{\omega} \times \mathbf{r}\right) \cdot \left(\boldsymbol{\omega} \times \mathbf{n}\right)$$

$$= \left(\dot{\mathbf{u}} + \dot{\boldsymbol{\omega}} \times \mathbf{r}\right) \cdot \mathbf{n} - \left(\boldsymbol{\omega} \times \mathbf{u}\right) \cdot \mathbf{n} \,, \tag{2.46}$$

where the translational acceleration vector of the centre of gravity of the body is $\dot{\mathbf{u}}$ and the angular acceleration vector of the body is $\dot{\boldsymbol{\omega}}$. Furthermore, the velocity of the incoming wave in the normal direction is given by

$$\frac{d}{dt}\left(\mathbf{n} \cdot \nabla \phi_I\right) = \mathbf{n} \cdot \frac{d}{dt}\left(\nabla \phi_I\right) + \nabla \phi_I \cdot \frac{d\mathbf{n}}{dt}$$

$$= \mathbf{n} \cdot \left(\frac{\partial \nabla \phi_I}{\partial t} + (\mathbf{U} \cdot \nabla) \nabla \phi_I \right) + \nabla \phi_I \cdot (\boldsymbol{\omega} \times \mathbf{n})$$

$$= \mathbf{n} \cdot \left(\frac{\partial \nabla \phi_I}{\partial t} + ((\mathbf{u} + \boldsymbol{\omega} \times \mathbf{r}) \cdot \nabla) \nabla \phi_I \right) - \mathbf{n} \cdot \left(\boldsymbol{\omega} \times \nabla \phi_I\right). \tag{2.47}$$

Finally, combining the results from Equations (2.44), (2.46) and (2.47) and substituting these with the time derivative of the body boundary condition given in Equation (2.34) leads to the following condition for the potential function φ:

$$\frac{\partial \varphi}{\partial n} = \mathbf{n} \cdot \left[\left(\dot{\mathbf{u}} + \dot{\boldsymbol{\omega}} \times \mathbf{r}\right) - \left(\boldsymbol{\omega} \times \mathbf{u}\right)\right]$$
$$- \mathbf{n} \cdot \left[\frac{\partial \nabla \phi_I}{\partial t} + \left(\left(\mathbf{u} + \boldsymbol{\omega} \times \mathbf{r}\right) \cdot \nabla\right) \nabla \phi_I - \left(\boldsymbol{\omega} \times \nabla \phi_I\right) \right]. \tag{2.48}$$

This is the body boundary condition for the potential function φ on the body surface $S_B(t)$. Once the potential function φ and the velocity potential ϕ are known, the time derivative of the velocity potential ϕ_t is given by

$$\phi_t = \frac{\partial \phi}{\partial t} = \varphi - \mathbf{U} \cdot \nabla \phi \,. \tag{2.49}$$

Hence, the hydrodynamic pressure due to the flow that is described by the perturbation velocity potential ϕ is given by the following form of Bernoulli's equation:

$$p_1 = -\rho \left(\varphi - \mathbf{U} \cdot \nabla \phi + \frac{1}{2} \left| \nabla \phi \right|^2 \right). \tag{2.50}$$

The function φ can be solved using the same source formulation that is used to solve the perturbation velocity potential ϕ. The source formulation expressed by means of the transient Green function is presented in Section 2.3.4. The potential function φ can be based on the same solution as the velocity potential ϕ if it satisfies the same boundary value problem otherwise, except that it satisfies different boundary conditions on the body surface S_B. Hence, the potential function φ has to satisfy the linear free surface boundary condition and be harmonic, i.e. satisfy Laplace's equation. Laplace's operator is applied to the potential function φ as follows:

$$\begin{aligned}\nabla^2\varphi &= \nabla^2\left(\frac{\partial\phi}{\partial t} + \mathbf{U}\cdot\nabla\phi\right)\\ &= \frac{\partial}{\partial t}\left(\nabla^2\phi\right) + \mathbf{U}\cdot\nabla\left(\nabla^2\phi\right) = 0,\end{aligned} \tag{2.51}$$

because $\nabla^2\phi = 0$. Thus, the potential function φ satisfies Laplace's equation and is a harmonic function. In addition, the linear free surface boundary condition at $z = 0$ is applied to the potential function φ as follows:

$$\begin{aligned}\frac{\partial^2\varphi}{\partial t^2} + g\frac{\partial\varphi}{\partial z} &= \frac{\partial^2}{\partial t^2}\left(\frac{\partial\phi}{\partial t} + \mathbf{U}\cdot\nabla\phi\right) + g\frac{\partial}{\partial z}\left(\frac{\partial\phi}{\partial t} + \mathbf{U}\cdot\nabla\phi\right)\\ &= \frac{\partial}{\partial t}\frac{\partial^2\phi}{\partial t^2} + \mathbf{U}\cdot\nabla\frac{\partial^2\phi}{\partial t^2} + g\frac{\partial}{\partial t}\frac{\partial\phi}{\partial z} + g\mathbf{U}\cdot\nabla\frac{\partial\phi}{\partial z}\\ &= \frac{\partial}{\partial t}\left(\frac{\partial^2\phi}{\partial t^2} + g\frac{\partial\phi}{\partial z}\right) + \mathbf{U}\cdot\nabla\left(\frac{\partial^2\phi}{\partial t^2} + g\frac{\partial\phi}{\partial z}\right) = 0\end{aligned} \tag{2.52}$$

because $\frac{\partial^2\phi}{\partial t^2} + g\frac{\partial\phi}{\partial z} = 0$ on $z = 0$. Hence, the potential function φ satisfies the linear free surface boundary condition. Furthermore, the radiation and bottom boundary conditions are satisfied by the transient Green function that is used to solve the potential function φ. The initial conditions at $t = 0$ are the same for the potential function φ and for the perturbation velocity potential ϕ.

The boundary condition for the potential function φ was derived applying the absolute time derivative of the fluid and the body velocities given in the normal direction on the point of the body surface. Hence, the first term inside the square

brackets on the right-hand side of the condition (2.48) does not give the acceleration of the point on the body surface (term $\dot{\mathbf{u}} + \dot{\boldsymbol{\omega}} \times \mathbf{r} - \boldsymbol{\omega} \times \mathbf{u}$). Similarly, the second term on the right-hand side does not give the fluid acceleration of the incoming wave. The potential function φ and its derivatives with respect to space coordinates do not give the fluid acceleration either. In a general form, the fluid acceleration is given by $\partial \nabla\phi / \partial t + (\nabla\phi \cdot \nabla)\nabla\phi$. On the other hand, the term $\varphi - \mathbf{U} \cdot \nabla\phi$ can be regarded as the rate of change of ϕ in the moving coordinate system, i.e. the rate of change of ϕ at a fixed point of fluid measuring from a moving body of which the velocity is **U** (Milne-Thomson, 1968, p. 89, 3-61). If the body is in constant translational motion, then the body acceleration is zero and the first term on the right-hand side in (2.48) is zero. Furthermore, if the body is in constant translational motion in calm water then the right-hand side is entirely zero. Hence, the potential function φ is also zero. Then, the Bernoulli's equation includes only the term $-\mathbf{U} \cdot \nabla\phi$ from the acceleration potential ϕ_t. From this it also follows that if the body is in steady motion, the term $\phi_t = \partial\phi / \partial t$ is not zero in a space-fixed coordinate system (Batchelor, 1967, p. 404). If the body is translating at constant forward velocity U_0 in calm water and the other motions are zero then the term gives $\varphi - \mathbf{U} \cdot \nabla\phi = -U_0 \, \partial\phi / \partial x$.

Bernoulli's equation includes the additional term $-\mathbf{U} \cdot \nabla\phi$ because the time derivative of the velocity potential is solved using the potential function φ instead of the direct solution of the ϕ_t term. The higher order derivatives of ϕ also do not appear in the boundary condition (2.48) because the potential function φ is used. The direct solution of the ϕ_t term includes second-order derivatives of ϕ with respect to the space variables; $(\mathbf{n} \cdot \nabla)\nabla\phi$ (Wu, 1998; Bandyk and Beck, 2011). The indirect solution applied to the present time domain method saves computational time because the evaluation of the higher order derivatives of the transient Green function is not needed.

The derivation of the boundary condition for the potential function φ was based on the absolute time derivative in the inertial reference frame. The potential function φ and the boundary condition for φ are scalars. However, the scalar functions include vector operations that have to be performed in the same coordinate system. Although the derivation is based on the inertial coordinate system, the velocity and acceleration components of the body are expressed in the body-fixed coordinate system. Hence, the vectors in the first term on the right-hand side in (2.48) are expressed in the body-fixed coordinate system. The transient Green function and the solved velocity potentials are expressed in the space-fixed coordinate system. Hence, the velocity potential of the incoming wave ϕ_I is also

expressed in the space-fixed coordinate system. In the second term on the right-hand side in (2.48), the body-related vectors are transformed to the space-fixed coordinate system expressing the orientation of the vectors in the same coordinate system before the vector operations with the terms that include ϕ_I. For the incoming wave term, the body-related vectors are ($\mathbf{u} + \boldsymbol{\omega} \times \mathbf{r}$) and $\boldsymbol{\omega}$ for which the coordinate transformations are performed. In this case, the normal vector is also given in the space-fixed coordinate system. The transformation of the translational and angular velocities using the transformation matrices [**L**] and [**B**] were given in Section 2.1.

The body accelerations appear on the right-hand side of the boundary condition for the potential function φ in Equation (2.48). However, equations of motion have not yet been solved that give the accelerations for the freely floating body, i.e. the accelerations are unknown. The acceleration potential exists in Bernoulli's equation that is used to determine the forces and moments on the body. The forces and moments are needed in the equations of motion, and the accelerations are not known until the equations of motion are solved. In the present time domain method, an iterative solution procedure is applied to solve the accelerations and the function φ. The applied methods in the time integration are given in Section 2.4.4. Another technique is to combine the boundary value problem of the acceleration potential and the equations of motion to solve the acceleration of the body directly (Wu and Eatock Taylor, 1996; Bandyk and Beck, 2011).

2.3.3 Green function

The solutions of the perturbation velocity and acceleration potentials are obtained by applying Green's theorem. The potentials are expressed with source distributions over the body where the source distributions are represented by a transient Green function. The transient Green function satisfies the boundary conditions on the free surface and far away from the body. The unknown source strengths are obtained by satisfying the body boundary conditions on the hull surface. By means of Green's theorem, the potentials are expressed with integral equations over the hull surface where the integrand includes the transient Green function. The integral equations for the potentials are given in the following section. This section presents the transient Green function.

The formulation of the transient Green function is given by Finkelstein (1957), Stoker (1958), and Wehausen and Laitone (1960). Here, the transient Green function is expressed in the following form (Wehausen and Laitone, 1960, p. 491, Eq. (13.49)):

$$G = \frac{1}{R} - \frac{1}{R'} + 2\int_0^\infty \left[e^{k(z+z')} \sqrt{gk} \sin(\sqrt{gk}(t-\tau)) J_0(kr) \right] dk , \tag{2.53}$$

where $R = \sqrt{(x-x')^2 + (y-y')^2 + (z-z')^2}$,

$R' = \sqrt{(x-x')^2 + (y-y')^2 + (z+z')^2}$,

$r = \sqrt{(x-x')^2 + (y-y')^2}$.

The transient Green function is given in the space-fixed coordinate system. In the above equation, J_0 is the Bessel function of the first kind of order zero. The field point P is at the point (x, y, z), and the source point Q is at (x', y', z'). The image source Q' is located at the point $(x', y', -z')$. The present time is t and the time delay $t-\tau$ gives the memory effect at time t of the fluid flow at time τ.

The transient Green function satisfies Laplace's equation:

$$\nabla^2 G = 0 , \qquad z < 0, \quad P \neq Q, \quad t \geq \tau, \tag{2.54}$$

the free surface boundary condition:

$$\frac{\partial^2 G}{\partial t^2} + g\frac{\partial G}{\partial z} = 0 , \qquad z = 0, \tag{2.55}$$

and the radiation and bottom conditions:

$$\nabla G \to 0 , \qquad z \to -\infty, \ r \to \infty. \tag{2.56}$$

In addition, the transient Green function satisfies the following initial conditions:

$$G = 0 \ \text{and} \ \frac{\partial G}{\partial t} = 0 , \qquad t = \tau. \tag{2.57}$$

The transient Green function can be decomposed as follows:

$$G = G^{(0)} + G^{(t)} , \tag{2.58}$$

where the impulsive part is given as

$$G^{(0)} = \frac{1}{R} - \frac{1}{R'} , \tag{2.59}$$

and the memory part is

$$G^{(t)} = 2\int_0^\infty \left[\mathrm{e}^{k(z+z')}\sqrt{gk}\,\sin(\sqrt{gk}\,(t-\tau))J_0(kr)\right]dk\,. \tag{2.60}$$

Derivatives of the memory part of the transient Green function $G^{(t)}$ with respect to x, y and z are as follows:

$$\frac{\partial G^{(t)}}{\partial x} = -2\frac{(x-x')}{r}\int_0^\infty \left[k\,\mathrm{e}^{k(z+z')}\sqrt{gk}\,\sin(\sqrt{gk}\,(t-\tau))J_1(kr)\right]dk\,, \tag{2.61}$$

$$\frac{\partial G^{(t)}}{\partial y} = -2\frac{(y-y')}{r}\int_0^\infty \left[k\,\mathrm{e}^{k(z+z')}\sqrt{gk}\,\sin(\sqrt{gk}\,(t-\tau))J_1(kr)\right]dk\,, \tag{2.62}$$

$$\frac{\partial G^{(t)}}{\partial z} = 2\int_0^\infty \left[k\,\mathrm{e}^{k(z+z')}\sqrt{gk}\,\sin(\sqrt{gk}\,(t-\tau))J_0(kr)\right]dk\,. \tag{2.63}$$

Above, J_1 is the Bessel function of the first kind of order one. Derivatives of the impulsive part $G^{(0)}$ with respect to x, y and z are given as

$$\frac{\partial G^{(0)}}{\partial x} = -\frac{x-x'}{R^3} + \frac{x-x'}{R'^3}\,, \tag{2.64}$$

$$\frac{\partial G^{(0)}}{\partial y} = -\frac{y-y'}{R^3} + \frac{y-y'}{R'^3}\,, \tag{2.65}$$

$$\frac{\partial G^{(0)}}{\partial z} = -\frac{z-z'}{R^3} + \frac{z+z'}{R'^3}\,. \tag{2.66}$$

The memory part of the transient Green function $G^{(t)}$ can be given in a non-dimensional form. In the non-dimensional form, the Green function and its derivatives can be expressed as a function of two variables β and μ. First, the following definitions are given for the time and space variables in the memory part:

$$T = t - \tau$$
$$X = x - x'$$
$$Y = y - y'$$
$$Z = z - z' \qquad Z' = z + z'$$

The vertical distance Z' between the image source point and field point can be expressed with a spherical coordinate θ. The coordinate is given as $\cos\theta = \mu = -\frac{Z'}{R'}$. Hence, μ is bounded in the domain $0 \le \mu \le 1$. The parameter μ is zero if the image source and field points are on the free surface, i.e. $Z' = 0$. If $\mu = 1$ the two points are on the same vertical axis. Furthermore, the non-dimensional time is given by $\beta = T\sqrt{\frac{g}{R'}}$. In addition, the integration variable k is replaced by $\lambda = kR'$ and with these definitions the memory part of the Green function can be expressed as follows:

$$G^{(t)} = \sqrt{\frac{g}{R'^3}}\hat{G}^{(t)}(\mu,\beta), \tag{2.67}$$

where the non-dimensional memory part is given by

$$\hat{G}^{(t)}(\mu,\beta) = 2\int_0^\infty \left[\mathrm{e}^{-\lambda\mu}\sqrt{\lambda}\sin(\beta\sqrt{\lambda})J_0(\lambda\sqrt{1-\mu^2}) \right] d\lambda . \tag{2.68}$$

The derivatives with respect to x, y and z can be given in the following form using the non-dimensional expressions:

$$\frac{\partial G^{(t)}}{\partial x} = -\sqrt{\frac{g}{R'^3}}\frac{X}{rR'}\hat{G}^{(xy)}(\mu,\beta), \tag{2.69}$$

$$\frac{\partial G^{(t)}}{\partial y} = -\sqrt{\frac{g}{R'^3}}\frac{Y}{rR'}\hat{G}^{(xy)}(\mu,\beta), \tag{2.70}$$

$$\frac{\partial G^{(t)}}{\partial z} = \sqrt{\frac{g}{R'^3}}\frac{1}{R'}\hat{G}^{(z)}(\mu,\beta). \tag{2.71}$$

The non-dimensional derivatives are as follows:

$$\hat{G}^{(xy)}(\mu,\beta) = 2\int_0^\infty \left[\mathrm{e}^{-\lambda\mu}\lambda\sqrt{\lambda}\sin(\beta\sqrt{\lambda})J_1(\lambda\sqrt{1-\mu^2}) \right] d\lambda , \tag{2.72}$$

$$\hat{G}^{(z)}(\mu,\beta) = 2\int_0^\infty \left[\mathrm{e}^{-\lambda\mu}\lambda\sqrt{\lambda}\sin(\beta\sqrt{\lambda})J_0(\lambda\sqrt{1-\mu^2}) \right] d\lambda . \tag{2.73}$$

If $\mu = 0$ then an analytic solution can be used for $G^{(t)}$ (Wehausen and Laitone, 1960; Magee and Beck, 1989). The solution is given in the non-dimensional form as follows:

$$\hat{G}^{(t)}(\beta, \mu = 0) = \frac{1}{16}\pi\beta^3\sqrt{2}\left[J_{1/4}\left(\frac{1}{8}\beta^2\right)J_{-1/4}\left(\frac{1}{8}\beta^2\right) + J_{3/4}\left(\frac{1}{8}\beta^2\right)J_{-3/4}\left(\frac{1}{8}\beta^2\right)\right], \tag{2.74}$$

where J_ν is the Bessel function of order ν (Abramowitz and Stegun, 1972). The function $\hat{G}^{(t)}(\beta, \mu = 0)$ is shown in Figure 2.2. The derivatives of the memory part at $\mu = 0$ can also be solved and the derivatives expressed as a combination of the Bessel functions in similar forms as the above equation.

The Green function term $\hat{G}^{(t)}(\mu, \beta)$ is shown in Figure 2.3, and the derivatives $\hat{G}^{(xy)}(\mu, \beta)$ and $\hat{G}^{(z)}(\mu, \beta)$ are shown in Figures 2.4 and 2.5 respectively.

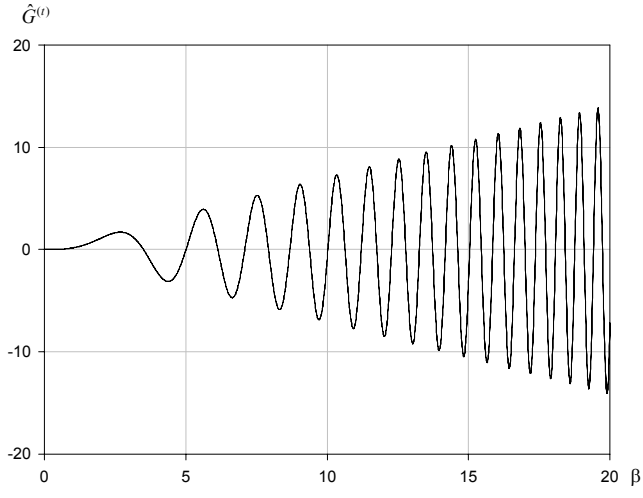

Figure 2.2. The transient Green function term $\hat{G}^{(t)}$ at $\mu = 0$.

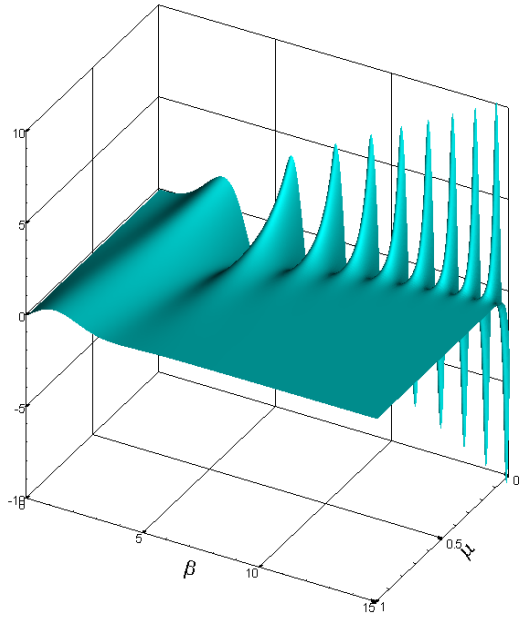

Figure 2.3. The transient Green function term $\hat{G}^{(t)}$.

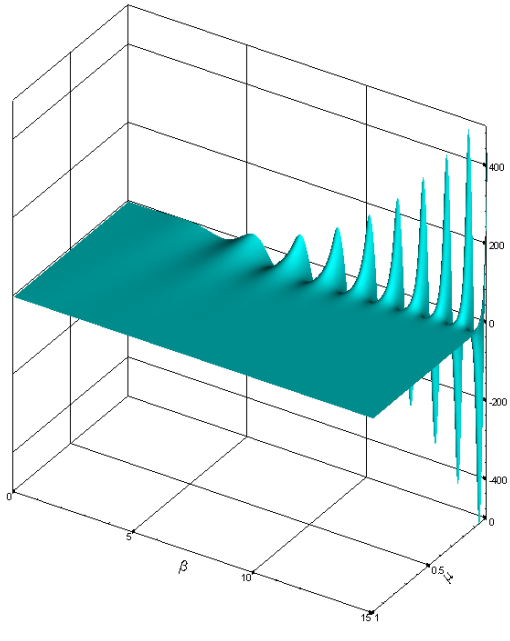

Figure 2.4. Derivative term $\hat{G}^{(xy)}$ of the transient Green function.

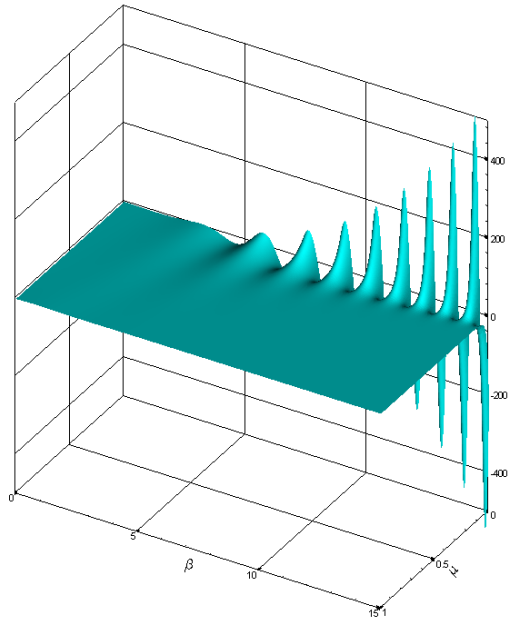

Figure 2.5. Derivative term $\hat{G}^{(\tau)}$ of the transient Green function.

2.3.4 Velocity and acceleration potentials

The velocity potential ϕ and the Green function G can be expressed by means of Green's theorem as follows (see, e.g., Newman, 1977):

$$\iiint_V \left(\phi \nabla^2 G - G \nabla^2 \phi\right) dV = \iint_S \left(\phi \frac{\partial G}{\partial n} - G \frac{\partial \phi}{\partial n} \right) dS \,, \tag{2.75}$$

where V is the fluid volume inside the boundary surface S. The derivation of the integral equations of the velocity potential starting from Green's theorem is presented by, for example, Brard (1972), and Guevel and Bougis (1982). In the present boundary value problem, the surface S includes the body and free surfaces, S_B and S_F. At infinity and on the sea bottom, the integrals vanish because of the boundary conditions. The Green function has a singularity if the field and source points have the same coordinates, $P = Q$. The singularity can be avoided by defining a small sphere with a surface S_ε around the singularity point (Newman, 1977). Hence, the integral equation can be represented with the velocity potential and the Green function on the surfaces where the functions satisfy Laplace's equation. Furthermore, the derived integral equation is integrated with respect to time τ and the free surface boundary condition is taken into account together with the initial conditions at $\tau = 0$ and $\tau = t$ on the surface S_F. This derivation for the integral

equation is given by Lin and Yue (1991), and Ferrant (1991). They showed that the integral equation can be written in the following form:

$$
\begin{aligned}
-2\pi\phi(P,t) &= \iint_{S_B(t)} \left(\phi(Q,t)\frac{\partial G^{(0)}(P,Q)}{\partial n} - G^{(0)}(P,Q)\frac{\partial \phi(Q,t)}{\partial n} \right) dS \\
&+ \int_0^t \left[\iint_{S_B(\tau)} \left(\phi(Q,\tau)\frac{\partial G^{(t)}(P,Q,t,\tau)}{\partial n} - G^{(t)}(P,Q,t,\tau)\frac{\partial \phi(Q,\tau)}{\partial n} \right) dS \right] d\tau \\
&+ \frac{1}{g}\int_0^t \left[\int_{\Gamma_F(\tau)} U_N \left(\phi(Q,\tau)\frac{\partial G^{(t)}(P,Q,t,\tau)}{\partial \tau} - G^{(t)}(P,Q,t,\tau)\frac{\partial \phi(Q,\tau)}{\partial \tau} \right) d\Gamma \right] d\tau \,.
\end{aligned}
\tag{2.76}
$$

The surface and line integrals, $S_B(\tau)$ and $\Gamma_F(\tau)$, as well as the derivative in the normal direction are expressed in the source point coordinates Q at (x', y', z'). The first integral depends on time t in the body nonlinear solution because the wetted surface of the body is changing. The source and field points P and Q in the impulsive part of the Green function $G^{(0)}$ depend on time t in the body-nonlinear solution because the body position is updated during the calculation. In the body-linear solution, the co-ordinates of the source and field points remain the same during the calculation as they were at time $t = 0$. The line integral $\Gamma_F(\tau)$ is evaluated at the intersection of the body and the free surface. The velocity $U_N = \mathbf{U}_\Gamma \cdot \mathbf{N}$ is the two-dimensional velocity of Γ_F in the normal direction $\mathbf{N} = \mathbf{N}(Q,\tau)$ where $\mathbf{N}$ is the normal vector of Γ_F at $z = 0$.

The above equation is the solution to the exterior problem and a similar equation can be derived for the interior problem. Adding the exterior and interior problems together, the integral equation can be presented with sources and dipoles. The integral equation for the velocity potential using only the distribution of sources can be written as follows:

$$
\begin{aligned}
\phi(P,t) &= \frac{1}{4\pi}\iint_{S_B(t)} \sigma(Q,t)G^{(0)}(P,Q)dS \\
&+ \frac{1}{4\pi}\int_0^t \left[\iint_{S_B(\tau)} \sigma(Q,\tau)G^{(t)}(P,Q,t,\tau)dS \right] d\tau \\
&- \frac{1}{4\pi}\frac{1}{g}\int_0^t \left[\int_{\Gamma_F(\tau)} \sigma(Q,\tau)G^{(t)}(P,Q,t,\tau)u_n U_N d\Gamma \right] d\tau \,,
\end{aligned}
\tag{2.77}
$$

where the source strength is σ. The velocity $u_n = \mathbf{u} \cdot \mathbf{n}$ is the velocity of the body in the normal direction at the intersection of the body and the free surface at source point Q at time τ. In the body linear solution, the product of the velocities can be given as $u_n U_N = U_0^2 N_x^2$ where N_x is the component of the normal vector of the contour Γ_F in the x-direction. At zero speed, the line integral vanishes. The line integral appears for surface-piercing bodies.

From the above equation, the derivatives of the velocity potential with respect to the field coordinates x, y and z can be determined as follows:

$$\begin{aligned}\nabla\phi(P,t) = & \frac{1}{4\pi}\iint_{S_B(t)}\sigma(Q,t)\nabla G^{(0)}(P,Q)dS \\ & + \frac{1}{4\pi}\int_0^t\left[\iint_{S_B(\tau)}\sigma(Q,\tau)\nabla G^{(t)}(P,Q,t,\tau)dS\right]d\tau \\ & - \frac{1}{4\pi}\frac{1}{g}\int_0^t\left[\int_{\Gamma_F(\tau)}\sigma(Q,\tau)\nabla G^{(t)}(P,Q,t,\tau)u_n U_N d\Gamma\right]d\tau\,, \end{aligned} \tag{2.78}$$

where the operator ∇ is given in the field point coordinates (x, y, z).

In the above integral equations of the velocity potential and its derivatives, the source strengths are unknown at time t. The unknown source strengths can be solved using the condition of the velocities of the fluid and body on the body surface, i.e. the body boundary condition (2.26). The body boundary condition is $\partial\phi/\partial n = \mathbf{n}\cdot\nabla\phi = \left(\mathbf{U}\cdot\mathbf{n} - \partial\phi_I/\partial n\right)$. Hence, taking a dot product for $\mathbf{n}$ from both sides of Equation (2.78) the term $\mathbf{n}\cdot\nabla\phi$ can be replaced by $\left(\mathbf{U}\cdot\mathbf{n} - \partial\phi_I/\partial n\right)$. Thus, the unknown source strengths of the velocity potential can be solved from the following equation

$$\begin{aligned} -\frac{1}{4\pi}\iint_{S_B(t)}\sigma(Q,t)\frac{\partial G^{(0)}(P,Q)}{\partial n}dS = & -\left(\mathbf{U}\cdot\mathbf{n} - \frac{\partial\phi_I}{\partial n}\right) \\ & + \frac{1}{4\pi}\int_0^t\left[\iint_{S_B(\tau)}\sigma(Q,\tau)\frac{\partial G^{(t)}(P,Q,t,\tau)}{\partial n}dS\right]d\tau \\ & - \frac{1}{4\pi}\frac{1}{g}\int_0^t\left[\int_{\Gamma_F(\tau)}\sigma(Q,\tau)\frac{\partial G^{(t)}(P,Q,t,\tau)}{\partial n}u_n U_N d\Gamma\right]d\tau\,, \end{aligned} \tag{2.79}$$

where the normal derivative $\partial/\partial n = \mathbf{n}\cdot\nabla$ is given with respect to the field point coordinates (x, y, z). The terms have been rearranged so that the unknown source

strengths at time t have been moved to the left-hand side. The source strengths from previous times τ are known and the memory part of the Green function is zero at $\tau = t$. Once the source strengths are known, the velocity potential can be determined from Equation (2.77) and the derivatives from Equation (2.78).

In the acceleration potential method, the above equations are also valid for the potential function φ, replacing ϕ with φ. In solving the source strengths for the potential function φ, the condition $\partial\varphi/\partial n = \mathbf{n}\cdot\nabla\varphi$ for the acceleration potential is applied. Hence, the condition $\left(\mathbf{U}\cdot\mathbf{n} - \partial\phi_I/\partial n\right)$ in the above Equation (2.79) is replaced by the condition given by the right-hand side of Equation (2.48):

$$\mathbf{n}\cdot\left[\left(\dot{\mathbf{u}} + \dot{\boldsymbol{\omega}}\times\mathbf{r}\right) - \left(\boldsymbol{\omega}\times\mathbf{u}\right)\right] - \mathbf{n}\cdot\left[\frac{\partial\nabla\phi_I}{\partial t} + \left(\left(\mathbf{u} + \boldsymbol{\omega}\times\mathbf{r}\right)\cdot\nabla\right)\nabla\phi_I - \left(\boldsymbol{\omega}\times\nabla\phi_I\right)\right].$$

Thus, applying Equation (2.79) the source strengths for the potential function φ can be solved and then the potential function φ can be expressed with a similar equation to Equation (2.77). The time derivative of the velocity potential is finally given by Equation (2.49): $\phi_t = \varphi - \mathbf{U}\cdot\nabla\phi$.

2.3.5 Pressure loads and equations of motion

The pressure on the body can be determined from Bernoulli's equation

$$p_1(P,t) = -\rho\left[\frac{\partial\Phi}{\partial t} + \frac{1}{2}\left|\nabla\Phi\right|^2 + gz\right], \tag{2.80}$$

where the velocity potential is the combination of the perturbation and incoming wave velocity potentials $\Phi = \phi + \phi_I$. Using $\phi + \phi_I$ and the acceleration-potential solution for ϕ_t given by Equation (2.49), Bernoulli's equation can be written in the following form:

$$p_1(P,t) = -\rho\left[\varphi - \mathbf{U}\cdot\nabla\phi + \frac{1}{2}\left|\nabla\phi\right|^2 + \frac{\partial\phi_I}{\partial t} + \frac{1}{2}\left|\nabla\phi_I\right|^2 + \nabla\phi\nabla\phi_I + gz\right], \tag{2.81}$$

where the pressure terms are defined in the space-fixed coordinate system.

Forces and moments on the body are obtained by integrating the pressure over the wetted surface of the body. The forces $\mathbf{F} = (F_1, F_2, F_3)$ and moments $\mathbf{M} = (F_4, F_5, F_6)$ can be determined as follows

$$F_i(t) = \int_{S_B(t)} p_1(P_0,t) n_{0i} dS\,, \qquad i = 1,2,...,6, \tag{2.82}$$

where n_{0i} are components of the normal vectors. The normal vector for the forces is given as

$$\mathbf{n} = n_{01}\mathbf{i} + n_{02}\mathbf{j} + n_{03}\mathbf{k}\,, \tag{2.83}$$

and the generalized normal vector for the moments is defined as follows:

$$\mathbf{r} \times \mathbf{n} = n_{04}\mathbf{i} + n_{05}\mathbf{j} + n_{06}\mathbf{k}\,. \tag{2.84}$$

The position vector from the centre of gravity of the body pointing to the point P_0 on the body surface is $\mathbf{r} = x_0\mathbf{i} + y_0\mathbf{j} + z_0\mathbf{k}$. The point P_0 is given in the body-fixed coordinate system at (x_0, y_0, z_0). In addition, the vector components in $\mathbf{n}$ and $\mathbf{r} \times \mathbf{n}$ are expressed in the body-fixed coordinate system. Thus, the forces and moments are expressed in the body-fixed coordinate system. The transformations of the position and normal vector between the body-fixed and space-fixed coordinate systems are given by Equations (2.9) and (2.11). The pressure is scalar and determined at the centroid of the panel on which the coordinates are known in body-fixed and space-fixed coordinate systems. Hence, the pressure is known at point P_0 on the body surface. The forces and moments are expressed in the body-fixed coordinate system because the equations of motion given in the coordinate system are fixed on the body and the origin is at the centre of gravity.

The accelerations of the body are solved from the equations of motion. The equations of motion are valid in the inertial coordinate system and the time derivatives are absolute time derivatives (Salonen, 1999). Hence, the absolute accelerations of the centre of gravity of the body in the body-fixed coordinate system are given by

$$\mathbf{a} = \dot{\mathbf{u}} = \frac{d}{dt}\mathbf{u} = \frac{\delta}{\delta t}\mathbf{u} + \boldsymbol{\omega} \times \mathbf{u} = \begin{Bmatrix} \dot{u} + qw - rv \\ \dot{v} + ru - pw \\ \dot{w} + pv - qu \end{Bmatrix}, \tag{2.85}$$

where $\delta/\delta t$ means the derivative with respect to time in the body-fixed coordinate system. The equations of motion in the body-fixed coordinate system at the centre of gravity of the body can be written as follows

$$\begin{aligned} m\dot{\mathbf{u}} &= \mathbf{F} + \mathbf{F}_G \\ [\mathbf{I}]\dot{\boldsymbol{\omega}} + \boldsymbol{\omega} \times ([\mathbf{I}]\boldsymbol{\omega}) &= \mathbf{M} \end{aligned} \tag{2.86}$$

or in component form:

$$\begin{aligned} &m(\dot{u} + qw - rv) = F_1 + F_{G1} \\ &m(\dot{v} + ru - pw) = F_2 + F_{G2} \\ &m(\dot{w} + pv - qu) = F_3 + F_{G3} \\ &I_{44}\dot{p} + I_{45}\dot{q} + I_{46}\dot{r} + (I_{66} - I_{55})qr - I_{45}rp + I_{64}pq + I_{56}(q^2 - r^2) = F_4 \\ &I_{54}\dot{p} + I_{55}\dot{q} + I_{56}\dot{r} + (I_{44} - I_{66})rp - I_{56}pq + I_{45}qr + I_{64}(r^2 - p^2) = F_5 \\ &I_{64}\dot{p} + I_{65}\dot{q} + I_{66}\dot{r} + (I_{55} - I_{44})pq - I_{64}rq + I_{56}rp + I_{45}(p^2 - q^2) = F_6 \end{aligned} \tag{2.87}$$

Here, m is the mass of the body and I_{ij} are the mass moment of inertias of the body with respect to the body-fixed coordinate system about the centre of gravity. The components of the gravity force F_{Gi} in the body-fixed coordinate system are given by

$$\begin{aligned} \mathbf{F}_G = (F_{G1}, F_{G2}, F_{G3}) &= -mg[\mathbf{L}]^{-1} \\ &= mg(\sin\eta_5, -\sin\eta_4\cos\eta_5, -\cos\eta_4\cos\eta_5). \end{aligned} \tag{2.88}$$

The translational velocity components in the body-fixed coordinate system are u, v and w in the x_0-, y_0- and z_0-directions, respectively. The angular velocities in the body-fixed coordinate system are p, q and r about the x_0, y_0 and z_0 axis, respectively. The translational and angular velocities are transformed to the space-fixed coordinate system using the transformation matrices, Equations (2.1) and (2.2):

$$\begin{aligned} \dot{\mathbf{x}}_G &= [\mathbf{L}]\mathbf{u} \\ \boldsymbol{\Omega} &= [\mathbf{B}]\boldsymbol{\omega} \end{aligned} \tag{2.89}$$

In the above, the vectors of the body velocities are $\dot{\mathbf{x}}_G = (\dot{\eta}_1, \dot{\eta}_2, \dot{\eta}_3)$ and $\boldsymbol{\Omega} = (\dot{\eta}_4, \dot{\eta}_5, \dot{\eta}_6)$ in the space-fixed coordinate system and $\mathbf{u} = (u, v, w)$ and $\boldsymbol{\omega} = (p, q, r)$ in the body-fixed coordinate system.

2.3.6 Hull girder loads

The rigid hull girder loads are the normal force (V_1), lateral shear force (V_2), vertical shear force (V_3), torsion moment (V_4), vertical bending moment (V_5) and lateral bending moment (V_6). The hull girder loads are determined in the body-fixed coordinate system. The positive direction of the forces (V_1, V_2, V_3) is the

same as that of the axis of the body-fixed coordinate system. The moments (V_4, V_5, V_6) are defined about the axis in the body-fixed coordinate system. The internal hull girder loads at cross section x_p of the body can be determined as follows:

$$V_i(t,x_p) = \int_{V(x_p)} a_{mi}\, dm - \int_{S_B(x_p)} p_1 n_{pi}\, dS\,, \quad i = 1, 2, ..., 6, \tag{2.90}$$

where a_{mi} are the acceleration components of the mass dm. The integrations are carried out from the stern of the body to the cross section x_p. For the hydrodynamic forces and moments, the integration includes the wetted surface of the body $S_B(x_p)$ to a cross section at x_p. The hydrodynamic forces and moments are integrated external pressure loads. For the inertia forces and the moment of inertia terms, the integration is performed over the volume $V(x_p)$ of the mass distribution of the body from the stern to a cross section at x_p. In the above equation, n_{pi} are the components of the generalized normal vectors for the forces and moments. The vector definitions for the pressure-induced loads are shown in Figure 2.6 and for the accelerations of mass-induced loads in Figure 2.7. For the hydrodynamic forces, the components of the normal vector are the same as the components of the body normal vector expressed in body-fixed coordinate system as follows

$$n_{p1}\mathbf{i} + n_{p2}\mathbf{j} + n_{p3}\mathbf{k} = n_{01}\mathbf{i} + n_{02}\mathbf{j} + n_{03}\mathbf{k} = \mathbf{n}\,. \tag{2.91}$$

The normal vector $\mathbf{n}$ is determined at the same point on the body surface as the pressure. The generalized normal vector for the hull girder moments is defined as

$$n_{p4}\mathbf{i} + n_{p5}\mathbf{j} + n_{p6}\mathbf{k} = (\mathbf{r} - \mathbf{r}_p) \times \mathbf{n}\,, \tag{2.92}$$

where the vector $\mathbf{r} - \mathbf{r}_p$ is the position vector of the body surface area dS from the point (x_p, y_p, z_p) at the cross section x_p.

The acceleration of the mass dm is given as

$$\mathbf{a}_m = \dot{\mathbf{u}} + \dot{\boldsymbol{\omega}} \times \mathbf{r}_m + \boldsymbol{\omega} \times (\boldsymbol{\omega} \times \mathbf{r}_m) - \mathbf{g}\,, \tag{2.93}$$

where the vector $\mathbf{g} = [\mathbf{L}]^{-1}(0,0,-g)$ includes the gravity acceleration components in the body-fixed coordinate system. The gravity forces due to $\mathbf{g}$ should be understood as external forces and hence it is negative. The sign is then the same as for the pressure forces and also the same as for the gravity forces in the equations of motion. The vector $\mathbf{r}_m$ is the position vector of the mass dm from the centre of gravity of the body. The acceleration components a_{mi} for the forces are given as

$$a_{m1}\mathbf{i} + a_{m2}\mathbf{j} + a_{m3}\mathbf{k} = \mathbf{a}_m \,. \tag{2.94}$$

The acceleration components a_{mi} for the moments are defined as

$$(\mathbf{r}_m - \mathbf{r}_p) \times \mathbf{a}_m = a_{m4}\mathbf{i} + a_{m5}\mathbf{j} + a_{m6}\mathbf{k} \,, \tag{2.95}$$

where $\mathbf{r}_m - \mathbf{r}_p$ is the position vector of the mass dm from the point (x_p, y_p, z_p) at the cross section x_p.

The above formulation includes the hull girder forces and moments due to the hydrostatic equilibrium. The still water forces and moment can be subtracted to obtain the internal hydrodynamic forces and moments due to the body motions. In this work, the still water loads have been subtracted from the hull girder loads. In the present time domain method, the hull girder forces and moments are defined at $\mathbf{r}_p = x_p\mathbf{i}$, i.e. at the centre line of the body and at the same height as the global centre of the gravity of the body. The vertical shear force and bending moment can be determined when the longitudinal mass distribution is known. The integration of the masses is only carried out in the longitudinal x_0-direction assuming symmetric mass distribution in the y-direction. For example, to obtain the torsion moment, the mass distribution or the distribution of the mass moment of inertia about the x-axis have to be known.

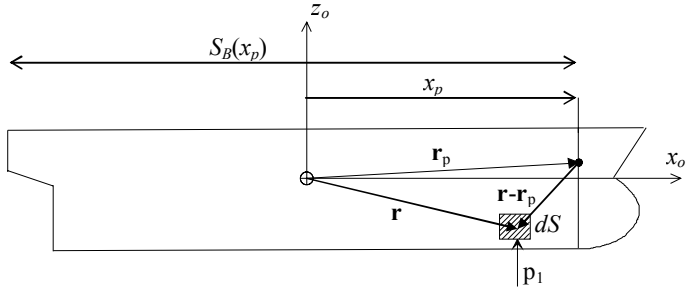

Figure 2.6. Definitions of the position vectors for the hull surface element dS. The hull girder loads are defined at the cross section x_p.

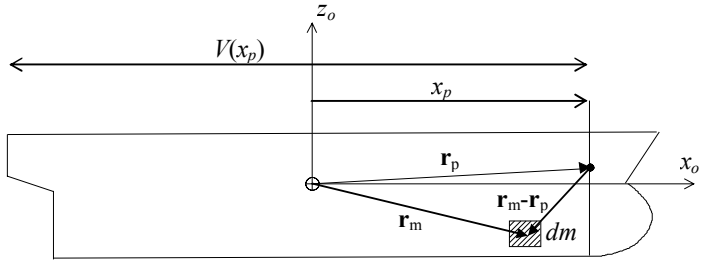

Figure 2.7. Definitions of the position vectors for the mass *dm*. The hull girder loads are defined at the cross section x_p.

2.4 Numerical solutions

2.4.1 Panel method

Velocity potentials are expressed by means of the integral equations, as presented in Section 2.3.4. The equations include integrals over the body surface. Hence, for complex body geometries the body surface has to be approximated. In this work, the body surface is discretized by panels and the velocity potential is determined using a constant panel method (Hess and Smith, 1962). The velocity potential can be evaluated from Equation (2.77) if the source strengths are known. The unknown source strengths can be solved from the integral Equation (2.79). This equation can be expressed as a system of linear equations as follows

$$[\mathbf{A}]\boldsymbol{\sigma} = \mathbf{f} \,. \tag{2.96}$$

In the present calculation method, the system of linear equations is solved by LU-decompostion (see, e.g., Press et al., 1997). The unknown source strengths in the vector $\boldsymbol{\sigma}$ are $\sigma_j = \sigma(Q_j, t)$ where $j = 1 \ldots N_P$ and N_P is the number of panels on the hull surface. The source strengths are determined at source points Q_j at time t. The collocation point of the source strengths is at the centroid of the panels. The terms in the matrix [**A**] are given by

$$A_{ij} = -\frac{1}{4\pi}\,\mathbf{n}_i \cdot \iint_{S_j} \nabla G^{(0)}(P_i, Q_j)\, dS_j \,, \tag{2.97}$$

where $i = 1 \ldots N_P$ and $j = 1 \ldots N_P$. The integration is performed over the panel area S_j. The field points P_i and source points Q_j are determined at time t. The operator

∇ is given in the field point coordinates (x, y, z) and the normal vectors are determined at the field points $\mathbf{n}_i = \mathbf{n}(P_i, t)$.

The terms of the vector **f** are the following:

$$
\begin{aligned}
f_i &= -\mathbf{n}_i \cdot \left(\mathbf{U}(P_i,t) - \nabla\phi_I(P_i,t)\right) \\
&+ \frac{1}{4\pi} \sum_{k=1}^{N_\tau - 1} c_k \left[\sum_{j=1}^{N_P} \left(\sigma_j(Q_j,\tau_k)\ \mathbf{n}_i \cdot \iint_{S_{Bj}} \nabla G^{(t)}(P_i,Q_j,t,\tau_k) dS_j \right) \right] \Delta\tau \\
&- \frac{1}{4\pi}\frac{1}{g} \sum_{k=1}^{N_\tau - 1} c_k \left[\sum_{j=1}^{N_P} \left(\sigma_j(Q_j,\tau_k)\ \mathbf{n}_i \cdot \int_{\Gamma_{Fj}} \nabla G^{(t)}(P_i,Q_j,t,\tau_k) u_{nj} U_{Nj}\, d\Gamma_j \right) \right] \Delta\tau \ .
\end{aligned}
\tag{2.98}
$$

Here, the terms f_i, $i = 1...N_P$ are evaluated at the centroid of each panel. A trapezoidal rule is used in time integration of the convolution integral. The integration variable is τ and the index in the summation expression is $k = 1 \ldots N_\tau - 1$. Hence, $c_k = 0.5$ if $k = 1$ and otherwise $c_k = 1.0$ in the trapezoidal rule. The present time is t at $k = N_\tau$. The memory part of the transient Green function is not defined if $\tau = t$ and hence the time integration ends at $N_\tau - 1$. The field point coordinates are determined at time t, $P = P(t)$ and the source points at time τ, $Q = Q(\tau)$. The integral over the single panel area as well as the line integral at the waterline are carried out at time τ at the source point Q: $dS = dS(Q,\tau)$ and $d\Gamma = d\Gamma(Q,\tau)$. Furthermore, the velocities in the line integral are determined at time τ at the source point Q, $U_N = U_N(Q, \tau)$ and $u_n = u_n(Q, \tau)$. The collocation point of the waterline integral is approximated at the centroid of the panels.

In the acceleration potential method, the condition $\mathbf{n}_i \cdot \left(\mathbf{U}(P_i,t) - \nabla\phi_I(P_i,t)\right)$ is replaced by the condition given by the right-hand side of Equation (2.48) in solving the source strengths for the potential function φ.

Once the source strengths are solved for ϕ and φ, the velocity potential ϕ and the potential function φ can be determined using Equation (2.77), which can be expressed in a similar form to Equation (2.98).

Quadrilateral or triangular panels can be used in the time domain computer program. In the present computer program, the impulsive part $G^{(0)}$ in the transient Green function and the integrals over the panel area are determined by a method given by Newman (1986). Numerical integration rules are applied to integrate the memory part $G^{(t)}$ of the transient Green function values over a panel area. The

integration over the quadrilateral panel area can be determined using Gauss quadratures:

$$\iint_S f(x,y,z)dS \approx \sum_{i=1}^{N_G}\sum_{j=1}^{N_G} W_i W_j f(\xi_{1i},\xi_{2j})\left|\mathrm{J}(\xi_{1i},\xi_{2j})\right| \tag{2.99}$$

The Jacobian determinant is |J| to transform integrals to the local panel coordinates (ξ_1, ξ_2). The number of integration points is N_G. If $N_G = 1$ then the integration is the same as a midpoint rule. In this work, the midpoint rule has been used to integrate the memory part unless otherwise stated. The triangular panels are integrated with the midpoint rule.

The computational time can be reduced if the time delay $t - \tau$ is truncated in the convolution integral and by not using the whole time history starting from $\tau = 0$. This means that the number of time steps N_τ in the convolution integral is not the same as the total number of time steps N_T in the calculation. The history of the fluid motion from the past time has an effect on the fluid motion at the present time t, i.e. the memory effect. The memory effect decreases when the time delay $t - \tau$ increases. Furthermore, the influence of the memory effect depends on the damping characteristic of the body motion. It was also noted that the memory effect has a greater influence on the responses if the body linear solution was used and the responses were moderate compared with the body nonlinear solution and if the response amplitudes were large. In this work, the number of oscillation cycles of the responses was used as a general guideline to determine the truncation of the memory effect. In the regular and irregular wave calculation for the model test ship, the number of response cycles was roughly at least 5-10 before the truncation of the memory effect. The results for the model test ship are presented in Chapter 4.

A parallel computation is an efficient method to reduce the computational time in the panel methods. The most time-consuming part is Equation (2.98) in which the integral equations are solved for each panel, $i = 1...N_P$. The integrals for multiple panels can be computed simultaneously using parallel algorithms in the computer code. In the present computer code, the last two terms on the right-hand side of Equation (2.98) and the term in Equation (2.97) have been evaluated using parallel algorithms.

2.4.2 Numerical solution of the Green function

The memory part of the transient Green function was given in a non-dimensional form in Equation (2.68) as follows:

$$\hat{G}^{(t)}(\mu,\beta) = 2\int_0^\infty \left[\mathrm{e}^{-\lambda\mu}\sqrt{\lambda}\sin(\beta\sqrt{\lambda})J_0(\lambda\sqrt{1-\mu^2}) \right] d\lambda \,.$$

The memory part can be expressed as a series expansion. The series expansion has been derived and presented by, e.g., Lamb (1932, Art. 255). In numerical computations, the series expansion can be used to solve the memory part. For large values of β, asymptotic expansions can be applied. The combination of the series and asymptotic expansions solving the memory part are given by Newman (1992). Applying the series and asymptotic expansions, the solution domain in the β-μ plane is divided into sub-domains in which the different solution schemes are applied (Liapis and Beck, 1985). Polynomial approximations and Filon's integral formulae have been used in addition to the series and asymptotic expansions (Lin and Yue, 1991; Sen, 2002). Clement (1998) showed that the transient Green function can also be expressed as a solution of an ordinary differential equation. The solution procedures of the ordinary differential equation were proposed by Clement (1998) and the solution for this differential equation using the Taylor series expansions was presented by Chuang et al. (2007).

In this work, the memory part of the transient Green function and its derivatives are solved using a numerical integration. One benefit of the numerical integration is that the whole β-μ domain can be solved with the same method. However, the accuracy of the numerical solution has to be controlled. The numerical integration of the memory part is based on an adaptive Gauss-Kronrod quadrature formula. The N_G -point Gauss quadrature rule for an integral over an interval [a,b] can be expressed as follows (see, e.g., Press et al., 1997):

$$I = \int_a^b f(x)dx \approx \sum_{i=1}^{N_G} W_i f(x_i)\,, \qquad x_i \in [a,b], \tag{2.100}$$

where W_i are the weight coefficients. In the ordinary Gauss quadrature formulae, a constant number of points are used and if the number of the points is increased, the previous results cannot be reused. However, according to the Gauss-Kronrod rules, the previous function calls can be reused, hence, reducing the computational time and improving the accuracy. In the adaptive integration, the integration interval is subdivided into smaller intervals in which the estimated largest errors

exist. The interval of the estimated largest error is bisected and the Gauss-Kronrod rule is applied to each subinterval. The error at each interval is estimated by comparing the result between the 21-point Gauss-Kronrod rule and the 10-point Gauss rule. The absolute and relative errors are given by the following formulae:

$$\varepsilon_{abs} = \left| I_K - I_G \right| \tag{2.101}$$

$$\varepsilon_{rel} = \frac{\left| I_K - I_G \right|}{\left| I_K \right|} \tag{2.102}$$

Subscript K is for the 21-point Gauss-Kronrod rule and G is for the 10-point Gauss rule for the estimated integrals. The numerical solution of the Gauss-Kronrod-based adaptive algorithm was implemented using the QUADPACK Fortran code package (Piessens et al., 1983).

In the present numerical integration, the integral given by Equation (2.68) was solved over the interval [0, λ]. The upper limit was set to $\lambda = 30/\mu$ and hence the term $e^{-\lambda\mu}$ approaches zero at large λ in the numerical integration. As target values, the absolute and relative errors were set to 0.0 and 10^{-10}, respectively. The order of magnitude of the estimated relative error after the numerical integration was 10^{-10} at the large part of the μ-β domain. However, at small μ values (about $\mu < 0.1$) and large β values (about $\beta > 10$), the relative error was in the order of 10^{-8}. If μ was close to zero the numerical integration failed at large β values, typically if $\beta > 10$ and $\mu < 10^{-3}$. At $\mu = 0$, the memory part $\hat{G}^{(t)}$ and also the derivatives $\hat{G}^{(xy)}$ and $\hat{G}^{(z)}$ were determined using the Bessel function expressions as given in Equation (2.74) for $\hat{G}^{(t)}$.

The numerical integration solution based on the adaptive Gauss-Kronrod rule was compared with the series solution. The series solution is based on the series expansion and its asymptotic expansions (Newman, 1992). The series solution was calculated in two parts: the series expansion was used at interval $\beta = 0 \ldots 9$ and the asymptotic expansion when $\beta > 9$. The memory part solved by the numerical integral rule and the series solution are shown in Figure 2.8. The memory part is given for three different values of μ. The lines for the two different solutions are indistinguishable in the figures. The absolute difference between the numerical integration and the series solution was in the order of 10^{-8} or smaller. Only in the vicinity of $\mu = 9$ was the order of magnitude in the absolute difference 10^{-5}. The difference near $\beta = 9$ is due to the numerical inaccuracies in the series expansion

solution. However, more accurate, and faster solutions, can be used in connection with the series expansion than are applied in this work (Newman, 1992). Obviously, the numerical integration is time-consuming. The rough order of magnitude of an average computing time in evaluating the memory part using the numerical integration lasts about 4…5 times longer than the series solution.

In this work, the numerical integration was used to evaluate the memory part of the transient Green function beforehand. Hence, the computation time of the numerical integration is not crucial in the time domain calculation. The application of the pre-calculated memory part in the time domain calculation is explained in the next section.

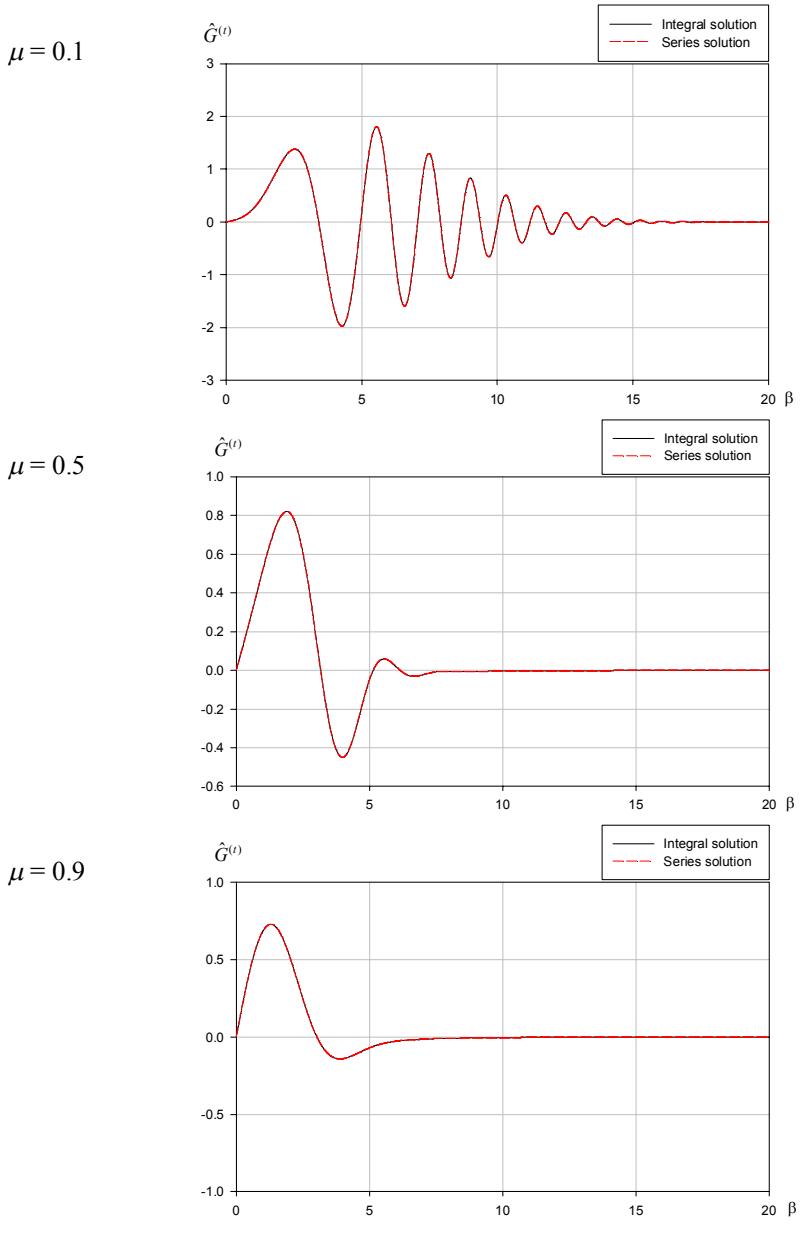

Figure 2.8. The memory part $\hat{G}^{(t)}$ of the Green function given at three values of μ. The solutions are based on the numerical integration rule and the series solution. The lines of the two solutions are indistinguishable.

2.4.3 Interpolation method of the pre-calculated Green function

The most time-consuming part of the calculation is the solution of the memory part of the transient Green function because of the convolution integral. The solution time of the memory part is proportional to the number of time steps in the convolution integral multiplied by the number of panels squared, $N_\tau \times N_P^2$. At every time step, $N_\tau \times N_P^2$ evaluations of the memory part are necessary in the body nonlinear solution. The memory part is a function of the coordinates between the source and field points and time delay $t - \tau$. It does not depend on the frequency of the oscillation of the body or the heading and ship speed. Hence, the memory part can be evaluated beforehand at several non-dimensional parameters β and μ. During the calculation in the time domain, the values of the memory part can be interpolated from the pre-calculated results by, for example, applying a bilinear interpolation (Ferrant, 1991).

In this work, the interpolation algorithm is based on the finite element presentation of the memory part of the Green function in the β-μ plane. The memory part is solved beforehand and the results are stored in the file. In the beginning of the calculation, the table $\hat{G}^{(t)}(\mu, \beta)$ is read into the computer's memory. During the calculation the values of the memory part are interpolated from the table using the finite element shape functions. Nine-node quadrilateral elements are used to describe the shape functions. The finite element approximation for the memory part can be given as follows:

$$\widetilde{G}(\xi_1, \xi_2) = \sum_{j=1}^{9} N_j(\xi_1, \xi_2) \hat{G}_j^e \,, \tag{2.103}$$

where the finite element shape functions are the following (Zienkiewicz, 1971):

$$\begin{aligned}
N_1 &= \frac{1}{4}(1-\xi_1)(1-\xi_2)(\xi_1\xi_2) \\
N_2 &= \frac{1}{4}(1+\xi_1)(1-\xi_2)(-\xi_1\xi_2) \\
N_3 &= \frac{1}{4}(1+\xi_1)(1+\xi_2)(\xi_1\xi_2) \\
N_4 &= \frac{1}{4}(1-\xi_1)(1+\xi_2)(-\xi_1\xi_2) \\
N_5 &= \frac{1}{2}(1-\xi_1^2)(1-\xi_2)(-\xi_2) \\
N_6 &= \frac{1}{2}(1-\xi_2^2)(1+\xi_1)(\xi_1)
\end{aligned} \tag{2.104}$$

$$N_7 = \frac{1}{2}(1-\xi_1^2)(1+\xi_2)(\xi_2)$$
$$N_8 = \frac{1}{2}(1-\xi_2^2)(1-\xi_1)(-\xi_1)$$
$$N_9 = (1-\xi_1^2)(1-\xi_2^2)$$

The convention of the local node numbers and part of the global finite element mesh are shown in Figure 2.9.

In Equation (2.103), the finite element approximation is $\widetilde{G}(\xi_1,\xi_2)$ of the memory part and the pre-calculated memory part is $\hat{G}_i^e$ at node number *i* of element *e*. Thus, the pre-calculated memory part is given as a finite element mesh and the pre-calculated values have been determined at nodal points β and μ. The coordinates ξ_1,ξ_2 are the element local coordinates of β and μ inside the element *e*. The nodes of the element are at points $\xi_1 = \pm 1$ and $\xi_2 = \pm 1$. During the calculation, the element number where the required β and μ lie can be found directly if constant size elements are used in the β-μ domain, i.e. constant spacing of $\Delta\beta$ and $\Delta\mu$. Hence, a time-consuming searching algorithm from the tabulated values is not needed. When the element number is known, the corresponding node numbers are obtained directly from the connection table of the elements and nodes. At the known element, the finite element approximation of the memory part of the Green function at the point (β, μ) can be determined from Equation (2.103). The derivatives $\hat{G}^{(xy)}(\mu,\beta)$ and $\hat{G}^{(z)}(\mu,\beta)$ are also presented with the finite element approximation.

In the presented calculation cases in this work, the constant spacing of the nodes β and μ were $\Delta\beta = 0.01$ and $\Delta\mu = 0.01$. The range of the calculation domain was $0 \le \mu \le 1$ and $0 \le \beta \le 40$. In the calculation, β is seldom outside $\beta > 40$. The memory part of the Green function is also very narrow-banded, close to $\mu = 0$ for a large β. Outside the tabulated domain, the memory part of the Green function was calculated instead of interpolated if $\beta > 40$ and $\mu < 0.05$; otherwise the memory part was set to zero.

The memory part of the transient Green function at three μ values as a function of β is shown in Figure 2.10. The results are based on the numerical integration and interpolation using the finite element approximation. In the figures, the values of the memory part were determined at points β and μ, which are located at halfway between the nodes. Hence, the distances of the points are greatest from the nodes where the values of the pre-calculated memory part were evaluated. In this case,

the interpolation probably gives the largest error. The integrated values were determined at the points β and μ. Thus, the figures show the differences between the numerical integration and the finite element approximation and hence the accuracy of the interpolation. At the two largest μ values in the figures, the differences between the integrated and interpolated solutions cannot be seen. At the smallest μ value in the figures, $\mu = 0.005$, the interpolation gives somewhat larger results for the peak values than the integration if $\beta > 15$. At very small μ values, the difference increases if β increases. In the time domain calculation, the evaluation of the memory part is about 30 times faster using the finite element approximation than the series solution.

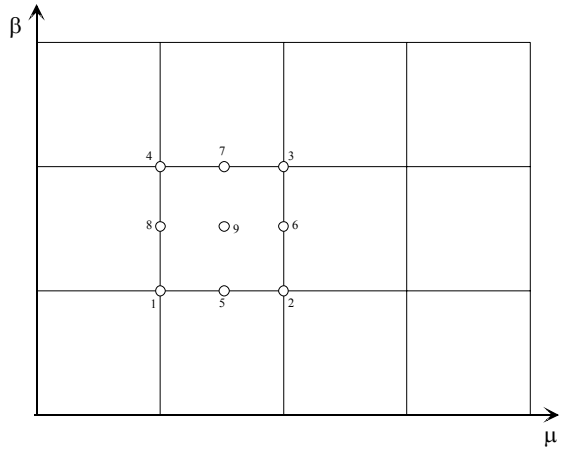

Figure 2.9. Element local node number convention.

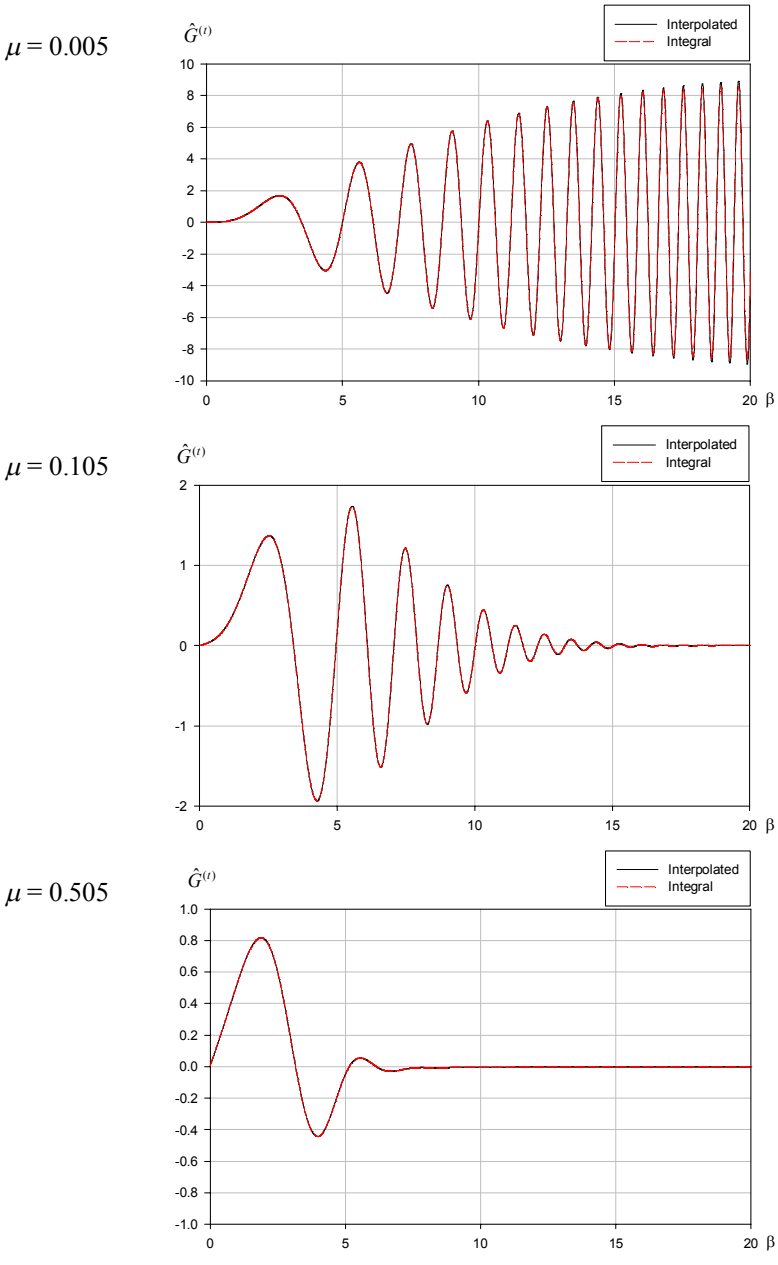

Figure 2.10. The memory part of the Green function at three μ values based on the numerical integration and interpolation with the finite element approximation.

2.4.4 Time integration

The accelerations of the body at the centre of gravity are solved from the equations of motion. Once the accelerations are known, the velocities and motions can be determined using time integration. In the acceleration potential method, the accelerations of the body have to be known because they appear in the body boundary condition of the potential function φ. The body motions and velocities are predicted by the time integration from the previous time step, but the equation of motions that gives the accelerations is not yet solved. In the present time domain method, an iterative solution is applied using a predictor-corrector scheme in the time integration.

The time integration of the velocities and motions is based on the modified Euler method and a predictor-corrector scheme (Isaacson and Keller, 1966, p. 388). For the motions and velocities, the predictor part is given as follows:

$$\begin{aligned} u_{k+1}^{(1)} &= u_k + a_k \Delta t \\ x_{k+1}^{(1)} &= x_k + U_k \Delta t \end{aligned} \tag{2.105}$$

and the corrector is given by

$$\begin{aligned} u_{k+1} &= u_k + \left(a_k + a_{k+1}^{(1)}\right)\frac{\Delta t}{2} \\ x_{k+1} &= x_k + \left(U_k + U_{k+1}^{(1)}\right)\frac{\Delta t}{2} \end{aligned} \tag{2.106}$$

where $\Delta t = t_{k+1} - t_k$ is the time step size. The velocities u_k are (u, v, w, p, q, r) and the accelerations a_k are $(\dot{u}, \dot{v}, \dot{w}, \dot{p}, \dot{q}, \dot{r})$. The body motions x_k are given in the space-fixed coordinate system and the velocity components U_k are expressed as $(\dot{\mathbf{x}}_G, \boldsymbol{\Omega}) = (\dot{\eta}_1, \dot{\eta}_2, \dot{\eta}_3, \dot{\eta}_4, \dot{\eta}_5, \dot{\eta}_6)$ in the space-fixed coordinate system. The transformation from the body-fixed to space-fixed coordinate system is given by Equations (2.1) and (2.2) for the translational and angular velocities respectively.

The surge velocity has been kept constant during the calculation in the studies presented in this work. At forward speed, the constant surge velocity is the same as the forward speed U_0 of the body. Hence, the surge acceleration is zero and the surge motion is the same as the distance of the centre of gravity from the origin of the space-fixed coordinate system.

The iteration can be repeated applying the corrector again and solving the equations of motion until a desired accuracy has been reached. The results presented

in this work were calculated using one iteration to save computation time. This means that the corrector was calculated once at every time step. The accuracy of the time integration was monitored during the calculation, determining an estimate of the error (Isaacson and Keller, 1966, p. 393). The estimate of the error is defined as the difference between the solution of the predictor and corrector, and it can be given as follows for the motions:

$$\delta_{k+1} = x_{k+1}^{(1)} - x_{k+1} . \tag{2.107}$$

The estimate of the error is not a true error estimate but gives an insight into the accuracy of the time integration after the solution of the corrector. An example of the estimate of the error in heave and pitch as a function of non-dimensional time is given in Figure 2.11 for the model test ship (details of the model tests are given in Chapter 4). The estimate of the error was calculated at every time step, and it is given as a function of time in the figures for the heave and pitch motions. The heave and pitch motions are divided by the first harmonic component that was determined from the time histories of the motions. Hence, the non-dimensional estimate of the error gives an estimate for the relative error in the time integration of the motions at different time steps. The heave and pitch amplitudes are predicted with the estimate of the relative error in the amplitudes below 1%.

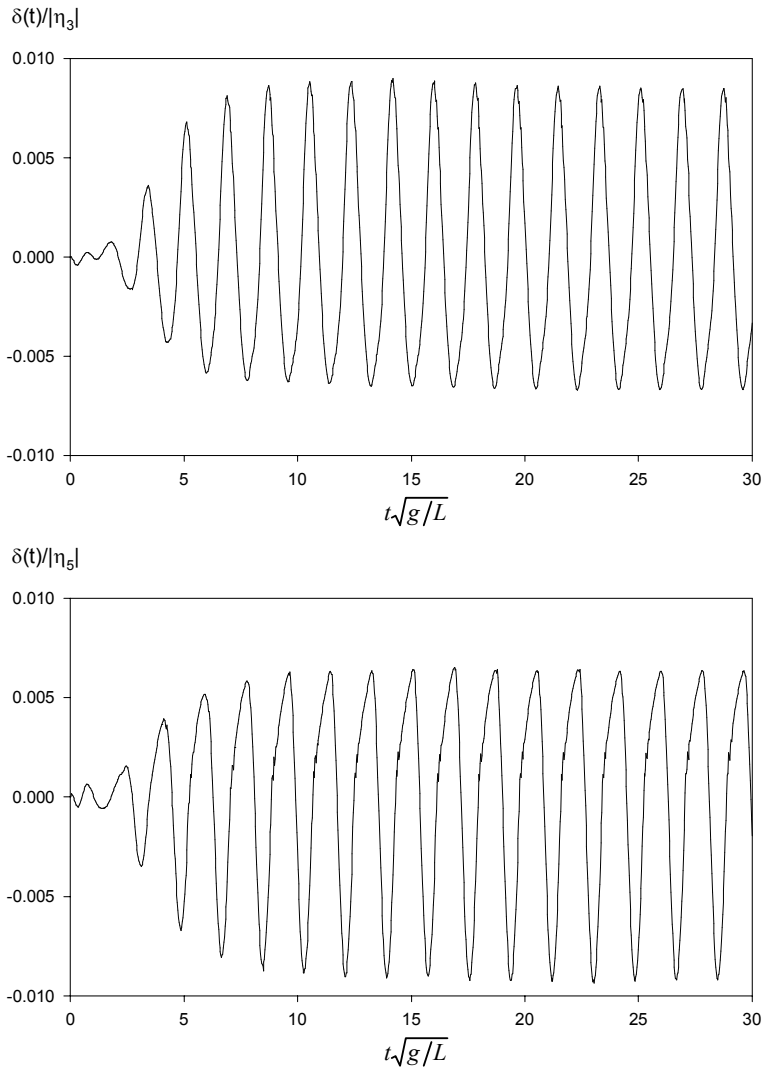

Figure 2.11. The estimate of the error for heave (η_3) and pitch (η_5) determined for the model test ship (RoPax ship) in regular waves at forward speed Fn = 0.25. The body nonlinear solution at wave amplitude a/L = 0.013 and wave frequency $\omega\sqrt{L/g}$ = 2.21. The length of the ship is L.

2.4.5 Body linear and nonlinear solutions

In the body linear solution, the body position is not updated during the calculation and the wetted surface of the body is the same as at $t = 0$ for all $t > 0$. The pressure is solved for the mean wetted surface below the mean water level $z = 0$. In the body nonlinear solution, the instantaneous position of the body is updated during the calculation. The pressure is solved for the instantaneous, wetted surface of the body below $z = 0$.

In the body linear solution, the impulsive part of the transient Green function is solved only once because it does not change during the calculation. The body geometry remains the same and the distances between the source and field points are the same as they were at the first time step. The matrix [**A**] in Equation (2.96) includes the impulsive part of the transient Green function and the matrix is also factorized only once. The factorized form can be used to solve the source strengths in the subsequent time steps. It is also possible to reduce the calculation time using the calculated results of the memory part from the previous time steps. If the memory part is solved once for the time delay $t - \tau$, the results can be used in the subsequent time steps. The distance between the coordinates of the field points and source points does not change for the same values of $t - \tau$ because the body position is not updated. However, this was not applied in the present computations and the calculation was performed in the same way as the body nonlinear solution, i.e. solving the memory part at every time step for all $t - \tau$.

The fluid velocity squared term $0.5\left|\nabla\Phi\right|^2$ in Bernoulli's equation is included in the body linear and nonlinear solutions. Hence, the body linear solution is not properly linearized. The inclusion of the fluid velocity squared term is not consistent with the linear free surface boundary condition in the body linear and nonlinear solutions either. The fluid velocity squared term is a higher order term, and it is not included in the dynamic free surface boundary condition. The effect of the fluid velocity squared term on responses is presented and discussed in detail in Sections 4.4, 4.5.4 and 4.5.6.

Most of the results presented in this work have been calculated using constant panel meshes. In the constant panel mesh, the geometry and size of the panels remains the same during the calculation and the panel mesh is the same as at time $t = 0$ for all $t > 0$. The normal and position vectors (**n** and **r**) of the body expressed in the body-fixed coordinate system also remain the same during the calculation as they were at $t = 0$.

In the body nonlinear solution, and using the constant panel mesh, the body position is updated during the calculation and, at every time step, all of the panels are checked to find out if they are above or below the free surface level. The panel is considered wet if all of the corner points of the panel are below the water level, $z = 0$. Otherwise, the panel is dry and then it is not included in the solution. Hence, the number of panels that are included in the solution can be varied in the body nonlinear solution.

The line integral at the waterline is determined at the centroid of the panels. The centroid of the panels lies some distance, $z < 0$, below the waterline (unless the panel is not exactly horizontal at $z = 0$). Hence, this is an approximation of the line integral because it is not determined at $z = 0$. In the body nonlinear solution, and if the constant panel mesh is used, the line integral is determined for the panels that are wet and closest to the waterline. If one of these panels becomes dry the memory effect is lost from this panel. In the body linear solution, the memory effect due to the line integral is preserved.

Alternatively, the hull surface can be re-panelized at each time step in the body nonlinear solution, fitting the cross sections of the body with cubic splines up to the waterline. The number of panels remains the same during the calculation unless the cross section is out of the water completely. However, the normal and position vectors of the body change during the calculation in the body nonlinear solution. The panel size and geometry also change. Thus, the velocity of the centroid of the panel can be different from the velocity of the fixed point on the body. Hence, applying the substantial derivative for the fluid on the body point, the velocity of the point that is followed is not necessarily the same as the velocity of the body point. In the spline-fitted mesh, the velocity $\mathbf{U}$ of the point on the body is determined using the backward difference method in the substantial derivative, i.e. the velocity $\mathbf{U}$ in the term $\mathbf{U} \cdot \nabla \phi$. The benefit of spline-fitted mesh is that the memory effect in the line integral is not lost because the same panels are located at the waterline, although the body position is updated during the calculation. However, only part of the studies for cones was calculated using the spline-fitted panel mesh.

In addition to the body linear and nonlinear solutions, the time domain method includes the option to solve forces and moments using a so-called body-wave nonlinear solution. The body-wave nonlinear solution is the same as the body nonlinear solution but additional nonlinear effects are included with the Froude-Krylov and hydrostatic restoring forces and moments. The Froude-Krylov and hydrostatic restoring pressures are solved up to the free surface elevation $z = \zeta$. The applied formulation is an extension of the theory that is based on the linear

free surface boundary condition. The additional Froude-Krylov and hydrostatic restoring forces and moments are approximations and they include a higher order error. However, the formulations used in this work are consistent within the linear theory (Faltinsen, 1990, p. 21). The free surface elevation is defined up to the incoming wave surface, and the radiated-diffracted waves are not taken into account. The free surface elevation ζ of the incoming wave is determined from the linear dynamic boundary conditions as follows:

$$\zeta g + \frac{\partial \phi_I}{\partial t} = 0 . \tag{2.108}$$

The velocity potential of the incoming wave ϕ_I was given in Equation (2.30). Hence, the pressure due to the incoming wave increases exponentially up to the wave elevation $z = \zeta$. For each panel, the panel is checked to find out if it is below the free surface ζ and above $z = 0$. The additional hydrostatic and Froude-Krylov pressures are calculated for these panels. The panel is also checked to find out if it is above the free surface ζ when $z < 0$ and for this panel the total pressure is set to zero. The additional hydrostatic and Froude-Krylov pressures are calculated from Bernoulli's equation for the contributions of the incoming wave and hydrostatic pressures. The additional pressures are taken into account in the Froude-Krylov and hydrostatic restoring forces and moments in the body-wave nonlinear solution.

2.4.6 Computation procedure of the time domain method

The calculation procedure of the computer program for wave load predictions in the time domain (WAVETD) is presented in Figure 2.12. The programming language was Fortran 90.

The program includes two options to evaluate the Green function. The Green function can be calculated beforehand or solved during the time domain calculation. The pre-calculated memory part of the Green function and the derivatives of it are read into the computer's memory at the beginning of the calculation.

Before the time domain calculation, the hull surface of the body is discretized by panels and the basic hydrostatic calculations are carried out. The time domain calculation is performed in the defined operating conditions in regular or irregular waves at forward or zero speed at the arbitrary heading angle. All the results presented in this work have been calculated in head seas however.

The program includes options for the body linear and nonlinear solutions, and the body-wave nonlinear solution that includes additional nonlinearities in hydrostatic and Froude-Krylov forces and moments.

At the beginning of the time domain calculation, the impulsive part of the transient Green function is solved and the matrix [**A**] of Equation (2.96) is generated. The matrix [**A**] is the same for the perturbation velocity and acceleration potentials. In the body linear solution, the matrix [**A**] is only generated once in the first time step. In the body nonlinear solutions, the floating position of the body is updated at every time step, and for this reason the matrix [**A**] has to be generated again at every time step. Next, the boundary conditions for the perturbation velocity and acceleration potentials are formed, and the memory part is then solved to obtain the vector **f**. The vector **f** includes the body boundary conditions and the memory part with known source strengths from previous time steps. The unknown source strengths for the perturbation and acceleration potentials are solved from the system of linear equations (2.96). After that, the perturbation velocity and acceleration potentials can be solved and pressures at each panel can be calculated using Bernoulli's equation. Forces and moments in the equations of motion are obtained by integrating pressures over the wetted surface of the body. The equations of motion are solved to obtain the six-degree freedom accelerations. Time integration is applied to determine the velocities and motions of the body.

The basic results, including, for example, ship motions and accelerations at the centre of gravity, are stored in the ASCII file during the calculation. Detailed results are stored in the binary file for post-processing purposes. The detailed results include the pressures for each panel at every time step.

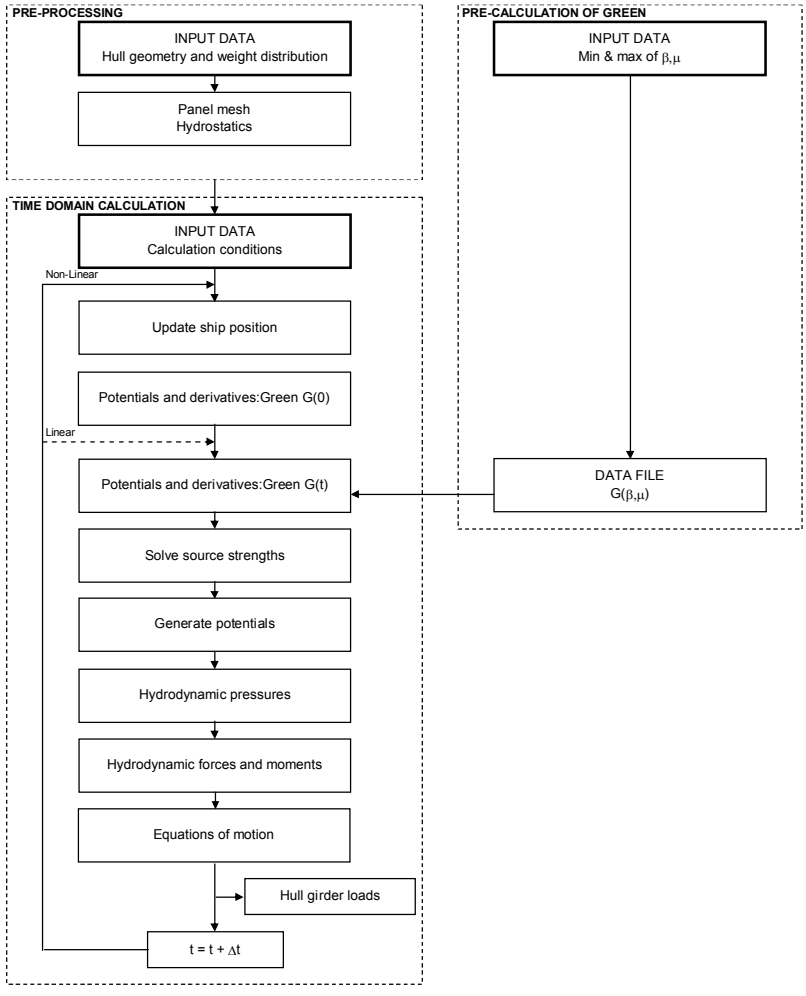

Figure 2.12. Computation procedure of the time domain computer program WAVETD.

3. Results of simple body geometries

3.1 Hemisphere

3.1.1 General

In this Section 3.1, the body linear solution is applied to calculate an impulse response function for a hemisphere. Added mass and damping coefficients can be determined with the impulse response function. For the hemisphere, the added mass and damping coefficients based on an analytical solution are given by Hulme (1982). The calculated added mass and damping coefficients in heave are compared with the given analytical results. The comparison gives a basis verification of the body linear solution at zero speed in forced heave motion without coupling to other modes of motion.

3.1.2 Impulse response, added mass and damping

The added mass and damping coefficients can be determined by applying a Fourier transformation for an impulse response function given in the time domain. Here, small motions are assumed and the hydrodynamic pressure can be expressed by a linear form of Bernoulli's equation without the fluid velocity squared term. The velocity potential is the solution of the linear free surface and body boundary conditions. The body boundary condition is expressed for a specific body motion and hence the six degrees of freedom motions are decoupled. In this work, the impulse response approach is only applied at zero speed. The details of the derivation and relations between the frequency and time domain methods are given by Cummins (1962) and Ogilvie (1964). King et al. (1989) and Bingham et al. (1994) gave a general linear formulation of the impulse response method to determine hydrodynamic forces and moments in a body-fixed coordinate system with forward speed.

The radiation force in the direction i can be expressed as follows:

$$F_i = -\rho \int_{S_0} \frac{\partial \phi}{\partial t} n_i \, dS \,, \tag{3.1}$$

where $i = 1,2,\ldots,6$ and $n_i = n_{0i}$, see Equations (2.83) and (2.84). The integration is performed over the mean wetted surface S_0 because small motions are assumed in the body linear solution. Following Wehausen (1971), the radiation velocity potential ϕ_i is the convolution of the arbitrary body motion η_i and radiation velocity potential ψ_i due to impulse:

$$\phi_i(P,t) = \int_0^t \ddot{\eta}_i(\tau)\psi_i(P,t-\tau)d\tau \,, \tag{3.2}$$

where $\ddot{\eta}_i$ is the body acceleration. The same was given by Cummins (1962) in a slightly different form. Using the above Equation in Equation (3.1), the following formulae can be derived for the added mass and damping coefficients:

$$A_{ij}(\omega) = A_{ij}(\infty) + \int_0^\infty L_{ij}(\tau)\cos\omega\tau \; d\tau \tag{3.3}$$

$$B_{ij}(\omega) = \omega \int_0^\infty L_{ij}(\tau)\sin\omega\tau \; d\tau \tag{3.4}$$

The integrals are Fourier cosine and sine transforms of the impulse response function $L_{ij}(\tau)$. The impulse response function $L_{ij}(\tau)$ is defined as follows:

$$L_{ij}(\tau) = \rho \int_{S_0} \frac{\partial \psi_j(P,\tau)}{\partial t} n_i dS \,. \tag{3.5}$$

The term $A_{ij}(\infty)$ is the added mass at infinity frequency:

$$A_{ij}(\infty) = \rho \int_{S_0} \psi_j(P,\tau=0) n_i dS \,. \tag{3.6}$$

The radiation velocity potential due to impulse ψ_j can be solved by applying the body boundary condition for the unit step velocity:

$$\frac{\partial \psi_i}{\partial n} = \begin{cases} 0 & t < 0 \\ n_i & t > 0 \end{cases} \tag{3.7}$$

or

$$\frac{\partial \psi_i}{\partial n} = H(t) n_i \tag{3.8}$$

where $H(t)$ is the step function, $H(t) = 1$ if $t > 0$, and $H(t) = 0$ if $t < 0$ (Derrick and Grossman, 1982, p. 251). This boundary condition can be given in another form taking the time derivative from both sides and expressing the time derivative of the step function by a delta function. Hence, the time derivative of the radiation velocity potential due to impulse can be solved directly using the following boundary condition:

$$\frac{\partial}{\partial n}\left(\frac{\partial \psi_i}{dt}\right) = \delta(t) n_i, \tag{3.9}$$

where $\delta(t)$ is the Dirac delta function, which is zero otherwise, except at $t = 0$. The Dirac delta function has the following property: $\int_{-\infty}^{\infty} \delta(t)\, dt = 1$ (Derrick and Grossman, 1982, p. 254). The body boundary condition given by Equation (3.9) is used to solve the time derivative of the velocity potential using the source formulation. Hence, the solution is based on the acceleration potential method where the potential function is $\varphi = \partial \psi_i / dt$.

The approach of the impulse response function was applied to verify that the time domain method solved the radiation problem correctly in forced heave motion at zero speed. The added mass and damping coefficients were determined for the hemisphere and compared with the analytical solution given by Hulme (1982). The analytical solution for the hemisphere has often been used to verify and validate the numerical methods (see, e.g., Lin and Yue, 1991).

In the time domain calculation, the hemisphere was discretized by panels, and the number of panels on the half body was 800. The panel mesh of the hemisphere is shown in Figure 3.1. The radiation velocity potential due to impulse was solved using the boundary condition given in Equation (3.9). The time domain prediction for the heave impulse response function $L_{33}(\tau)$ is shown in Figure 3.2. The impulse response function is given in a non-dimensional form as a function of non-dimensional time. The time step size was $\Delta\tau\sqrt{g/L} = 0.094$ in the calculations.

The reference length L is the radius of the hemisphere and ∇ is the displacement. The heave added mass and damping coefficients are presented in Figures 3.3 and 3.4, respectively. The calculated impulse response function and the added mass and damping coefficients are in good agreement with the analytical solution given by Hulme (1982). The oscillation in the calculated impulse response function is due to the irregular frequencies (John, 1950). The irregular frequencies can be seen clearly in the figures of the added mass and damping coefficients. The first irregular frequency for heave exists at approximately $kL \approx 2.5$. The irregular frequencies can exist in the integral equations using panel methods for bodies oscillating on the free surface (see, e.g., Lee and Sclavounos, 1989).

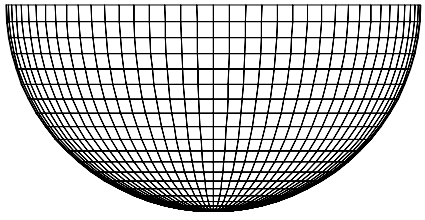

Figure 3.1. The panel mesh of the hemisphere.

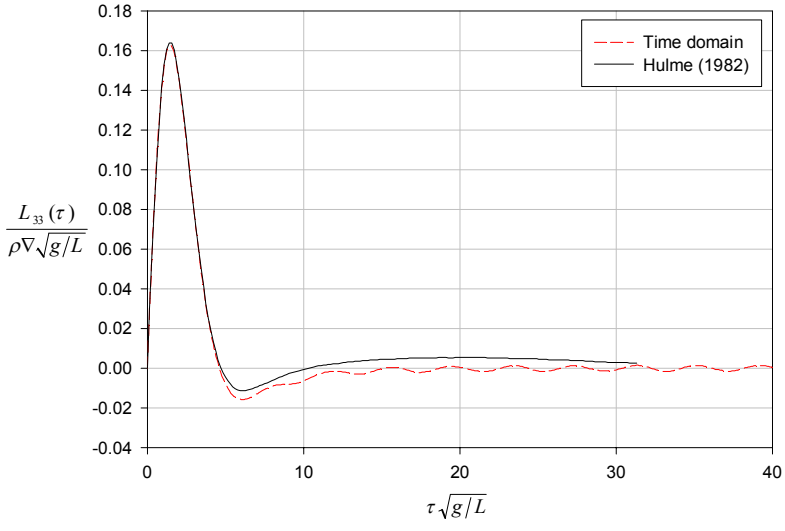

Figure 3.2. Heave impulse response function of the hemisphere as a function of time.

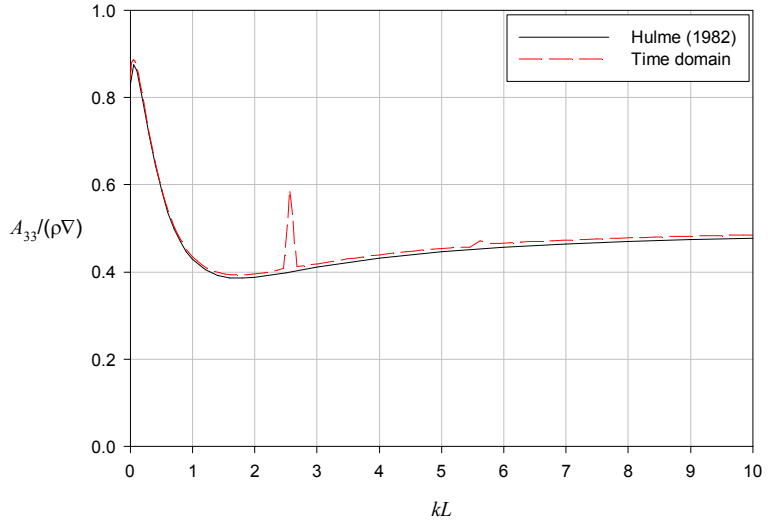

Figure 3.3. Heave added mass of the hemisphere as a function of the wave number.

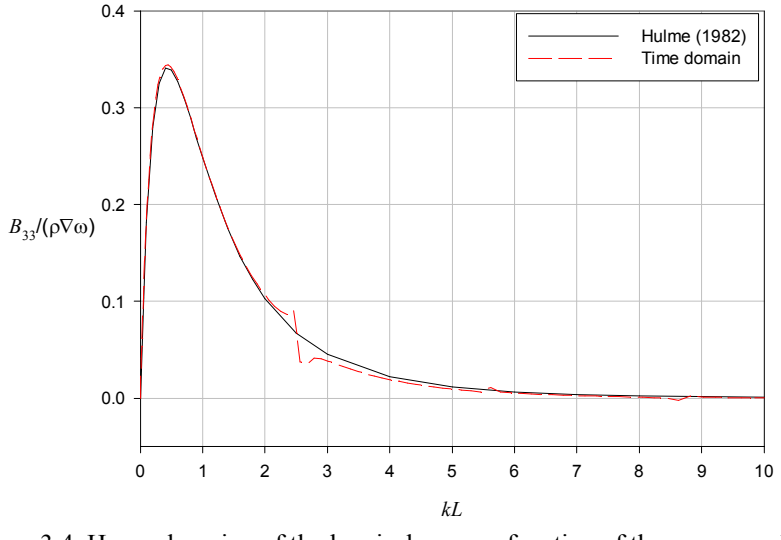

Figure 3.4. Heave damping of the hemisphere as a function of the wave number.

3.2 Cones

3.2.1 General

In this Section 3.2, hydrodynamic forces are given for cones in harmonic heave motion on the free surface. The body linear solution is applied to calculate impulse response functions for cones with two different deadrise angles of 30 and 45 degrees. The impulse response function is used to determine the added mass and damping coefficients. The added mass and damping coefficients are compared with results obtained from a linear frequency domain method. The time domain method is also verified using two simple force formulations for the linear heave radiation force. The simple force formulations are based on the added mass and damping coefficients and the memory function of heaving cones. These simple force formulations are based on the same theoretical background as the time domain method, which should give the same results for the radiation forces.

The body nonlinear solution is used to study nonlinearities in hydrodynamic forces. Different heave amplitudes and frequencies are used when cones are in harmonic forced heave motions on the free surface. The aim is to gain an insight into the nonlinearities in heave radiation forces that are caused by changes to the wetted surface of the body. The contribution of the different terms in Bernoulli's equation in vertical heave forces is also studied. Moreover, the nonlinear heave radiation forces are compared with two simple solutions. The two simple solutions are based on the non-dimensional representation of the linear added mass and damping coefficients and the memory function of heaving cones. The non-dimensional representation of the heave radiation forces are scaled using instantaneous displacements to obtain an approximation for the nonlinear heave radiation forces. The approximation methods are justified for cones because of the similarity of the cone geometries.

The linear and nonlinear calculation with cones is also carried out to investigate the effects of body geometries and panel meshes on the solution. The aim is to obtain information on practical calculations of ship hull forms. Spline-fitted panel meshes of cones are used in addition to the constant panel mesh approach to determine nonlinear heave radiation forces. This gives an insight into the effect on the results if the panel continuously changes piecewise between dry and wet in time.

Furthermore, the effects on the results of non-wall-sided body shapes close to the free surface are studied with cones. Close to the free surface, the transient Green function is a strongly oscillating function. The oscillation of the memory part

increases at small values of the parameter μ when the non-dimensional time β increases. At the free surface $z = 0$, this parameter is $\mu = 0$. The oscillation can induce instabilities in the solution, especially if the body has horizontal body shapes or the inclination angle of the body shapes are small at the free surface. The instability in the transient Green function solution was studied by, for example, Duan and Dai (1999), and Datta et al. (2011). In order to avoid the instability in the solution, Datta et al. (2011) modified the ship geometry by adding an artificial vertical row of panels below the waterline. Duan and Dai (1999) developed modified integral equations for flared bodies. They applied a separate wall-sided surface around the body surface and introduced a new integral equation. Hence, the integral equations include both the wall-sided surface and the body surface in the solution.

In the present calculations of the cones, the distance of the centroid of the panels from the free surface is increased to avoid instabilities. In the calculation, a straightforward approach is applied in which the first row of the panels is not exactly at the mean water level. This is only applied to the cone with a 30 degree deadrise angle. The aim is to obtain information for the practical calculation of bodies that have horizontal shapes close to the water plane. In the calculation of the model test ship in Chapter 4, a criterion will be set for the vertical distance of the centroid of the panel from the free surface if the panel is going to be included in the solution. Studies with the cone give an insight into the effect on the results if part of the cone geometry close to the free surface is not included in the solution.

3.2.2 Impulse response, added mass and damping

Impulse response functions, and added mass and damping coefficients were determined for two cones with deadrise angles of 30 and 45 degrees. The impulse response functions, and the added mass and damping coefficients were determined in the same way as for the hemisphere in Section 3.1.2. Thus, the heave radiation force includes the ϕ_t term and the fluid velocity squared, and the hydrostatic terms were excluded from Bernoulli's equation. The results shown in this section are based on the body linear solution and the acceleration potential method. The added mass and damping coefficients are compared with the results obtained from the frequency domain method, which is based on the three-dimensional Green function (Iwashita, 1997).

For the cone with a 45 degree deadrise angle, two different panel meshes were used: coarse and fine. The second cone has a deadrise angle of 30 degrees, and a rather coarse mesh was used in the calculation to study the effects of the coarse

mesh on the radiation forces. In typical ship applications, the panel mesh can be coarse in order to reduce the computational time. For the cones with 45 degree deadrise angles, the numbers of panels on the half body below the still water level were 240 and 800 in the coarse and fine meshes, respectively. The number of panels was 180 for the cone with a 30 degree deadrise angle. The panel meshes of the cones are shown in Figure 3.5. The fine panel mesh of the 45 degree cone is shown in the figure. The radius of the cone at the still water level is r_c and the height is h_c from the apex of the cone to the still water level. The deadrise angle of the cone is β_c. The reference length L in the non-dimensional forms is the diameter $2r_c$ at the still waterline. The volume of the cone is $\nabla = 1/3\,\pi\, r_c^2 h_c$.

The impulse response function for the cone of 30 degrees started to oscillate strongly at the beginning of the calculation and the calculation gave a divergent solution. Thus, it was necessary to increase the vertical distance of the centroid of the panels from the free surface. In order to avoid the oscillation due to the panels near the free surface, the upper edges of the first row of panels were shifted downwards from the free surface. The upper edge of the first panel row that was included in the solution was $0.04 \times h_c$ below the mean water level $z = 0$. This gave a convergent solution. In addition, the memory part of the transient Green function was integrated over the panels using the 2-point Gaussian quadrature rule to increase the accuracy of the solution. On the other hand, the calculations of vertical forces given in Sections 3.2.3 and 3.2.4 gave convergent and stable solutions without shifting the panels from the free surface. Trial calculations showed that the solution started to be divergent at lower frequencies than those used here to calculate the vertical forces. The impulse excites all of the frequencies and, for this reason, the low frequencies can cause the divergent solution for the impulse response function. Duan and Dai (1999) also observed that with regard to the instabilities in the transient Green function solution, the lower frequencies gave a worse solution compared with higher oscillation frequencies. However, all of the calculations presented here for the cone of 30 degrees are based on the same panel mesh in which the upper edges of the first row of panels were shifted downwards from the free surface.

In Figure 3.6, the impulse response function, added mass and damping coefficients are given for the cone with a deadrise angle of 45 degrees. The results are given for the coarse and fine panel meshes. The impulse response function with the coarse mesh oscillates more than with the fine mesh. However, the coarse and fine meshes give nearly the same results for the added mass and damping coefficients. Differences can be seen in the vicinity of the first irregular frequency

$\omega\sqrt{L/g}$ ≈ 2.5. The agreement is good between the time and frequency domain methods.

The impulse response function and the added mass and damping coefficients for the cone with a deadrise angle of 30 degrees are shown in Figure 3.7. The time domain solution of the damping coefficient is close to the frequency domain solution. The added mass coefficient is, to some extent, at a higher level than the frequency domain result. The irregular frequencies are also located at slightly smaller frequencies. One reason for these differences could be due to the increased distance of the panels from the free surface in the time domain solution. In the time domain calculation, the increased distance means a small gap between the free surface and the cone. Although, the rather coarse mesh can also have an effect on the results, and the impulse response function could have been better determined if a denser mesh had been used. Smaller panel sizes will improve the accuracy of the solution.

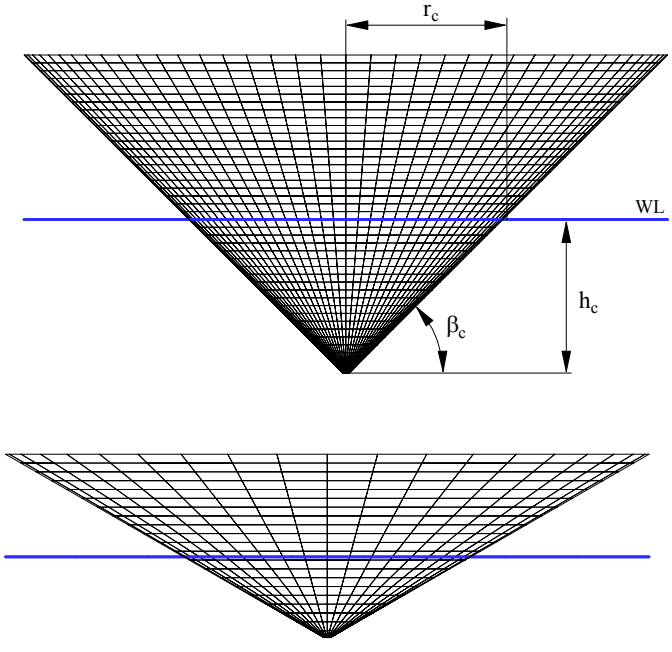

Figure 3.5. Panel meshes of the cones with deadrise angles of (from top to bottom) 45 and 30 degrees. The characteristic length of the cone is $L = 2r_c$.

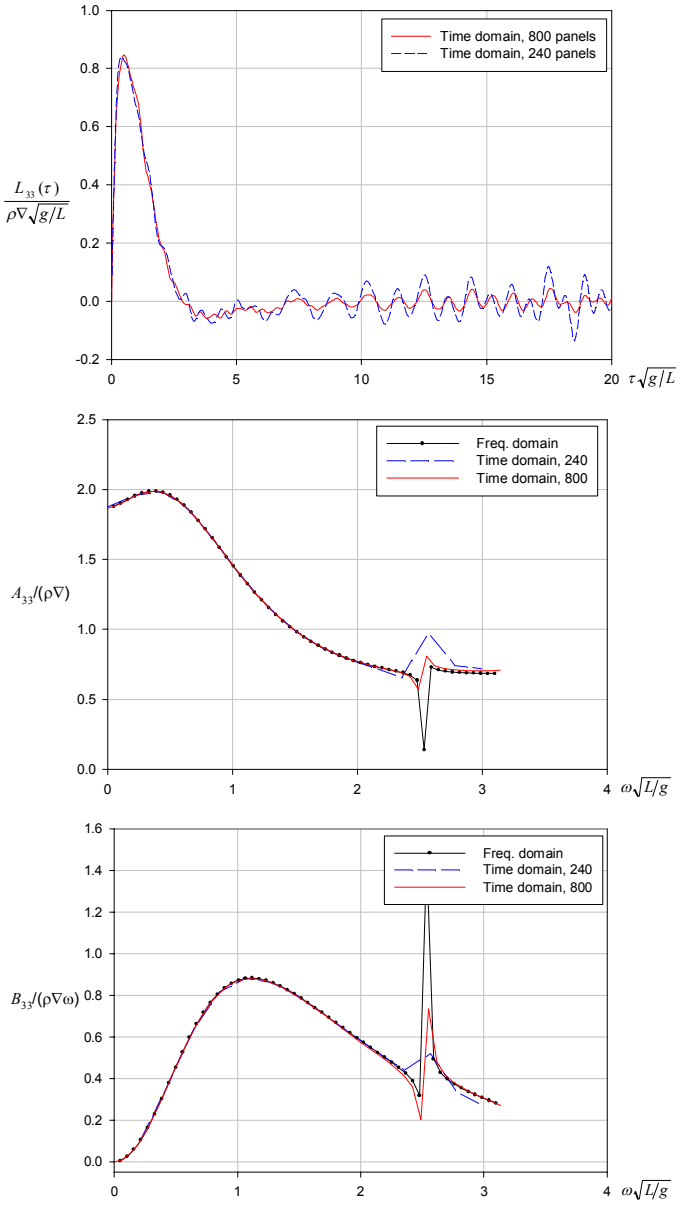

Figure 3.6. Impulse response function, added mass and damping coefficients for the cone with a deadrise angle of 45 degrees. The results are given for two panel meshes: the numbers of panels are 240 and 800 on the half body below the still water level.

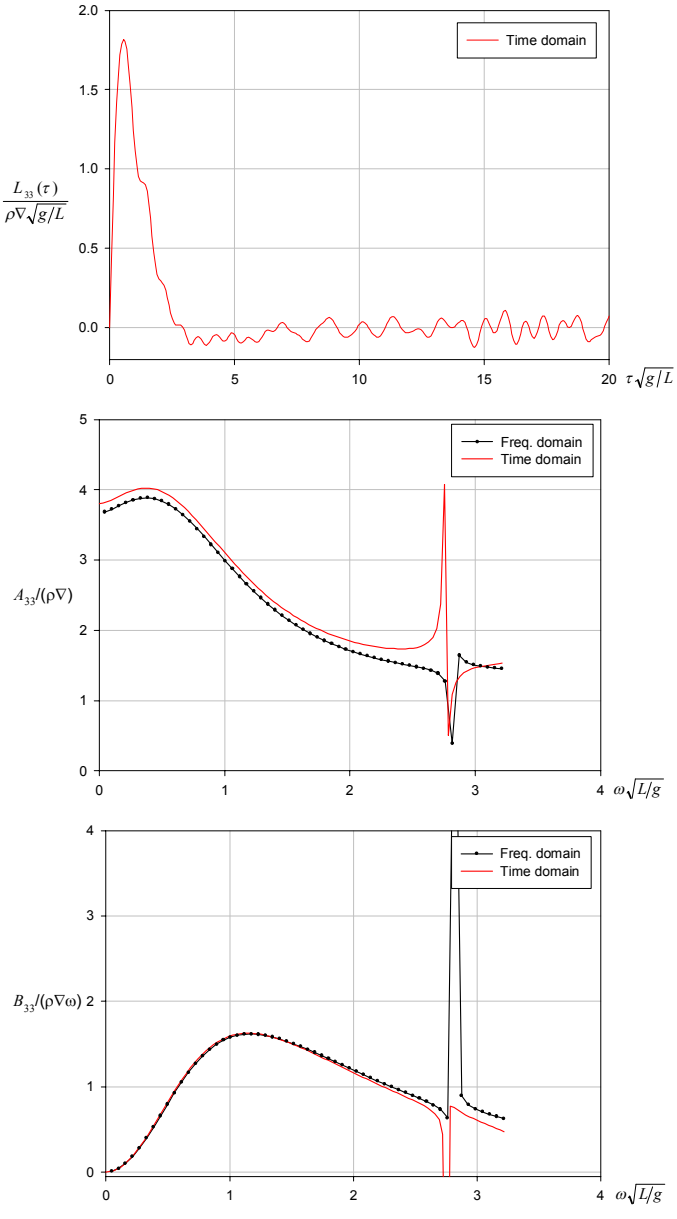

Figure 3.7. Impulse response function, added mass and damping coefficients for the cone with a deadrise angle of 30 degrees.

3.2.3 Linear vertical forces

The impulse response function and the added mass and damping coefficients can be used to determine linear radiation forces. The linear heave radiation force can be expressed in terms of added mass and damping coefficients for a harmonic motion as follows:

$$F_{R3}(t) = -A_{33}(\omega)\ddot{\eta}_3(t) - B_{33}(\omega)\dot{\eta}_3(t), \tag{3.10}$$

where $\dot{\eta}_3$ is the heave velocity and $\ddot{\eta}_3$ is the heave acceleration. The linear heave radiation force can also be expressed by means of the impulse response function $L_{33}(t-\tau)$ as follows:

$$F_{R3}(t) = -\ddot{\eta}_3(t)A_{33}(\infty) - \int_0^t \ddot{\eta}_3(\tau)L_{33}(t-\tau)d\tau, \tag{3.11}$$

where $A_{33}(\infty)$ is the heave added mass at the infinity frequency. The heave motion is given by

$$\eta_3(t) = |\eta_3|\cos(\omega t + \varepsilon), \tag{3.12}$$

where $|\eta_3|$ is the heave amplitude and the phase shift $\varepsilon = -90°$ was used to start the heave motion from zero at $t = 0$. The cones were in forced heave motion and hence the motions, velocities and accelerations were known at every time step. Thus, an iterative solution was not necessary for solving the acceleration potential in the time domain method.

The method based on the added mass and damping coefficients (Coefficient method) and the method based on the impulse response function and the infinity added mass in heave (Memory function method) have to give the same results for the linear heave radiation force. The direct time domain calculation method (Time domain method) has to give the same results as the coefficient and memory function methods. All of the methods are based on the same boundary conditions. The radiation forces based on the coefficient and memory function methods were calculated using the time domain results of the added mass and damping, not the frequency domain results. The midpoint rule was used to integrate the memory part over the panel area in the time domain method.

The linear heave radiation force for the cone with deadrise angle of 45 degrees is shown in Figure 3.8 at three different heave oscillation frequencies: $\omega\sqrt{L/g}$ = 0.5, 1.0 and 2.0. The fine mesh was used in the calculations. The results for the cone with a deadrise angle of 30 degrees are presented in Figure 3.9. In all of the cases in Figures 3.8 and 3.9, the three approaches gave the same results for the linear heave radiation forces. At the beginning of the calculations, the coefficient method deviates from the time domain and memory function methods because the heave velocity is not zero at $t = 0$. Hence, the radiation forces have a contribution from the damping coefficient and heave velocity.

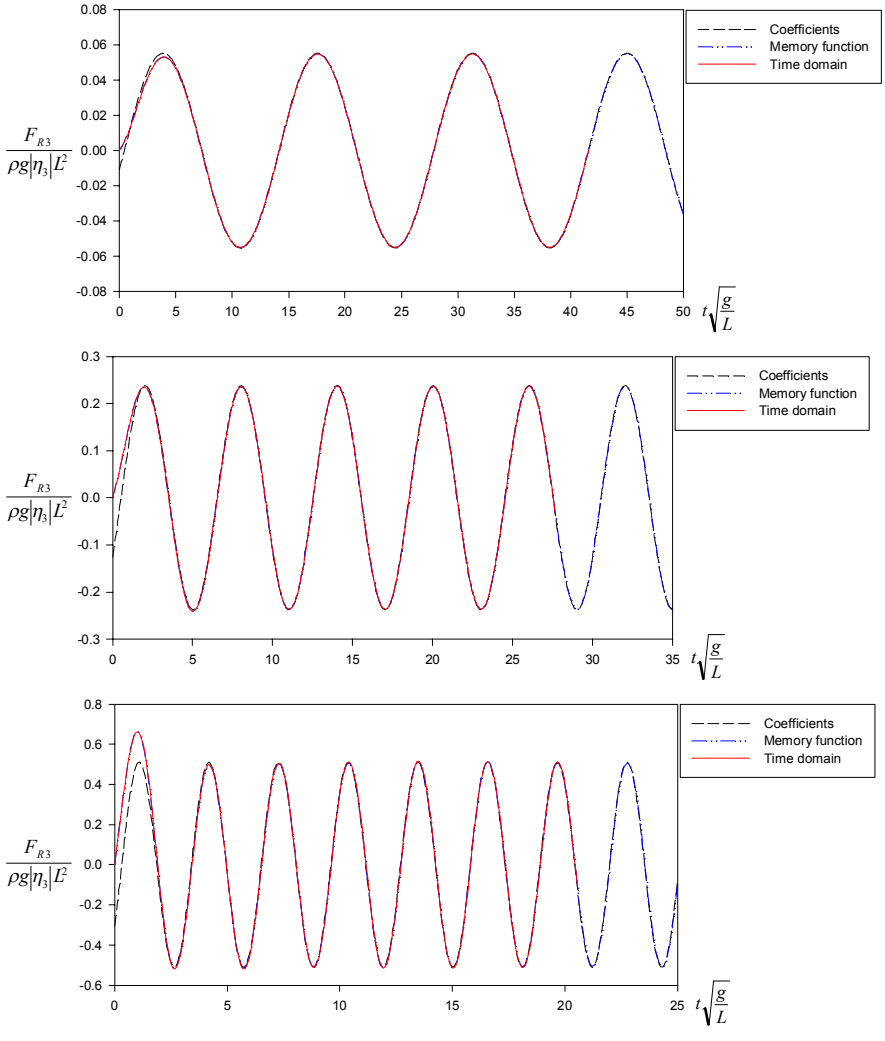

Figure 3.8. Linear heave radiation force for a cone with a deadrise angle of 45 degrees calculated at three different heave oscillation frequencies (from top to bottom): $\omega\sqrt{L/g}$ = 0.5, 1.0 and 2.0.

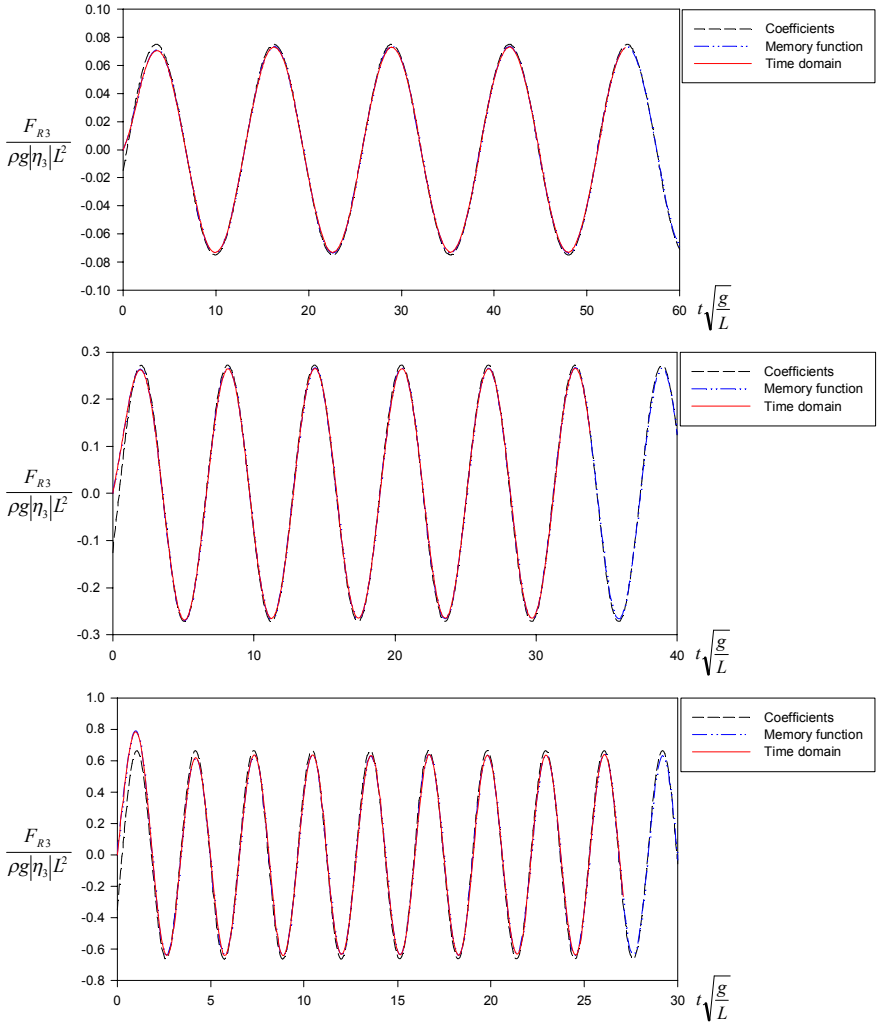

Figure 3.9. Linear heave radiation force for a cone with deadrise angle of 30 degrees calculated at three different heave oscillation frequencies (from top to bottom): $\omega\sqrt{L/g}$ = 0.5, 1.0 and 2.0.

3.2.4 Nonlinear vertical forces

Nonlinear heave forces are presented in this section for the cones with deadrise angles of 30 and 45 degrees. The body nonlinear solution was used when the cones were oscillating at a given heave amplitude and frequency. The radiation forces include the time derivative of the velocity potential ϕ_t and fluid velocity squared $0.5|\nabla\phi|^2$ terms in Bernoulli's equation. Numerical integration of the memory part of the Green function over the panel area was performed using the midpoint rule. The time domain calculations were carried out using the same panel meshes as in the previous section.

The results presented in this section are based on the acceleration potential method. As the body was in harmonic forced motion in the calculations, the heave motions, velocities and accelerations were known at each time step, giving an accurate body boundary condition in the acceleration potential method. An iterative algorithm in the time integration of the motion was not necessary.

The backward difference solution for the time derivative of the velocity potential gave the same results for linear heave forces as the acceleration potential method. For nonlinear heave forces the results were similar in most cases though differences exist. An example is given in Figure 3.10, in which the heave radiation force is given at three heave frequencies, $\omega\sqrt{L/g}$ = 0.5, 1.0 and 2.0, and the heave amplitude is $|\eta_3|/L$ = 0.10. At the low heave frequencies, the solutions gave about the same results. At the highest heave frequency, the difference solution gives lower predictions for the minimum force amplitudes. The peaks in the backward difference solution occur when the panels change from wet to dry or from dry to wet.

Contributions by the pressure components in Bernoulli's equation are shown in Figure 3.11 for the cone of 30 degrees. The forces were calculated at the heave frequencies $\omega\sqrt{L/g}$ = 0.5, 1.0 and 2.0, and the heave amplitude was $|\eta_3|/L$ = 0.05. The hydrostatic pressure term clearly dominates the total force if the heave frequency is low, $\omega\sqrt{L/g}$ = 0.5. The contribution of the time derivative of the velocity potential ϕ_t is small and the fluid velocity squared term $0.5|\nabla\phi|^2$ is almost insignificant. At the higher heave frequencies $\omega\sqrt{L/g}$ = 1.0 and 2.0, the effect of the pressure term ϕ_t becomes significant. The fluid velocities also increase at the higher heave frequencies and, hence, the pressure forces due to the fluid velocity squared term increase too.

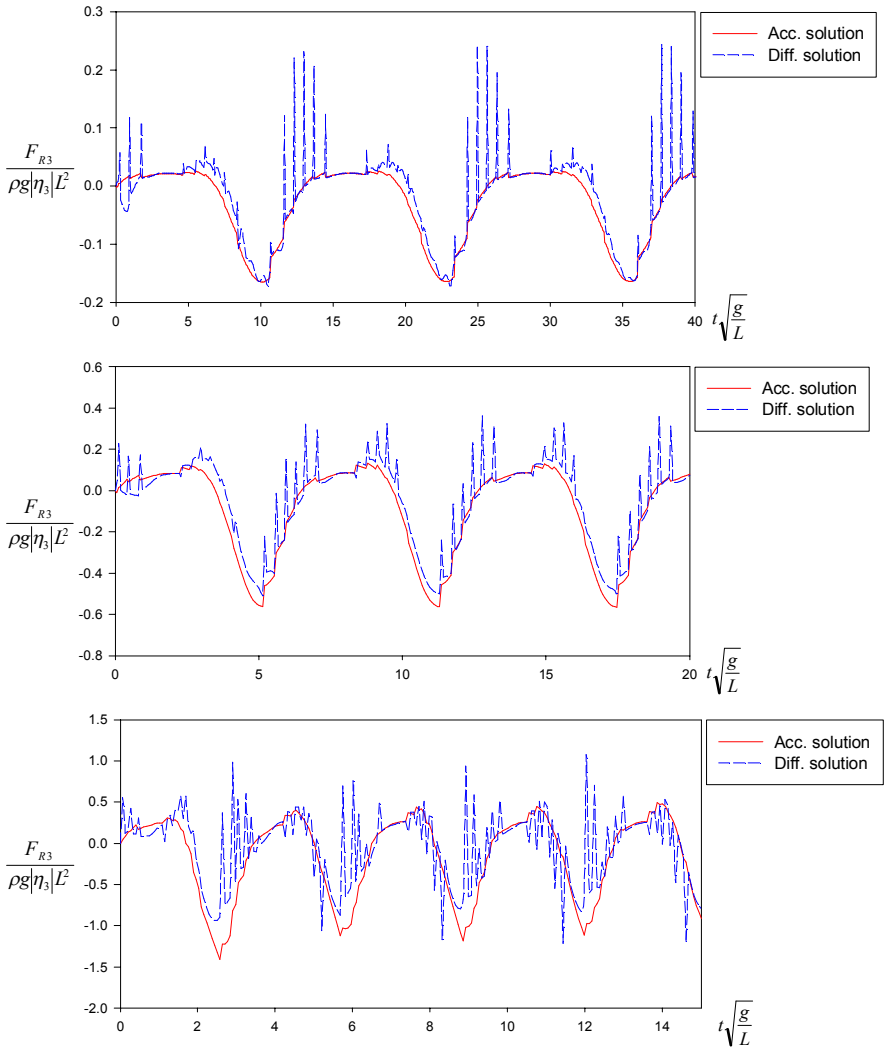

Figure 3.10. Comparison of the nonlinear heave radiation forces for a cone with a deadrise angle of 30 degrees calculated with the acceleration potential method (Acc. solution) and the backward difference method (Diff. solution). The heave oscillation frequencies are (from top to bottom) $\omega\sqrt{L/g}$ = 0.5, 1.0 and 2.0. The heave amplitude is $|\eta_3|/L$ = 0.10.

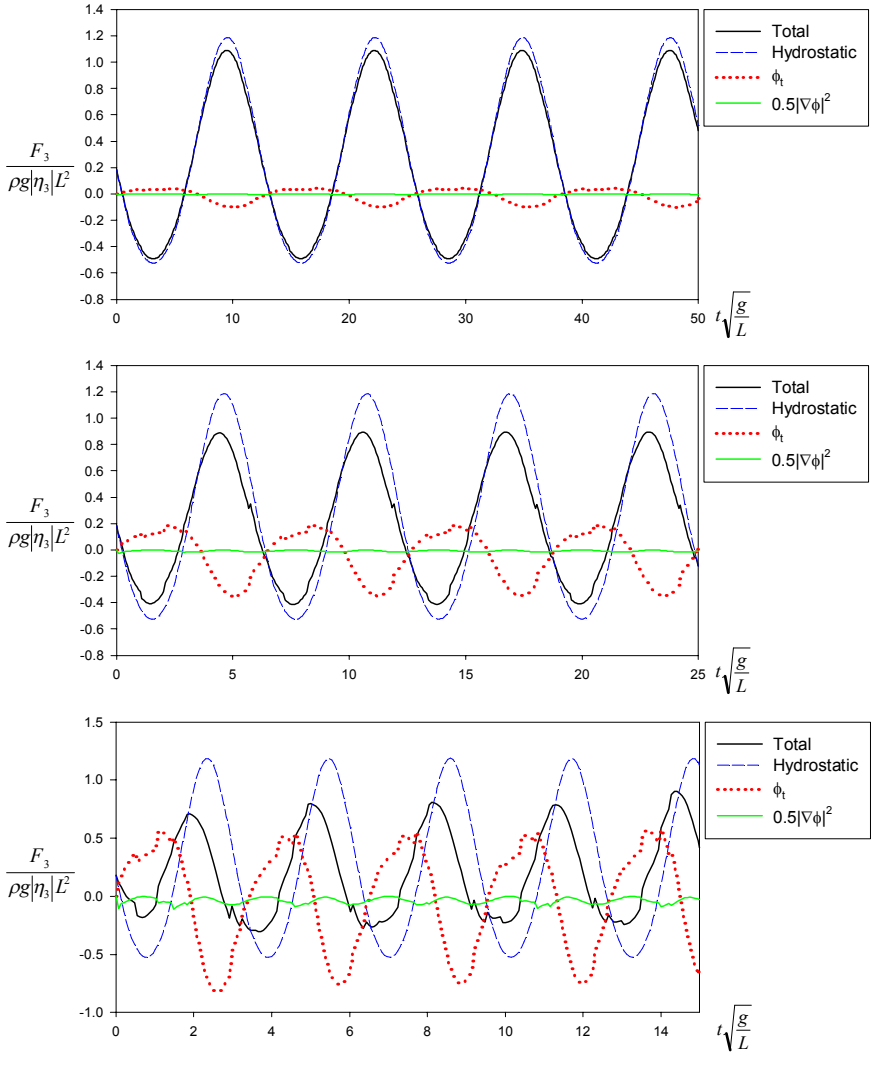

Figure 3.11. Effects of the different pressure components on the nonlinear heave force for a cone with a deadrise angle of 30 degrees calculated at three different heave oscillation frequencies (from top to bottom): $\omega\sqrt{L/g}$ = 0.5, 1.0 and 2.0. The heave amplitude is $|\eta_3|/L$ = 0.05.

Nonlinear heave radiation forces were investigated using the body nonlinear solution. The results for the cones together with the linear radiation forces are presented in the figures below. The linear radiation forces are given for comparison purposes to obtain an insight into the significance of nonlinearities. The figures for the cone with a deadrise angle of 30 degrees also include results calculated with the spline-fitted mesh. The solution of the constant panel mesh is discontinuous because the number of panels in the solution depends on whether the panels are above or below the free surface. The solution of the spline-fitted panel mesh is continuous because the body geometry is updated at every time step and the number of the panels on the wetted surface is constant. The comparison gives an insight into the effect on results if the solution continuously changes piecewise in time.

The nonlinear heave radiation forces for the cone with a deadrise angle of 30 degrees are shown in Figure 3.12 calculated at the heave oscillation frequencies $\omega\sqrt{L/g}$ = 0.5, 1.0 and 2.0. The heave amplitude was $|\eta_3|/L$ = 0.05. The magnitude of the heave radiation forces increases with the heave frequency. The nonlinearities in the heave radiation forces can be seen clearly. In the constant panel mesh method, the changes of the panel between wet and dry have an effect on the results, and discontinuities in the heave radiation forces can be seen. The solved velocity potential has a jump to the next level when a new row of panels becomes wet or the row of panels becomes dry. The spline-fit updated body can also be seen to give larger negative amplitudes than the constant panel mesh method. However, the spline-fitted and constant panel meshes give almost the same predictions for the heave radiation forces. At a larger heave amplitude $|\eta_3|/L$ = 0.10, the heave radiation forces are shown in Figure 3.13. The differences between the linear and nonlinear radiation forces are greater than the smaller heave amplitude $|\eta_3|/L$ = 0.05. The heave radiation forces of the constant and spline-fitted panel meshes are again close to each other.

The heave radiation forces for the cone with a deadrise angle of 45 degrees are shown in Figures 3.14 and 3.15 at the heave amplitudes $|\eta_3|/L$ = 0.05 and 0.10, respectively. The forces were calculated at the heave frequencies $\omega\sqrt{L/g}$ = 0.5, 1.0 and 2.0. The nonlinearities increase if the oscillation amplitude increases. However, the differences between linear and nonlinear radiation forces are smaller than for the cone of 30 degrees. The results are based on the constant panel mesh and the time histories of the radiation forces are smoother than with the cone of 30 degrees. The changes in the fluid velocities on the body surface are smaller than with the cone of the smaller deadrise angle. The discontinuities are

also smaller because the panel mesh was denser and hence the changes in velocity potentials are smaller between panels.

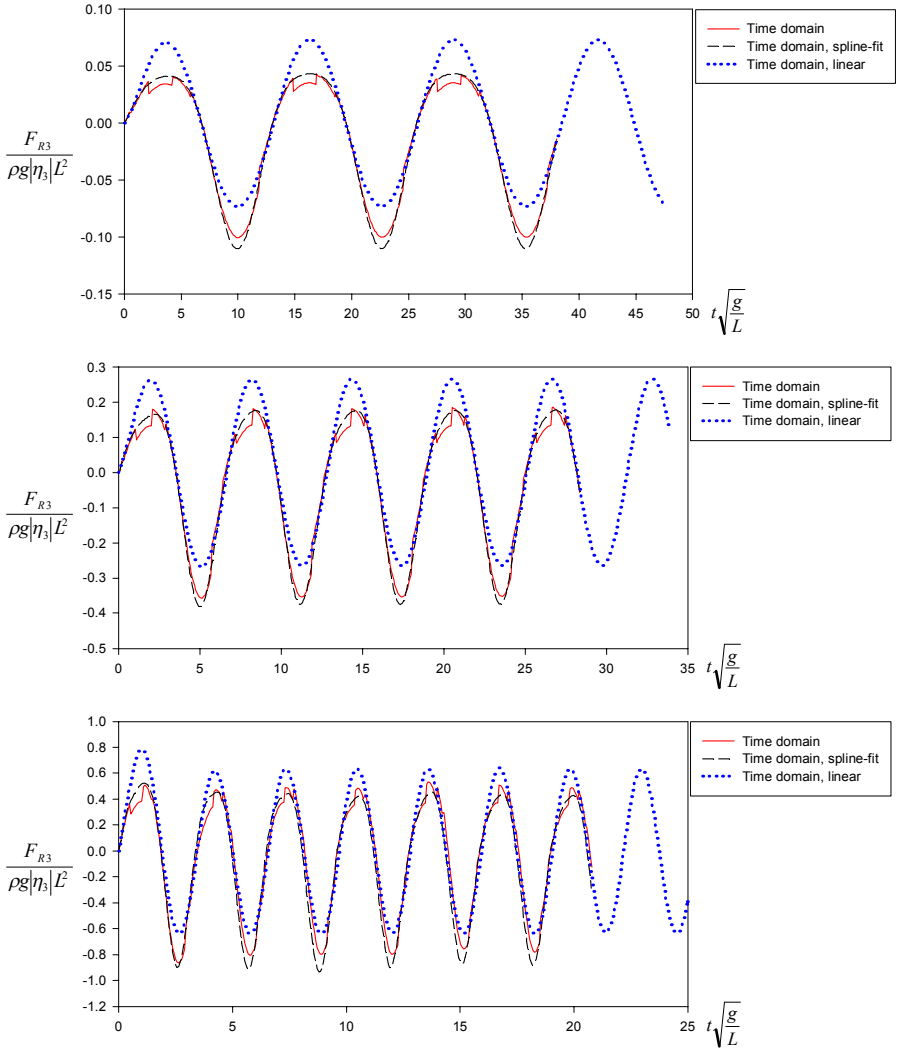

Figure 3.12. Nonlinear heave radiation force for a cone with a deadrise angle of 30 degrees calculated at three different heave oscillation frequencies (from top to bottom): $\omega\sqrt{L/g}$ = 0.5, 1.0 and 2.0. The heave amplitude is $|\eta_3|/L$ = 0.05.

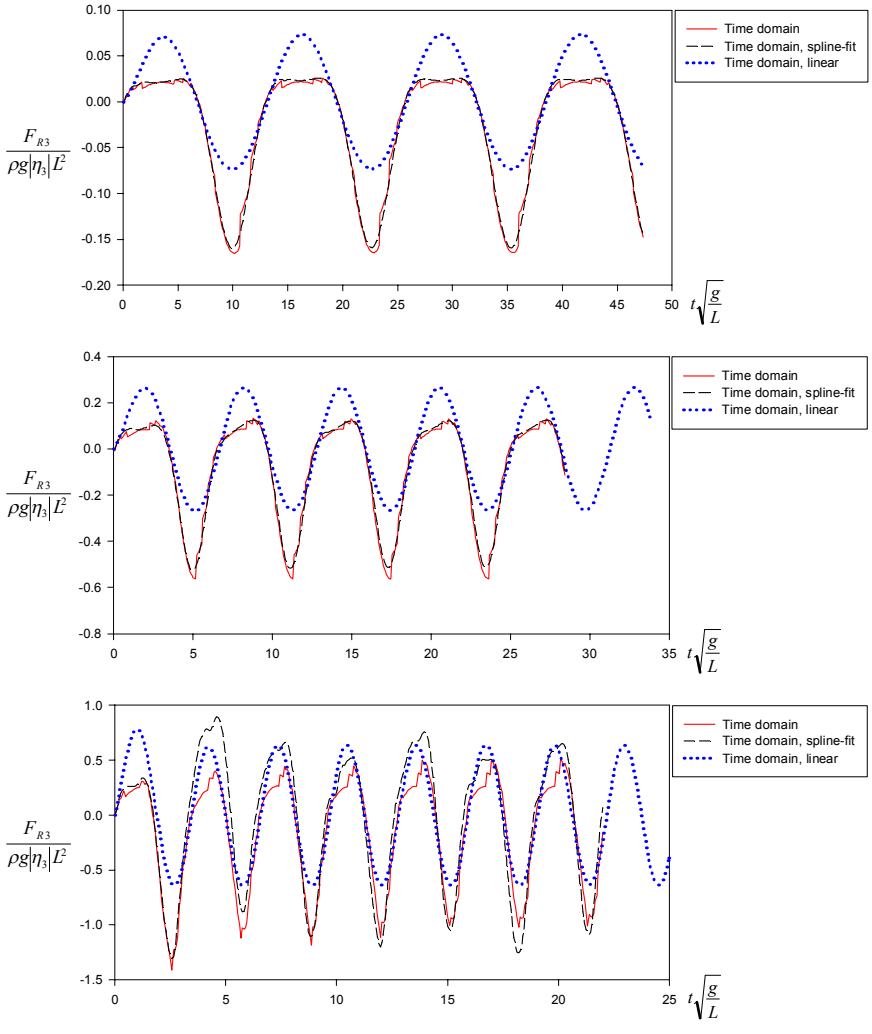

Figure 3.13. Nonlinear heave radiation force for a cone with a deadrise angle of 30 degrees calculated at three different heave oscillation frequencies (from top to bottom): $\omega\sqrt{L/g}$ = 0.5, 1.0 and 2.0. The heave amplitude is $|\eta_3|/L$ = 0.10.

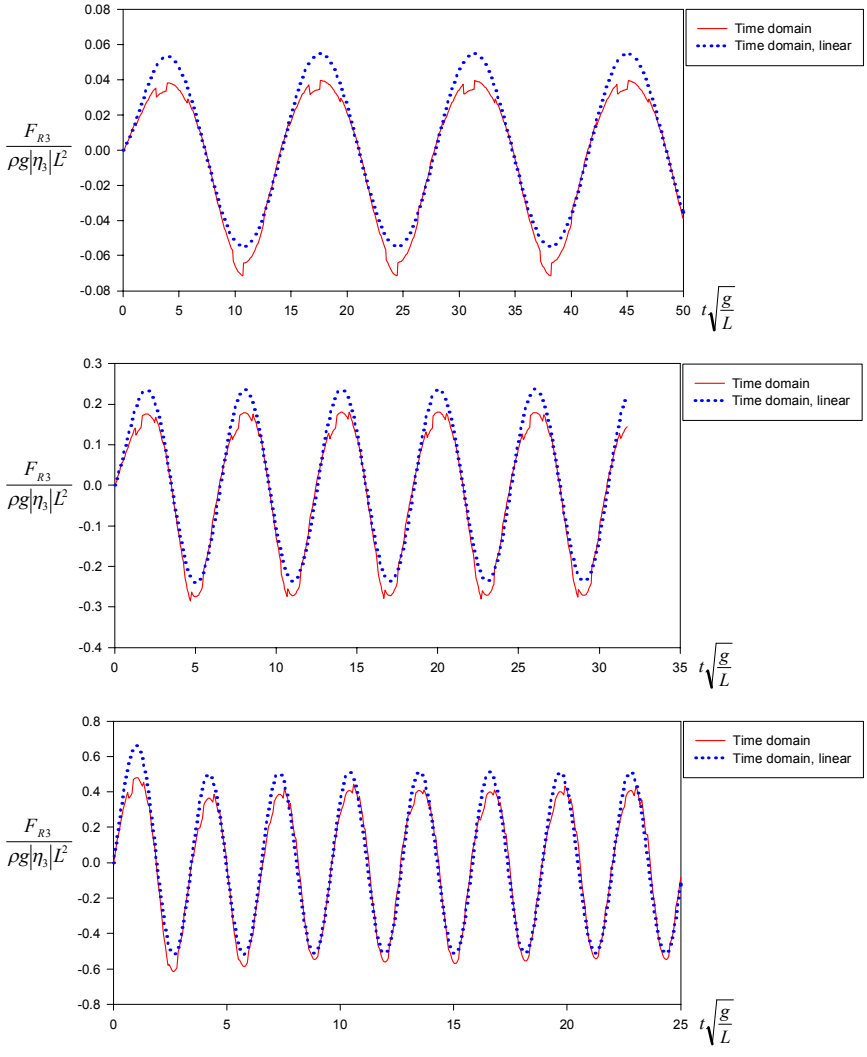

Figure 3.14. Nonlinear heave radiation force for a cone with a deadrise angle of 45 degrees calculated at three different heave oscillation frequencies (from top to bottom): $\omega\sqrt{L/g}$ = 0.5, 1.0 and 2.0. The heave amplitude is $|\eta_3|/L$ = 0.05.

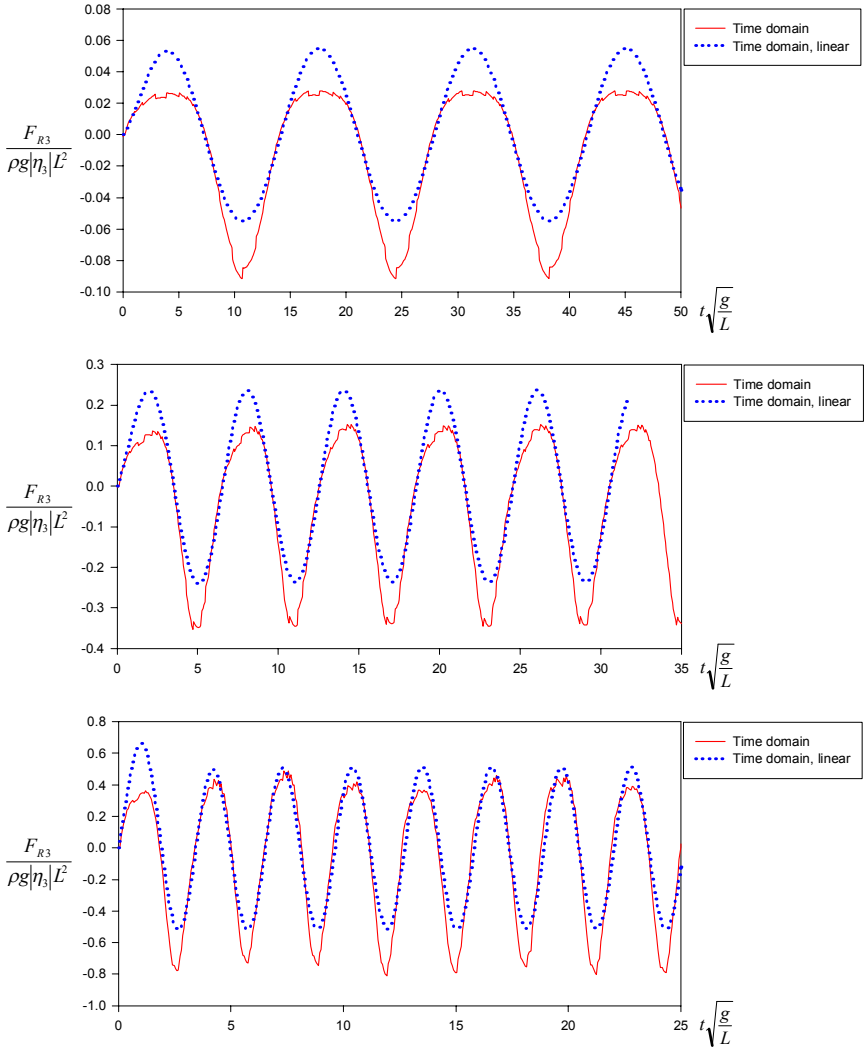

Figure 3.15. Nonlinear heave radiation force for a cone with a deadrise angle of 45 degrees calculated at three different heave oscillation frequencies (from top to bottom): $\omega\sqrt{L/g}$ = 0.5, 1.0 and 2.0. The heave amplitude is $|\eta_3|/L$ = 0.10.

Furthermore, the nonlinear heave radiation forces were approximated using two simple solutions. The solutions are based on the added mass and damping coefficients and the impulse response function of heaving cones. The added mass and damping coefficients and the impulse response function for the cones were determined in Section 3.2.2. The linear radiation forces are given by Equations (3.10) and (3.11), which are based on the added mass and damping and the impulse response function of heaving cones, respectively. In the simple solutions, the nonlinear effect due to the changing geometry of the cone below the still water level in forced heave motion was taken into account using the instantaneous displacement at every time step. The instantaneous displacement of the cone was used to represent the non-dimensional forms of the added mass and damping coefficients and the memory function to the dimensional forms. This approximation is applicable to cone-shaped bodies because of the geometrical similarity. The body shape of the cone is independent of the instantaneous draught. The instantaneous displacement of the cone at time t is given by

$$\nabla(t) = 1/3\,\pi\, r_c(t)^2 h_c(t)\,, \tag{3.13}$$

and the instantaneous characteristic length of the cone is defined as follows:

$$L(t) = 2\, r_c(t)\,. \tag{3.14}$$

The displacement and length can be calculated directly if the heave motion of the body is known. The height and radius of the cone are related by the equation $h_c(t) = r_c(t)\tan\beta$. The applied approach is an approximation because it is based on the linear formulation of the radiation forces as given by Equation (3.1). In the nonlinear formulation, the integration over the body surface depends on time, $S_0 = S_0(t)$. Hence, scaling the impulse response function using the displacement of the cone from the present time step to the past time steps is an approximation. The fluid velocity squared term is also not included in the linear hydrodynamic quantities. Here, the hydrodynamic quantities mean the inertia forces due to the added mass, the damping forces and the forces due to the impulse response function term. However, the simple solutions give an approximation for the order of magnitude of the nonlinear radiation forces. Moreover, the simple solutions give an insight into the relative contribution of the different hydrodynamic quantities affecting the body.

Approximations of the nonlinear heave radiation forces are shown in Figure 3.16 for the cone with a deadrise angle of 30 degrees. The approximations are the simple solutions of the force based on the added mass and damping coefficients (Coefficients), and the impulse response function and the infinity heave added

mass coefficient (Memory function). The body linear and nonlinear solutions of the force are also shown in the figure. In addition, the forced heave motion, velocity and acceleration are presented in the figures. The non-dimensional force and time in the figures are non-dimensionalized by the displacement ∇ and characteristic length L at the initial position when $t = 0$. The calculations were carried out at the heave oscillation frequency $\omega\sqrt{L/g}$ = 1.0 and the heave amplitude $|\eta_3|/L$ = 0.10. The time domain method and the two simple solutions give close to the same results. A small difference can be seen when the radiation force has the minimum value. The minimum amplitude exists when the body is in the lowest position where the acceleration has the maximum amplitude and the heave velocity is close to zero. Hence, the inertia forces are dominant over the damping forces. The maximum force amplitudes exist when the cone is moving downwards and the heave motion is passing the zero level where the heave velocity has the minimum amplitude. Thus, the damping forces are dominant over the inertia forces.

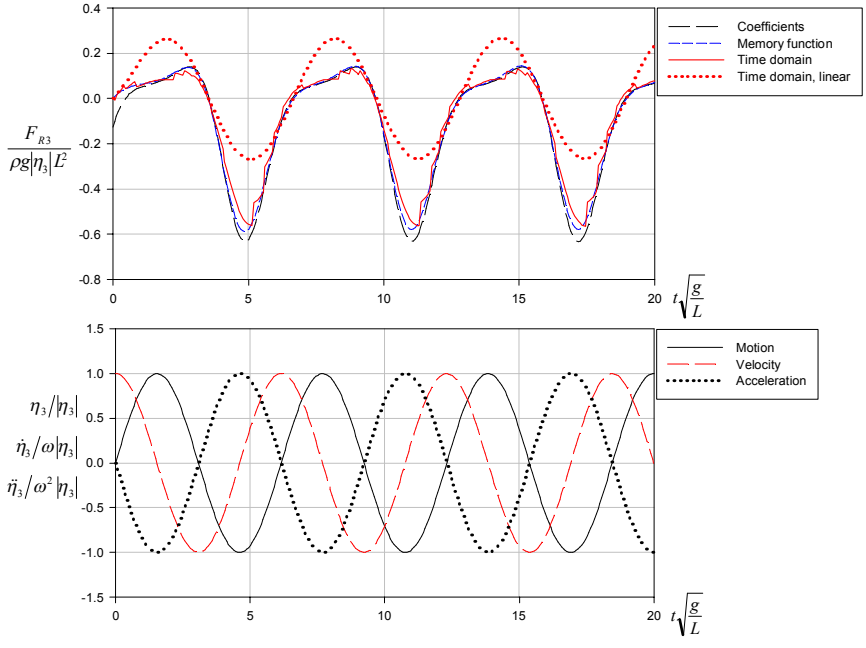

Figure 3.16. Nonlinear time domain solution and approximated solutions for the heave radiation force (top) and motion, velocity and acceleration (bottom) for a cone with a deadrise angle of 30 degrees calculated at a heave frequency $\omega\sqrt{L/g}$ = 1.0 and heave amplitude $|\eta_3|/L$ = 0.10.

The nonlinear heave radiation force for the cone with a deadrise angle of 30 degrees is shown in Figure 3.17 at the heave frequency $\omega\sqrt{L/g}$ = 2.0 and amplitude $|\eta_3|/L$ = 0.10. Here, the heave amplitude is the same as in Figure 3.16 but the frequency is higher. As the frequency is higher, the heave velocities and accelerations are greater. The maximum force occurs when the heave velocity reaches the largest negative value at the same time as the body moves downwards, e.g. $t\sqrt{g/L} \approx 42$. This is related to the impact problem when the body enters the water. However, the impact is not taken into account properly because of the large panel size and the large time step size. The duration of the impact pressure is short and the peak pressure is very local. The peak pressure also occurs close to the free surface elevation. The methods applied in this work are based on the linear free surface condition. The actual free surface elevation is not taken into account when the body enters the water. This is the so-called von Karman approach in impact problems (von Karman, 1929). The Wagner approach in impact problems takes into account the actual free surface elevation when the body enters the water (Wagner, 1932).

An approximation of the nonlinear heave radiation force is also shown in Figure 3.17. The approximation is based on the simple solution expressed by the infinity added mass and the impulse response function of the heaving cone (Memory function). The differences between the time domain method and the simple solution are greater than the results that were obtained at the lower heave frequency. The difference was further studied to find out if the fluid velocity squared term could have an effect on results. The force of the simple solution was determined without the fluid velocity squared term, but the time domain method included the term. The nonlinear heave radiation force calculated with the time domain method and without the fluid velocity squared term is also presented in the figure. Without this term, the maximum amplitude increases and the minimum amplitude decreases, though the differences are relatively small. Hence, the fluid velocity squared term alone cannot explain the differences between the simple solution and the time domain method. However, the differences can explain the approximated memory effect in the simple solution. The memory effect is approximated in the simple solution using the displacement of the cone at the present time instant. Thus, the memory effect in the simple solution does not take into account the correct instantaneous displacements and wetted surfaces of past times.

A comparison of the forces calculated with the constant and spline-fitted panel meshes is shown in Figure 3.17. The constant panel mesh approach gives somewhat smaller force values than the spline-fitted mesh, especially when the heave motion has the maximum value. In the constant panel mesh calculation, part of

the panels can be above the water level and hence they are not included in the solution. Thus, the wetted surface of the body is smaller than the spline-fitted body surface. The smaller wetted surface and hence the smaller surface for pressures can have an effect on the smaller forces in the constant panel mesh approach. Hence, the constant panel mesh approach can underestimate the radiation forces, especially if the panel mesh is coarse.

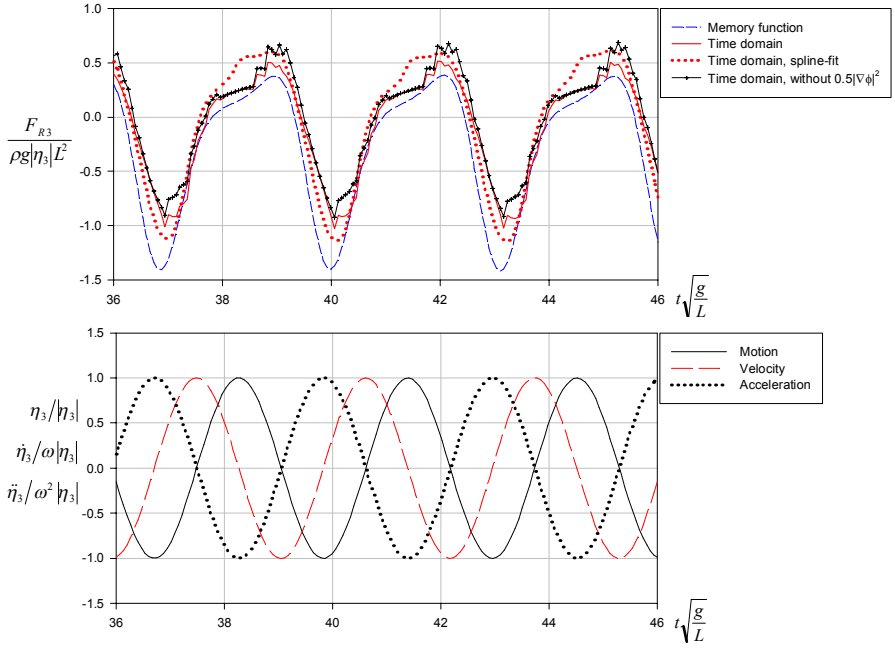

Figure 3.17. Nonlinear heave radiation force (top) and motion, velocity and acceleration (bottom) for a cone with a 30 degree deadrise angle calculated at the heave frequency $\omega\sqrt{L/g}$ = 2.0 and heave amplitude $|\eta_3|/L$ = 0.10. The upper figure also includes the approximation of the heave radiation force based on the memory function approach.

3.3 Wigley hull forms

3.3.1 General

Wigley hull forms are widely used in validations to develop seakeeping calculation methods. For example, linear frequency domain results are given by Journee (1992) and linear and nonlinear time domain results by, for example, Lin and Yue (1991), Kataoka et al. (2002) and Sen (2002). The results in this Section 3.3 for

the Wigley hull forms are given to validate the present time domain method. The regular wave results are given as transfer functions of heave and pitch, and transfer functions of the heave and pitch exciting forces and moments. Moreover, the added mass and damping coefficients in heave and pitch are shown. Convergence studies of the time step size and the size of the panel mesh are also presented. The calm water results are given as the sinkage of the hull and the wave-making resistance coefficients. The results of the time domain method are compared with the existing experimental results.

3.3.2 Responses in regular head waves with forward speed

The model test results of the Wigley hull forms were presented by Journee (1992). Four different Wigley hull forms were tested and different responses were reported including added mass and damping coefficients, motions, and exciting forces and moments. In this work, the calculation and comparison with the model test results are given for the Wigley III hull form as denoted by Journee (1992). In the model tests, the main dimensions of the Wigley III were length L = 3.0 m, breadth B = 0.3 m and draught T = 0.1875 m. The midship coefficient was 0.6667. The same dimensions were used in the calculations. The panel mesh of the hull is shown in Figure 3.18. All of the results presented here were calculated in head waves. At time t = 0, the wave amplitude was a, the forward speed was U_0 and the other motions were zero. The results were calculated using the acceleration potential method to solve the time derivative of the velocity potential in Bernoulli's equation. In addition to the acceleration potential method, the added mass and damping coefficients were determined with the backward difference method.

Time histories of the heave and pitch motions calculated with different panel meshes are shown in Figure 3.19. Half of the hull was discretized by 180, 320 and 500 quadrilateral panels. The wave frequency was $\omega\sqrt{L/g}$ = 2.24 and the forward speed Fn = 0.30. In the calculations, the number of time steps in one period was $T_e/\Delta t$ = 46 where T_e was the encounter wave period. The calculation results are based on the body linear solution. The figure shows that the different mesh sizes have an effect on the convergence of the solution for the heave and pitch amplitudes and the amplitudes fluctuate somewhat between the coarse and fine meshes. However, the difference in the amplitudes of the heave and pitch is less than 3% between the different meshes. In the rest of the calculations, the number of panels was 320 on half of the Wigley III hull form.

The calculation results using three different time step sizes are presented in Figure 3.20. The calculations were performed using the number of time steps in one encounter period $T_e/\Delta t$ = 23, 46 and 92. The calculated time histories of the heave and pitch motions are based on the body linear solution. The wave frequency was $\omega\sqrt{L/g}$ = 2.24 and the forward speed Fn = 0.30. The number of time steps $T_e/\Delta t$ = 46 gives 2% lower heave and pitch amplitudes than the shortest time step size for which the number of time steps in one period is $T_e/\Delta t$ = 92. However, the differences between the longest and shortest time step sizes are 15% and 4% in heave and pitch, respectively. The longest time step size gives lower motion amplitudes than the shorter time step sizes. In the rest of the calculations for the Wigley III hull form, the number of time steps in one encounter period was about 50 to determine the body motions, forces and moments. The used time step size gives sufficiently good accuracy with a reasonable calculation time. However, a smaller number of time steps in one period was also used to save computation time, but only if the motions were small outside the natural periods of heave and pitch.

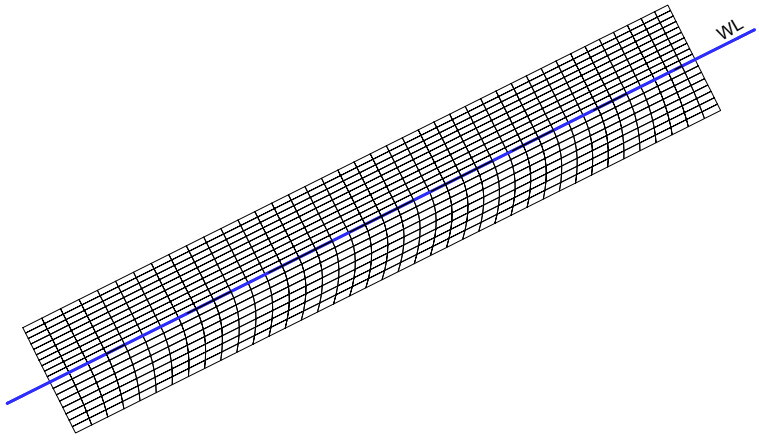

Figure 3.18. The panel mesh of the Wigley III hull form. The number of panels on the half hull below the still waterline (WL) is 320.

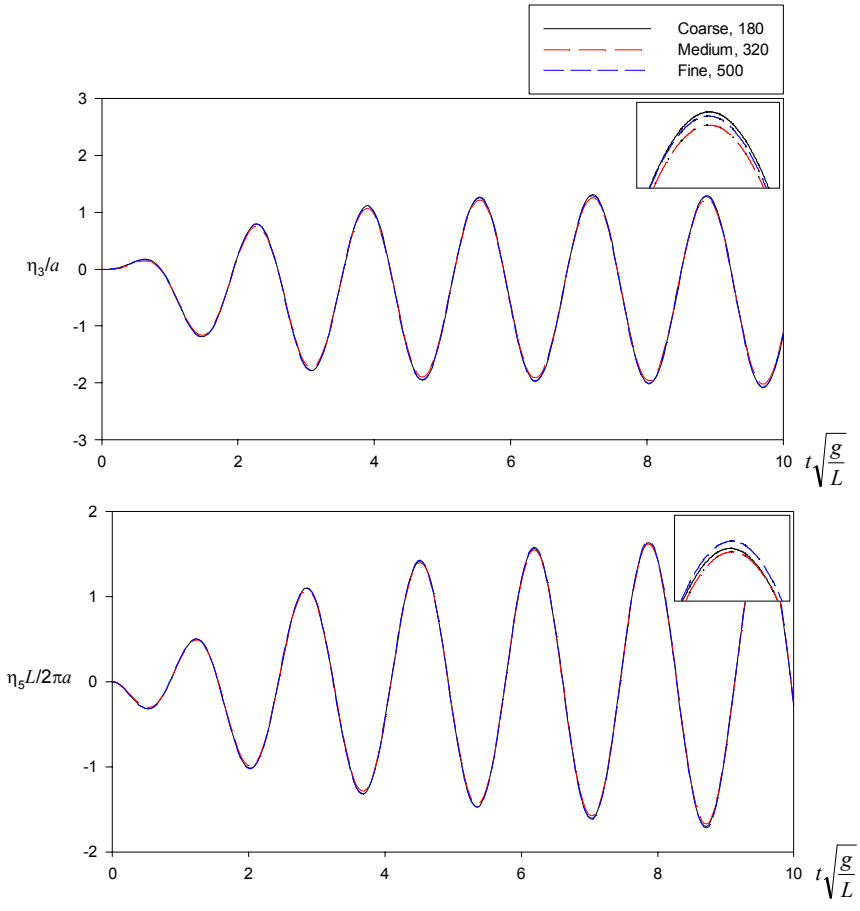

Figure 3.19. Time histories of the heave and pitch motions at forward speed Fn = 0.30 in head waves at wave frequency $\omega\sqrt{L/g}$ = 2.24. The number of panels was 180, 320 and 500 on the half hull.

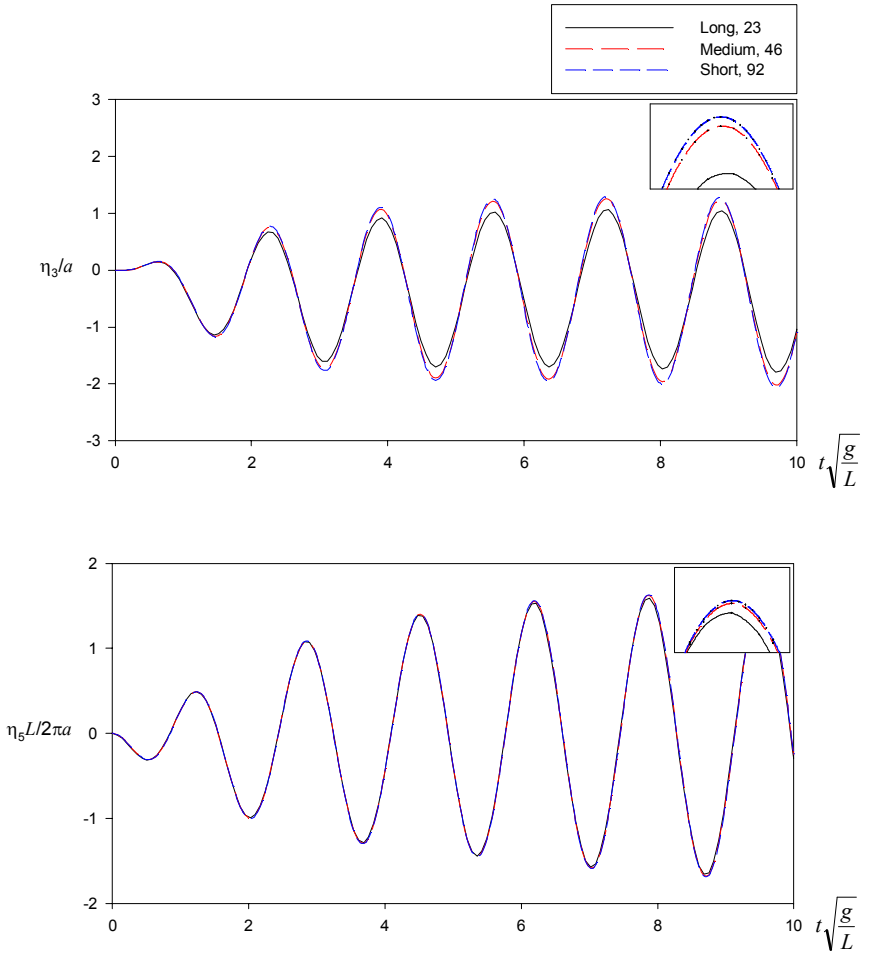

Figure 3.20. Time histories of the heave and pitch motions at forward speed Fn = 0.30 in head waves at wave frequency $\omega\sqrt{L/g}$ = 2.24. The number of time steps in one period was $T_e/\Delta t$ = 23, 46 and 92. The number of panels was 320 on the half hull.

The added mass and damping coefficients can be determined by means of the impulse response function. The body motions and the velocity potential components can be decoupled to formulate the body boundary condition for the different six degrees of freedom motions. This was applied to the hemisphere and the cones above in the heave motion at zero speed. However, the time domain method is formulated in the space-fixed coordinate system and the impulse response function cannot be applied straightforwardly to determine the added mass and

damping coefficients at forward speed (Lin and Yue, 1991). In the body-fixed coordinate system, King et al. (1989) and Bingham et al. (1994) applied the impulse response function to determine the hydrodynamic coefficients at forward speed. They used a linearized body boundary condition in the body-fixed coordinate system. In this work, the added mass and damping coefficients at forward speed were determined from the forced oscillation in calm water. The body was oscillating harmonically at the given heave or pitch amplitude and frequency. The time histories of the radiation forces and moments in heave and pitch were calculated and Fourier transforms were performed to define the added mass and damping coefficients. The added mass is the in-phase component with the body acceleration of the radiation force or moment and the damping is the out-of-phase component, or the component in phase with the velocity.

The heave and pitch added mass and damping coefficients in heave are shown in Figure 3.21 and in pitch in Figure 3.22 at the Froude number $Fn = 0.3$. The body linear and nonlinear solutions for the added mass and damping coefficients are given in the figures. In the body nonlinear solution, the oscillation amplitudes were the same as in the experiments. The heave amplitude was 0.025 m and the pitch amplitude 1.5 degrees. The acceleration potential method was used to solve the time derivative of the velocity potential determining the added mass and damping coefficients. In addition to the acceleration potential method, the backward difference method was also applied to the body nonlinear solution. The acceleration potential and backward difference methods give similar predictions for the added mass and damping coefficients. Furthermore, the body linear and nonlinear solutions are close to each other. The diagonal coefficients, A_{ii} and B_{ii}, are in good agreement with the experiments. Moreover, the predictions for the cross-coupling added mass coefficients are satisfactory, but larger differences exist in the cross-coupling damping terms. For the pitch added mass and damping coefficients, the body nonlinear solution gives better results than the body linear solution. In the body nonlinear solution, the forward speed effects are taken into account at the instantaneous floating position. Hence, the angle of attack due to pitch in the steady flow is determined for the actual body geometry below the mean water level. In the body linear solution, the pitch angle and the forward speed are taken into account in the body boundary condition on the mean wetted surface of the hull, i.e. the coupling of the actual floating position of the body geometry and the steady flow is not taken into account.

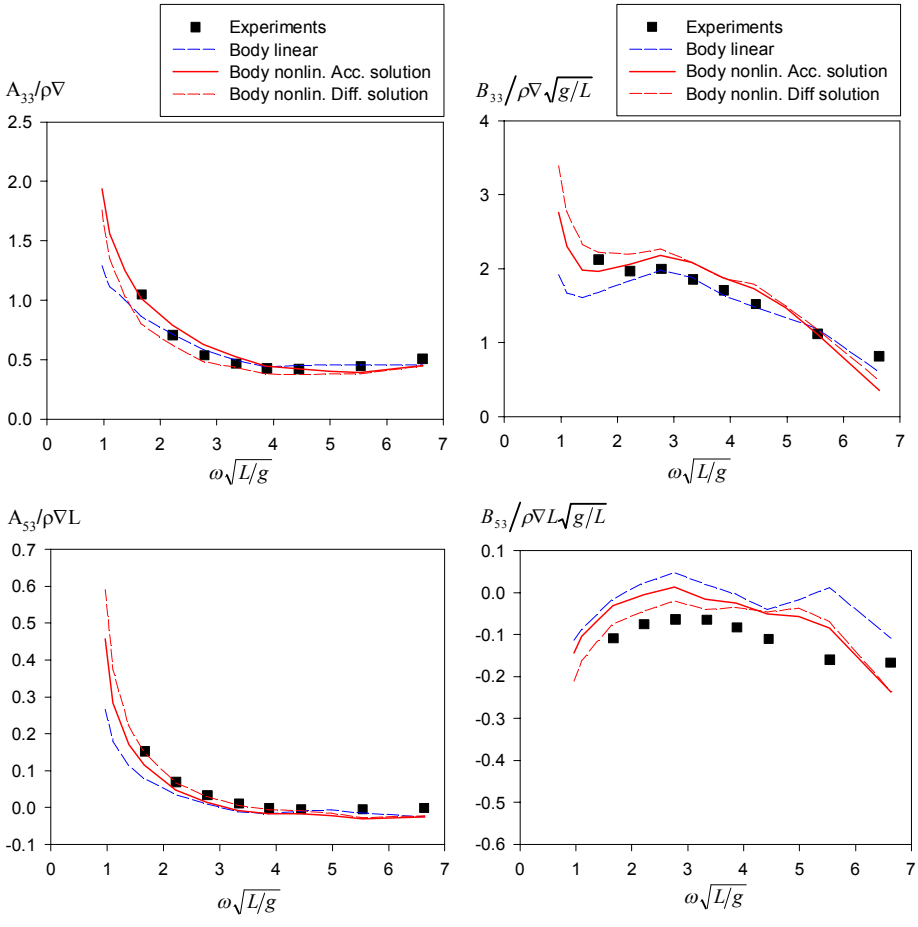

Figure 3.21. Heave and pitch added mass and damping coefficients in heave *Fn* = 0.3. The experimental results are from Journee (1992).

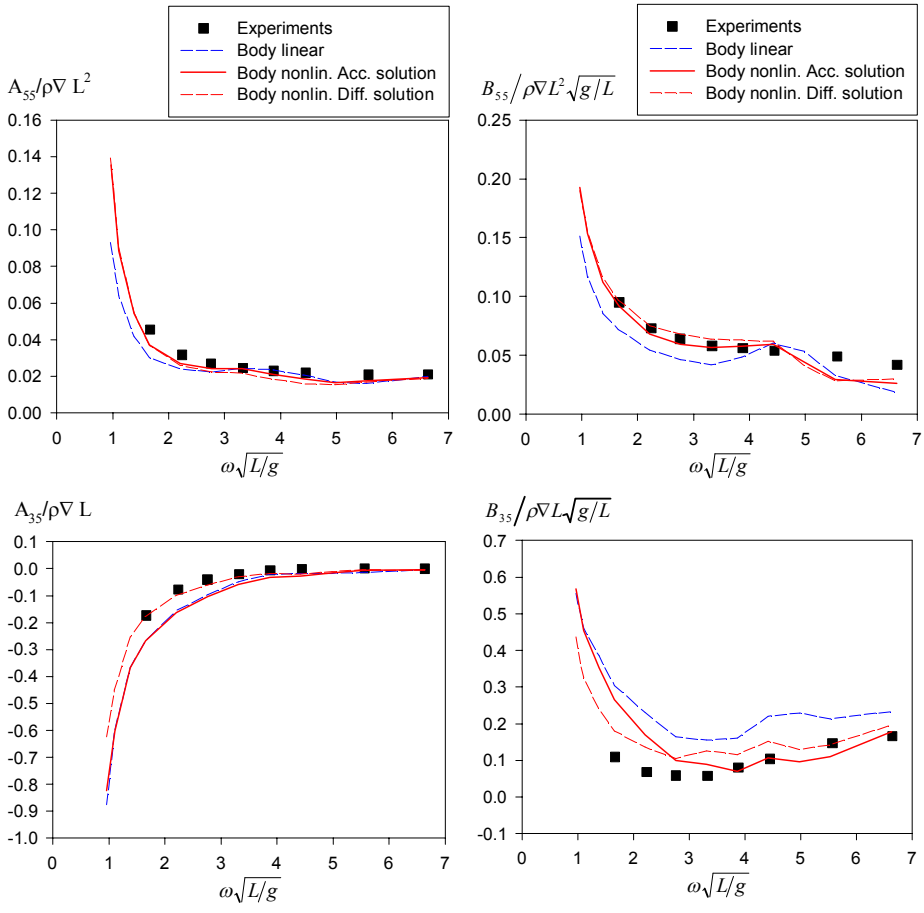

Figure 3.22. Heave and pitch added mass and damping coefficients in pitch at *Fn* = 0.3. The experimental results are from Journee (1992).

The transfer functions of the responses were determined using harmonic analysis for the calculated time histories. In the harmonic analysis, a Fourier series is fitted to the time history data. The amplitudes of the transfer functions are defined as the ratio of the response first harmonic to the wave first harmonic. The response phase angles are defined as leads with regard to the wave crest at the centre of gravity of the ship. Before the harmonic analyses, time history data were cut at the beginning of the calculation until the steady harmonic oscillation was reached.

The transfer functions of the heave force and pitch moment at forward speed Fn = 0.30 in head waves are shown in Figures 3.23 and 3.24. In the calculation, the body motions were set to zero and, hence, the body linear solution was used. The incoming wave amplitude was a/L = 0.0083 in the calculation. The exciting heave force is well predicted by the calculation method. The pitch moment is also well predicted, but near the resonance the pitch moment is at a slightly lower level than the model test results.

The transfer functions of the heave and pitch at forward speed Fn = 0.30 in head waves are shown in Figures 3.25 and 3.26. In the calculations, the wave amplitude was a/L = 0.0067. Calculations were carried out using the body linear and nonlinear solutions. In general, the calculated motions are in close agreement with the model test results. At the heave resonance, the calculation overestimates the heave motion. At the longer waves, the body nonlinear solution gives somewhat larger amplitudes for the heave motion than the body linear solution. The body linear and nonlinear solutions give good predictions for the pitch. However, the body nonlinear solution gives slightly lower amplitudes near the resonance of the pitch. The body nonlinear calculations were performed using a constant panel mesh, which can have an effect on the results. The hydrodynamic pressure piecewise continued in time if the panels became wet or dry. This was shown in the calculations of the cones in Section 3.2.4. This could be one reason for the small differences between the body linear and nonlinear solutions.

The transfer function of the relative motion at the bow is presented in Figure 3.27. The relative motion z_r was determined at the longitudinal position of 0.85L from the stern. The relative motion is defined as the vertical motion between the ship's vertical motion and the incoming wave. The calculated results are clearly below the model test results. The ship motions are calculated quite well, so one reason could be the wave pattern and the wave elevation at the bow. In the calculation method, the actual wave elevation due to the body motion and the forward speed of the body is not taken into account.

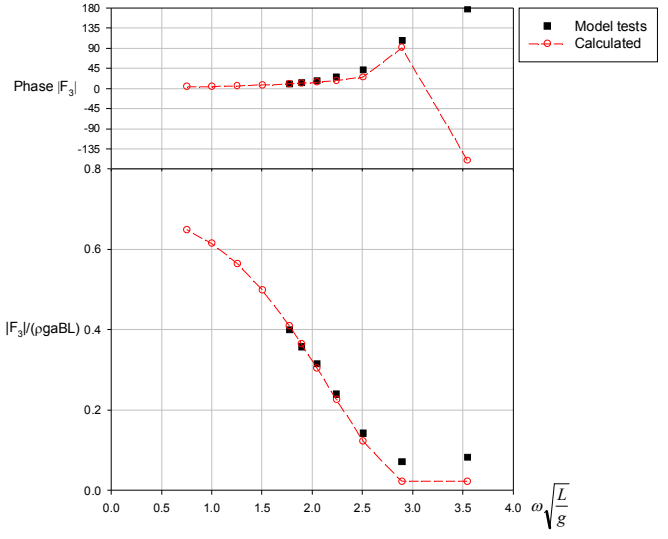

Figure 3.23. Heave force of the Wigley III in head waves at *Fn* = 0.30. The model test results are from Journee (1992).

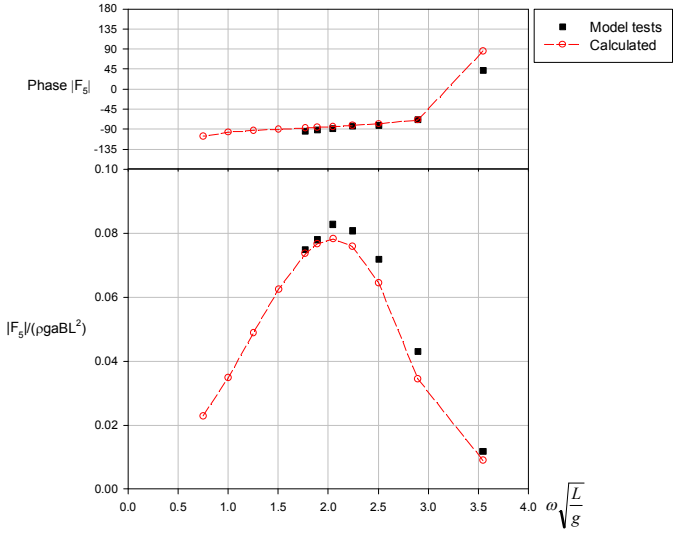

Figure 3.24. Pitch moment of the Wigley III in head waves at *Fn* = 0.30. The model test results are from Journee (1992).

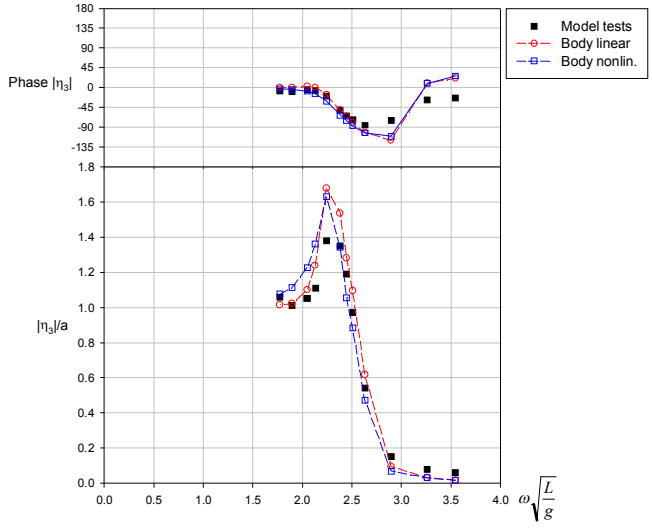

Figure 3.25. Heave of the Wigley III in head waves at *Fn* = 0.30. The model test results are from Journee (1992).

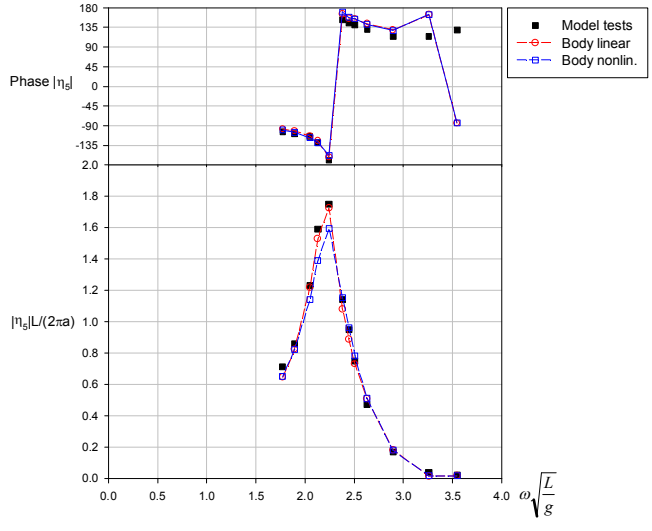

Figure 3.26. Pitch of the Wigley III in head waves at *Fn* = 0.30. The model test results are from Journee (1992).

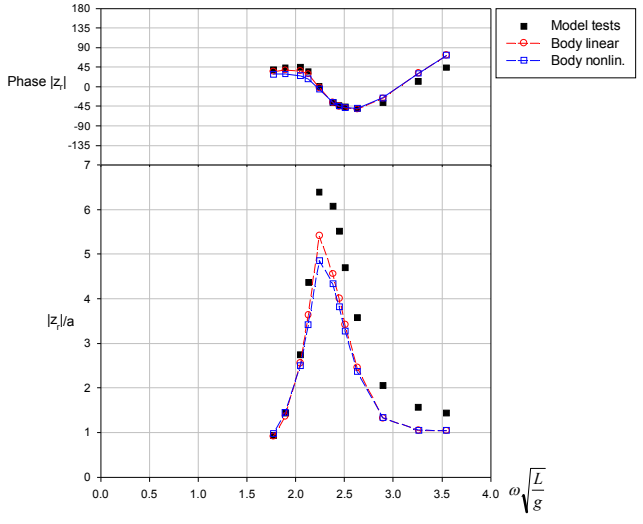

Figure 3.27. Relative motion of the Wigley III at 0.85L in head waves at Fn = 0.30. The model test results are from Journee (1992).

3.3.3 Responses in calm water with forward speed

The resistance of the Wigley hull forms is widely studied with numerical methods and by model testing. For example, comparative studies of the model test resistance predictions are given in ITTC (1984). In this work, model test results for residual resistance coefficients are obtained from Matusiak (2001) where the Wigley hull form was the same as in the ITTC (1984) studies. The model test values for sinkage are obtained from ITTC (1984).

The wave-making resistance coefficient is defined as

$$C_w = \frac{F_1}{0.5\,\rho U_0^2 S_{wsa}}, \tag{3.15}$$

where S_{wsa} is the wetted surface of the hull. Here, the residual resistance coefficient from the experiments are compared with the calculated wave-making resistance coefficient. In the experiments, the residual resistance was determined by subtracting the frictional resistance from the towing force according to the standard resistance prediction procedures given by ITTC (International Towing Tank Conference).

The Wigley hull form in the calm water studies is given by

$$y = \frac{B}{2}\left[1-\left(\frac{2x}{L}\right)^2\right]\left[1-\left(\frac{z}{T}\right)^2\right] \tag{3.16}$$

where $-\frac{L}{2} \le x \le \frac{L}{2}$ and $0 \le z \le -T$. The length of the ship model in the tests was $L = 7.5$, beam $B = 0.75$ and draught $T = 0.47$ (Matusiak, 2001). In the calculation, the half hull below the still water level was discretized by 320 panels, and constant panel mesh was used. The calculation was performed using the body nonlinear solution. At the beginning of the time domain calculation, a cosine-squared speed ramp was applied to accelerate the hull from zero to the constant forward speed.

Time histories of the forward speed, sinkage and trim, and the wave-making resistance are shown in Figure 3.28. The sinkages at the fore and aft perpendiculars are z_{FP} and z_{AP}, respectively. After the transient phase when the forward speed has reached the constant value, slowly decaying oscillation can be noticed. The oscillation frequency ω is given by the frequency parameter $\kappa = \omega U/g = 1/4$. If the frequency parameter is $\kappa = 1/4$, the generated wave system of the moving ship is travelling with the group velocity, which is the same as the speed of the ship (see, e.g., Faltinsen, 1990). The effect of the accelerated ship on the wave resistance has been studied by Wehausen (1964). The slowly decaying oscillation in steady motion when the ship starts at rest was studied further with calculations and model tests by Doctors et al. (2008) and with the calculations by Lin and Yue (1991).

The wave-making resistance of the Wigley hull form is shown in Figure 3.29 as a function of the Froude number. In the same figure, the residual resistance coefficient from the experiments is also shown. The agreement is relatively good compared with the model test results. At high speed, Froude number above 0.45, the calculation method overestimates the wave-making resistance.

The sinkage of the Wigley hull is presented in Figure 3.30. The rather significant deviation in the model test results is due to the non-dimensional form when the speed of the hull is low and because the magnitude of sinkage is small at low Froude numbers. The calculated results are at a slightly higher level than the model test results if the Froude number is above 0.20.

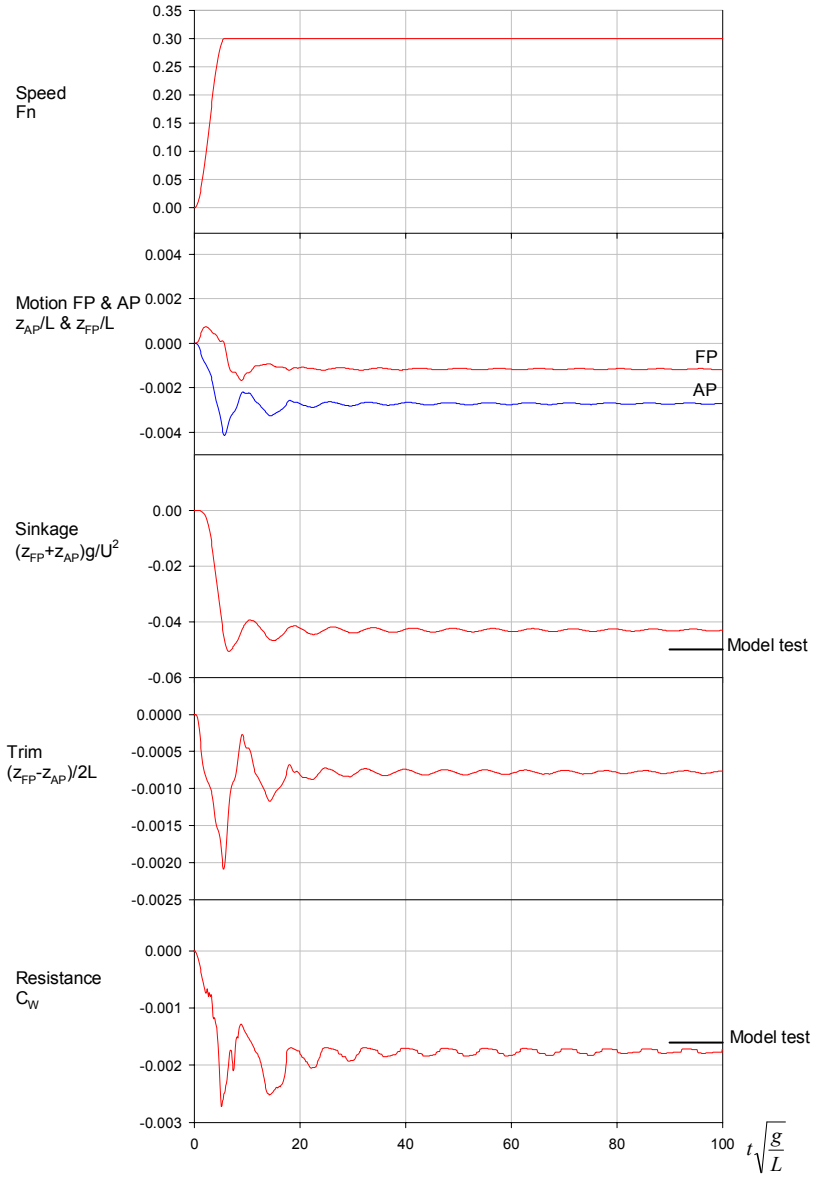

Figure 3.28. Time histories of the forward speed, motion at fore and aft perpendicular (FP and AP), sinkage and trim, and the wave-making resistance for the Wigley hull form accelerating from zero speed to a steady speed of $Fn = 0.30$.

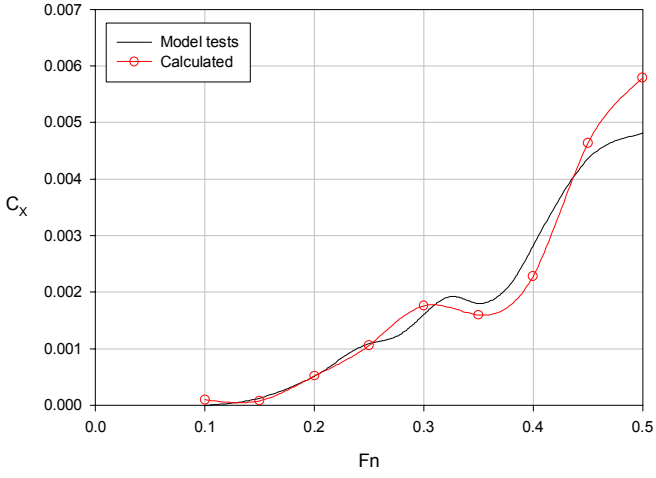

Figure 3.29. Wave-making resistance coefficient for the Wigley hull form. The experimental results are from Matusiak (2001).

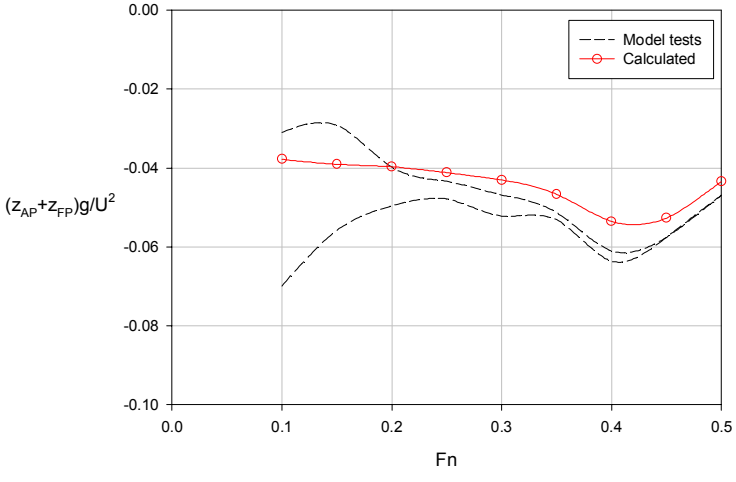

Figure 3.30. The sinkage of the Wigley hull form. The model test results are rough upper and lower estimates from the studies given in ITTC (1984).

4. Results of the model test ship

4.1 General

In this chapter, model tests and model test results for the roll-on roll-off passenger (RoPax) ship are presented. The model tests were carried out in calm water and in regular and irregular head waves at zero and forward speeds. Motions, accelerations and hull girder loads were measured in the model tests.

Model test results for the RoPax ship are presented together with the calculated responses. Responses in calm water and in regular and irregular head waves are studied using the model test and calculated results. The calculated responses are compared with the model test results.

First, the model test ship and model tests are described, and then the calculation parameters and panel meshes for the RoPax ship used in the calculation are given. The model test and calculated results are first presented in calm water at different forward speeds. After that, the results in regular and irregular head waves are given at zero and forward speeds. The short-term predictions of the extreme loads are also reviewed, and one approach is applied to predict short-term extreme values for hull girder loads. The short-term predictions are given for the RoPax ship in the same sea states in which the model tests were carried out.

The RoPax ship used in this work is the same as that used in the earlier investigations by Kukkanen (2009, 2010). However, the time domain method was based on the backward difference method, and only the first attempt tried to solve the responses using the acceleration potential method at zero forward speed. The numerical algorithms, including a filtering algorithm, were also different, as was the panel mesh of the ship hull in the earlier investigations. The model tests were also carried out in oblique waves but only the results in head seas are used in this work.

4.2 Model tests and the model test ship

The main dimensions and weight data of the RoPax ship used in the model tests are given in Table 4.1. The ship has a bulbous bow and a flat bottom stern at the waterline. The lines drawings are shown in Figure 4.1. The weight distribution and the still water bending moment and shear force distribution along the length of the ship are presented in Figure 4.2. In the figure, the vertical shear force is positive upwards and the vertical bending moment is positive in hogging.

The model tests were carried out in the towing tank with a length of 130 m. The breadth of the tank is 11 m and the depth of the water is 5.5 m. The waves were generated by a wedge-type wave maker at the end of the towing tank and absorbed by a plywood beach at the opposite end of the tank. At zero speed tests, the distance of the ship model was 60 m from the wave maker. In head seas tests, the attachment of the model to the carriage allowed the model free basic modes of motions: pitch, heave and roll. The yaw, sway and surge motions were slightly restricted and drifting of the model was prevented.

The ship model was manufactured to a scale of 1:39.024. The height of the ship model was 15.6 m in full scale from the base line to the main deck. Before the model tests in waves, the radii of the gyrations and the centre of gravity of the ship model were adjusted in swing table experiments.

A segmented ship model was used and the force and moment transducers were installed in two cut-off sections. The locations of the force and moment transducers are shown in Figure 4.1. The midship transducer was at frame 4 (x/L = 0.40) and the fore ship transducer at frame 6.5 (x/L = 0.65). The characteristic length L of the ship is the length between the perpendiculars L_{pp}. The transducers were installed at the centre line and the vertical distance from the base line was the same as the centre of gravity of the ship. The transducer measured the six component forces and moments. In this work, the results are given for the vertical shear force at fore ship and for the vertical bending moment at midship. According to the calibration certificate of the force transducers, the measurement uncertainties were 4.25% and 3.25% for the shear force and bending moment, respectively. Furthermore, the heave and pitch motions were measured at the centre of gravity of the ship model, and the vertical accelerations were measured at the aft and fore perpendiculars and at the centre of gravity of the ship model. Incoming waves were measured with a wave sensor that was at the front of the ship model installed on the carriage.

Impact experiments were carried out in calm water for the ship model to define the natural frequency of the foundation and the attachment of the transducers between the segments. The measured first natural frequency was about 9 Hz. In the measurements, the sampling frequency was 100 Hz and signals were low-pass filtered with the cut-off frequency of 5 Hz. All signals were analog-to-digital converted and stored on the computer's hard disk during the measurements.

The model tests were carried out in calm water at five different speeds: Fn = 0.05, 0.10, 0.20, 0.25 and 0.30. The aim was to obtain model test data for the sinkage of the ship and the hull girder loads due to the forward speed of the ship in calm water. The model test results in calm water are presented in Section 4.4.

The regular wave tests were carried out in head waves at zero speed (Fn = 0.0) and at forward speed Fn = 0.25. The tests were performed at three different wave amplitudes and at 5 to 10 different wave frequencies. The relative wave amplitudes related to the ship length were a/L = 0.006, a/L = 0.013 and a/L = 0.019. The wave amplitudes were a = 1 m, 2 m and 3 m in full scale. The model test results in regular waves are presented in Section 4.5.

The irregular wave tests were conducted at zero speed and at forward speed in head waves. The significant wave heights in the irregular waves were H_s = 5.0 m and H_s = 9.0 m at forward speed Fn = 0.25 and at zero speed, respectively. The irregular wave generation and the irregular wave test results are presented in Section 4.6.

All of the model test results are given in non-dimensional form. The responses in regular waves are given in the following non-dimensional forms:

Heave:	$\lvert\eta_3\rvert/a$
Pitch:	$\lvert\eta_5\rvert L/2\pi a$
Vertical acceleration:	$\lvert a_z\rvert L/ga$
Shear force:	$\lvert V_3\rvert/\rho gBLa$
Bending moment:	$\lvert V_5\rvert/\rho gBL^2a$

The regular waves are described by a non-dimensional wave amplitude a/L and a non-dimensional wave frequency $\omega\sqrt{L/g}$. In the non-dimensional forms, the length L is the length between the perpendiculars L_{pp}, and the breadth B is the waterline breadth B_{wl}. The vertical bending moments at midship are given at cross section x/L = 0.40 and the vertical shear forces at fore ship are given at cross section x/L = 0.65. The calculated and model test results for the shear forces and bending moments are given at the same cross sections. The shear forces and the

bending moments presented in waves do not include the still water shear forces and the still water bending moments. In irregular wave results, the non-dimensional forms of responses are otherwise the same, but the characteristic of the wave is defined with the significant wave height H_s instead of the wave amplitude a. The irregular waves are described in dimensional form with a significant wave height H_s and with a zero crossing wave period T_z (or spectrum peak period T_p).

Table 4.1. Main dimensions and weight data of the RoPax ship. The aft perpendicular is AP at lines drawing frame 0, CL is the centre line and BL is the base line. The distance of the aft perpendicular is 6.5 m in full scale from the transom of the ship.

Quantity	Symbol	Unit	Value
Length over all	L_{oa}	[m]	171.4
Length between perpendiculars	L_{pp}	[m]	158.0
Breadth max. at waterline	B_{wl}	[m]	25.0
Draught	T	[m]	6.1
Displacement	∇	[m^3]	13 766
Block coefficient	C_B	–	0.55
Centre of gravity:			
From AP	x_{CG}	[m]	74.9
From CL	y_{CG}	[m]	0.0
From BL	z_{CG}	[m]	10.9
Radius of gyration in pitch	k_{yy}/L_{pp}	–	0.25
Transverse metacentric height	GM_{T0}	[m]	2.8

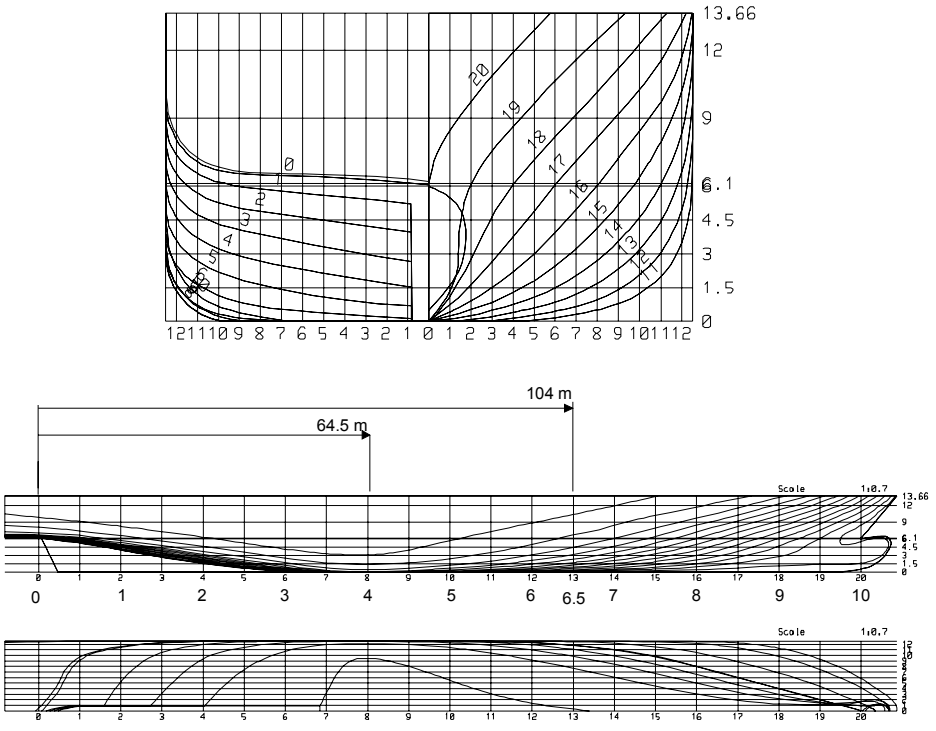

Figure 4.1. Lines drawings of the RoPax ship. The longitudinal locations of the force transducers are measured from the AP (frame 0). The midship transducer was located at frame 4 and the fore ship transducer at frame 6.5.

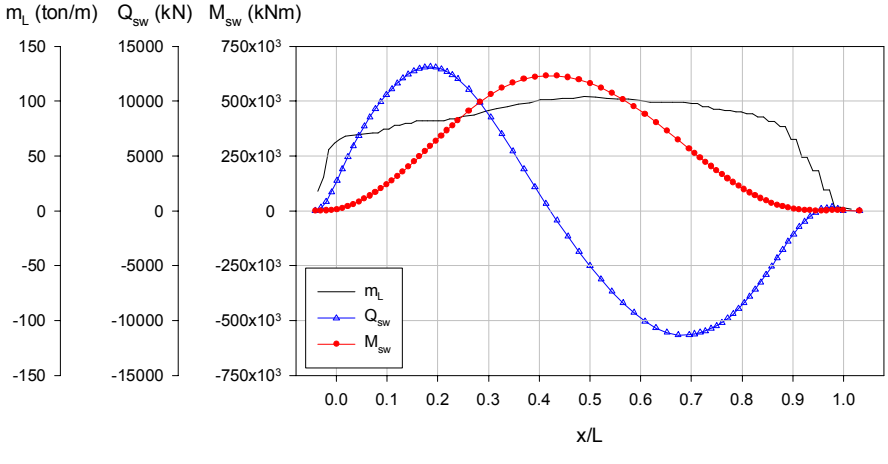

Figure 4.2. Weight distribution (m_L) and still water vertical shear force (Q_{sw}) bending moment (M_{sw}).

4.3 Calculation parameters of the model test ship

The panel meshes of the RoPax ship are shown in Figure 4.3. The numbers of panels on the half hull below the still waterline were 491 and 327 in the fine and coarse meshes, respectively. The transom of the ship was not included on the panel mesh. Hence, the transom was always dry and the pressure was the same as the atmospheric pressure at the transom. The fine mesh was used in the regular wave calculation and the coarse mesh in the irregular waves. The transfer functions of the responses calculated by the two different panel meshes are shown in Figure 4.4 at zero speed and in Figure 4.5 at forward speed $Fn = 0.25$. The wave amplitude was $a/L = 0.006$. At zero speed, the results obtained from the two different panel meshes are almost identical. At forward speed $Fn = 0.25$, the heave motion is about the same though small differences exist in pitch, shear force and bending moment. With the coarse mesh, the pitch is at a slightly higher level and the shear force and bending at a lower level than with the fine mesh. The differences between the two panel meshes are small however.

The RoPax ship has a flat bottom at the stern and the stern is above the still water level from the aft perpendicular to the transom. Hence, a large part of the stern is out of the water in the still water condition, but at forward speed the flat bottom stern is at least partly wet because of the sinkage of the ship and the wave formation. If the RoPax ship is in the waves, the wetted area of the stern varied constantly due to the ship motions, the incoming waves and the waves created by the ship. The calculation showed that high pressure peaks occurred on the panels at the flat bottom stern at the beginning of the calculation. The ship motions became large and the time integration of the motions failed only a few time steps after starting the calculation. The oscillation of responses increased exponentially in time and the calculation finally broke down. The analyses in connection with the cones showed that if the panel is close to the free surface and the inclination angle between the panel and the free surface is small, i.e. non-wall-sided panel, the solution can start to oscillate. To avoid the unstable oscillation, the vertical distance of the centroid of the panel was increased from the free surface. Hence, the same type of approach was applied to the ship as to the cone to avoid the unstable oscillation on the panels close to the free surface. For the model test ship, a criterion was set for the panel distance from the still water level if the panel was considered wet and the velocity and acceleration potentials were solved for this panel. The panel was wet in the calculation if all the corner points of the panel were below $z = 0$ and the distance of the centroid of the panel was ε_{wet} below $z = 0$. However, the incoming wave and the hydrostatic pressures were calculated without the criterion ε_{wet}. Hence, this criterion only had an effect on the hydrodynamic pressures induced by the perturbation velocity potential ϕ. The criterion ε_{wet} for

the centroid had an effect on panels that had a small inclination angle with respect to the free surface. If the panels had a large inclination angle, the distance of the centroid was well below the still water level because the panel corner points also had to be below the still water level. For the RoPax ship, the criterion in the present calculation was $\varepsilon_{wet} = 0.05 \times T$ where T was the draught of the ship. For the panel dimensions at the stern, this criterion corresponded to about $\varepsilon_{wet} / \sqrt{S_P} = 0.2$ where S_P was an average panel area. In still water, this criterion had an effect on seven panels at the stern and two at the bow when the ship hull was discretized by the fine mesh. Hence, these panels were dry the whole time in the body linear solution. In the body nonlinear solution, the panels became wet if the distance of the centroid from $z = 0$ was larger than ε_{wet} and all the corner points of the panels were below $z = 0$.

The calculations were carried out using the acceleration potential method. The solution of the acceleration potential is based on the body boundary condition in which the ship accelerations are required at the same time step as when the ship accelerations are solved from the equations of motion. In this work, an iterative solution was used to solve the acceleration potential. The solution includes that of the ship motions using the time integration and that of the potentials using the panel method. The motions of the ship have an effect on the solutions of the potentials and vice versa. In addition, the size of the panels and the time step size have an effect on the accuracy of the solution. Smaller panel sizes and a shorter time step size will improve the accuracy. However, both will increase the calculation time. Abrupt changes in the velocity and acceleration potentials can induce unwanted changes in ship motions. At the beginning of the calculation, a small inaccuracy in the hydrostatic force or moment can induce a rapid change in motions and the time integration can fail. In the constant panel mesh method, the change of the panels from dry to wet or wet to dry can induce unexpected variations in potentials in the body nonlinear solution. The error in motions and potentials can accumulate in time. In the calculation method, a numerical filter was used to smooth the time history signal. The filter was applied to the body motions on the terms that appear in the body boundary conditions. The filtered terms were $\mathbf{U} \cdot \mathbf{n}$ in the body boundary condition of the velocity potential and $\mathbf{n} \cdot \left[\left(\dot{\mathbf{u}} + \dot{\boldsymbol{\omega}} \times \mathbf{r} \right) - \left(\boldsymbol{\omega} \times \mathbf{u} \right) \right]$ in the body boundary condition of the acceleration potential. Hence, the filtering was only performed on the ship motion in terms solving the source strengths of the potentials. The time history was low-pass filtered during the calculation using a first order Butterworth-type infinite impulse response filter (IIR filter, see, e.g., Press et al., 1997). The used filter is soft and has no sharp cut-off frequency. The low-order filter proved to be a reliable choice. Higher order filters were also tested but it was noted that the solution broke down. One reason is the phase shift of the filter, which increases if the order of the filter

increases. Furthermore, the panel size also limits the highest possible wave frequencies, or wave lengths, that can be taken into account in the calculations. For the fine panel mesh of the ship, the panel characteristic length is $\sqrt{S_P}/L = 0.012$. In here, the area of the panel S_P is based on the average of the panel areas from the panel mesh. The characteristic length of the panel $\sqrt{S_P}/L = 0.012$ can be compared with the wave length λ_w/L, which gives $\omega\sqrt{L/g} = 22.8$ (in dimensional form $\omega = 5.7$ rad/s) for the wave frequency. The calculation results presented here are based on the low-pass filtered signals using cut-off frequencies $\omega_c\sqrt{L/g} = 12.6$ and $\omega_c\sqrt{L/g} = 25.2$ for zero speed and for forward speed $Fn = 0.25$, respectively. Obviously, the cut-off frequency has to be lower than the Nyqvist frequency $f_s/2$ where $f_s = 1/\Delta t$ is the sampling frequency. In Figure 4.6, the heave and pitch motions are shown where the responses were low-pass filtered using the used cut-off frequency $\omega_c\sqrt{L/g} = 25.2$ ($\omega_c = 7\omega_e$) and higher cut-off frequency ($\omega_c = 10\omega_e$). The maximum heave amplitudes are slightly attenuated at the lower cut-off frequency. For pitch, the cut-off frequencies give almost identical results.

The time step used in the calculation was $\Delta t\sqrt{g/L} = 0.025$. At the heave resonance, the numbers of time steps in one period were $T_e/\Delta t = 114$ and 73 at zero speed and at forward speed $Fn = 0.25$. The heave natural period was about 7 s ($\omega_{n3}\sqrt{L/g} = 3.6$). The number of time steps in one period was greater than in the Wigley III calculation because of the more complex hull geometry. The larger number of the time step in one period was also used at zero speed than the number used at forward speed because relative motions at the stern were greater at zero speed. At zero speed, the flat bottom stern induced pressure peaks when the stern entered the waves.

In the calculation, the constant panel mesh was used and the integration of the Green function over the panel area was performed using the midpoint rule.

At the beginning of the calculation, the wave ramp was applied to increase the wave amplitude monotonically from zero to the target amplitude. A cosine-squared wave ramp was used and the duration of the ramp was $t\sqrt{g/L} = 5$ at the beginning of the calculation.

The vertical bending moments are given at $x/L = 0.40$ and the shear forces at $x/L = 0.65$. The ship motions are given at the centre of gravity of the ship. The verti-

cal accelerations are given at the fore and aft perpendiculars and at the centre of gravity of the ship. The locations are the same as in the model tests.

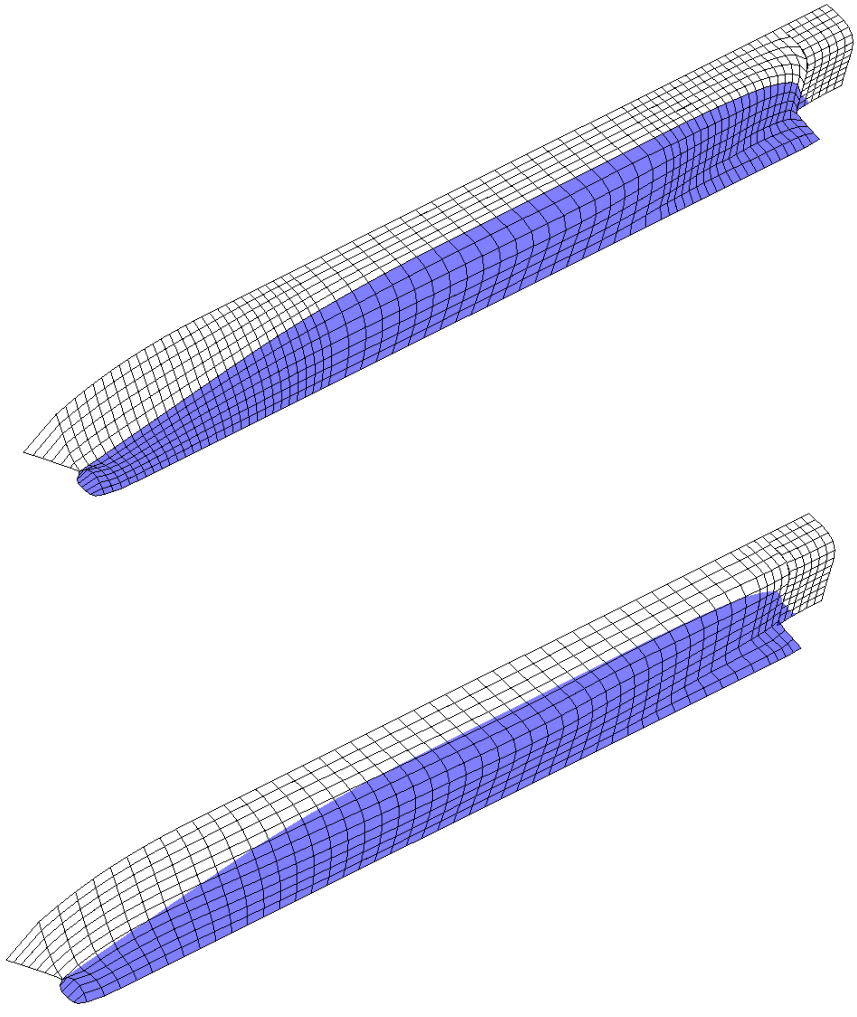

Figure 4.3. Panel meshes of the RoPax ship in the calculations. The numbers of panels are 491 (upper) and 327 (lower) on the half body below the still waterline.

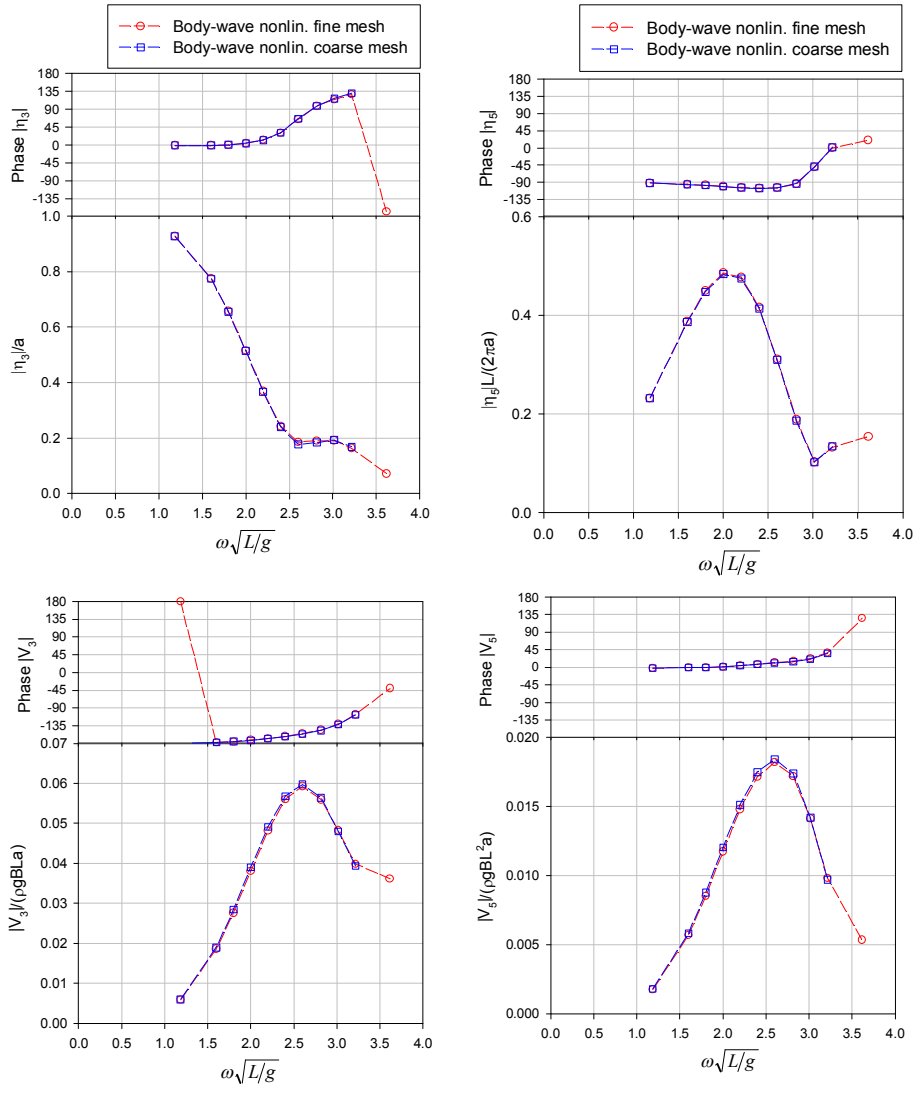

Figure 4.4. Heave, pitch, shear force and bending moment at Fn = 0.0 in head seas calculated with two different panel meshes. The wave amplitude was a/L = 0.006 in the body-wave nonlinear solution.

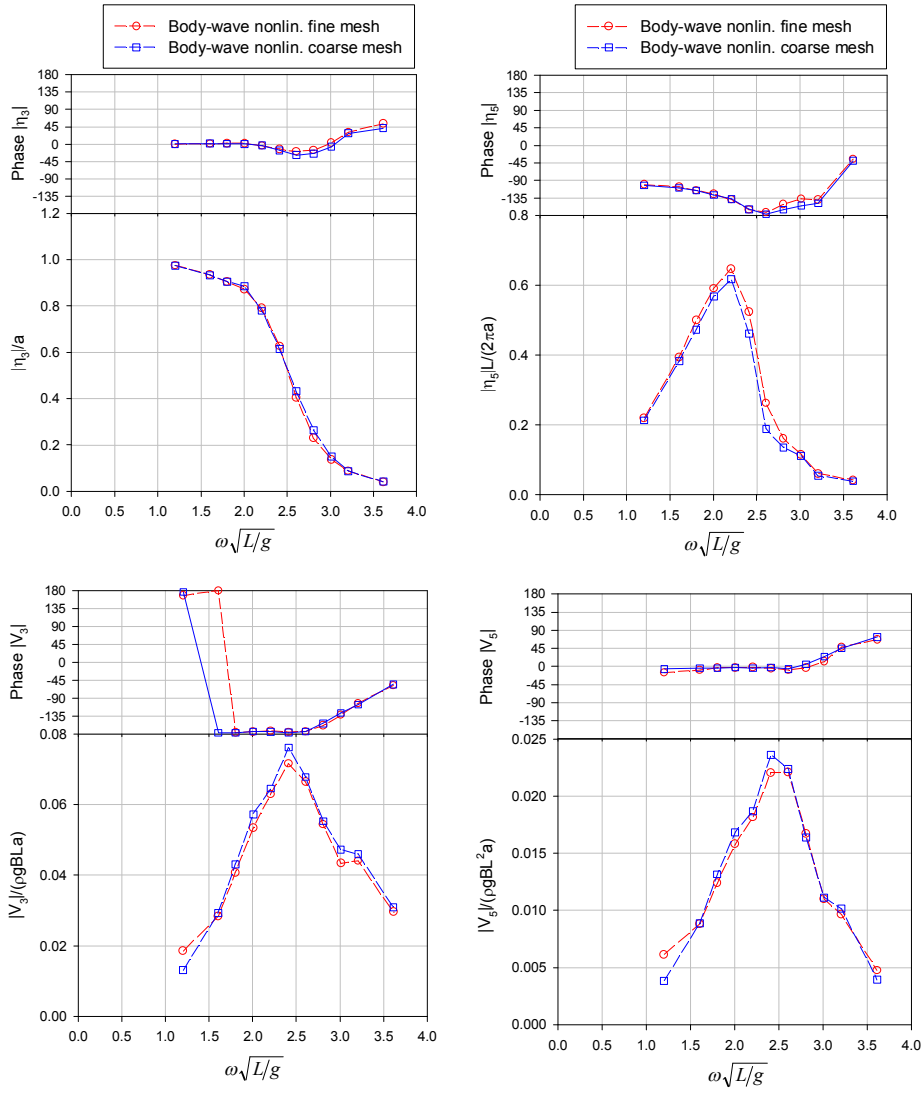

Figure 4.5. Heave, pitch, shear force and bending moment at Fn = 0.25 in head seas calculated with two different panel meshes. The wave amplitude was a/L = 0.006 in the body-wave nonlinear solution.

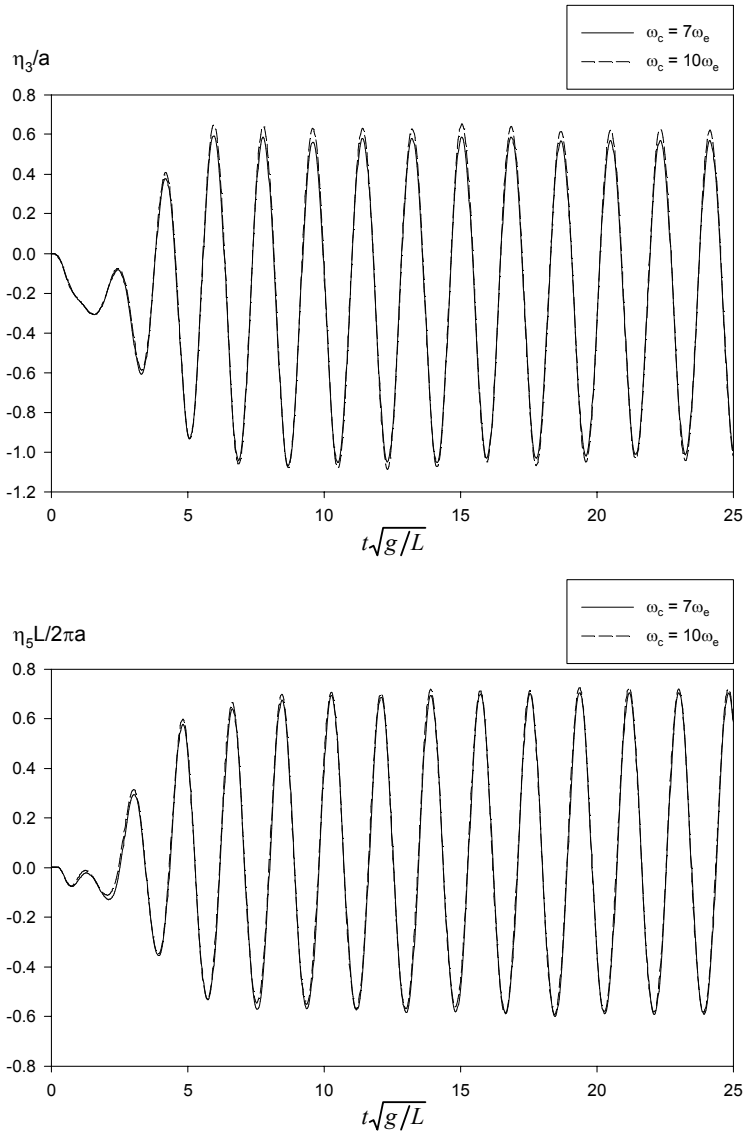

Figure 4.6. Time histories of heave and pitch calculated using two different cut-off frequencies in the low-pass filter. The forward speed is Fn = 0.25, the wave frequency is $\omega\sqrt{L/g}$ = 2.21 and the wave amplitude is a/L = 0.006.

4.4 Results in calm water

The aim of the model tests in calm water was to investigate the steady flow effects on the hull girder loads. Responses in calm water were also calculated with the time domain method and the results compared with those of the model tests. The body nonlinear solution was used in the calculation. The sinkage at the centre of gravity of the ship is shown in Figure 4.7 as a function of the ship speed. The vertical shear force at fore ship and the vertical bending moment at midship are presented in Figure 4.8. In the figures, the hull girder loads are given without the still water shear force and bending moment.

The trends of the calculated sinkage, shear force and bending moment are similar to those in the model tests. The vertical bending moment increases with the speed. The steady pressure and wave pattern due to the forward speed induce a sagging bending moment on the hull girder. The calculated shear force and the bending moment deviate from the model test results at the highest speed. In the dimensional form, the steady bending moment is –70300 kNm at midship and the shear force 1100 kN at fore ship at $Fn = 0.25$. The values are based on the model test results. The steady bending moment is about 11% of the maximum still water bending moment and the shear force is about 13% of the maximum still water shear force. Thus, the steady hull girder loads are relatively small compared with the still water bending moment and shear force. The trim was small in the model tests and calculations. At forward speed $Fn = 0.25$, the trim was 0.14 degrees in the model tests and the calculation gave –0.05 degrees.

The calculated results are also shown in the figures without the fluid velocity squared term $0.5|\nabla\phi|^2$ in Bernoulli's equation. The fluid velocity squared term affects the responses in calm water at forward speed. Comparing the calculated responses, the sinkage is greater and the shear force and bending moment smaller if the term is included in Bernoulli's equation. However, the difference is rather small, especially for the bending moment. The responses are also slightly closer to the model test results if the term is excluded. The sinkage at the highest speed $Fn = 0.30$ is an exception where the time domain method without the fluid velocity squared term deviates clearly from the model test result. Thus, the fluid velocity squared term has an effect on the responses in calm water at forward speed but the significance is not as great as the effects due to other terms in Bernoulli's equation. In calm water, the other terms are hydrostatic pressure and pressure due to the term $\varphi - \mathbf{U}\cdot\nabla\phi$. The potential function φ is zero if the body is in pure constant translational motion in calm water. At forward speed U_0, the pressure component due to the term $-U_0\,\partial\phi/\partial x$ induces mean shift in the heave force.

Hence, this term has an effect on the sinkage of the ship and on the steady hull girder loads. It should be noted that the pressure terms in Bernoulli's equation in this work are defined in the space-fixed coordinate system and not with respect to a moving frame. The meaning of the pressure term $\varphi - \mathbf{U} \cdot \nabla \phi$ was discussed in Section 2.3.2.

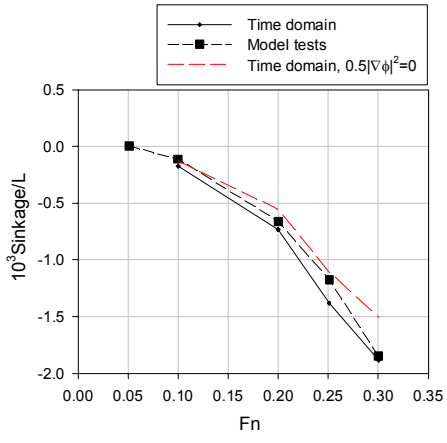

Figure 4.7. Sinkage at the centre of gravity of the ship in calm water as a function of the ship speed

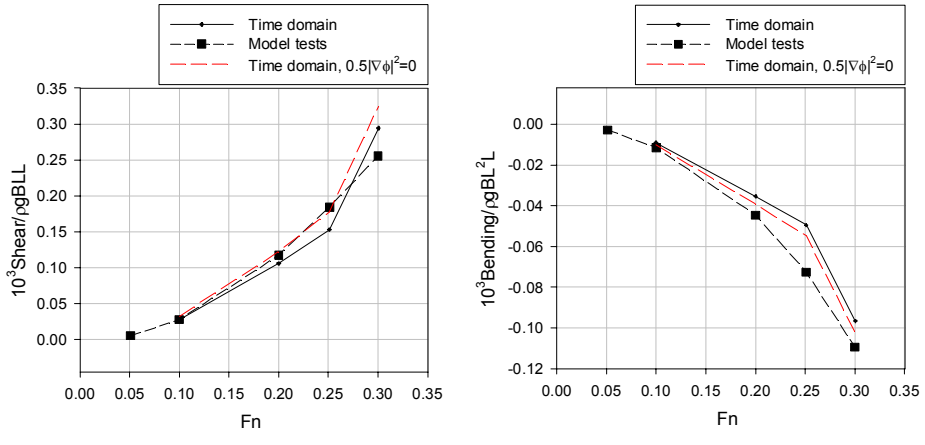

Figure 4.8. Shear force at the fore ship (left) and vertical bending moment at midship (right) in calm water as a function of the ship speed.

4.5 Results in regular waves

4.5.1 General

Motions and hull girder loads were measured and calculated for the model test ship in regular head waves and the transfer functions were determined from the time histories. The harmonic analysis was performed for the model test time histories and the same procedure was applied for the calculated data. In the harmonic analysis, a Fourier series was fitted to the recorded data. The time history of the response X in regular waves can be presented as a sum of the harmonic components as follows:

$$X(t) = X^{(0)} + X^{(1)}\cos\left(\omega_e t + \varepsilon^{(1)}\right) + X^{(2)}\cos\left(2\omega_e t + \varepsilon^{(2)}\right) + X^{(3)}\cos\left(3\omega_e t + \varepsilon^{(3)}\right) + \ldots, \quad (4.1)$$

where $X^{(0)}$ is the mean of the response, $X^{(i)}$ is the ith harmonic component of the response, $\varepsilon^{(i)}$ is the ith phase angle of the ith harmonic response and i = 1, 2, 3, …, ∞. The encounter frequency is ω_e. The phase angle of the response is defined as leads with respect to the wave crest at the centre of gravity of the ship. The first harmonic component gives the linear transfer function for the responses. The transfer functions or the response amplitude operators (RAO) are defined as the ratio of the response first harmonic to the wave first harmonic.

In addition to the transfer functions, the results are presented in a pseudo-transfer function format. The pseudo transfer function includes the maximum and minimum amplitudes obtained directly from the time history data. Hence, the pseudo transfer function is given separately for the maximum and minimum amplitudes. The pseudo transfer functions are presented in the same non-dimensional form as the linear transfer functions but the given pseudo transfer functions are not necessarily linear with respect to the wave amplitude. Furthermore, the results are given as the relative magnitude of the higher order harmonic components with respect to the first harmonic component.

The results are given at zero speed and forward speed Fn = 0.25 in head seas. Hull girder loads are presented for the vertical shear force at fore ship and vertical bending moment at midship. The calculated responses are given for the body linear and nonlinear solutions as well as for the body-wave nonlinear solution. The model test and calculated results are given as follows:

1. Transfer functions of responses from model tests at three different wave amplitudes

2. Transfer functions of responses and comparisons using the body linear and nonlinear solutions
3. Investigations of the responses in the time domain and studies of the effect of the fluid velocity squared term on responses at forward speed
4. Comparison of responses obtained with the backward difference and acceleration potential methods
5. Studies of nonlinearities in loads with transfer functions, pseudo transfer functions and higher order harmonic components of responses at different wave amplitudes

4.5.2 Transfer functions from the model tests

The transfer functions of heave, pitch, vertical shear force and bending moment at zero speed in head seas are shown in Figure 4.9. The model test results are shown at three wave amplitudes: $a/L = 0.006$, $a/L = 0.013$ and $a/L = 0.019$. However, the results for the pitch motion at wave amplitude $a/L = 0.006$ was omitted because of the unreliable data obtained from the model test measurements at zero speed. The transfer functions at forward speed $Fn = 0.25$ in head seas are shown in Figure 4.10. The mean of the measurements from the different wave amplitudes are also shown in the figures.

At zero speed, the model test results for the responses are close to each other at the three different wave amplitudes. Hence, the nonlinearities are relatively small in the first harmonic components of the responses with respect to the first harmonic component of the wave amplitude.

At forward speed, the first harmonic components of the responses are relatively close to each other at the two lowest wave amplitudes: $a/L = 0.006$ and $a/L = 0.013$. However, the results of the highest wave amplitude $a/L = 0.019$ clearly deviate from the two other wave amplitudes. Hence, nonlinearities increase when the wave amplitude is higher than $a/L = 0.013$. One reason for the nonlinearities is the large relative motions that occurred at the highest wave amplitude in the tests at forward speed. The motions of the ship model were large and deck wetness and bow slamming occurred. A large part of fore ship was out of the waves about the resonance of heave.

In the following sections, in which the calculated transfer functions are compared with the model test transfer functions, the model test results in the transfer functions are given as the mean values, as the differences were small between the different wave amplitudes. This clarifies the presentation of the model test results in the figures. The exception, however, is the highest wave amplitude $a/L = 0.019$

at forward speed $Fn = 0.25$ for which the mean values are based on the two lowest wave amplitudes. If the calculated transfer functions are compared with the model test transfer functions at the highest wave amplitude at forward speed then the model test results are also given at the highest wave amplitude. However, other results than the comparison of the calculated and model test transfer functions are given at the defined wave amplitudes. In all other cases, the used wave amplitudes are given in the figures in the following sections.

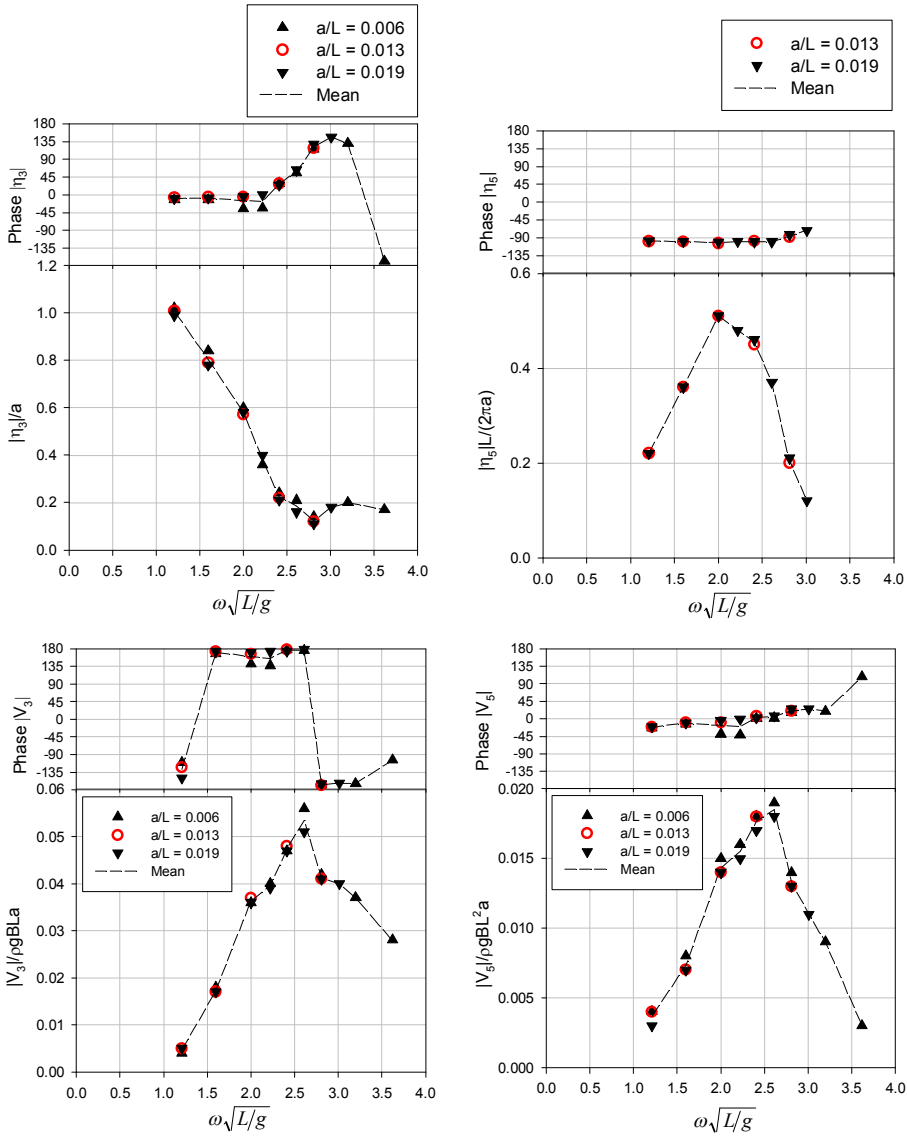

Figure 4.9. Model test results for heave and pitch, and vertical shear force and bending moment at $Fn = 0.0$ in head seas at different wave amplitudes a/L.

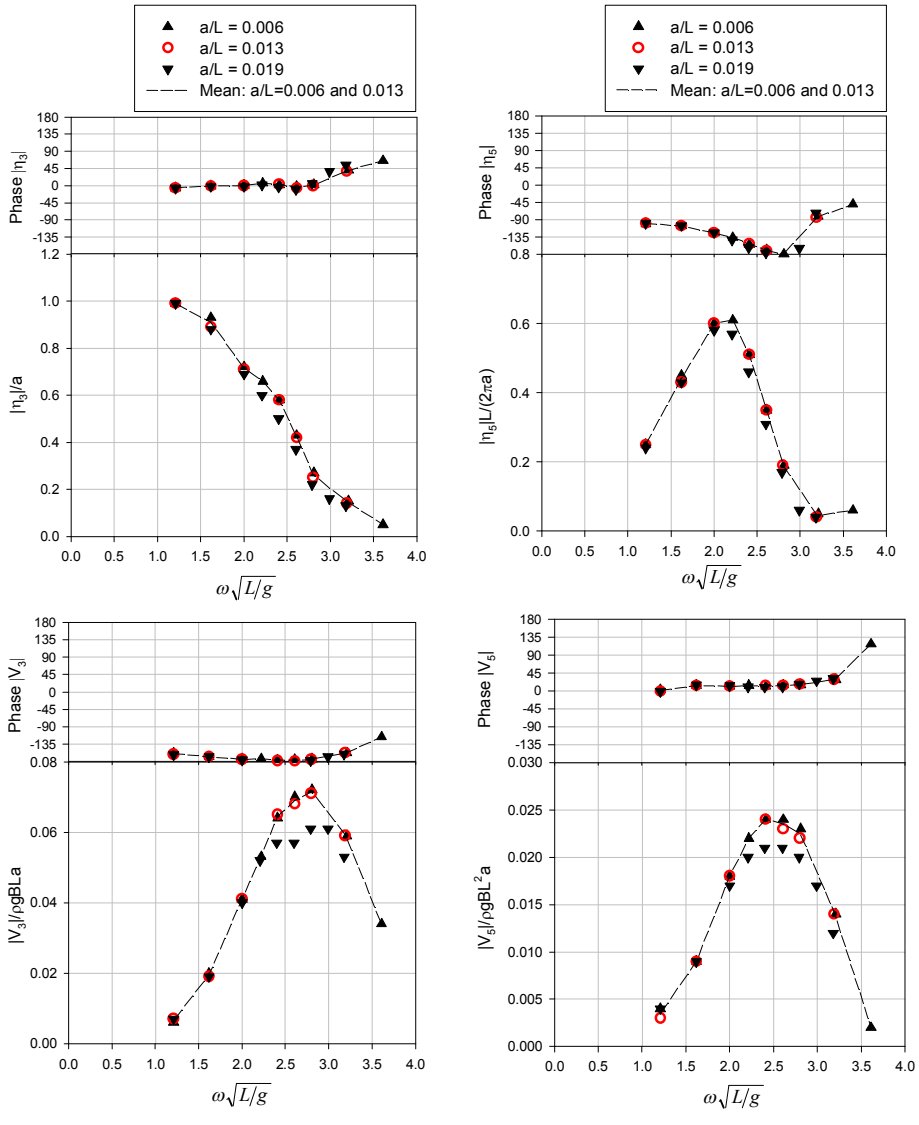

Figure 4.10. Model test results for heave and pitch, and vertical shear force and bending moment at $Fn = 0.25$ in head seas at different wave amplitudes a/L

4.5.3 Comparison of the body linear and nonlinear solutions

At zero speed, the transfer functions are presented in Figure 4.11 for heave, pitch, shear force and bending moment. The results using the time domain calculation method are given for the body linear and nonlinear solutions. The wave amplitude was $a/L = 0.006$ in the calculation. The body linear and nonlinear solutions give almost the same results, and the solutions are in good agreement with the model test results. The body nonlinear solution gives a slightly higher prediction for the shear force and bending moment. The vertical accelerations at the centre of gravity, and aft and fore perpendiculars are shown in Figure 4.12. The calculation gives somewhat smaller accelerations than the model tests but the trend as a function of the frequency is the same as in the model tests.

At forward speed $Fn = 0.25$, the body linear and nonlinear solutions are shown in Figure 4.13 for the heave, pitch, shear force and bending moment. The wave amplitude was $a/L = 0.006$ in the calculation.

The body nonlinear solution and the model test results of the shear force and bending moment are close to each other at forward speed $Fn = 0.25$. The transfer function of the calculated shear force exists at somewhat lower wave frequencies than in the model tests. The pitch motion is also close to the model test results, but the calculation gives a rather high heave amplitude at the resonance. Furthermore, vertical accelerations are presented in Figure 4.14 calculated with the body nonlinear solution. The calculated accelerations are in close agreement with the model test results. It can be seen from the figure that the accelerations are clearly larger at the bow than the stern.

The comparison between the body nonlinear solution and the model tests at forward speed showed that the *body nonlinear solution* gives relatively good predictions for responses. However, the *body linear solution* clearly overestimates the responses at forward speed compared with the model test results. Heave is close to the body nonlinear solution but other responses are well above the body nonlinear results. The pitch motion has a high peak at $\omega\sqrt{L/g} = 2.21$ and the shear force and bending moment at $\omega\sqrt{L/g} = 2.41$. For the Wigley III hull form, the body linear and nonlinear solutions gave about the same predictions for heave and pitch. The Wigley hull form has a pointed stern and bow and hence the hull geometry deviates from the RoPax hull, especially at the stern. In the body linear solution, the flat bottom stern was out of the waves in the calculation. However, a large part of the stern was in the waves in the model tests because of the sinkage, ship motions and wave pattern due to the steady flow at forward speed. In the

body nonlinear solution, the sinkage of the ship and the instantaneous floating position due to the ship motions are taken into account.

For the transom stern ships at high forward speed, the high heave and pitch resonance are also observed in the linear frequency domain predictions compared with the model test results. However, extended theoretical approaches have been developed to take into account the flow pattern properly at the transom stern which improved the calculated predictions (Ahmed et al., 2005; Elangovan et al., 2008). In the linear frequency domain methods, the steady flow is taken into account with so-called *m*-terms in the body boundary condition (see, e.g., Newman, 1978; Kim, 2005). The *m*-terms take into account the steady flow effects in solving the radiation velocity potentials. In the linear frequency domain methods, the velocity potentials due to steady flow, radiation and diffraction are decoupled. In the present time domain method expressed in the space-fixed coordinate system, the steady flow and flow due to radiation and diffraction are not decoupled. In both the linear frequency methods and the linear time domain method, the body boundary condition is expressed on the mean wetted surface of the body. Hence, the coupling of the actual floating position of the body geometry and the steady flow is not taken into account. In the body linear solution, the pitch angle and the forward speed are taken into account in the body boundary condition on the mean wetted surface of the hull. However, in the body nonlinear solution, the instantaneous floating position of the ship is updated at every time step, and the coupling of the actual floating position of the body geometry and the steady flow is therefore taken into account. In the body linear solution, this is only taken into account on the mean wetted surface of the hull.

In order to gain an insight into the floating position of the ship with respect to the waves and mean water level, the ship is shown at four time instants in Figure 4.15. The motions were calculated at the forward speed of the ship at $Fn = 0.25$ and the wave amplitude and wave frequency were $a/L = 0.006$ and $\omega\sqrt{L/g} = 2.21$, respectively. The floating positions of the ship are given at four time instants for one pitch period. In Figure 4.16, the ship position is otherwise given under the same conditions, but the wave amplitude is higher: $a/L = 0.013$. In the figures, the horizontal blue line is the mean waterline at $z = 0$ and the sinusoidal black line is the incoming wave elevation.

At the lower wave amplitude, the mean water level and incoming wave elevation are rather close to each other. Thus, it can be assumed that the solution of the perturbation velocity potential up to the $z = 0$ level gives a good approximation for the flow velocities. At the higher wave amplitude, however, there is a clear difference between the mean water level and the incoming wave elevation. At the

time instant $t = 0.25T$, the incoming wave crest is close to the bottom of the ship at the stern and the $z = 0$ line is clearly below the bottom. Hence, the solutions of the velocity potentials are obtained for a smaller area at the stern compared with the area of the stern that is below the incoming wave elevation. Moreover, the mean water level is above the incoming wave elevation at time instant $t = 0.75T$. Thus, the velocity potentials are solved for a larger area of the stern than if the velocity potential had been solved below the incoming wave elevation. On the other hand, the figures only represent the incoming wave elevation and not the actual free surface elevations due to the steady and unsteady flows. In the model tests, it was observed that a large part of the flat bottom stern was always in the waves. The steady flow had a clear effect on the wave formation at the stern. Thus, the variation between wet and dry during one encountered wave period was larger in the calculation than in the model tests, especially if the ship motions were large.

The time histories of relative motions are shown in Figure 4.17 at zero speed and in Figure 4.18 at forward speed $Fn = 0.25$. Model test results for the relative motions are not available. The relative motion z_r is defined as the difference between the vertical motion and the incoming wave elevation. Hence, the relative motion includes only the incoming wave and not the diffracted and the radiated waves due to forward speed and ship motions. The relative motions are given at the aft and fore perpendiculars at wave amplitude $a/L = 0.013$ and wave frequency $\omega\sqrt{L/g} = 2.21$. The bottom of the fore perpendicular is out of the wave if the non-dimensional relative motion z_r/a exceeds 3.1 and the main deck is below the wave if z_r/a is less than –3.8. The flat bottom stern is at the mean water level and hence the aft perpendicular is out of the wave if the non-dimensional relative motion is positive, and negative if it is in the wave. At forward speed, the relative motion is clearly higher at the bow than the stern. In addition, the relative motion at the bow is asymmetric. The relative motion downwards is greater than upwards. Hence, the bow enters the waves more deeply than it rises above the waves. In the model tests at forward speed, it was observed that the stern was not out of the water at small wave amplitudes. At the highest wave amplitude in the tests, $a/L = 0.019$, the emergence of the stern was still moderate and at least part of the flat bottom stern was in the waves. A large part of the stern was in the waves because of the wave formation due to the steady flow at forward speed. However, the stern rises out of the waves at zero speed in the model tests. The calculation shows that the relative motions at the stern are larger at zero speed than at forward speed. Hence, the stern can emerge out of the waves higher and a wave impact can occur when the stern enters the waves again. At high wave amplitudes, $a/L = 0.013$ and 0.019, in the model tests, stern impacts occurred when the flat bottom stern entered the waves. Based on the model tests, it was found

that the effect of the impact at the stern was small on the rigid hull girder loads. However, the ship model was not dynamically scaled, i.e. the structural dynamics of the hull girder were not modelled in the tests. Hence, possible impact-induced hull girder loads such as whipping loads were not considered in the model tests.

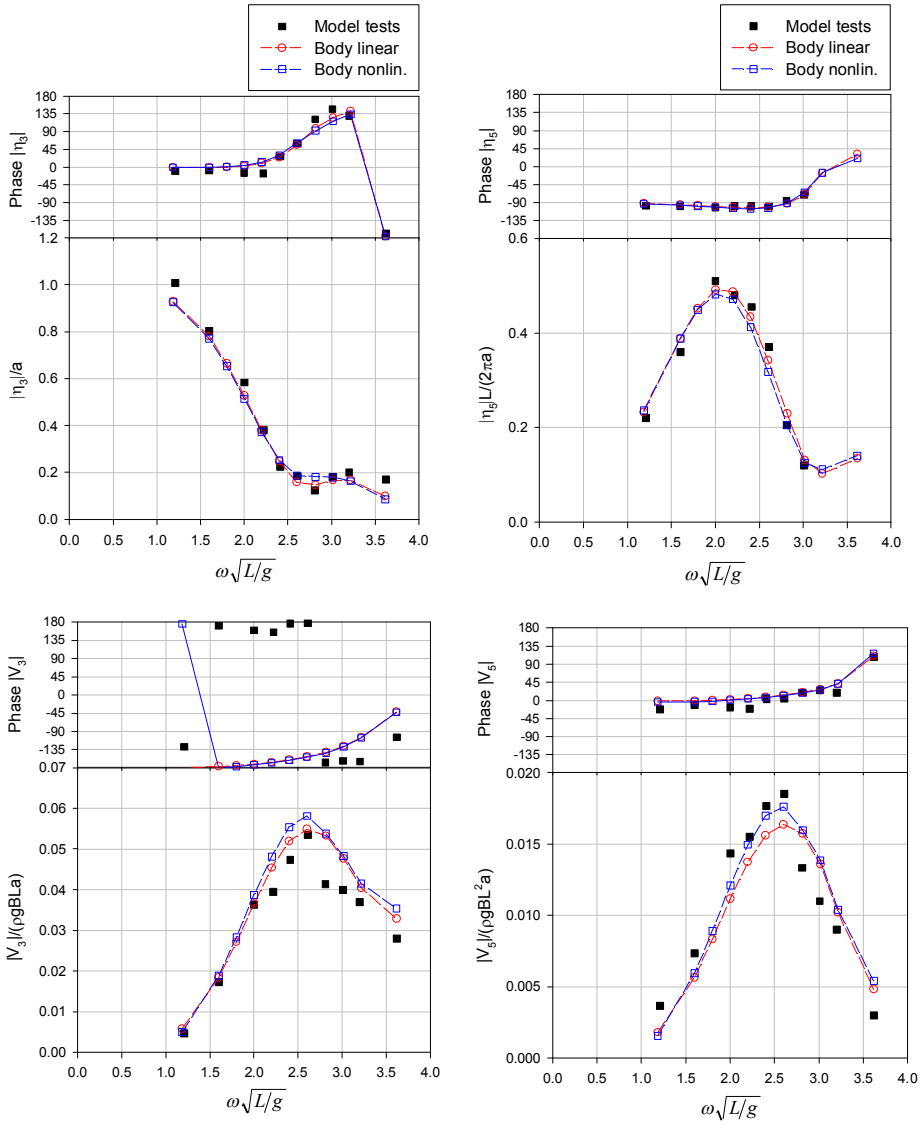

Figure 4.11. Heave, pitch, shear force and bending moment at Fn = 0.0 in head seas calculated with the body linear and nonlinear solutions. The wave amplitude was a/L = 0.006 in the body nonlinear solution.

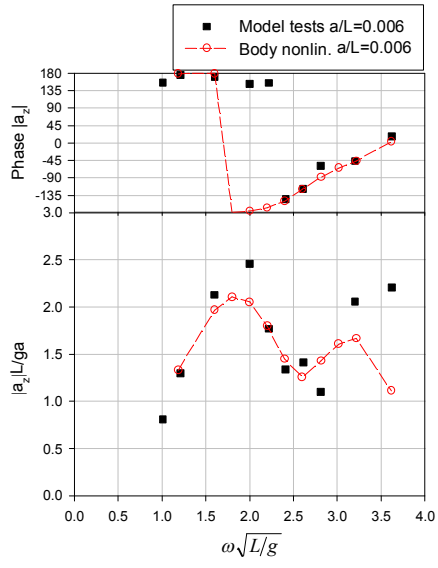

COG

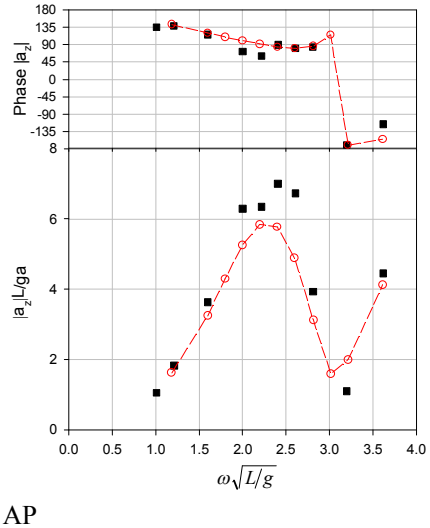

AP

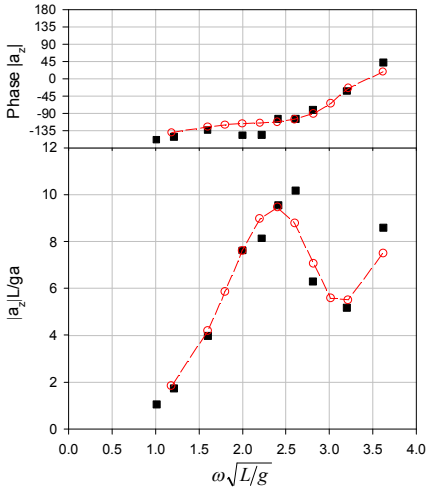

FP

Figure 4.12. Vertical accelerations at the aft perpendicular (AP), centre of gravity (COG) and fore perpendicular (FP) at Fn = 0.0 in head seas calculated with the body nonlinear solution at a/L = 0.006.

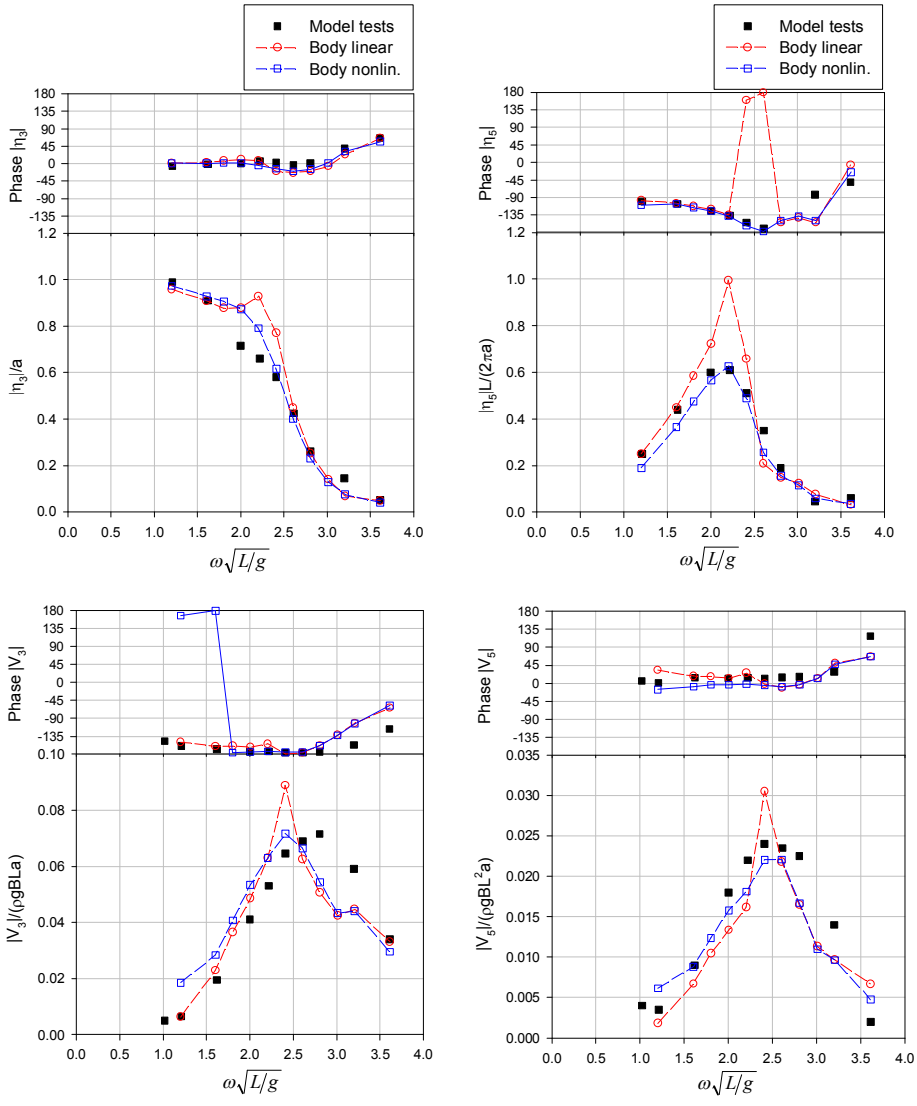

Figure 4.13. Heave, pitch, shear force and bending moment at Fn = 0.25 in head seas calculated with the body linear and nonlinear solutions. The wave amplitude was a/L = 0.006 in the body nonlinear solution.

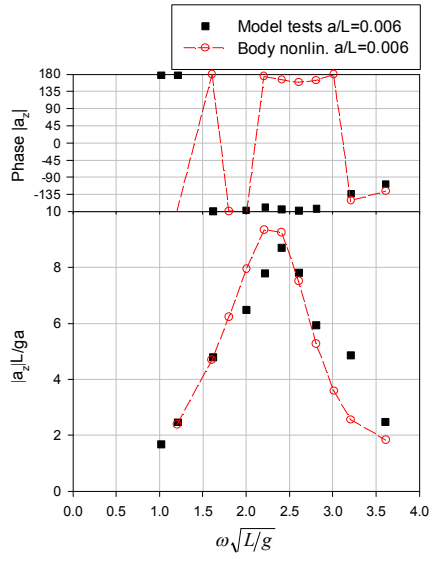

COG

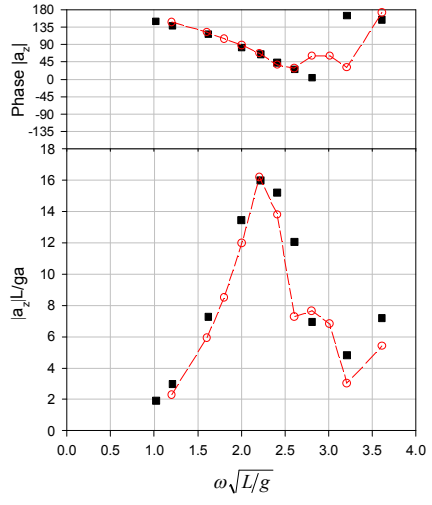

AP

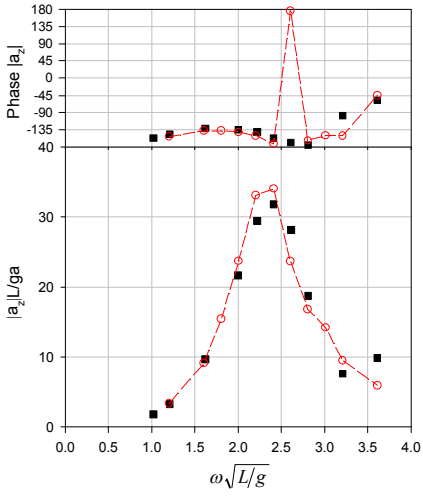

FP

Figure 4.14. Vertical accelerations at the aft perpendicular (AP), centre of gravity (COG) and fore perpendicular (FP) at Fn = 0.25 in head seas calculated with the body nonlinear solution at a/L = 0.006.

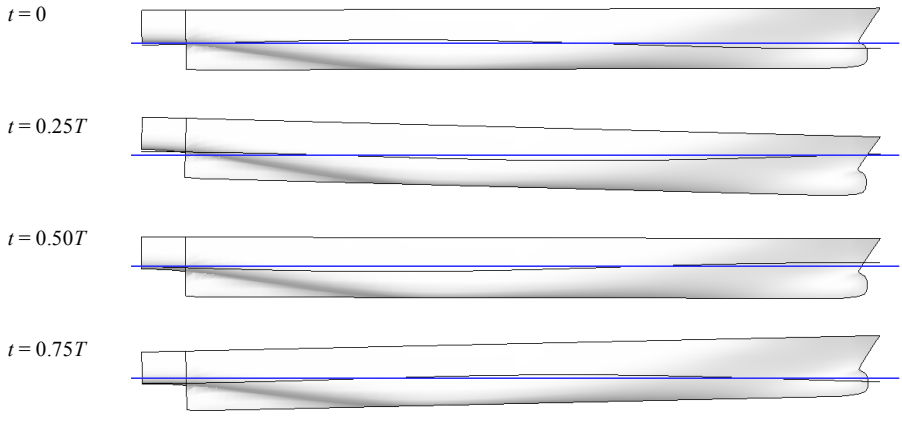

Figure 4.15. Ship motion at Fn = 0.25 in regular waves a/L = 0.006 and $\omega\sqrt{L/g}$ = 2.21 in head seas. The floating position of the ship is given at four time instants for pitch cycle T.

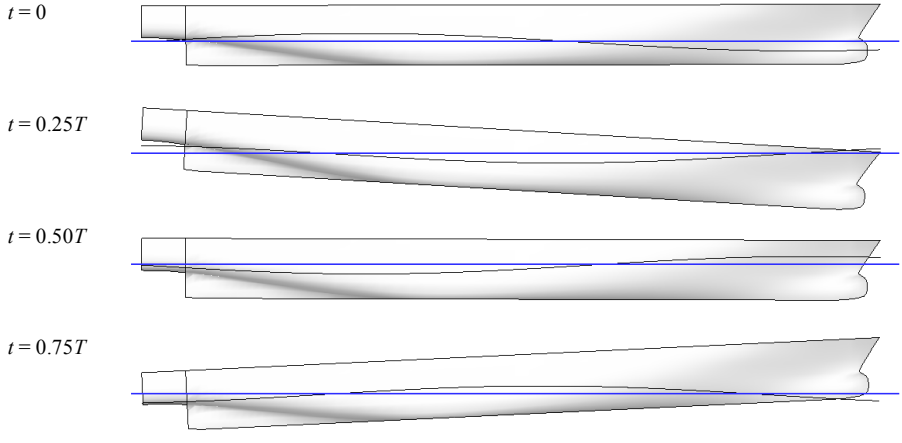

Figure 4.16. Ship motion at Fn = 0.25 in regular waves a/L = 0.013 and $\omega\sqrt{L/g}$ = 2.21 in head seas. The floating position of the ship is given at four time instants for pitch cycle T.

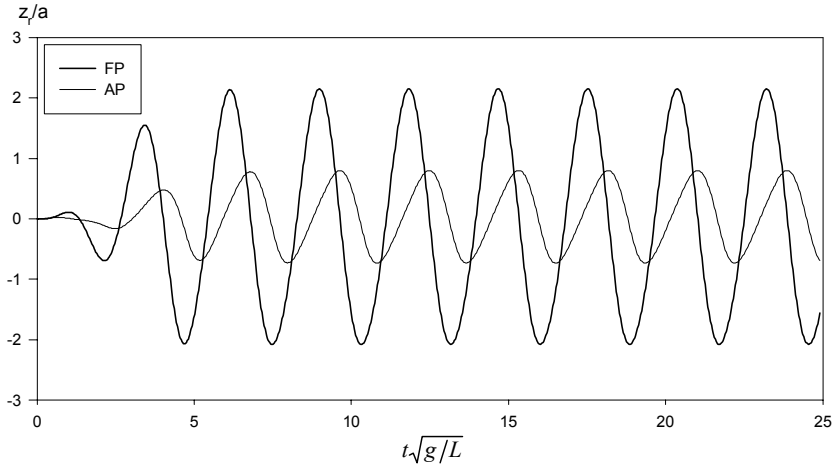

Figure 4.17. Relative motion at the fore (FP) and aft (AP) perpendiculars at *Fn* = 0.0 calculated using the body-wave nonlinear solution at *a*/*L* = 0.013 and $\omega\sqrt{L/g}$ = 2.21.

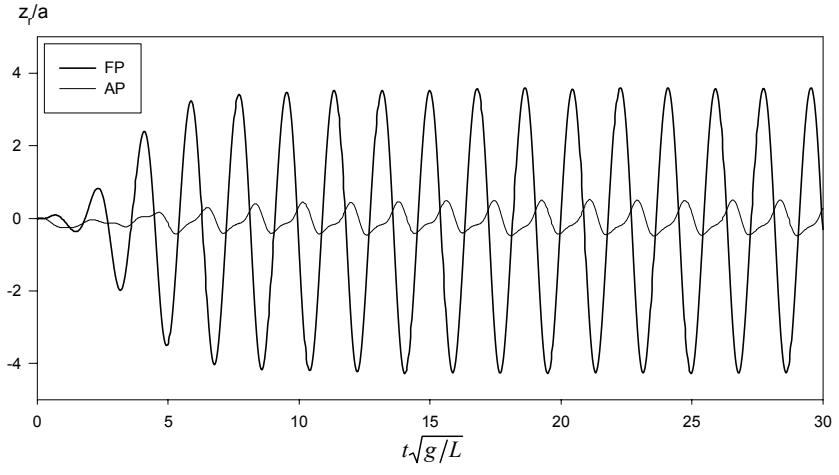

Figure 4.18. Relative motion at the fore (FP) and aft (AP) perpendiculars at *Fn* = 0.25 calculated using the body-wave nonlinear solution at *a*/*L* = 0.013 and $\omega\sqrt{L/g}$ = 2.21.

4.5.4 Comparisons in the time domain

The model test and calculated time histories of heave and pitch at zero speed are shown in Figure 4.19 and the shear force and bending moment in Figure 4.20. The calculation was carried out using the body-wave nonlinear solution. The wave frequency was $\omega\sqrt{L/g}$ = 2.41 and the wave amplitude a/L = 0.013. It can be seen from the figures that the calculated time histories follow the model test results well. The shear force is somewhat overestimated by the time domain method compared with the model test results. The same can be seen from the transfer functions that are presented in Figure 4.32.

At forward speed Fn = 0.25, the time histories from the model test and the calculation for heave and pitch are presented in Figure 4.21 and for the shear force and bending moment in Figure 4.22. The wave frequency was $\omega\sqrt{L/g}$ = 2.41 and the wave amplitude a/L = 0.013. The calculation was performed using the body-wave nonlinear solution. Heave is overestimated and pitch underestimated by the calculation compared with the model test results. The mean of the pitch deviates from zero and the positive amplitudes are greater and the negative amplitudes smaller than in the model tests. The shear force is close to the model test results and the bending moment has smaller amplitudes in the calculation than in the model tests.

Hence, the calculation gives better predictions for responses at zero speed than at forward speed. The same is noted from the transfer functions of the responses presented in the previous section. At forward speed, the free surface elevation around the ship is a combination of the steady and unsteady wave patterns, in addition to the incoming waves. The unsteady waves include the radiation and diffraction effects due to the ship motions and the scattering of the incoming waves. The wave formation of the steady and unsteady flows at the flat bottom stern of the ship can have an effect on the calculated predictions at forward speed. In the model tests at forward speed, the stern was always at least partly wet because of the free surface elevation at the stern. The actual free surface elevation is not taken into account because the linear free surface boundary condition is applied in the present method. The linear kinematic and dynamic free surface conditions are given in Equations (2.20) and (2.21), respectively. The fluid velocity squared term does not appear in the kinematic condition because the term is a higher order term. However, the term is included in Bernoulli's equation in the present calculations to calculate pressures. The calculation was repeated ignoring the fluid velocity squared term $0.5|\nabla\Phi|^2$ in Bernoulli's equation. The fluid velocity squared term had an effect on the calm water results presented in Section 4.4. However, the effect was rather small on the sinkage, steady shear force and bend-

ing moment. The time histories of the heave and pitch motions without the fluid velocity squared term are shown in Figure 4.23 at forward speed $Fn = 0.25$. The time histories of the shear force and bending moment are presented in Figure 4.24. The prediction of the heave motion is improved and the calculated time history about the same as in the model tests. The prediction for pitch is also improved, but the amplitudes are still slightly smaller than in the model tests. The bending moment is also closer to the model test results without the fluid velocity squared term. The shear force is slightly increased but still close to the model test results. Thus, the responses are closer to the model test results without the fluid velocity squared term in Bernoulli's equation. Ignoring the term in Bernoulli's equation is consistent with the linear free surface boundary condition. This is further discussed in Section 4.5.6 in which the effect of the fluid velocity squared term in transfer functions of responses is also presented.

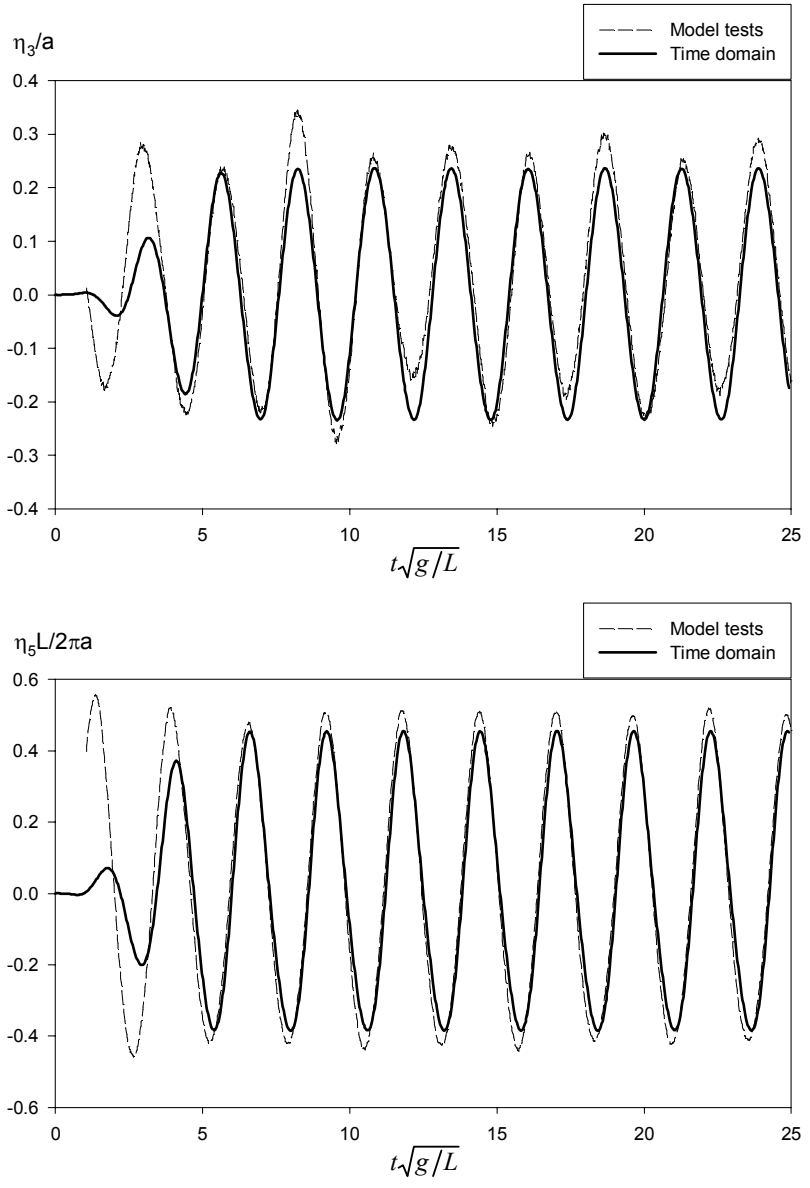

Figure 4.19. Time histories of heave and pitch at Fn = 0.0, $\omega\sqrt{L/g}$ = 2.41 and a/L = 0.013. Body-wave nonlinear solution.

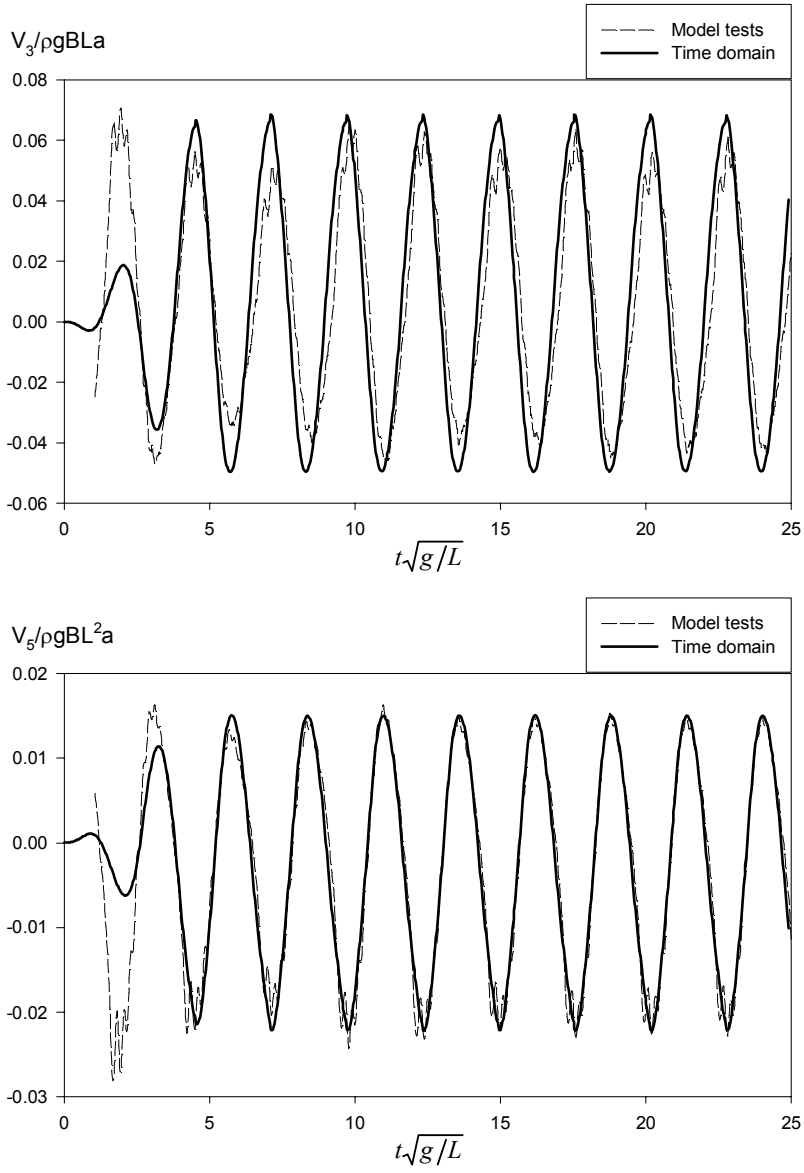

Figure 4.20. Time histories of shear force and the bending moment at Fn = 0.0, $\omega\sqrt{L/g}$ = 2.41 and a/L = 0.013. Body-wave nonlinear solution.

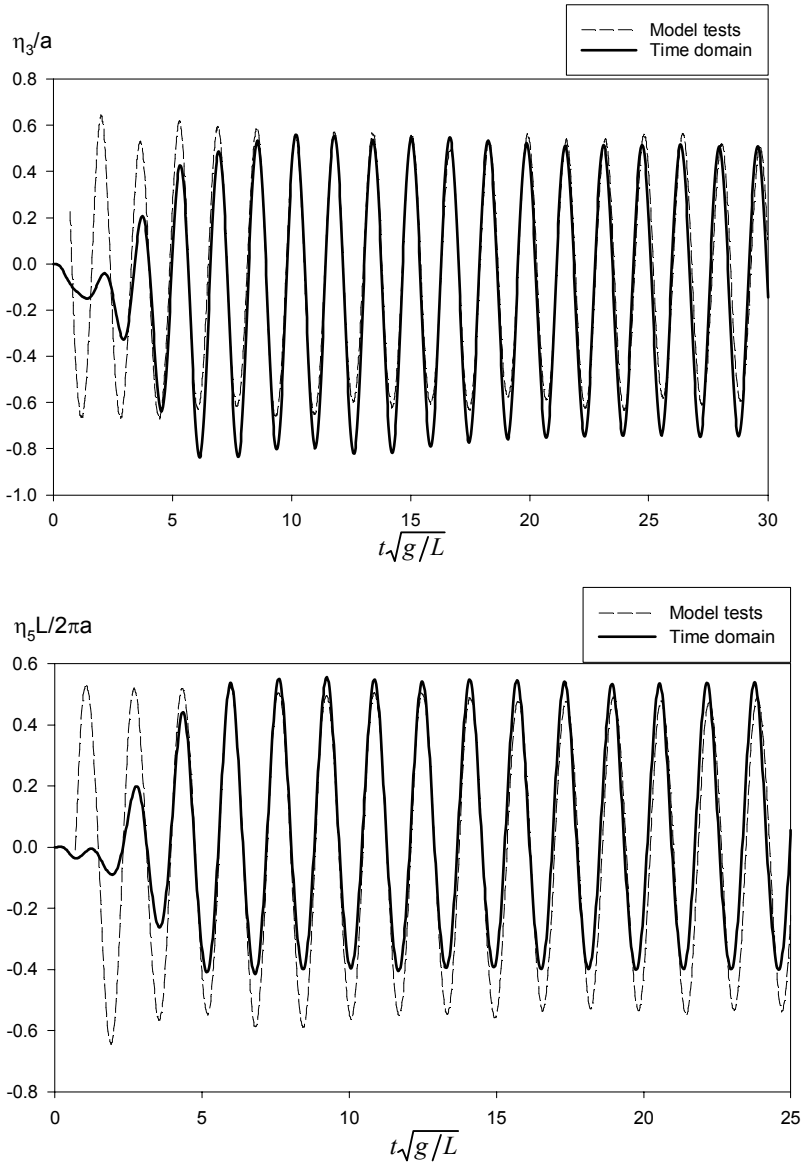

Figure 4.21. Time histories of heave and pitch at $Fn = 0.25$, $\omega\sqrt{L/g} = 2.41$ and $a/L = 0.013$. Body-wave nonlinear solution.

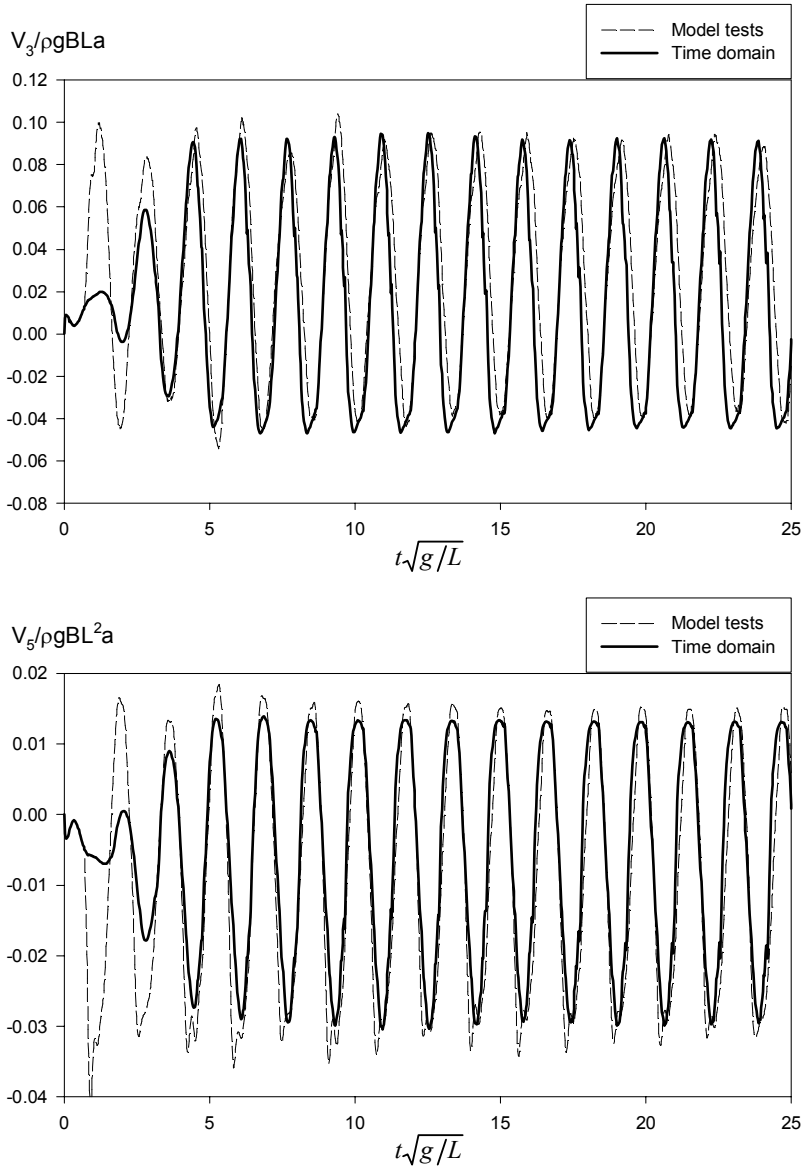

Figure 4.22. Time histories of shear force and bending moment at Fn = 0.25, $\omega\sqrt{L/g}$ = 2.41 and a/L = 0.013. Body-wave nonlinear solution.

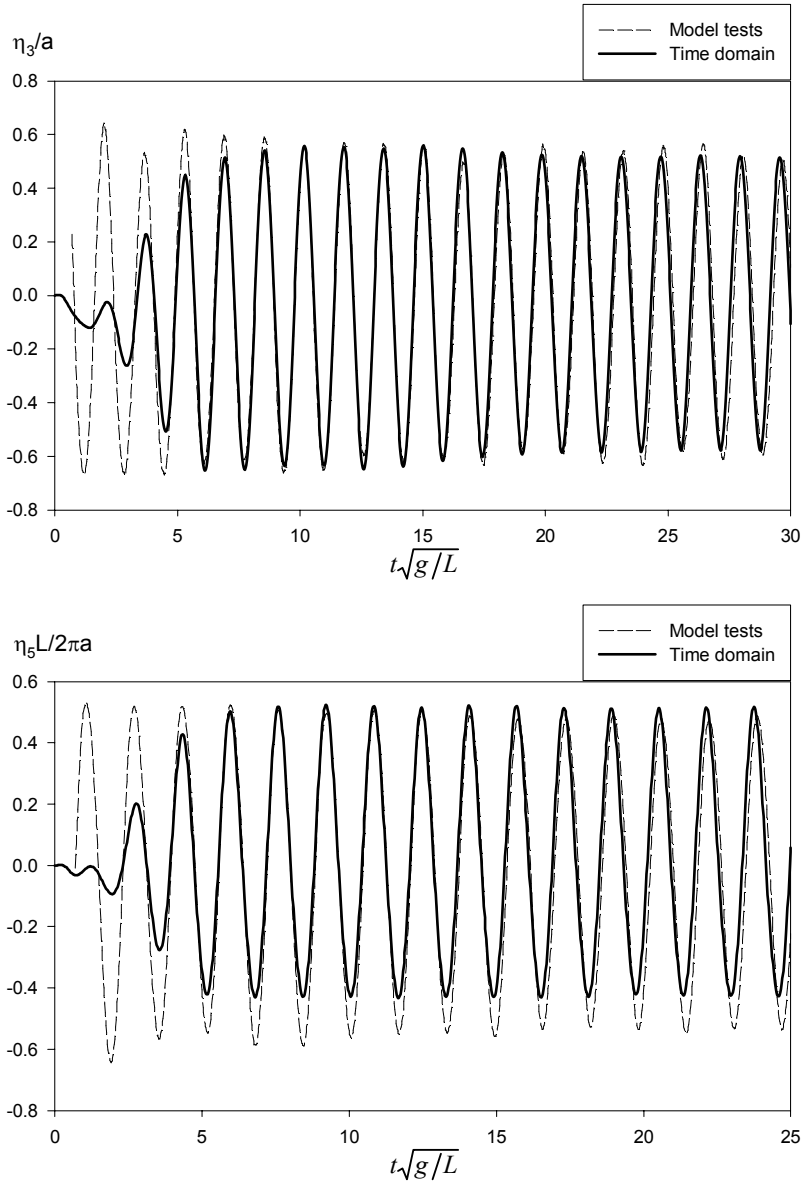

Figure 4.23. Time histories of heave and pitch at Fn = 0.25, $\omega\sqrt{L/g}$ = 2.41 and a/L = 0.013. Body-wave nonlinear solution without the fluid velocity squared term, $0.5|\nabla\Phi|^2 = 0$.

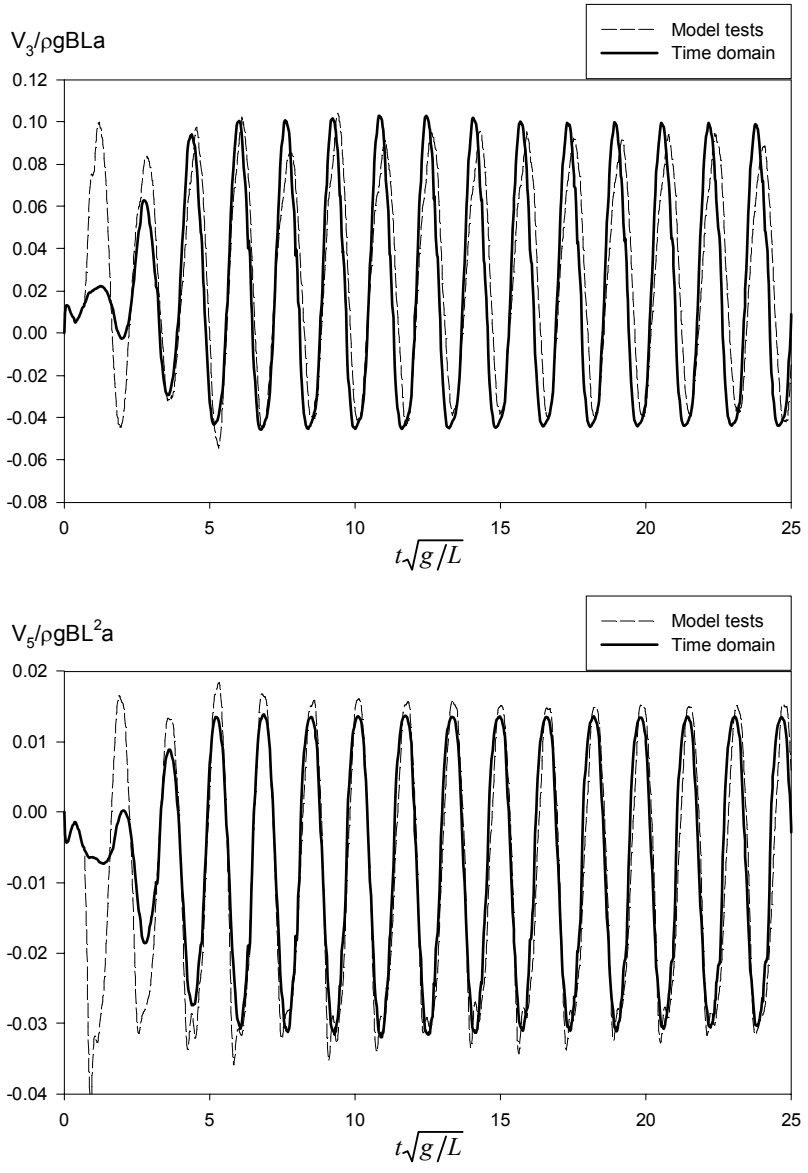

Figure 4.24. Time histories of the shear force and bending moment at Fn = 0.25, $\omega\sqrt{L/g}$ = 2.41 and a/L = 0.013. Body-wave nonlinear solution without the fluid velocity squared term, $0.5|\nabla\Phi|^2 = 0$.

4.5.5 Comparison of the acceleration potential and difference methods

Responses calculated by the acceleration potential and backward difference methods are compared when solving the time derivative of the velocity potential in Bernoulli's equation in this section. Transfer functions are given for heave and pitch and for the shear force and bending moment. The body nonlinear solution was used and the wave amplitude was a/L = 0.006 in the calculation. In the backward difference method, the calculation was carried out using the same parameters as in the acceleration potential method, except that the low-pass filtering was performed for the radiation-diffraction pressure term $-\rho\left(\phi_t + 0.5|\nabla\phi|^2\right)$. This was necessary in order to obtain convergent results for the perturbation velocity potential. The filter characteristic and the cut-off frequency were the same as in the acceleration potential method.

At zero speed, the transfer functions of responses are shown in Figure 4.25. At zero speed, the acceleration potential solution gives a better prediction of the shear force and bending moment than the model test results. For heave and pitch, the differences between the two solutions are quite small.

The two solutions were investigated in more detail by calculating the radiation-diffraction forces of heave, F_{P3}. The radiation-diffraction force is based on the perturbation velocity potential, and the force was determined from the hydrodynamic pressure of $-\rho\left(\phi_t + 0.5|\nabla\phi|^2\right)$. Figure 4.27 presents the heave force F_{P3} based on the acceleration potential and backward difference methods. The heave forces F_{P3} are given with the body nonlinear solution at wave amplitude a/L = 0.006 and at wave frequency $\omega\sqrt{L/g}$ = 2.21 at zero speed. The body linear solution is given as a reference. The time histories shown in the figure are similar in type to those for the cones. When the heave force F_{P3} is negative, the bow is moving downwards into the water. The maximum amplitudes of the acceleration potential and backward difference methods are almost the same. However, the minimum amplitude of the acceleration potential method is greater than of the backward difference method. The amplitudes of the nonlinear heave forces F_{P3} are close to the linear prediction.

The transfer functions of the responses at forward speed Fn = 0.25 are shown in Figure 4.26. The acceleration potential method and the backward difference method give similar results for the pitch, shear force and bending moment. However, the heave motion is predicted better by the backward difference method than the acceleration potential method compared with the model test results.

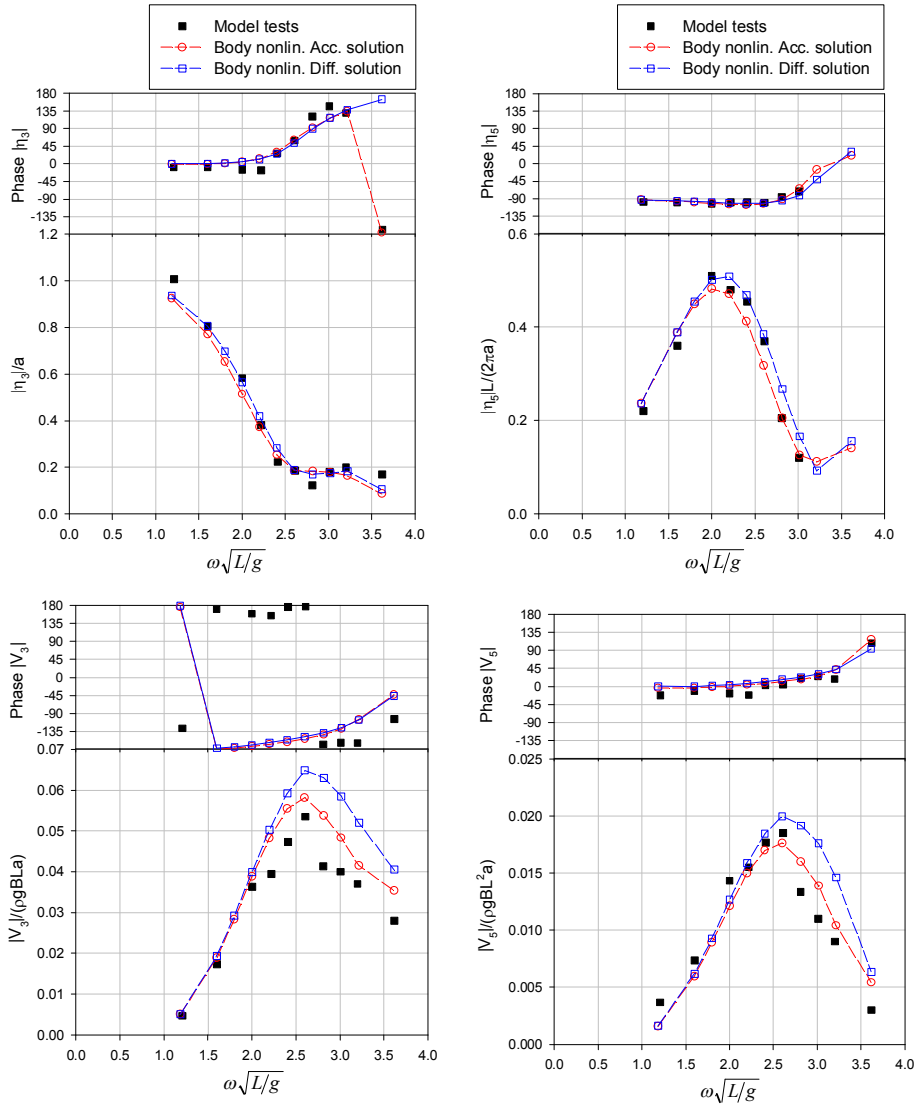

Figure 4.25. Heave, pitch, shear force and bending moment at Fn = 0.0 in head seas calculated with the acceleration potential (Acc. solution) and the backward difference (Diff. solution) methods. The wave amplitude was a/L = 0.006 in the calculation.

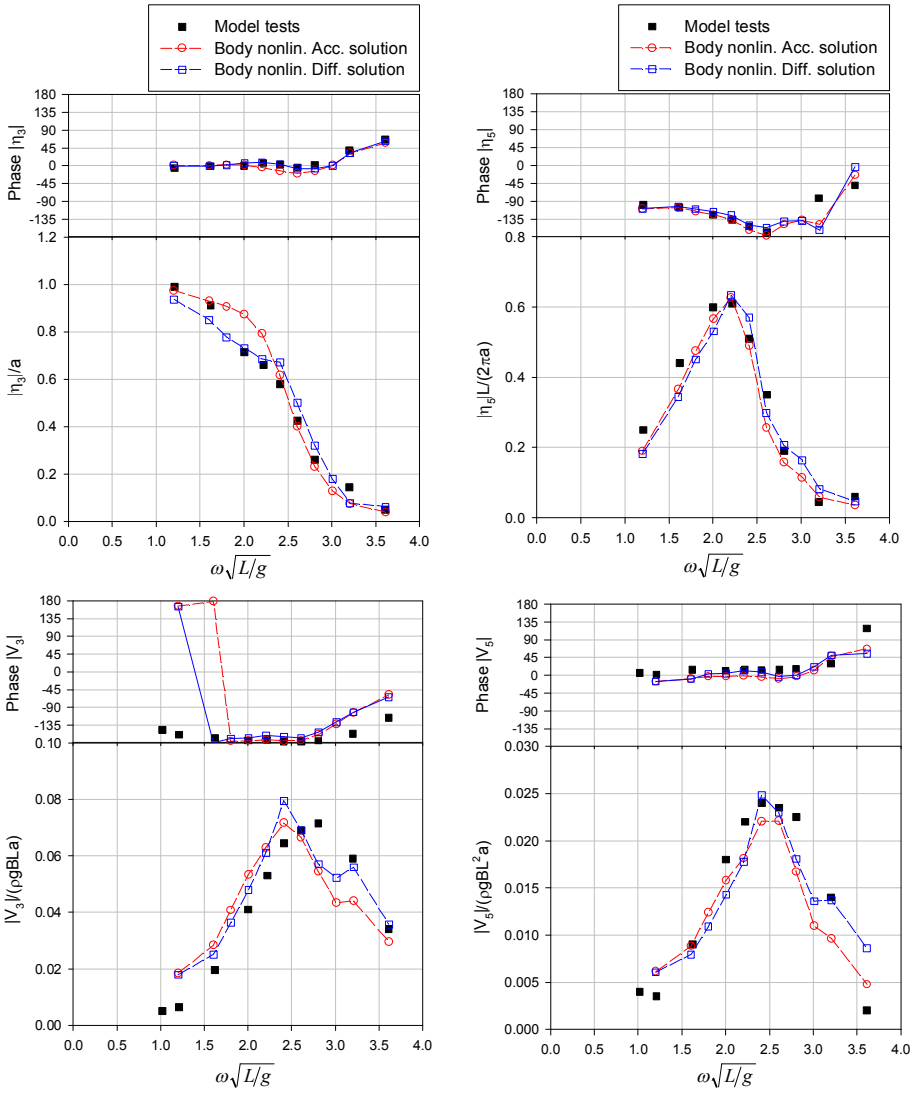

Figure 4.26. Heave, pitch, shear force and bending moment at Fn = 0.25 in head seas calculated with the acceleration potential (Acc. solution) and the backward difference (Diff. solution) methods. The wave amplitude was a/L = 0.006 in the calculation.

The differences in heave at forward speed were further investigated by calculating the radiation-diffraction forces of heave, F_{P3}. The heave forces F_{P3}, based on the acceleration potential and difference methods, are shown in Figure 4.28 at forward speed Fn = 0.25. The heave forces F_{P3} are given with the body nonlinear solution at wave amplitude a/L = 0.006 and wave frequency $\omega\sqrt{L/g}$ = 2.21. The body linear solution is given again as a reference. The acceleration potential method gives similar results for heave force F_{P3} calculated with the body linear and nonlinear solutions. However, heave force F_{P3} calculated with the difference method clearly deviates from the solutions of the acceleration potential method. Heave force F_{P3} calculated with the difference method in the body nonlinear solution also deviates significantly from the body linear solution. The amplitudes of the heave forces F_{P3} obtained with the difference method are considerably smaller in the body nonlinear solution. As the differences between the body linear and nonlinear solutions are big, it is questionable whether the difference method gave convergent results. More detailed investigations showed that the radiation-diffraction force of heave with the difference method has noise due to the $\Delta\phi/\Delta t$ -term and, hence, the prediction for the force was unreliable. The magnitude of the force due to the $\Delta\phi/\Delta t$ -term was small and the radiation-diffraction force of heave consisted almost entirely of the term $\mathbf{U}\cdot\nabla\phi$. One reason for the unreliable results can be the flat bottom stern that induced abrupt changes in the flow when the stern entered the waves. The numerical derivation using the velocity potentials from present and previous time steps gave peaks when the flow pattern changed abruptly. The inaccuracy affected the solutions of source strengths and velocity potentials and was accumulated in the time stepping. Peaks in the difference solution also occurred when the panels changed from wet to dry or from dry to wet. This was shown in connection with studies with cones; see Figure 3.10.

The calculation was also repeated to study whether the acceleration potential and difference methods could give similar results to those of the body linear solution at forward speed. The radiation-diffraction forces of heave, F_{P3}, are shown in Figure 4.29 at forward speed Fn = 0.25. With the body linear solution, both the acceleration potential and difference methods give about the same results. In addition, the time histories of the heave and pitch motions are shown in Figure 4.30 and the shear force and bending moment in Figure 4.31. In the figures, the body linear solutions are shown with the acceleration potential and difference methods. The acceleration potential and difference methods give almost the same results for the responses, and the differences only exist at the beginning of the time histories.

Thus, *the body linear solution* gave about the same prediction for the responses if the acceleration potential or backward difference method was used. Nevertheless, *the body nonlinear solution* gave different results. The solution of the backward difference method applied in this work included noise due to the $\Delta\phi/\Delta t$-term which induced uncertainty in the response predictions for the model test ship. The body nonlinear solution for the radiation-diffraction force of heave clearly also deviated from the body linear predictions if the backward difference method was used. The prediction for the radiation-diffraction force of heave with the backward difference method in the body nonlinear solution was not consistent with the body linear solution. The acceleration potential method gave stable and reliable results for the responses and hydrodynamic forces.

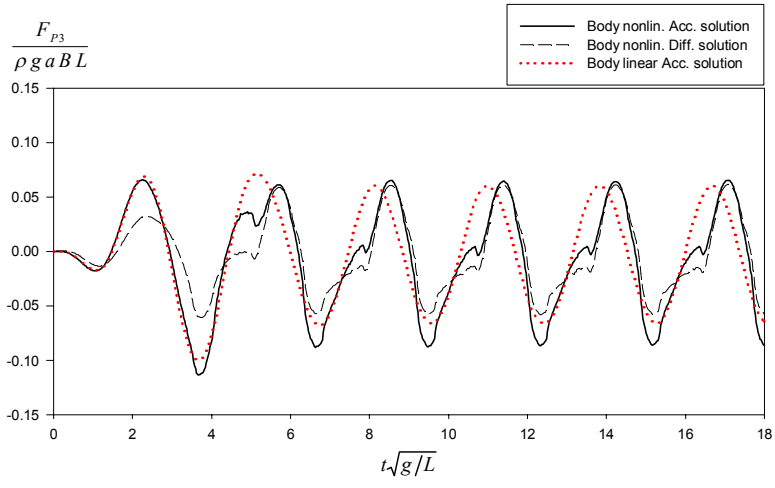

Figure 4.27. Radiation-diffraction force of heave based on the acceleration potential and difference methods. Body nonlinear solution at Fn = 0.0, a/L = 0.006 and $\omega\sqrt{L/g}$ = 2.21. The body linear solution with the acceleration potential method is also given.

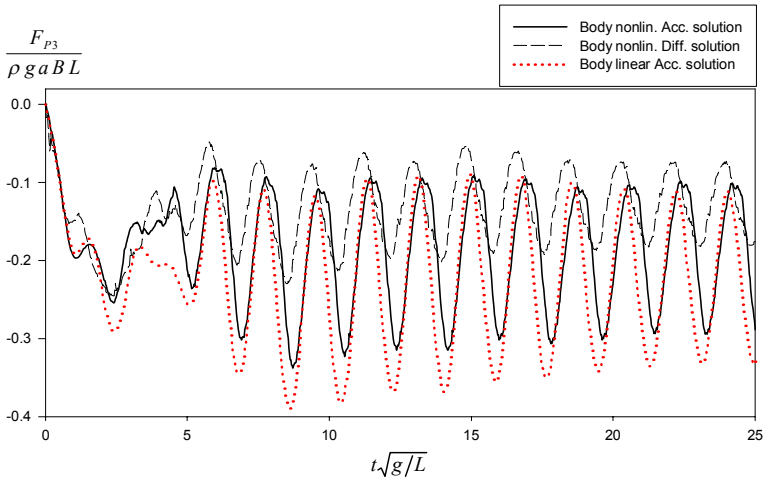

Figure 4.28. Radiation-diffraction force of heave based on the acceleration potential and difference methods. Body nonlinear solution at Fn = 0.25, a/L = 0.006 and $\omega\sqrt{L/g}$ = 2.21. The body linear solution with the acceleration potential method is also given.

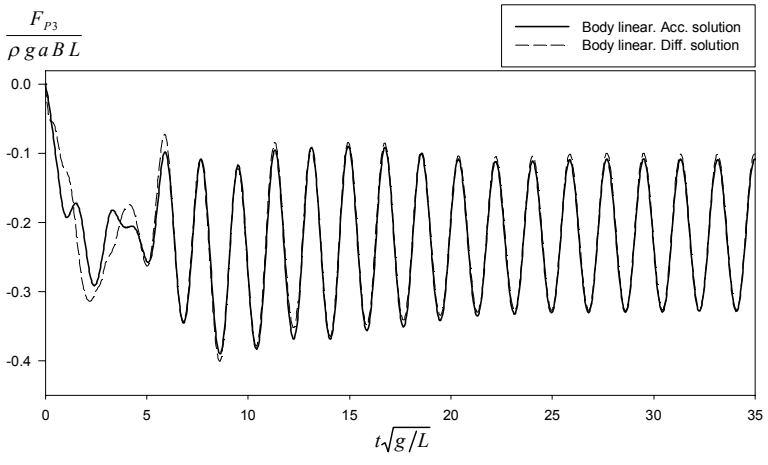

Figure 4.29. Body linear solution for the radiation-diffraction force of heave based on the acceleration potential and difference methods at Fn = 0.25 and wave frequency $\omega\sqrt{L/g}$ = 2.21.

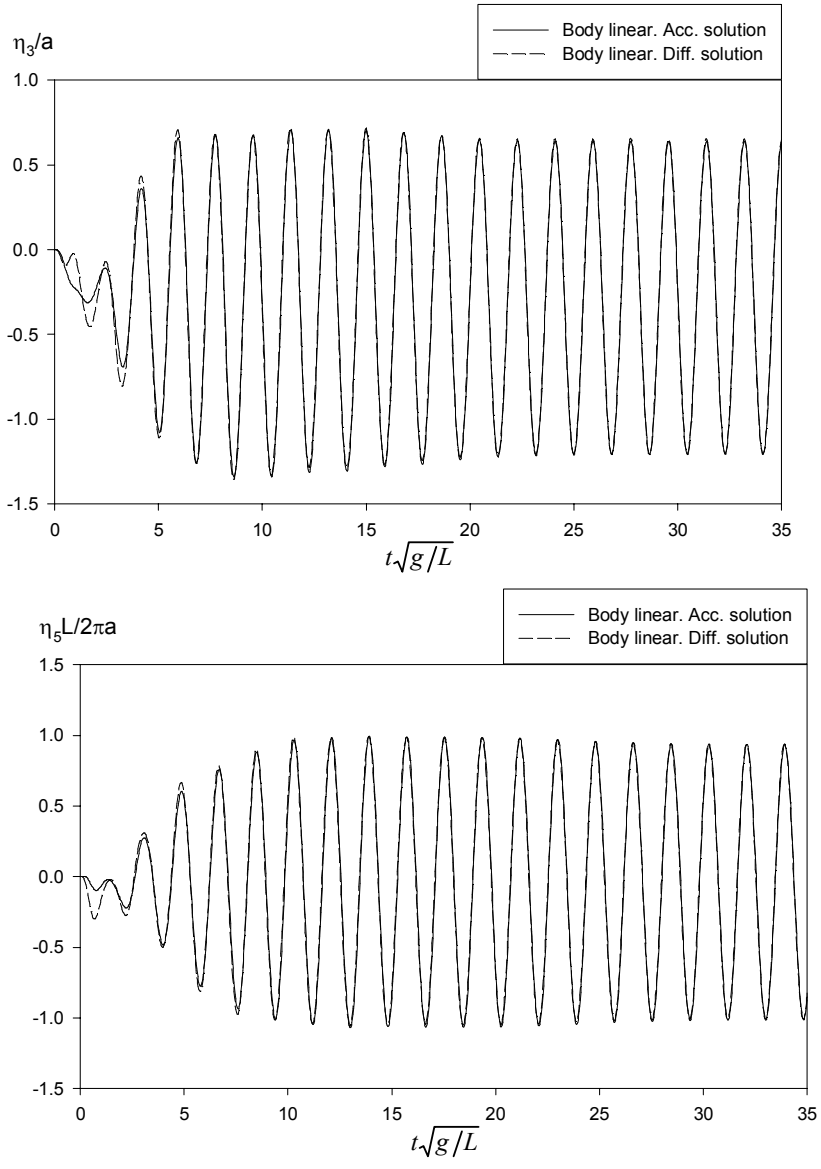

Figure 4.30. Heave and pitch calculated by the acceleration potential and difference methods at $Fn = 0.25$. Body linear solution at $\omega\sqrt{L/g} = 2.21$.

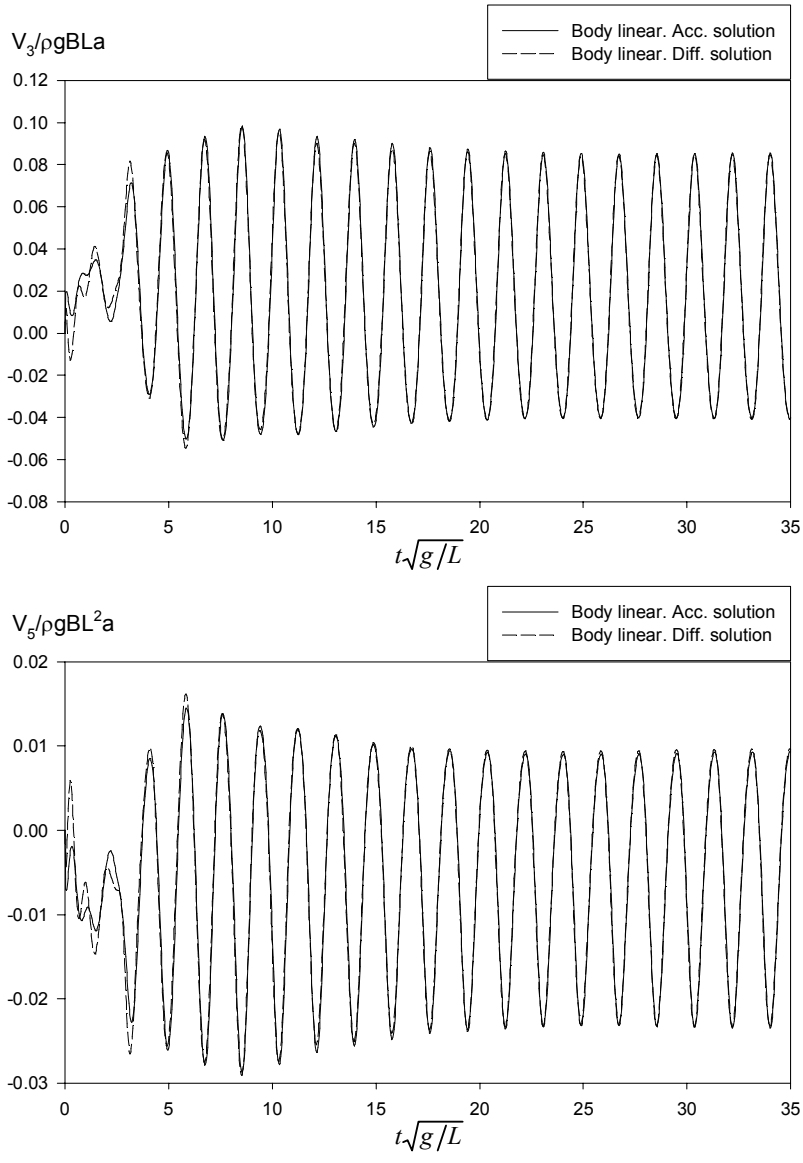

Figure 4.31. Shear force and bending moment calculated by the acceleration potential and difference methods at Fn = 0.25. Body linear solution at $\omega\sqrt{L/g}$ = 2.21.

4.5.6 Nonlinearities of responses

The nonlinearities in the hull girder loads are studied with the model test and the calculated results. The studies are presented with transfer functions, pseudo transfer functions and higher order harmonic components of responses at different wave amplitudes. The model tests and calculations were carried out using three different wave amplitudes in regular head waves. The wave amplitudes were a/L = 0.006, a/L = 0.013 and a/L = 0.019. The calculated results are compared with the model test results.

At zero speed, the transfer functions of the responses at the three wave amplitudes are shown in Figure 4.32 for heave, pitch, shear force and bending moment. The responses were calculated with the body-wave nonlinear solution. The body linear solution is also shown in the figures. The transfer functions of heave and pitch are practically the same at the three wave amplitudes. The shear force and bending moment increase slightly if the wave amplitude increases. The body linear solution gives the lowest prediction for the shear force and bending moment. However, the calculated responses are close to the model test results. Thus, the calculation method gives a good prediction for the first harmonic component of the responses at zero speed. In the model tests, the transfer functions of heave, pitch, shear force and bending moment are close to each other at the three different wave amplitudes. The transfer functions of the model tests at the three wave amplitudes are shown in Figure 4.9. Hence, based on the model test results and the calculated results the nonlinearities in the first harmonic components are relatively small at zero speed.

At forward speed, the transfer functions of heave, pitch, shear force and bending moment are shown in Figure 4.33 at wave amplitudes a/L = 0.006 and 0.013. The pitch is slightly higher at the higher wave amplitude, but the shear force and bending moment are almost the same at the two wave amplitudes. Heave clearly has higher amplitudes compared with the model test results. The calculated heave amplitude is also higher at a/L = 0.013 than at the lower wave amplitude a/L = 0.006. The high amplitudes in the calculated heave motion have already been discussed in Section 4.5.3 where the transfer function based on the body linear solution was given. The body linear solution gave high amplitude peaks for the responses around the heave resonance. It was concluded that the calculation method cannot take into account the steady flow at the stern region properly if the stern is a flat bottom stern close to the free surface. However, the calculation method takes into account the instantaneous floating position of the ship if the body nonlinear solution is used. This improves the results compared with the body linear solution as the uncertainties in the calculation of the differences in the

responses at different wave amplitudes do not necessarily mean that the first harmonic components of the responses are nonlinear with respect to the wave amplitude. It should also be noted that the model test results for the first harmonic components of the responses were close to each other at the wave amplitudes a/L = 0.006 and 0.013; see Figure 4.10.

At the wave amplitude a/L = 0.019 and forward speed Fn = 0.25, the transfer functions of heave, pitch, shear force and bending moment are shown in Figure 4.34. The heave is clearly overestimated compared with the model test results. The calculated predictions for the shear force and bending moment clearly also deviate from the model test results at the heave resonance. One reason for this deviation is the high heave amplitude from the calculation, but the discrepancy may also indicate that the motions at the high wave amplitude are too violent for the calculation method.

In the model tests, at the highest wave amplitude at forward speed Fn = 0.25, the motions of the ship model were large and deck wetness and bow slamming occurred. A large part of the bow was out of the waves when the relative motions were greatest around the resonance of the heave. In the calculation, the time histories included noise, and the prediction for the perturbation velocity potential was irregular, including high single peaks from time to time. The large motions and, particularly, the large relative motions with respect to the free surface elevation were discussed in Section 4.5.3. It was concluded that free surface elevation due to the steady and unsteady flow, especially at the stern, may have an effect on the calculated predictions. The calculation method cannot take into account the flow and waves at the stern properly if a large part of the stern varies between wet and dry. This can give incorrect predictions for the flow in the calculation. Furthermore, it was shown in Section 4.5.4 that omitting the fluid velocity squared term can improve the calculation results. Bernoulli's equation is then consistent with the linear free surface condition. Hence, the same approach was tried here and the calculation was repeated excluding the fluid velocity squared term from Bernoulli's equation. The responses calculated without the fluid velocity squared term are shown in Figure 4.34. Without the fluid velocity squared term, the heave amplitude clearly decreases at the resonance, and the heave amplitudes are close to the amplitudes calculated at the lower wave amplitudes that were presented in Figure 4.33. The pitch is also somewhat lower and close to the results of the lower wave amplitude a/L = 0.013. The calculated shear force and bending moment without the fluid velocity squared term are close to the model test results, but there is still some scatter in the calculation results, especially in the shear force. However, the responses are in line with the model test results and with the calculated results that were determined at the lower wave amplitudes. The results pre-

sented below were calculated without the fluid velocity squared term at the highest wave amplitude $a/L = 0.019$ when the ship had a forward speed of $Fn = 0.25$.

The transfer functions only include the first harmonic component of the response. Hence, the transfer functions do not necessarily give the whole picture of the responses, which can also include nonlinearities due to the higher order harmonic components or due to the mean shift of the responses. For these reasons, the harmonic analysis was carried out to obtain an insight into the magnitudes of the higher order components in the responses. The relative contribution of the three lowest harmonic components and the mean with respect to the first harmonic component are shown in Figure 4.35 for the shear force and the bending moment at zero speed. The second harmonic component is in the order of 5% to 10% of the first harmonic component for the bending moment. For the shear force, the contribution is less, at about 5%. The third harmonic component is small. The mean shift in the shear force and bending moment is significant. At forward speed $Fn = 0.25$, the relative contribution of the harmonic components and mean are presented in Figure 4.36. The second harmonic component is in the order of 10% to 15% of the first harmonic component for the shear force and bending moment. The relative contribution of the third harmonic component is less than 5% of the first harmonic component. The mean shift is significant. The calculated mean is close to the model test results. At the lowest wave frequencies the relative magnitude of the mean is large but the amplitudes of the responses are small.

In addition to the harmonic analysis, the pseudo-transfer functions were determined for the responses. The pseudo-transfer functions were defined directly from the time history series. The amplitudes were analysed separately from the maximum and minimum peaks. The peaks in the pseudo transfer functions are the average of the maximum or minimum peaks obtained from the time series. The same procedure was applied when analysing the model test data.

At zero speed, the pseudo-transfer function for the shear force and bending moment is shown in Figure 4.37. In the sagging condition, the bending moment is negative (minimum) and the shear force is positive (maximum). In the hogging, the sign of the responses is the opposite. The responses in the figures were determined using the body-wave nonlinear solution and the body nonlinear solution. The comparison of these two methods gives an insight into the nonlinear effects due to the additional Froude-Krylov and hydrostatic forces and moments that are determined up to the incoming wave elevation. The body-wave nonlinear solution gives a better prediction for the bending moment than the body nonlinear solution compared with the model test results. For the shear force, the result is not so clear. However, the effect due to the additional Froude-Krylov and hydrostatic

forces and moments is not large. Although the additional contribution is small, this does not mean that the total contribution due to the Froude-Krylov and hydrostatic forces and moments is small in the nonlinear loads. Only the effect of the additional part is small. The additional force and moment is due to the Froude-Krylov and hydrostatic pressure from the mean water level up to the incoming wave elevation. Most of the nonlinear Froude-Krylov and hydrostatic forces and moments are already included in the pressure because they are calculated at the actual floating position of the ship. This explains a large part of the nonlinearities in the sagging and hogging loads.

The pseudo transfer functions for the shear force and bending moment at forward speed $Fn = 0.25$ are presented in Figure 4.38. The body-wave nonlinear solution gives a better prediction for the sagging bending moment than the body nonlinear solution. For the hogging bending moment, the body-wave nonlinear solution gives somewhat lower peaks than the body nonlinear solution. For the shear force, the maximum peaks are predicted slightly better by the body-wave nonlinear solution than the body nonlinear solution.

Furthermore, the maximum and minimum peaks of the bending moment and the contribution of the steady bending moment at forward speed $Fn = 0.25$ are presented in Figure 4.39. The figure is given in a dimensional form in order to gain an insight into the contribution of the steady bending moment to the sagging and hogging bending moment. The maximum and minimum peaks are given for two wave amplitudes, $a/L = 0.006$ and 0.013 ($a = 1$ m and 2 m). It can be noted that the mean of the maximum and minimum at the longest and shortest waves is about the same as the steady bending moment in calm water. The steady bending moment was presented in Section 4.4, in Figure 4.8. The contribution of the steady bending moment also explains a large part of the differences between the sagging and hogging bending moment at the lower wave amplitude. However, the contribution of the steady bending moment is small at the higher wave amplitude. Hence, a large part of the mean of the harmonic components is explained by the steady part at low wave amplitudes. At higher wave amplitudes, the steady contribution is small and a large part of the differences in sagging and hogging is due to the ship motions in waves. In high waves, the wave loads induce larger loads on the hull girder when the bow enters the waves than when the bow moves out of the waves. Part of the nonlinearities is due to the higher order harmonic components, though their contribution is relatively small compared with the mean of the wave loads at the encounter frequency of the waves. At zero speed, the ship motions in waves also explain the major part of the nonlinearities. The relative motions were also larger at the stern at zero speed than at the forward speed, giving an additional contribution to the differences in sagging and hogging loads.

Hence, the actual floating position of the ship with respect to the waves at the encounter frequency explains a large part of the nonlinearities and differences in the sagging and hogging responses in high waves.

The effect of the wave steepness on the sagging and hogging loads is shown in Figures 4.40 and 4.41. The maximum and minimum peaks of the shear force and bending moment as a function of the non-dimensional wave number *ka* (*ka* = $(\omega^2/g)a$) are presented in Figure 4.40 at zero speed. At forward speed *Fn* = 0.25, the maximum and minimum peak amplitudes are presented in Figure 4.41. The non-dimensional wave number is the same as the wave slope of the regular wave. The peak amplitudes are given for three wave frequencies: $\omega\sqrt{L/g}$ = 2.01, 2.41 and 2.81. For each wave frequency, the responses from the calculation and from the model tests were determined at three wave amplitudes: *a*/*L* = 0.006, 0.013 and 0.019. Hence, the responses are also given at three non-dimensional wave numbers *ka* at the given wave frequency. In the figures, the difference in the sagging and hogging bending moment and shear force is clear. At zero speed, the differences in the shear forces and bending moments at different wave slopes are not big. At forward speed, the shear forces and bending moments deviate somewhat at the different wave slopes. The differences are, to some extent, greater at the small wave frequencies $\omega\sqrt{L/g}$ = 2.01 and 2.41 than at the highest wave frequency $\omega\sqrt{L/g}$ = 2.81. The trends of the sagging and hogging loads are similar in the model test and calculated results. At zero speed, the agreement with the model test results is good, and it is relatively good at forward speed *Fn* = 0.25.

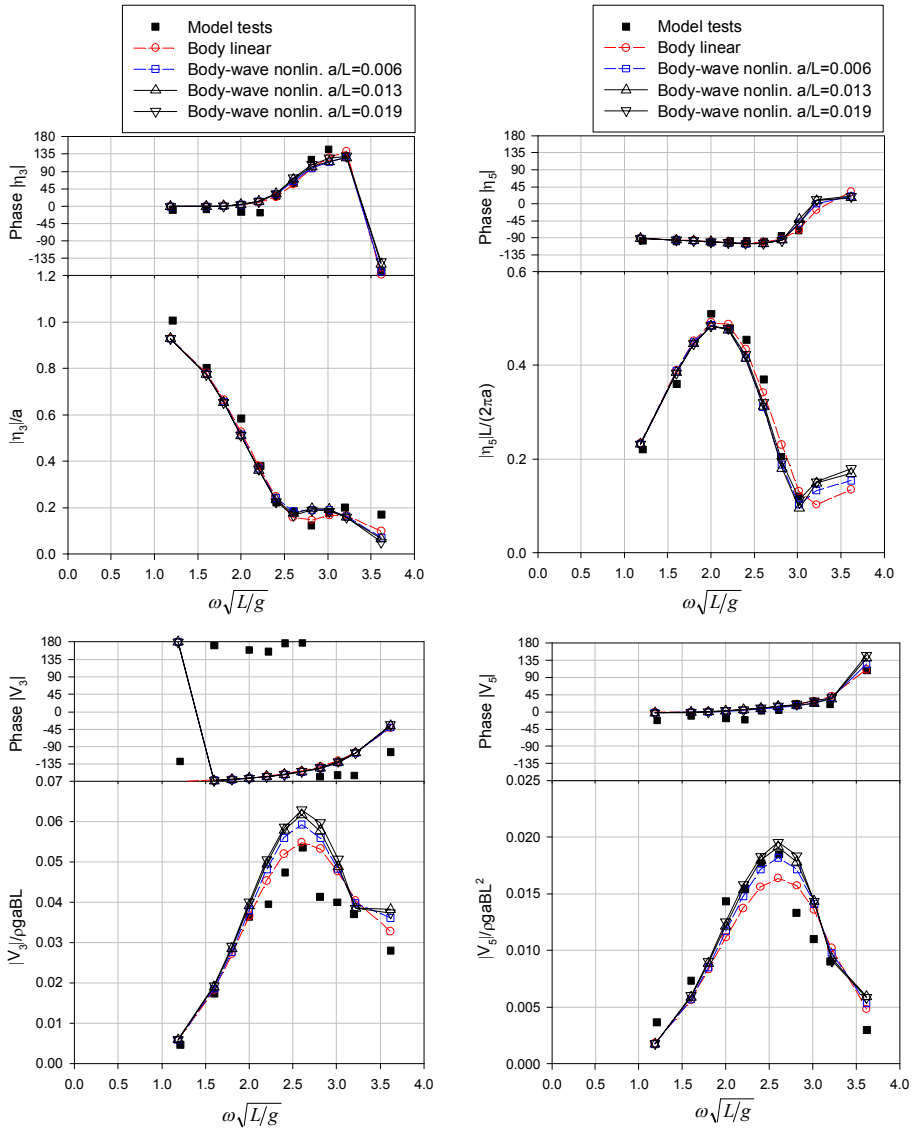

Figure 4.32. Transfer functions of heave, pitch, shear force and bending moment at Fn = 0.0. The body-wave nonlinear solutions are given at three different wave amplitudes.

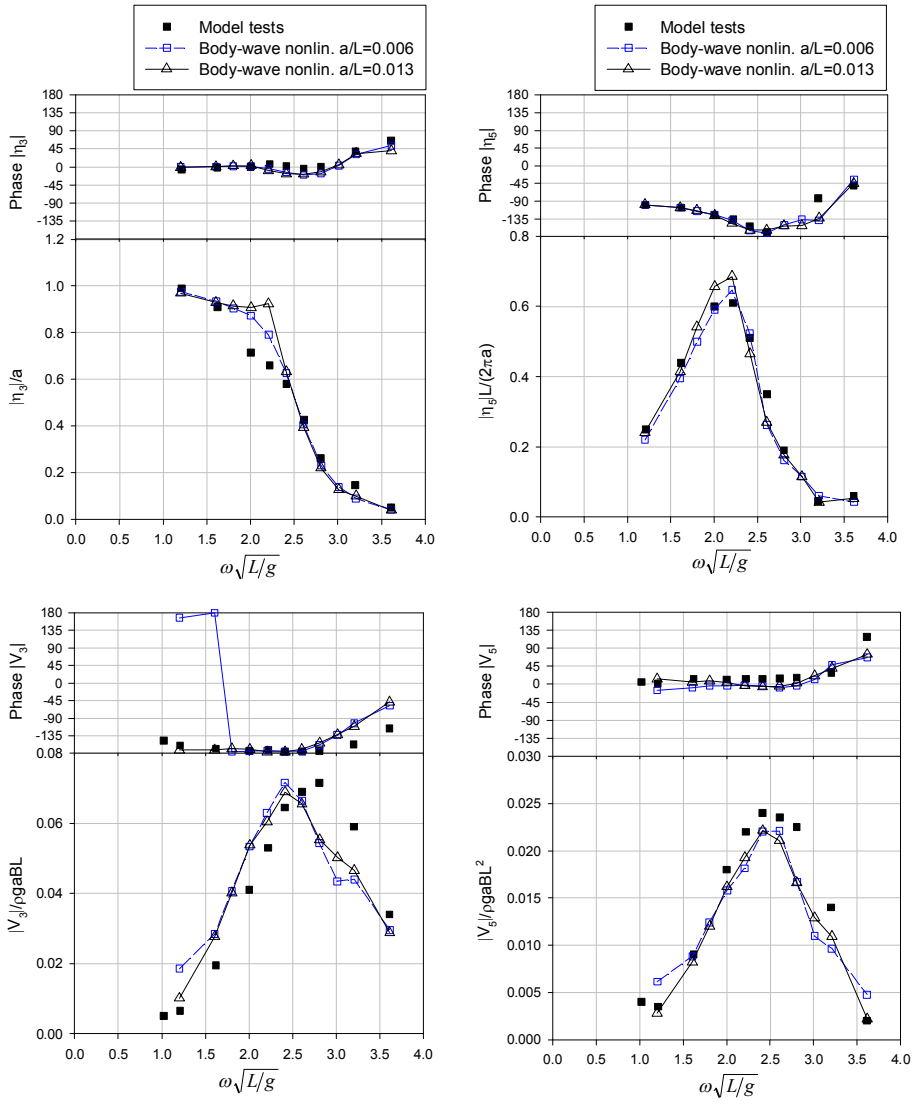

Figure 4.33. Transfer functions of heave, pitch, shear force and bending moment at Fn = 0.25. The body-wave nonlinear solutions are given at wave amplitudes a/L = 0.006 and a/L = 0.013.

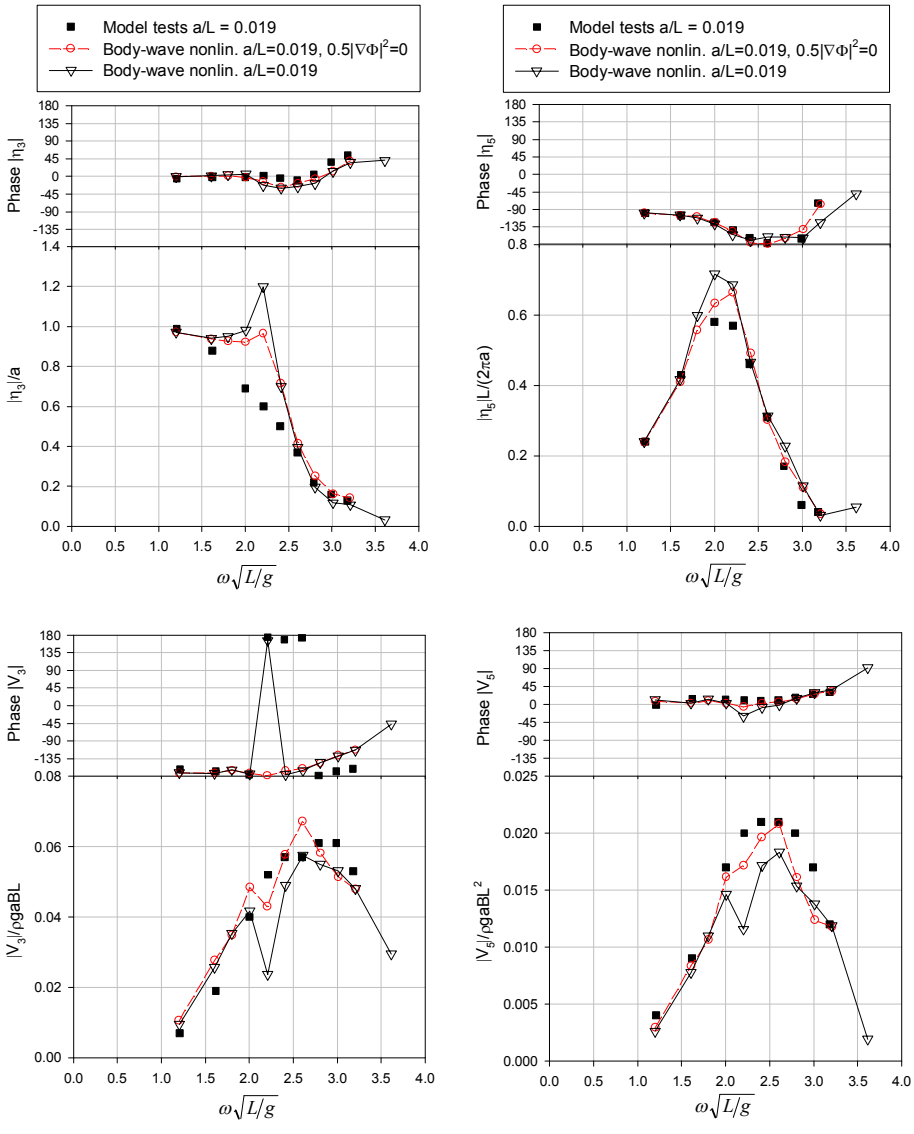

Figure 4.34. Transfer functions of heave, pitch, shear force and bending moment at $Fn = 0.25$. The body-wave nonlinear solutions are given at wave amplitude $a/L = 0.019$ with and without the fluid velocity squared term ($0.5|\nabla\Phi|^2 = 0$).

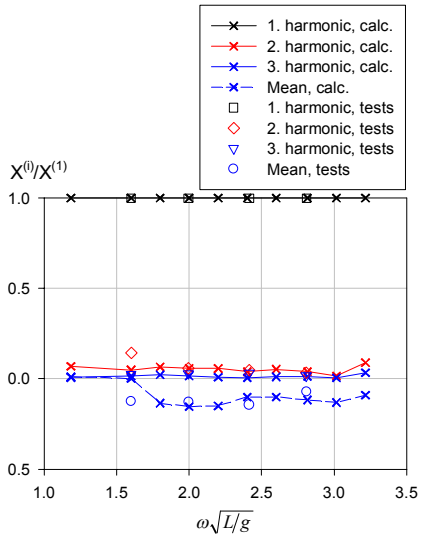

Shear force V_3

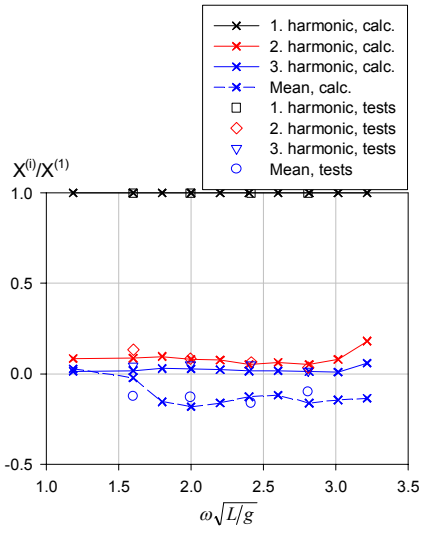

Bending moment V_5

Figure 4.35. Relative contributions of the harmonic components at Fn = 0.0. The wave amplitude in the model tests and calculation was a/L = 0.013. The calculated results are based on the body-wave nonlinear solution. Notice that the mean of the shear force is positive.

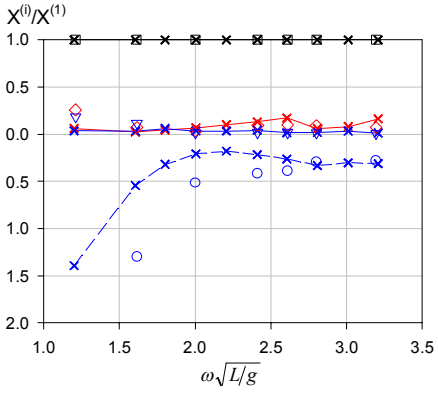

Shear force V_3

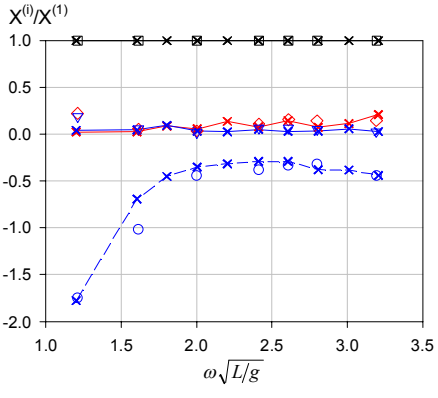

Bending moment V_5

Figure 4.36. Relative contributions of the harmonic components at Fn = 0.25. The wave amplitude in the model tests and calculation was a/L = 0.013. The calculated results are based on the body-wave nonlinear solution. Notice that the mean of the shear force is positive. See the legend of the symbols in Figure 4.35.

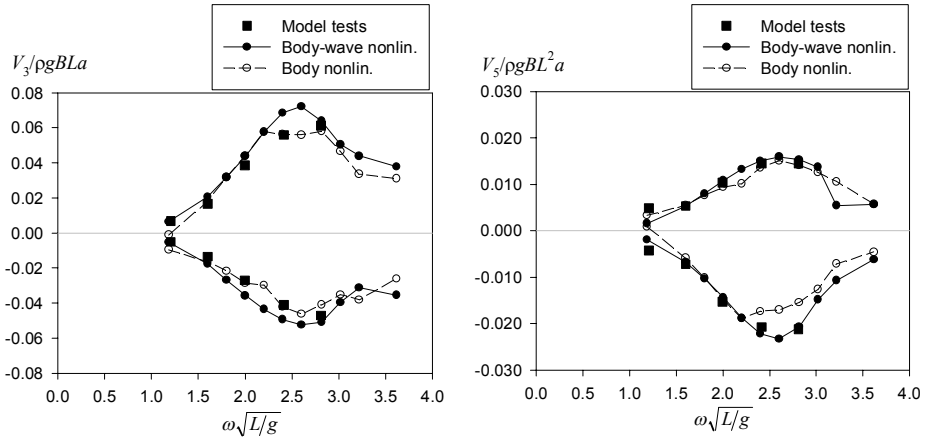

Figure 4.37. Maximum and minimum peaks of the shear force and bending moment at $Fn = 0.0$. The wave amplitude in the model tests and calculation was $a/L = 0.013$. The calculation was carried out using the body nonlinear and the body-wave nonlinear solutions.

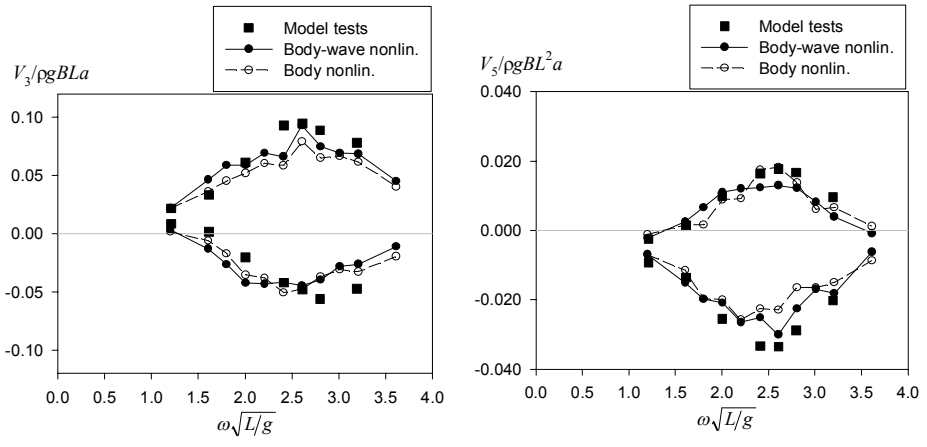

Figure 4.38. Maximum and minimum peaks of the shear force and bending moment at $Fn = 0.25$. The wave amplitude in the model tests and calculation was $a/L = 0.013$. The calculation was carried out using the body nonlinear and the body-wave nonlinear solutions.

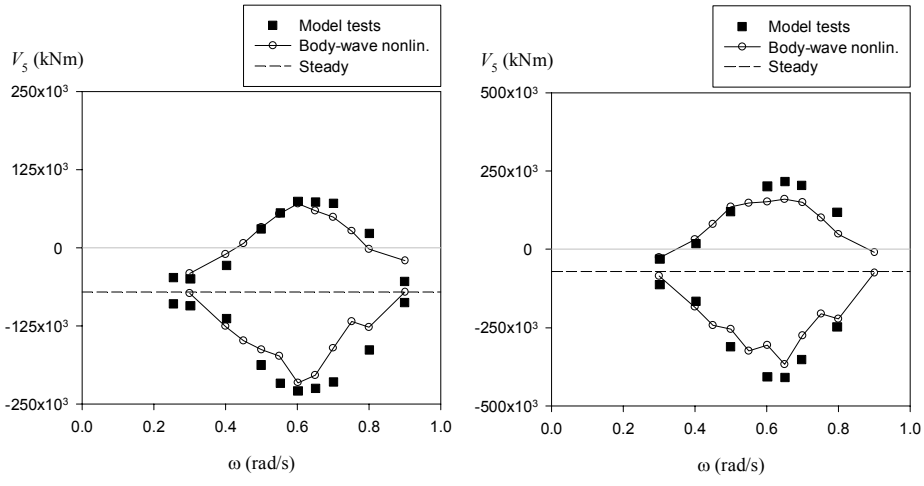

a = 1 m (a/L = 0.006) a = 2 m (a/L = 0.013)

Figure 4.39. Maximum and minimum peaks of the bending moment and the contribution of the steady bending moment at Fn = 0.25. The calculation was carried out using the body-wave nonlinear solution. The given steady bending moment is based on the model test results.

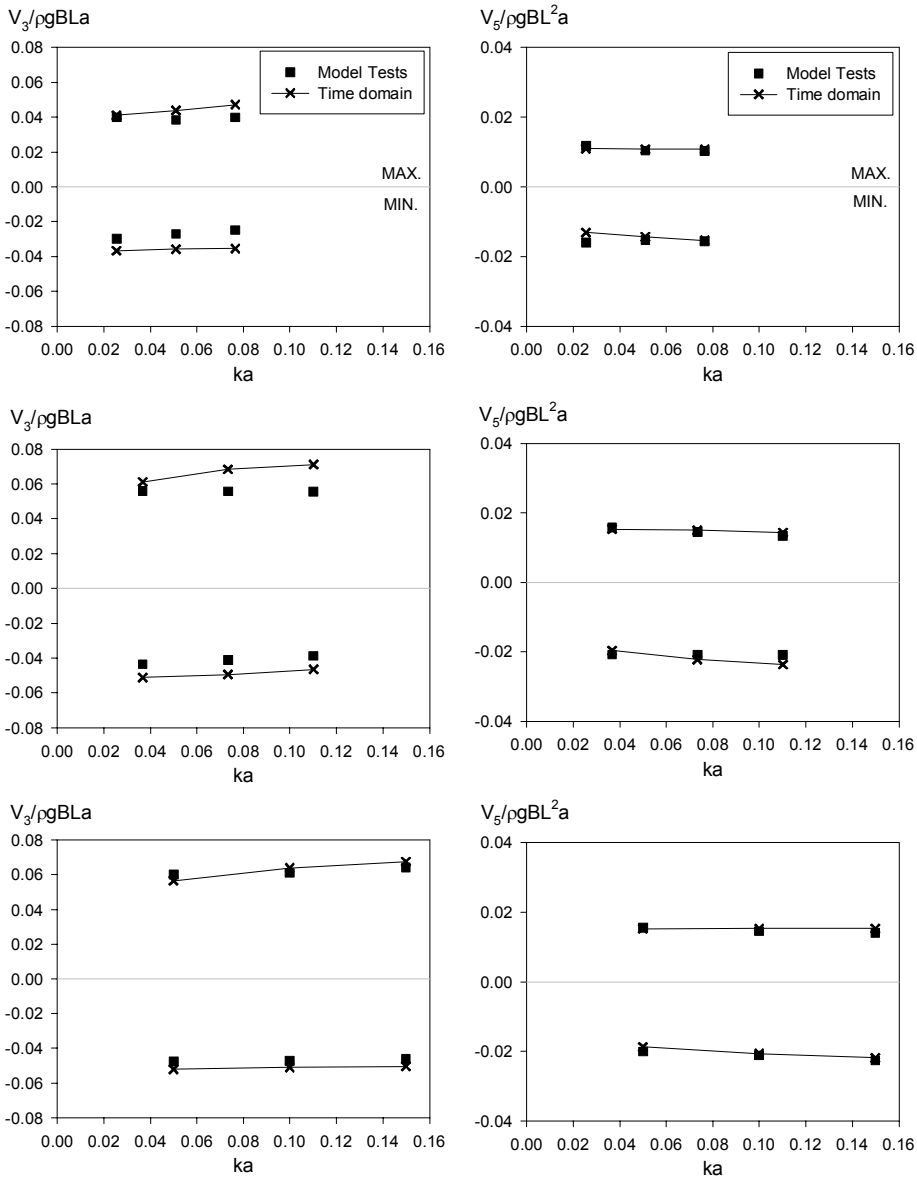

Figure 4.40. Shear force and bending moment as a function of the non-dimensional wave number *ka* at *Fn* = 0.0. The calculation was carried out using the body-wave nonlinear solution at wave frequencies $\omega\sqrt{L/g}$ = 2.01, 2.41 and 2.81 (from top to bottom).

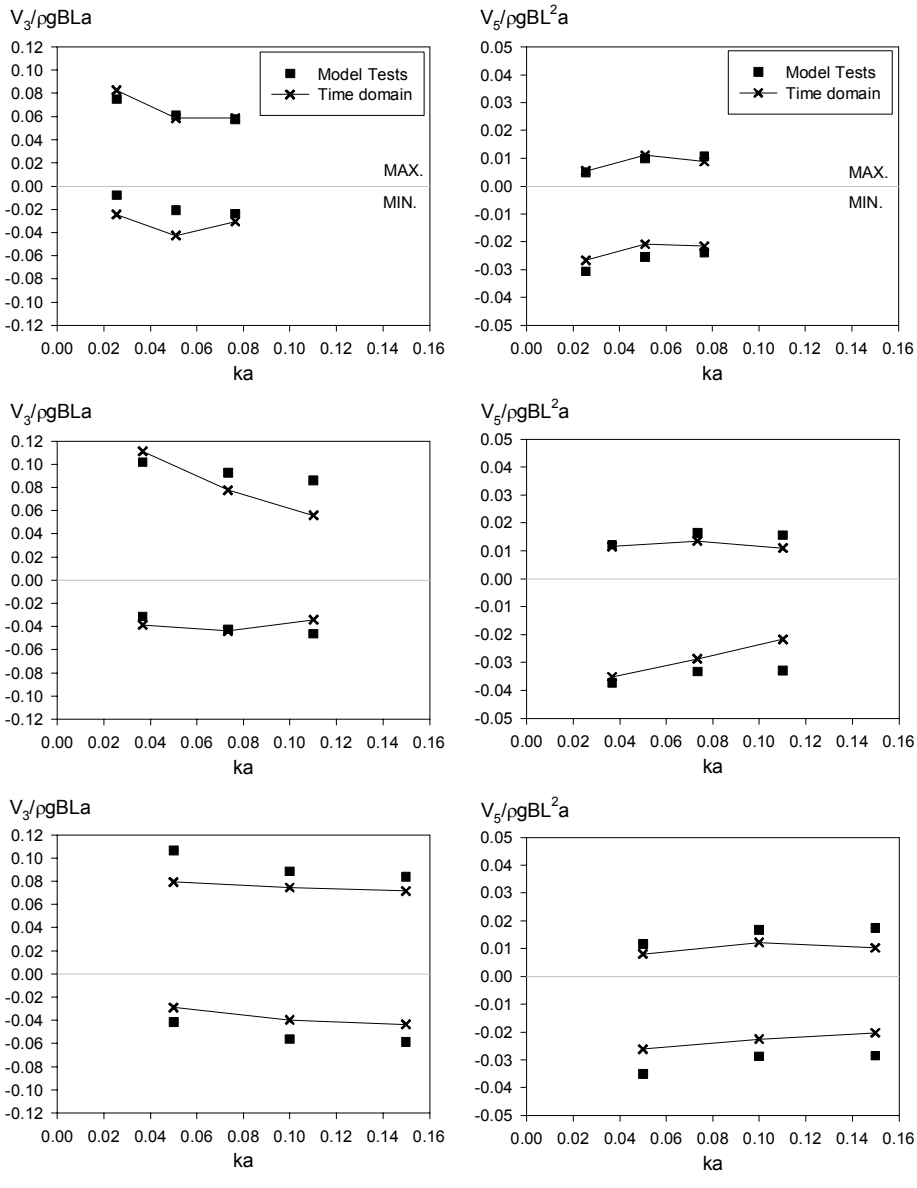

Figure 4.41. Shear force and bending moment as a function of the non-dimensional wave number *ka* at *Fn* = 0.25. The calculation was carried out using the body-wave nonlinear solution at wave frequencies $\omega\sqrt{L/g}$ = 2.01, 2.41 and 2.81 (from top to bottom).

4.6 Results in irregular waves

Model tests of the RoPax ship were carried out in different sea states in irregular head waves at forward and zero speeds. In this work, calculated responses and a comparison with the model test results are presented in sea stets where the significant wave heights are H_s = 5 m and H_s = 9 m at forward speed Fn = 0.25 and at zero speed, respectively. The results are given as statistical quantities, response spectra and peak distributions of responses. The responses are the heave and pitch motions and the vertical shear force at fore ship and the vertical bending moment at midship.

In the model tests and calculations, the irregular waves were generated using the modified Pierson-Moskowitz wave spectrum (ISSC wave spectrum). The wave spectrum can be expressed as follows (ITTC, 2002):

$$S_w(\omega) = 0.11 H_s^2 \left(\frac{2\pi}{T_1}\right)^4 \frac{1}{\omega^5} \exp\left[-0.44\left(\frac{2\pi}{T_1}\right)^4 \frac{1}{\omega^4}\right], \tag{4.2}$$

where T_1 is the mean wave period. The mean period and the peak period of the wave spectrum, T_p, can be given with the zero crossing period T_z as follows:

$$T_1 = 1.086 T_z \tag{4.3}$$

$$T_p = 1.408 T_z \tag{4.4}$$

The irregular long-crested waves were described as a sum of regular wave components with different amplitudes and phases. In this work, the linear wave theory is used and the irregular waves were generated with the following equation:

$$\varsigma(t) = \sum_{j=1}^{M} \mathrm{Re}\left\{ a_j e^{-\mathrm{i}\left(k_j x \cos\chi + k_j y \sin\chi\right)} e^{\mathrm{i}\left(\omega_j t + \varepsilon_j\right)} \right\}, \tag{4.5}$$

where M is the number of the regular wave components. The phases ε_j were a set of uniformly distributed random numbers in the range 0 ... 2π. The wave amplitude was determined from the wave spectrum $S_w(\omega)$:

$$a_j = \sqrt{2 S_w(\omega_j) \Delta\omega_j} \tag{4.6}$$

In order to obtain non-repeating random seas of arbitrary length, the frequencies ω_j of the harmonic wave components were chosen at random in each narrow

frequency band, i.e. there was an equal probability of ω_j having any value in the frequency range $\omega_{cj} \le \omega_j \le \omega_{cj+1}$ where ω_{cj} is the corner frequency of the frequency band. The time history of the irregular wave was generated in the same way in the model tests and the calculation.

At zero speed, the model test and calculated results are given in sea state H_s = 9.0 m where the zero crossing period was T_z = 10.5 s (T_p = 14.8 s). At forward speed Fn = 0.25, the sea state was H_s = 5.0 m and T_z = 8.5 s (T_p = 12.0 s). The duration of the irregular sea states in the time domain calculation was 1 h 15 min in both sea states H_s = 5.0 m and H_s = 9.0 m. In the model tests, the durations of the sea states were 1.6 hours and 0.6 hours in the sea states H_s = 9 m and H_s = 5 m, respectively. In the model tests, the numbers of encountered waves were approximately 510 and 370 in the sea states H_s = 9 m and H_s = 5 m, respectively.

In the calculation, the coarse panel mesh of the ship was used and the calculation was based on the body-wave nonlinear solution. The calculation parameters were the same as in the regular wave analyses; see Section 4.3. However, the fluid velocity squared term was excluded from Bernoulli's equation at forward speed Fn = 0.25. The reason for excluding the term was explained in Section 4.5.6. Examples of the time histories of the shear force and bending moment in irregular waves are given in Figure 4.42.

The mean and standard deviation of the responses are shown in Tables 4.2 and 4.3 at zero speed and forward speed Fn = 0.25, respectively. The standard deviation is $\sigma_x = \sqrt{\sigma_x^2}$ where the variance σ_x^2 of the process is defined as follows

$$\sigma_x^2 = \frac{1}{n-1}\sum_{i=1}^{n}(x_i - \bar{x})^2 \,. \tag{4.7}$$

In the above equation, the mean of the process is $\bar{x}$ and the number of samples is n.

At zero speed in the sea state H_s = 9 m, the standard deviations of heave and pitch in the calculation and model tests are close to each other. The standard deviation of the bending moment is the same. However, the shear force is about 20% bigger in the calculation than in the model tests. In regular waves, the calculated transfer function of the shear force is located at smaller wave frequencies than in the model tests. The peak frequency of the wave spectrum is about $\omega\sqrt{L/g}$ = 1.7 and exists at the frequencies at which the differences in the amplitudes were larg-

est. Thus, the shear force has higher amplitudes at the wave peak frequency in the calculation than in the model tests.

At the forward speed in the sea state H_s = 5 m, the standard deviation of the heave motion is about 15% greater in the calculation than in the model tests. The standard deviation of the pitch is about the same. The shear force is about 10% bigger and the bending moment 10% smaller in the calculation than in the model tests. The mean of the heave is of the same order of magnitude as the sinkage of the ship in calm water at forward speed Fn = 0.25.

The exceedance probabilities of the wave crests and troughs are shown in Figure 4.43 in the sea states H_s = 5 m and H_s = 9 m. The wave spectra are presented in Figure 4.44. The negative minimum peaks are given as absolute values. In the calculation results, the crests and troughs of the wave are close to each other. However, the maximum peaks are larger than the minimum peaks in the model tests. Hence, the waves in the model tests were sharper at the crests and the troughs were smoother giving an asymmetric shape for the irregular waves. However, the frequency contents of the wave spectra are about the same in the model tests and calculation.

At zero speed, the exceedance probabilities of heave, pitch, shear force and bending moment are presented in Figure 4.45 in the sea state H_s = 9 m. The response spectra are shown in Figure 4.46. The peak distributions of heave and pitch follow the model test results well. The sagging bending moment deviates at small exceedance probability levels from the model test results. In the sagging condition, the bending moment is negative (minimum) and the shear force is positive (maximum). The response spectra of the motions and the bending moment from the time domain method are close to the model test results. Furthermore, the peak distribution of the shear force is higher in the sagging condition and there are also differences in the hogging condition. The same is also visible in the response spectrum of the shear force, which is at a higher level in the calculation than in the model tests. The differences can explain the different location of the maximum shear forces on the frequency band. As stated above, the shear force has higher amplitudes at the wave peak frequency in the calculation than in the model tests.

At forward speed Fn = 0.25, the exceedance probabilities of heave, pitch, shear force and bending moment are shown in Figure 4.47 in the sea state H_s = 5 m. The response spectra are shown in Figure 4.48. The peaks of the minimum heave from the calculation are at a somewhat higher level than the model test minimum peaks. The overestimated heave in the calculation can also be seen in the response

spectrum of heave. The maximum and minimum peaks of pitch are predicted well by the calculation. The frequency content of the pitch in the model tests and calculation are also in good agreement with each other. The peak distributions of the shear force and bending moment in the sagging condition are quite close to the model test results. However, the exceedance probabilities of the peaks deviate in the hogging condition. The peaks of the shear force spectra are at about the same level in the calculation and model tests. However, the shear force is shifted slightly to the smaller frequencies. The same was also visible in the transfer function of the shear force. The frequency content of the bending moment is underestimated by the time domain method.

The irregular wave results are in line with the regular wave results at zero and forward speeds. However, the asymmetric wave elevation in the model tests can have an effect on the comparison between the model test and the calculation results. The predictions of the shear force and bending moment are probably higher in the model tests than in the calculation due to the asymmetric wave elevation. The higher wave crests in the model tests can induce higher loads, especially in the sagging condition. At forward speed in the model tests, the heave has higher maximum peaks at small exceedance probabilities and exceeds the minimum peaks at about the exceedance probability of 0.05. In the calculation, the minimum peaks are always at a higher level than the maximum peaks. Hence, the highest crests in the model tests increased the maximum heave peaks.

To summarize, heave and pitch are well predicted by the time domain calculation method in irregular waves. At zero speed, the bending moment is also well predicted but there are differences in shear force predictions. At forward speed, the calculation gives rather good predictions for the shear force but the bending moment is underestimated.

Table 4.2. Mean and standard deviation (St.Dev.) of responses in sea state H_s = 9.0 m and T_z = 10.5 s at Fn = 0.0.

		Time domain		Model tests	
		Mean $\overline{x}$	St.dev. σ_x	Mean $\overline{x}$	St.dev. σ_x
Wave	a/H_s	0.000	0.246	-0.003	0.251
Heave	η_3/H_s	–0.004	0.141	0.007	0.137
Pitch	$\eta_5 L/(2\pi H_s)$	0.002	0.097	0.003	0.096
Shear force	$V_3/(\rho g H_s BL)$	0.0018	0.0097	0.0014	0.0080
Bending moment	$V_5/(\rho g H_s BL^2)$	–0.0007	0.0030	-0.0006	0.0030

Table 4.3. Mean and standard deviation (St.Dev.) of responses in sea state H_s = 5.0 m and T_z = 8.5 s at forward speed Fn = 0.25.

		Time domain		Model tests	
		Mean	St.dev.	Mean	St.dev.
Wave	a/H_s	0.000	0.247	–0.004	0.250
Heave	η_3/H_s	–0.022	0.156	–0.028	0.136
Pitch	$\eta_5 L/(2\pi H_s)$	0.006	0.107	0.004	0.107
Shear force	$V_3/(\rho g H_s BL)$	0.0075	0.0143	0.0082	0.0130
Bending moment	$V_5/(\rho g H_s BL^2)$	–0.0027	0.0042	–0.0029	0.0046

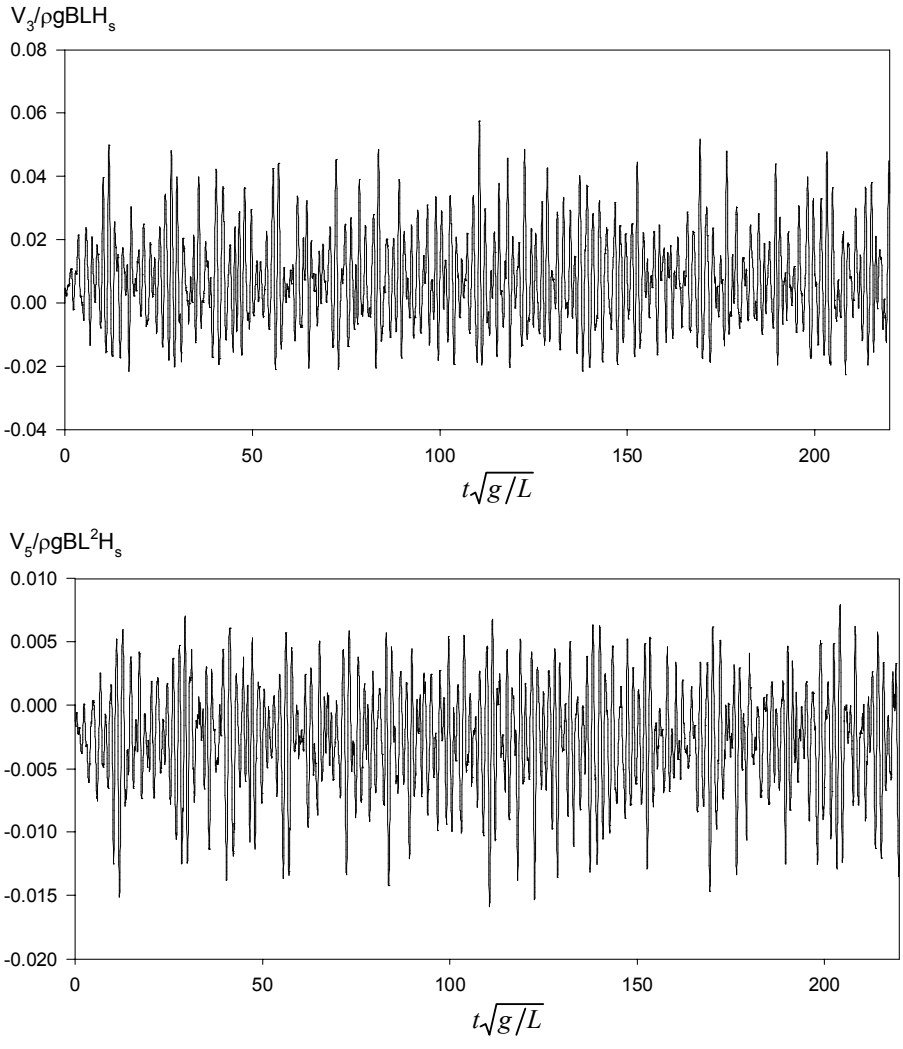

Figure 4.42. Examples of time histories of the shear force and bending moment at forward speed Fn = 0.25 in irregular head waves H_s = 5 m and T_z = 8.5 s.

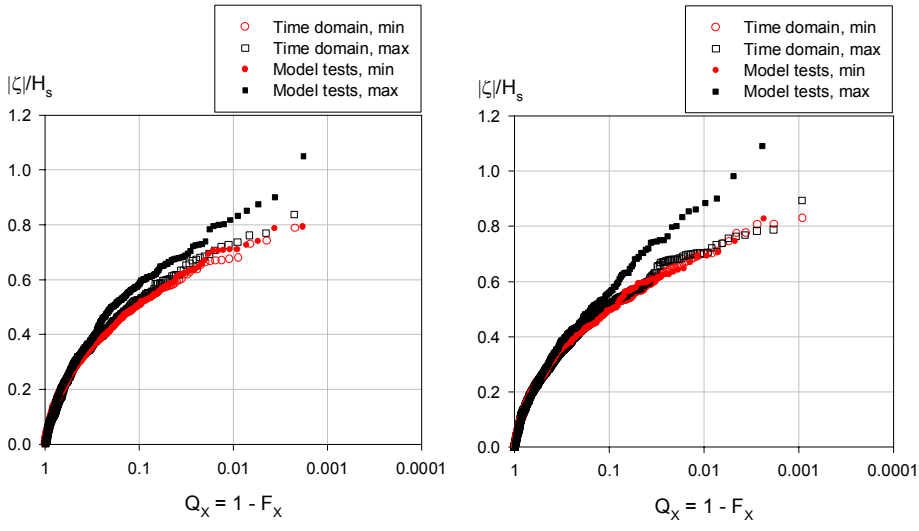

Figure 4.43. Exceedance probabilities of wave crests and troughs in sea state H_s = 9.0 m and T_z = 10.5 s at Fn = 0.0 (left) and in sea state H_s = 5.0 m and T_z = 8.5 s at forward speed Fn = 0.25 (right).

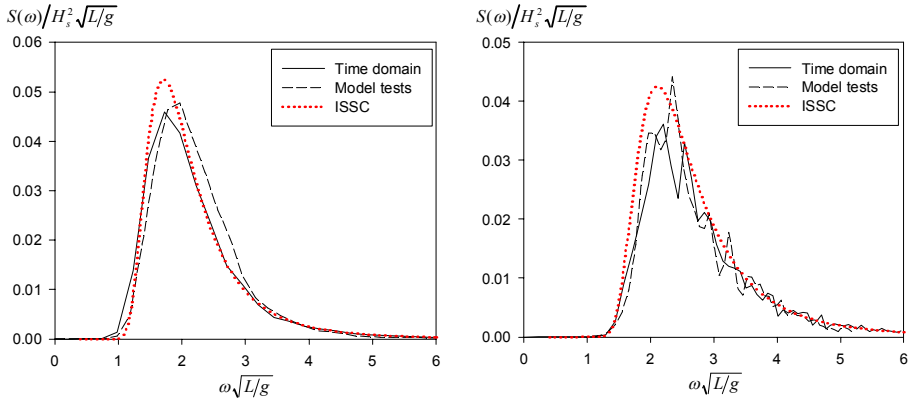

Figure 4.44. Wave spectra in sea state H_s = 9.0 m and T_z = 10.5 s at Fn = 0.0 (left) and in sea state H_s = 5.0 m and T_z = 8.5 s at forward speed Fn = 0.25 (right). ISSC is the theoretical wave spectrum calculated with Equation (4.2).

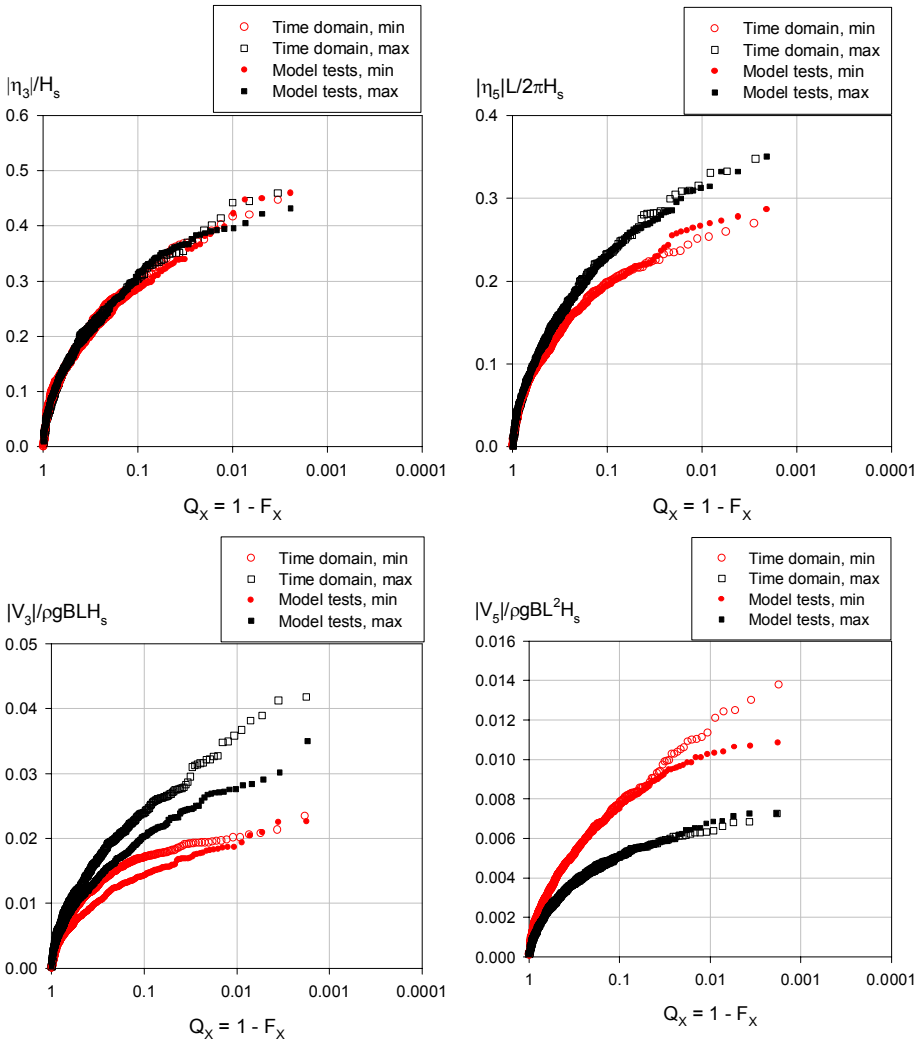

Figure 4.45. Exceedance probabilities of peaks in sea state H_s = 9.0 m and T_z = 10.5 s in head seas at Fn = 0.0

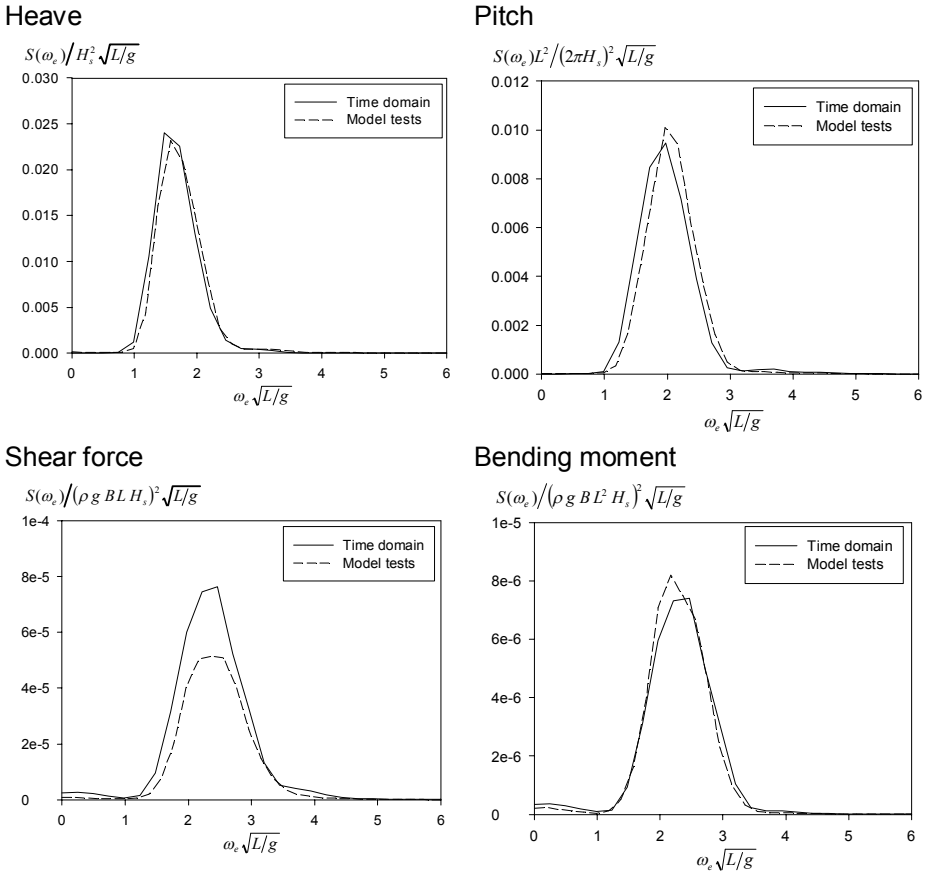

Figure 4.46. Response spectra as a function of the wave encounter frequency ω_e in sea state H_s = 9.0 m and T_z = 10.5 s in head seas at Fn = 0.0. At zero speed Fn = 0.0: $\omega_e = \omega$.

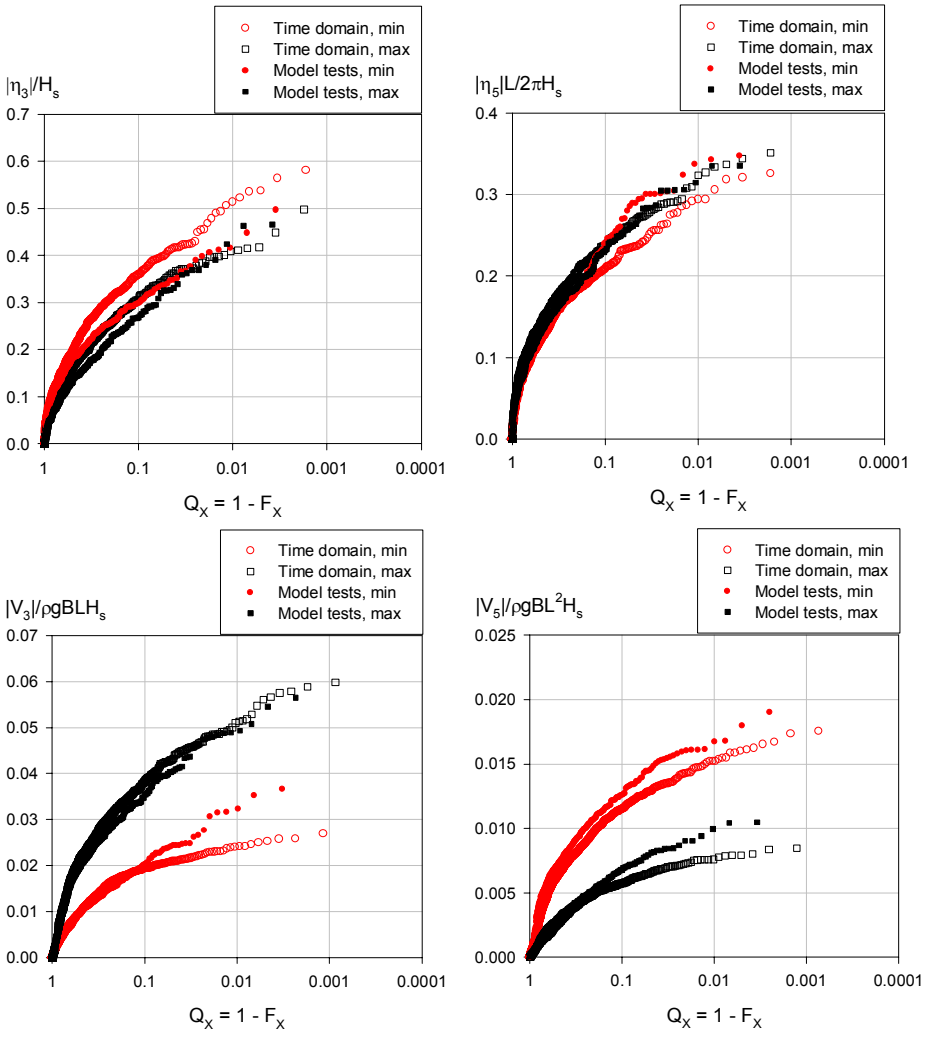

Figure 4.47. Exceedance probabilities of peaks in sea state H_s = 5.0 m and T_z = 8.5 s in head seas at forward speed Fn = 0.25.

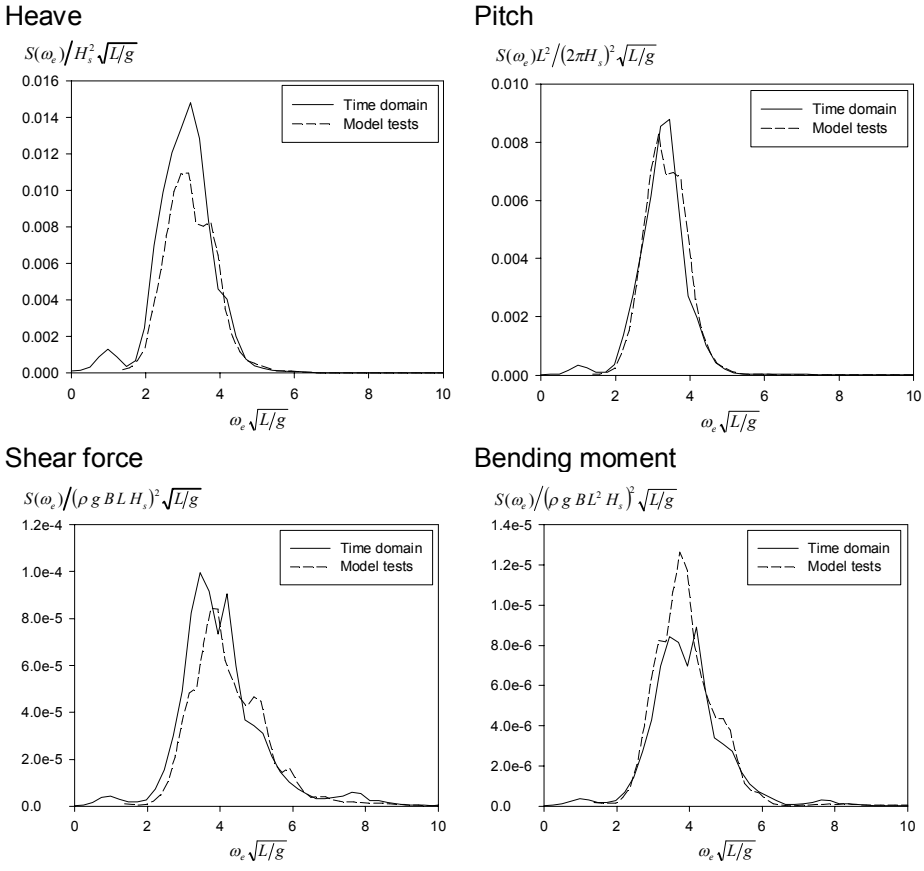

Figure 4.48. Response spectra as a function of the wave encounter frequency ω_e in sea state H_s = 5.0 m and T_z = 8.5 s in head seas at forward speed Fn = 0.25.

4.7 Wave load predictions

4.7.1 Background

In this work, existing methods and procedures were applied to determine short-term predictions for hull girder loads of the RoPax ship. The theory of the extreme value statistics can be found from, for example, Ochi (1990), and Price and Bishop (1974). In this section, the background and review of the design load predictions are given. An approach to predict short-term extreme values from time history data are described in the next section. The short-term extreme value predictions for the RoPax ship are given in the last section. The calculated predictions are based on the same irregular wave conditions as those used in the model tests. The comparison of the exceedance probabilities of the response peaks, the response spectra and the statistical values in the model tests and calculation were given in Section 4.6.

In structural analyses of ships, one of the first design bases is to define environmental and operating conditions. The environmental conditions are described, e.g. waves, winds, currents and ice. In this work, the environmental conditions focus on waves. The waves and their occurrence probabilities are normally given in the form of wave scatter diagrams for different sea areas, for example, in Global Wave Statistics (GWS, 1986). For the extreme wave load predictions of the ships, the International Association of Classification Societies (IACS, 2001) gives recommendations to use the wave data of the North Atlantic sea area. In the rules of the classification societies, this sea area is usually defined as the worst sea area, and it is intended to be used to design ships for unrestricted service.

In ship structural design, the wave load predictions are usually defined at the exceedance probability level of 10^{-8}. This corresponds to an occurrence that is expected to be encountered once in 20-25 years. In the IACS recommendations (IACS, 2001), a return period of at least 20 years, corresponding to about a 10^{-8} probability of exceedance per cycle, is recommended for use in designing wave-bending moments. The return period is defined as an event that is being exceeded on average once every n years. The return period is often used to define a so-called n-year wave. Thus, the n-year wave is a wave that is being exceeded on average once every n years.

The main operating conditions for ships are the speed and heading with respect to waves. The operating profile can vary considerably between different ship types. Depending of the ship type, other operating conditions should also be taken into account, for example, loading conditions. Furthermore, voluntary speed reduc-

tions or possible restrictions in speed or heading in high waves should be considered in order to define extreme waves in which the ship can operate safely.

In linear frequency domain methods, the linear superposition principle can be applied to obtain response spectra using transfer functions of responses and standard wave spectra. Once the response spectrum is known, the spectral moments can be determined to obtain the statistical properties of the response. The statistical properties can be determined at different sea states and in different operating conditions in irregular sea states. In linear methods, the wave elevation is Gaussian distributed with zero mean, and the derived responses are then also Gaussian with zero mean. Normally, it is assumed that the response peaks are narrow-banded and, hence, the response peaks follow the Rayleigh distribution. The extreme values in certain short-term conditions can be determined by applying extreme value statistics (see, e.g., Ochi, 1990). In each short-term condition, the environmental and operating conditions are constants and the response is a stationary random process. For the ship service life, several different conditions have to be considered in defining the long-term predictions for responses. Long-term predictions for responses can be defined using short-term response statistics and a joint probability density function of the different operating and environmental conditions (Sagrilo et al., 2011). The linear spectral method based on the long-term distribution of the stress responses can also be applied to fatigue predictions (Kukkanen and Mikkola, 2004).

In time domain methods, the calculation in irregular waves is carried out in a predefined short-term sea state. The sea state is described by the wave height and wave period. In extreme load predictions, the sea state is typically the worst sea state that gives a maximum response. The choice of the sea state depends on the operating sea area of the ship. The speed of the ship and the heading with respect to waves should also be estimated where maximum responses can occur. The time domain calculation is then performed in the defined sea state and operating conditions. The short-term extreme value of the response can be determined if the probability distribution of the response peaks is known. Moreover, the long-term prediction for the response can be defined from the time domain results if the short-term statistics are known. It is time-consuming to use nonlinear time domain methods however, as several different conditions have to be considered.

Short-term sea states in extreme load predictions can be defined as a return period of an n-year wave, for example, a 20-year wave. The n-year wave can be determined from the cumulative distribution function of wave heights. The data for the cumulative distribution functions of wave heights are available from the wave scatter diagrams. However, the cumulative distribution of the wave heights does

not give information on the occurrence probabilities of different wave periods. By applying a so-called contour line approach, both the wave periods and wave heights can be determined at the same probability of exceedance level (Baarholm and Moan, 2001). The contour line in the H_s-T_z plane gives an equal exceedance probability for sea states. Thus, the n-year wave, for example, a 20-year wave, is defined by means of wave heights and wave periods. The distribution functions for wave heights and periods are obtained from wave scatter diagrams. Joint probability distributions of H_s and T_z are modelled using a Weibull distribution for wave heights and a conditional Log-normal distribution for wave periods at a given H_s. To take into account the heavy weather avoidance in the design wave predictions, the limit for wave height can be defined, for example, re-scaling the Weibull distribution (Baarholm and Moan, 2001). The rescaling means that the extreme wave height will be limited to some realistic wave height at which the ship can operate safely.

Several different methods and models exist to determine and describe the short-term probability distribution of the response peaks (see, e.g., Jensen et al., 2000). Stochastic methods and different probability density functions for nonlinear responses in the time domain were studied by Wang and Moan (2004). They applied Weibull, Generalized Gamma and Pareto distributions for time history data of nonlinear bending moments in waves. They concluded that the Weibull distribution was able to represent the sagging and hogging nonlinearities in hull girder loads with reasonable accuracy and that the distribution was suitable for nonlinear peak value statistics. The simulation length should be long enough to obtain a sufficient number of peak values for the distribution to be estimated (Wu and Moan, 2006). The probability distribution of response peaks can also be determined by applying a Hermite transformation model (Winterstein, 1988). The probability distribution based on the Hermite transformation can be determined if the lowest statistical moments of the response are known. The lowest statistical moments are typically mean, variance, skewness and kurtosis.

Applying stochastic methods, the predicted extreme value does not necessarily occur in the time history data. The extreme value is a predicted value and typically also extrapolated from the calculated time history data. Hence, exactly the same hydrodynamic loads are not available. The hydrodynamic loads are sometimes needed as pressures that can be used in the structural strength analyses. A straightforward approach is to extrapolate a representative sample that can be scaled to the predicted extreme value from the time history data. However, this approach can lead to unrealistic wave sequences in which the extreme value can occur, for example, in breaking waves. Another straightforward procedure is to use the so-called design wave approach. In the design wave approach, one regular

sinusoidal wave with a wave height H and period T is defined for which a response has the same extreme value as that obtained from irregular waves. In this regular wave, the time domain calculation is repeated to obtain the time histories for the responses. For strongly non-linear responses, this is not necessarily as simple as it is for linear cases and the regular wave can give different accelerations and pressure loads to irregular waves. Linear frequency domain methods can be applied to determine the possible worst sea states for which the response can have the maximum values. The linear methods are used in order to reduce the number of sea states for which the time-consuming nonlinear calculation should be performed. Recently, methods have been developed to determine so-called critical wave episodes that give extreme values for responses in the time domain (see, e.g., Jensen, 2009). The critical wave episode is a short sequence of irregular waves that gives the extreme value prediction for a response in the time domain. The critical wave episode can be determined using first linear frequency domain methods. Applying linear frequency domain methods, the time history of irregular wave episodes is determined where the extreme value occurs. Using linear methods, several different conditions can be analysed before the time domain calculation and hence the computational time can be reduced.

In the following section, the short-term probability distribution of the response peaks is briefly explained and the probability distributions of the peaks for the RoPax ship are given. In this work, the Weibull distribution function is used to determine the probability distribution of the peaks in short-term sea states. The short-term extreme value predictions for the RoPax ship are given in the last section. The calculations and predictions are given in the same states as those in which the model tests were carried out. Hence, the used sea states are not necessarily the worst sea states for the design loads. The design sea states are not defined in this work. The design sea state for the RoPax ship was discussed briefly by Kukkanen (2009). It was assumed that the world-wide operation of the ship and the H_s-T_z contour lines were determined and that the sea states of different return periods were presented. The return period of a 1-year wave was about 10 m. Hence, the H_s = 9 m wave used in the present work is rather close to the 1-year wave. However, it is less than the 20- or 25-year wave, which is the normal design life of the ships. In model tests, the wave periods were selected so that the wave peak period of the shorter wave period, T_z = 8.5 s, was close to the maximum of the transfer function of the vertical bending moment at forward speed Fn = 0.25. This maximum value was based on the first calculations that were performed using a linear frequency domain method. The longer zero crossing wave period, T_z = 10.5 s, was based on the scatter diagrams, and a period was selected at which the highest waves typically occur. The wave height of 5 m was also

assumed to be an approximation of the highest wave height at which the ship could maintain the forward speed $Fn = 0.25$.

4.7.2 Short-term predictions of responses

Peak distribution is a probability function of maximum values that occur in sample data. The single extreme value is the maximum of all of the maximum peaks. However, the single extreme value can vary between different sample time histories even if they are calculated in the same conditions, for example, in the same irregular waves. This is due to the random nature of the irregular waves. Hence, the extreme values for one sample follow its probability distribution. The most probable extreme value is defined as an extreme value at which the extreme value distribution has the most probable value. However, the exceedance probability of the most probable value is high. The extreme value can also be defined using a so-called risk parameter or safety factor that defines the probability level at which the extreme value can be exceeded, for example, using a 1% exceedance probability level for the extreme value.

In this work, the peak distributions are determined using a three-parameter Weibull cumulative distribution function. The Weibull distribution is given by

$$F(x) = 1 - \exp\left[-\left(\frac{x - \gamma_w}{\alpha_w} \right)^{\beta_w} \right], \tag{4.8}$$

where the three parameters α_w, β_w and γ_w determine the scale, shape and location of the distribution, respectively. From the Weibull distribution, the most probable extreme value (MPEV) can be derived as follows:

$$\hat{x} = \gamma_w + \alpha_w (\ln N)^{\frac{1}{\beta_w}}, \tag{4.9}$$

where N is the number of response cycles. The extreme value with the exceedance probability level α_r can also be derived from the Weibull distribution. The equation is finally the same as that above but using N/α_r instead of N in Equation (4.9).

In this work, the parameters in the Weibull distribution were determined using parameter estimation of moments: mean and variance. The first two moments for the Weibull distribution are given in, for example, Ochi (1990). The goodness of fit can be studied with a so-called quantile-quantile plot (q-q plot). In the q-q plot, the original data are given on the x-axis and the fitted data on the y-axis. The

fitted data are determined with the estimated parameters from the inverse of the peak distribution function, i.e. solving x from Equation (4.8). The cumulative probability $F(x)$ is based on the original probabilities of the peaks. If the data fit the peak distribution perfectly, the q-q plot is a straight line, i.e. $y = x$. The q-q plots of the wave and the vertical bending moment at midship are shown in Figure 4.49. The figures are given separately for the maximum and minimum peaks, i.e. for the wave crests and troughs and for the hogging and sagging bending moments. The negative minimum peaks are given as absolute values. The calculation was performed at the forward speed of the ship $Fn = 0.25$ in head seas. The irregular sea state was $H_s = 5$ m and $T_z = 8.5$ s. It can be noted that the peaks of the wave follow the Weibull distribution well. However, the bending moment deviates from the Weibull distribution, especially the tail of the bending moment peaks. On the other hand, the tail part is significant for the extreme value predictions. The so-called peak-over-threshold method (Wu and Moan, 2006) can be applied to improve the estimate of the tail part in the peak distribution. In the peak-over-threshold method, only the peaks over a threshold are taken into account in fitting the probability distribution to the response peaks. Hence, the weight of the tail can be increased in estimating the parameters to the peak distribution. In this work, the parameters in the Weibull distribution were estimated using 90% of the highest peaks. Hence, the threshold levels for the responses were rather low. The threshold level was kept at a low level in order to obtain a large number of sample peaks in the parameter estimation. The statistical confidence decreases if the number of samples decreases. However, the threshold level can be increased if the duration of the sea state in the calculation is longer and a larger number of sample peaks are available.

The q-q plot of the shear force and bending moment are shown in Figure 4.50 at zero speed and Figure 4.51 at forward speed $Fn = 0.25$. The sea states in the calculation were $H_s = 9$ m and $H_s = 5$ m at zero and forward speeds, respectively. The plots are based on 90% of the highest peak values. At the forward speed, the tail part is closer to the line $y = x$ than if all the peaks were included. Hence, the highest peaks are better modelled in the Weibull distribution. At zero speed, the calculated peaks follow the Weibull distribution better than at forward speed.

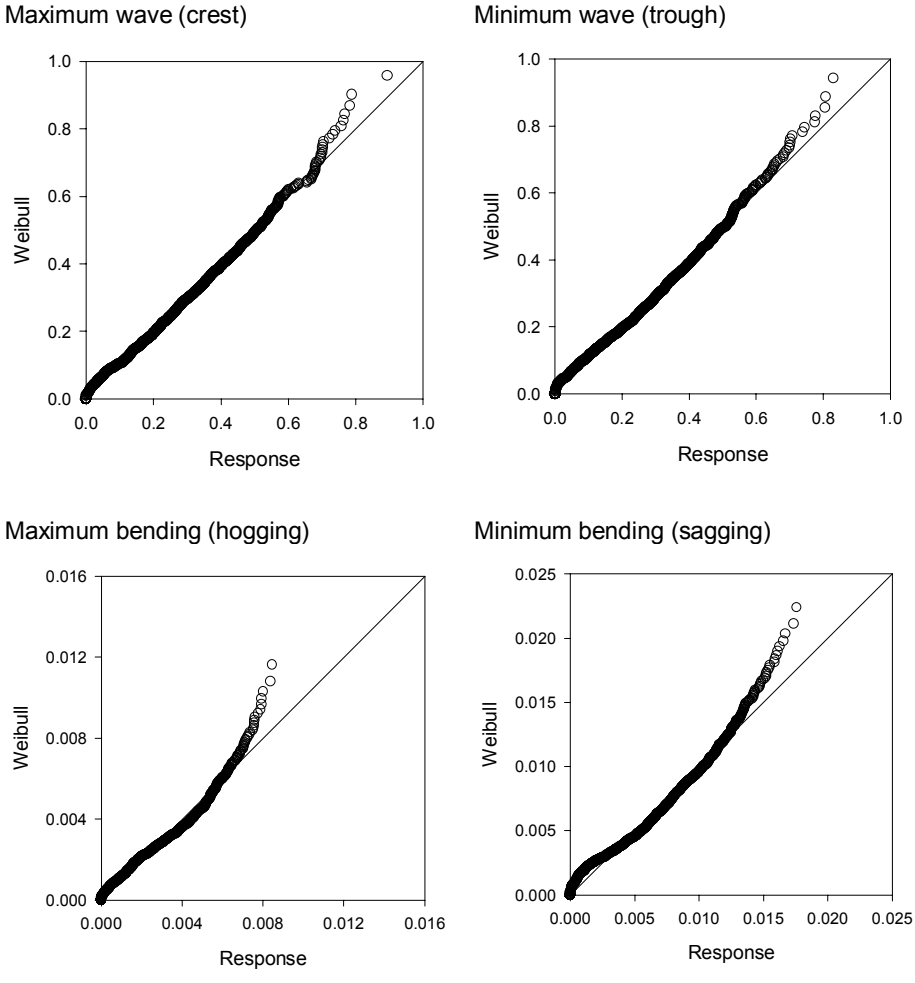

Figure 4.49. Goodness of fit of the Weibull distribution for the wave and bending moment given as a q-q plot. In the figures, the forward speed of the ship was Fn = 0.25, and the wave height and period were H_s = 5 m and T_z = 8.5 s. The wave and bending moment are given in non-dimensional forms: wave $|\zeta|/H_s$ and bending moment $|V_5|/(\rho g B L^2 H_s)$.

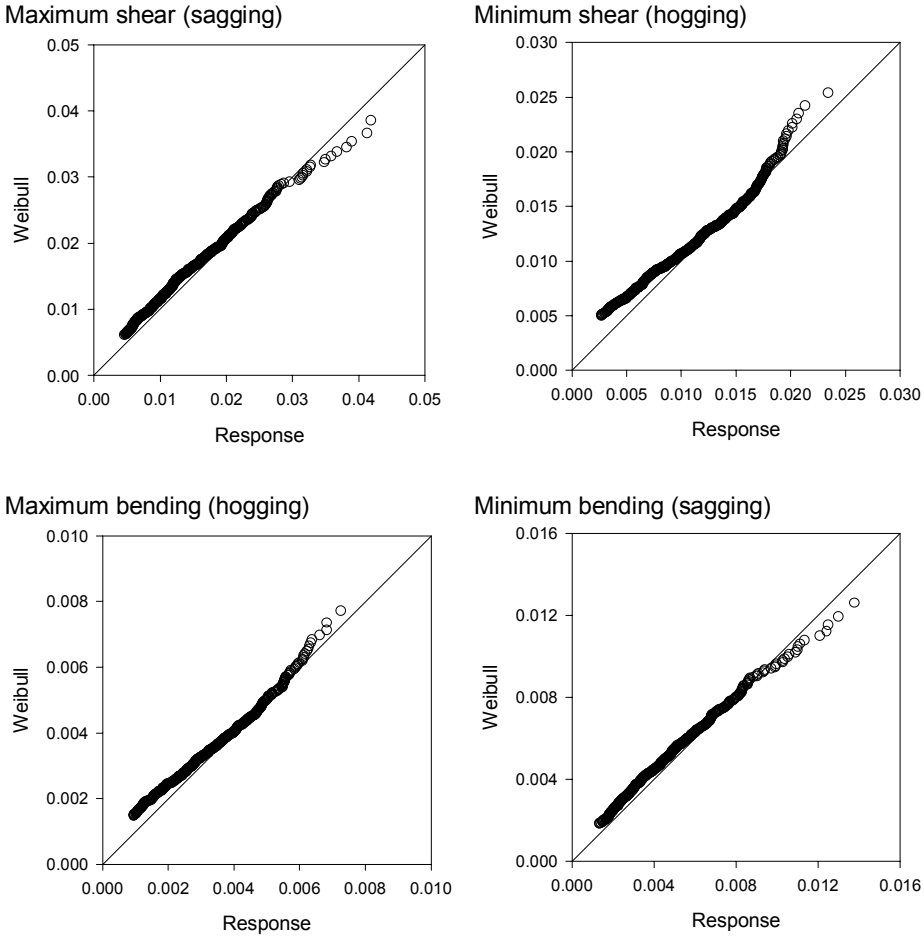

Figure 4.50. The q-q plot based on 90% of the highest peaks for the maximum and minimum shear force and the bending moment at $Fn = 0.0$ in sea state $H_s = 9$ m and $T_z = 10.5$ s. The shear force and bending moment are given in non-dimensional forms: shear force $|V_3|/(\rho g B L H_s)$ and bending moment $|V_5|/(\rho g B L^2 H_s)$.

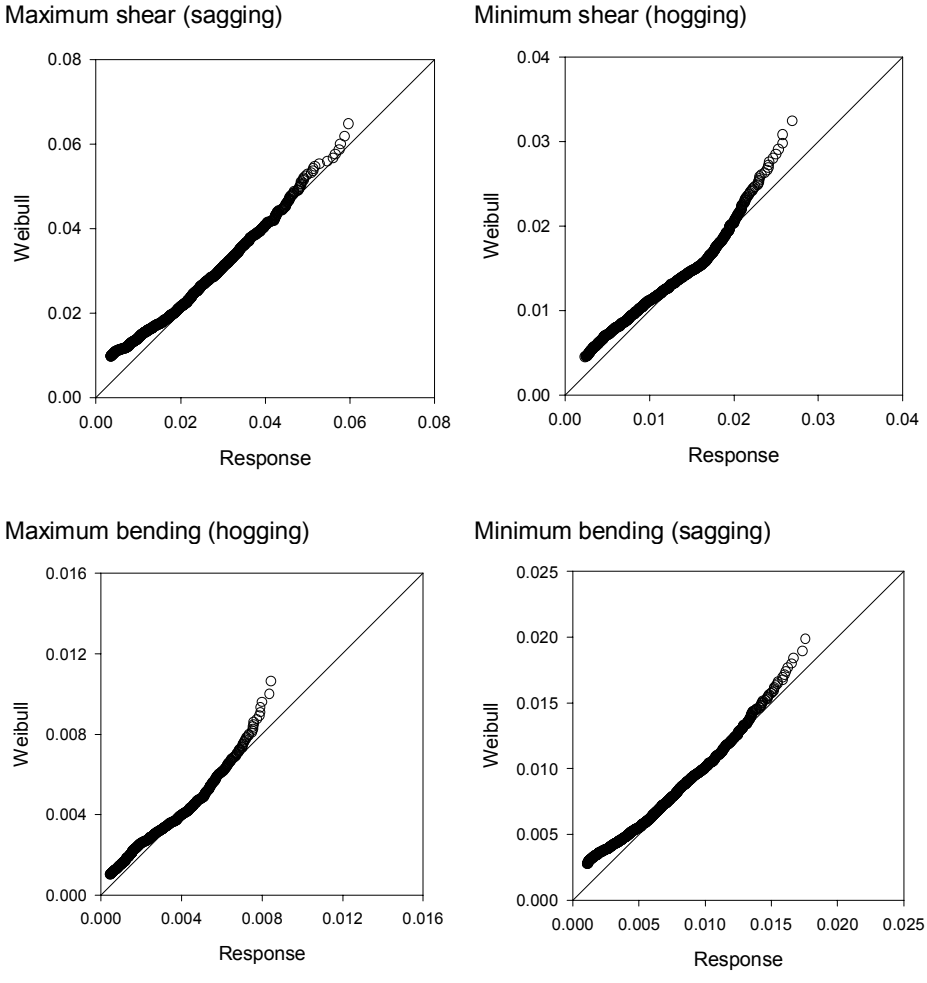

Figure 4.51. The q-q plot based on 90% of the highest peaks for the maximum and minimum shear force and the bending moment at forward speed Fn = 0.25 in sea state H_s = 5 m and T_z = 8.5 s. The shear force and bending moment are given in non-dimensional forms: shear force $|V_3|/(\rho g B L H_s)$ and bending moment $|V_5|/(\rho g B L^2 H_s)$.

4.7.3 Short-term predictions for the model test ship

The most probable extreme values (MPEV) of the shear force at the fore ship and the bending moment at midship were determined from the results of the time domain method and from the model tests. The extreme value predictions are based on the Weibull distribution. The predictions were determined for the sea state duration of three hours. The MPEV predictions from the model test results were determined in the same way as the calculated extreme values. The peak values and extreme value predictions of the shear force and bending moment are given as absolute values. In the sagging condition, the bending moment is negative (minimum) and the shear force is positive (maximum). In the hogging condition, the signs of the force and moment are opposite. The linear distributions given in the figures below are based on the Rayleigh distribution of peaks. The linear predictions were determined using the transfer functions of the shear force and the bending moment. The transfer functions were based on the body-wave nonlinear solution at wave amplitude $a/L = 0.013$. The transfer functions were multiplied by the wave spectra to obtain the response spectra. The variances of the responses that are needed in the Rayleigh distribution were determined from these response spectra.

In Table 4.4, the MPEV predictions are given for the hull girder loads at zero speed in the sea state $H_s = 9$ m and $T_z = 10.5$ s. The MPEV predictions from the time domain method for the bending moment are close to the model test predictions. However, the predictions for the shear force with the time domain method are overestimated. The same trend was also observed in Section 4.6 comparing the response spectra and peak distributions between the time domain method and model tests. The peak distributions of the calculated hull girder loads are presented in Figure 4.52. The difference between the linear and nonlinear predictions is significant.

At forward speed $Fn = 0.25$, the MPEV predictions are given in Table 4.5 at the sea state $H_s = 5$ m and $T_z = 8.5$ s. The MPEV prediction with the time domain method for the sagging bending moment (minimum) is the same as the model test prediction. The prediction for the shear force with the time domain method in the sagging condition (maximum) is also quite close to the model test prediction. However, the time domain method overestimates the predictions in the hogging condition for the shear force and the bending moment. The peak distributions based on the calculation are presented in Figure 4.53.

At zero speed, the ratios of the MPEV sagging and hogging bending moment are 1.6 and 1.5 in the calculation and model tests, respectively. The ratios of the shear

force are 1.5 and 1.4 in the calculation and model tests, respectively. Thus, the time domain method overestimates slightly the ratios between the sagging and hogging bending moment and shear force.

At forward speed, the ratios of the MPEV sagging and hogging bending moment are 1.9 and 1.6 in the calculation and model tests, respectively. Furthermore, the ratios for the shear force are 2.0 and 1.5 in the calculation and model tests, respectively. The differences between the ratios of the time domain method and model tests are mainly due to the underestimated hogging shear forces and bending moments obtained from the calculated time histories.

The ratio of the sagging and hogging loads is greater at forward speed than at zero speed. In the model tests at forward speed, the relative motions at the bow were larger and hence the nonlinear effects due to the changes in hull geometry during water entry and exit were also larger. This increased the nonlinearities in the hull girder loads. At zero speed, in addition to the loads on the bow, the flat bottom stern entered the waves, which can increase the sagging forces and moments. The calculation and model test results show that the hydrodynamic loads on the bow due to the forward speed induce greater differences in the sagging and hogging loads than the loads on the bow and the stern at zero speed. However, the wave impact loads can induce dynamic responses on the hull girder, i.e. hull girder vibrations in addition to the rigid hull girder responses. However, the possible effects of the stern impacts cannot be seen directly in the results presented here because the hull girder was assumed to be rigid in the calculation. In the model tests, the dynamic of the ship model was not scaled and the time histories were also low-pass filtered.

The rules of the classification societies give the sagging and hogging bending moments and shear forces for ships. Hence, it is possible to compare the predicted sagging and hogging loads with the values obtained from the rules. The ratios of the sagging and hogging loads for the bending moment at midship and for the shear force at fore ship are the same in the rules (IACS, 2010). From the rules, the ratio of sagging and hogging is 1.3. Thus, the rule gives a lower estimate for the sagging and hogging ratio. At zero speed, the calculated ratios are closer to those of the rule. However, the rule can set special requirements for the bending moment and shear force if the ship's main dimensions are unconventional or the forward speed is high. For this particular ship, the block coefficient is lower than the lower limit in the rules. For the RoPax ship, the block coefficient is $C_B = 0.55$ and the coefficient should be $C_B > 0.6$ in the rules. The speed is also one factor in the rules that can cause special requirements for the ship. These can increase the rule bending moment and shear force values in sagging or in both sagging and

hogging. It should also be noted that the calculated results are only based on two speeds at two sea states, and different extreme values can be obtained from other sea states. Hence, the ratio between calculated sagging and hogging moments and shear forces can also be different. Furthermore, to obtain the extreme design values for the hull girder loads, several sea states should be included in the analyses, especially higher waves and different wave periods. Moreover, the reliability of the predictions depends on the duration of the sea state. The reliability of the predictions can be improved using a longer duration of the sea state in both the calculation and model tests.

Table 4.4. Most probable extreme value (MPEV) of the bending moment and shear force in the sea states of three hours, H_s = 9.0 m and T_z = 10.5 s, Fn = 0.0 in head seas.

	Time domain Minimum	Time domain Maximum	Model tests Minimum	Model tests Maximum
Bending ($\|V_5\|/\rho gBL^2H_s$)	0.013	0.008	0.012	0.008
Shear ($\|V_3\|/\rho gBLH_s$)	0.027	0.041	0.023	0.033

Table 4.5. Most probable extreme values (MPEV) of the bending moment and shear force in the sea states of three hours, H_s = 5.0 m and T_z = 8.5 s, speed Fn = 0.25 in head seas.

	Time domain Minimum	Time domain Maximum	Model tests Minimum	Model tests Maximum
Bending ($\|V_5\|/\rho gBL^2H_s$)	0.021	0.011	0.021	0.013
Shear ($\|V_3\|/\rho gBLH_s$)	0.034	0.068	0.041	0.062

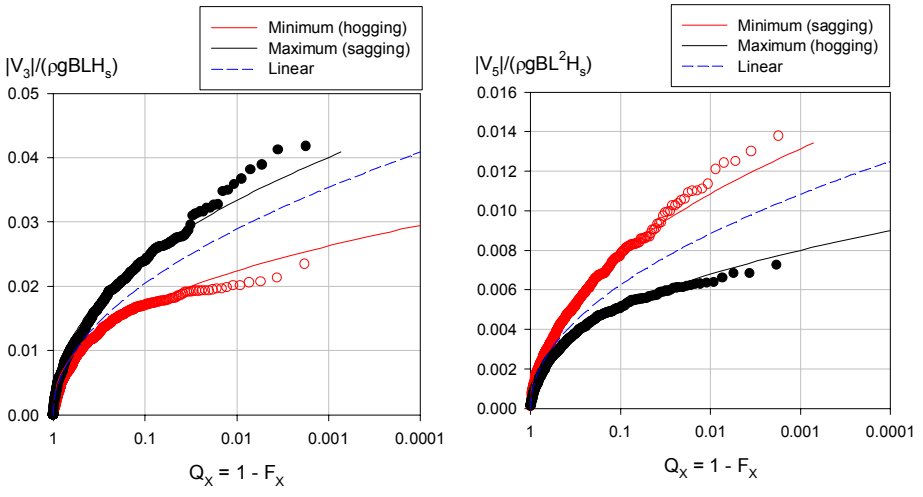

Figure 4.52. Peak distributions of shear force and bending moment at Fn = 0.0 in sea state H_s = 9 m and T_z = 10.5 s. The dots are the maximum and minimum peaks from the time domain calculation.

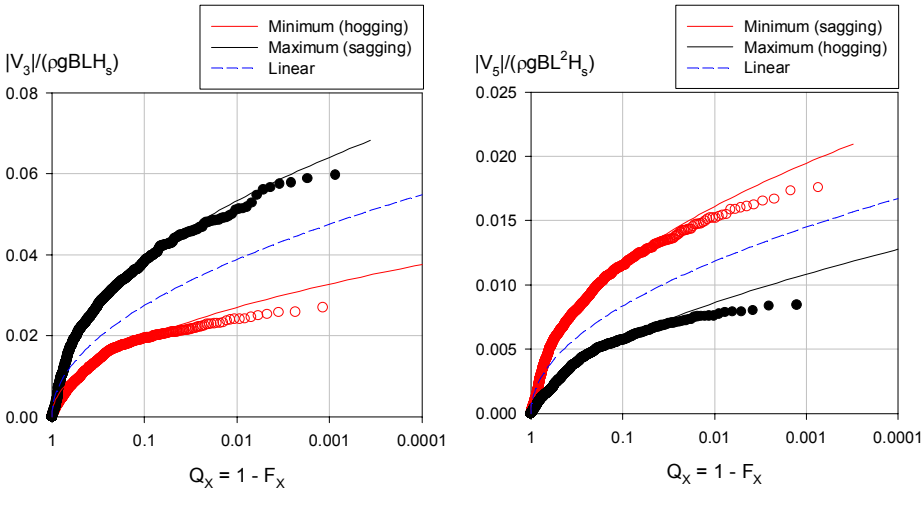

Figure 4.53. Peak distributions of shear force and bending moment at forward speed Fn = 0.25 in sea state H_s = 5 m and T_z = 8.5 s. The dots are the maximum and minimum peaks from the time domain calculation.

5. Discussions

5.1 Calculation method

The time domain method presented in this work is based on an inviscid and incompressible fluid and an irrotational flow. Hence, the fluid flow can be presented by means of the velocity potential. The velocity potential satisfies boundary conditions on the body surface and free surface and far away from the body at infinity. The boundary value problem is expressed in the space-fixed coordinate system. The exact body boundary condition is used in the body nonlinear solution. The free surface boundary condition is linear. The free surface boundary condition is satisfied on the mean free surface and the exact body boundary condition on the instantaneous wetted surface of the body. The amplitudes of the body motions can be large but the wave amplitudes are assumed to be small. The velocity potential is solved using the transient Green function in the time domain and the numerical solution is based on the source formulation, applying the constant panel method.

The time derivative of the perturbation velocity potential in Bernoulli's equation is solved with the acceleration potential method. The time derivative of the velocity potential is expressed using the potential function φ. The potential function otherwise satisfies the same boundary conditions as the perturbation velocity potential but the body boundary condition is different. The potential function φ is solved with a similar source formulation as the perturbation velocity potential.

In the acceleration potential method, the body accelerations are not yet solved from the equations of motion when they are needed in the boundary condition of the potential function. In the present time domain method, the acceleration potential method is based on an iterative solution. A predictor-corrector scheme is used in the time integration of motions and the corrector is applied once at every time step in solving the equations of motion. The iteration can be repeated by applying the corrector again and solving the equations of motion until a desired accuracy

has been reached. However, only one iteration cycle was used in this work. Increasing the number of iterations will increase the calculation time.

The given acceleration potential method can be further developed. In the expression of the perturbation velocity potential, Equation (2.77), the integral equation that includes the memory part of the Green function can be differentiated analytically with respect to time. Hence, the contribution of the time derivative of the velocity potential from the memory part can be obtained directly. Thus, only the time derivative of the impulsive part needs to be solved with the source formulation. The time derivative of the impulsive part can be solved by deriving a boundary condition for the term and applying a source formulation in the same manner as that used in the present acceleration potential method. The solution of the acceleration potential can also be coupled with the forces and moments in the equations of motion as presented by Wu and Eatock Taylor (1996), and Bandyk and Beck (2011). This could give a single representation for the unknown body accelerations that can be solved without iteration. However, this requires a further study of how this approach can be implemented in the present time domain method.

The memory part of the transient Green function is solved by applying a numerical integration. The numerical integration is based on the adaptive Gauss-Kronrod quadrature formulae. The numerical integration gives the desired accuracy and the numerical integration can be applied to the whole integration domain on the β-μ plane. However, the numerical integration is time-consuming compared with the series and asymptotic solutions. The accuracy of the numerical integration can also be worse if the parameter μ is approaching zero, i.e. the vertical coordinates of the source and field points are approaching the free surface. In the present calculation method, the Bessel function solution for the memory part and its derivatives are used when $\mu = 0$.

In the present calculation method, the values of the memory part of the transient Green function are interpolated from the pre-calculated table during the calculation. The interpolation algorithm is based on the finite element approximation of the memory part in the β-μ plane. The use of the pre-calculated Green function values reduces the computation time considerably. The finite element representation gives satisfactory approximation for the values of the memory part of the transient Green function in the practical computation.

The memory part of the transient Green function is a highly oscillating function close to the free surface. The oscillation of the memory part increases at small values of the parameter μ when the non-dimensional time β increases. If the pan-

els are non-wall-sided close to the free surface, the parameter μ takes small values. This can cause instabilities in the solution, and the solution can be divergent in the time integration. The memory part is also integrated over the panel area using midpoint or Gauss quadrature rules that give an approximation for the integral. The integration accuracy of the memory part can be improved using higher order integration rules. However, further studies are needed to investigate reasons and possible solutions for the instabilities.

In the calculation method, the body surface is discretized by panels, and numerical algorithms are used to solve the hydrodynamic boundary value problem. In the body nonlinear solution, the floating position of the body is updated at every time step. The pressure is determined on the instantaneous wetted surface of the body up to the mean water level. In the body linear solution, the floating position of the body is not updated and the pressure is determined on the mean wetted surface of the body. Furthermore, the time integrations are applied to solve the motions and the convolution integral of the transient Green function. Hence, the accuracy of the numerical solution depends on the applied numerical algorithms and the panel and time step sizes, i.e. the spatial and temporal discretization.

The constant panel mesh approach is used in the calculation method where the panel sizes and geometries are constants during the calculation. As the panel mesh is not updated during the calculation, the velocities and accelerations on the body surface can be evaluated exactly. If the panel mesh is updated during the calculation, the distortions of the panels have to be taken into account to determine the velocities and accelerations.

The line integral appears in the integral equations and the collocation points of the sources are approximated at the centroid of the panels. The line integral is also not taken into account properly in the constant panel mesh approach in the body nonlinear solution because it is solved for the panels that are closest to the mean water level. Hence, the line integral is not solved continuously on the mean waterline at the intersection of the body and the free surface. The influence of the memory effect is lost when a panel becomes dry. Further studies are needed to investigate the effect of the line integral on the response predictions and how to implement the line integral correctly to the constant panel mesh approach in the body nonlinear solution.

5.2 Simple body geometries

The time domain method was verified by calculating the added mass and damping coefficients in the heave for a hemisphere with the body linear solution. The calculated added mass and damping coefficients are in good agreement with an analytical solution. The presence of the irregular frequencies can be seen in the results of the added mass and damping coefficients. The irregular frequencies can exist in the integral equation solutions for bodies oscillating on the free surface. Methods have been developed to remove the irregular frequencies (see, e.g., Lee and Sclavounos, 1989; Lee et al., 1996). The methods for removing irregular frequencies are based on an additional integral representation for the interior problem, i.e. inside the body at the mean water level. However, removing the irregular frequencies in the body nonlinear solution is not necessarily straightforward because the body position is updated at every time step. The panel mesh for the interior problem should be updated at every time step on the mean water level and for this reason the constant panel mesh approach cannot be applied.

The calculation method was also verified by calculating the linear heave radiation forces for two heaving cones. The linear heave radiation forces were determined using the time domain method and two simple solutions when the cones were in the forced heave motion at the free surface in calm water. The time domain method gives the same results as the two simple solutions. The two simple solutions are based on the added mass and damping coefficients and the impulse response function of heaving cones. The time domain method and the two simple solutions have to give the same results because the solutions of these different methods have been derived from the same boundary value problem.

The body nonlinear solution was also used to study nonlinearities when the cones were forced to oscillate with different heave frequencies and amplitudes at the free surface in calm water. The studies show that the time domain method can predict nonlinearities in heave forces and that the nonlinearities increase if the heave amplitude increases. The nonlinearities are greater for the cone with the smaller deadrise angle. Experimental results for cones in harmonic heave motions are not available. However, cones are simple bodies to investigate with calculation methods, and nonlinear effects can be studied with different deadrise angles. Experiments of cones in harmonic heave motions are recommended to obtain validation data for nonlinear hydrodynamic forces.

Furthermore, the acceleration potential method gives a smooth prediction for the heave radiation forces of the cones. However, the forces from the backward difference method include sharp spikes in time histories. A calculation was also

carried out to study the differences between the constant and spline-fitted panel meshes. Time histories calculated with the constant panel mesh include discontinuities. The discontinuities exist when a panel row changes from dry to wet or vice versa, i.e. panels are included or excluded from the solution. However, the amplitude predictions of the heave forces with the constant and spline-fitted panel meshes are close to each other.

Motions, exciting forces and moments, and added mass and damping coefficients were determined for a Wigley hull form to validate the calculation method. The calculated heave, pitch and exciting forces and moments are in close agreement with the experimental results. However, the relative motion at the bow deviates from the experimental results. One reason for the poor prediction could be body-induced steady and unsteady bow waves that are not taken into account in the calculation method. The diagonal terms of the added mass and damping coefficients in the heave and pitch are in good agreement with the experimental results. The biggest deviations exist in the cross-coupling damping terms. The acceleration potential and backward difference methods give equivalent results for the added mass and damping coefficients.

The steady flow effects on sinkage and the wave-making resistance were studied using a Wigley resistance hull form, and comparisons between the calculation and model test results are presented. The comparisons show that the time domain method can predict sinkage and the wave-making resistance for the Wigley hull form.

5.3 Model test ship

Model tests were carried out for the RoPax ship in calm water and in regular and irregular head waves. The ship represents a typical hull form for roll-on roll-off and passenger ships. The model test ship has a bulbous bow and a flat bottom stern. Model test results for the ship motions and, especially, for the hull girder loads are seldom presented for this type of hull forms. In the model tests, the ship motions, accelerations and hull girder loads were measured. The vertical bending moment was measured at midship and the vertical shear force at fore ship. The responses were determined with the time domain method in the same conditions as in the model tests.

The RoPax ship has a flat bottom stern and a large part of the stern is above the still water level. In the time domain method, the hull of the ship is discretized by panels, and the stern panels of the RoPax ship are almost horizontal above the still water level. At forward speed, the flat bottom stern is at least partly in the

waves because of the sinkage of the ship and the wave formation. In waves, the wetted surface of the stern varies constantly due to the ship motions and waves. If the horizontal panels are close to the free surface, the solution can begin to oscillate and the oscillation can finally lead to a divergent solution. To avoid unstable oscillation, a criterion is applied for the vertical distance of the centroid of the panel from the free surface. This criterion was applied with the body nonlinear solution in the given calculation results for the RoPax ship.

Low-pass filtering of the time series is also necessary in order to obtain a convergent solution for the motions of the RoPax ship. The variation in the wetted surface of the hull with respect to the mean water level can induce abrupt and rapid changes to the fluid flow and, consequently, to the solution of the velocity potential. The abrupt and rapid changes can induce noise to the solution. The low-pass filter is applied to smooth the time histories of the motion terms that appear in the boundary conditions of the velocity and acceleration potentials. Hence, the applied low-pass filtering gives a smooth solution for the source strengths, and the velocity and acceleration potentials. This also improves the accuracy of the time integration of the motions. However, the cut-off frequency of the filter should be at least about five times higher than the oscillation frequency of the response in order to avoid attenuation of the response; though, the attenuation depends on the filter type and the characteristics of the filter.

Furthermore, small panel sizes should be used and the time step size should be short if the body has non-wall-sided panels close to the free surface. The accuracy of the integrals over the panel areas can be improved by increasing the number of points in the Gauss quadratures. The midpoint rule is sufficient if the geometry of the hull is smooth and wall-sided close to the free surface. Higher order integration rules should be applied to body geometries that have small inclination angles close to the free surface. However, the computational time increases if the number of integration points increases. In this work, the results given for the RoPax ship were calculated with the midpoint rule.

The acceleration potential and backward difference methods give the same predictions for the motions and hull girder loads with the body linear solution. However, the two methods give different predictions at forward speed in the case of the body nonlinear solution. Furthermore, the calculations show that the acceleration potential and difference methods give different predictions for the heave radiation-diffraction forces. The radiation-diffraction force calculated by the applied backward difference method with the body nonlinear solution is not consistent with the body linear solution. The radiation-diffraction force also deviates clearly compared with the results of the acceleration potential method. The accel-

eration potential method gives a similar type of radiation-diffraction force in the body linear and nonlinear solutions. The acceleration potential method also gives stable and reliable results for the responses and hydrodynamic forces.

Irregular frequencies were not detected as existing for the RoPax ship in the frequency ranges used in this work. This was confirmed by the heave and pitch added mass and damping coefficients calculated with a linear frequency domain method.

In calm water, loads and motions were calculated and measured in the model tests. The agreement with the calculations and model tests is quite good for the steady loads and sinkage of the ship. The shear forces and bending moments increase when the speed increases. The forward speed effects induce sagging loads on the hull girder. The steady bending moment and the shear force are both in the order of about 10% of the still water values. The calculation in calm water was also repeated without the fluid velocity squared term $0.5|\nabla\phi|^2$ in Bernoulli's equation. The terms in Bernoulli's equation are expressed in the space-fixed coordinate system, and the meaning of the terms was discussed at the end of Section 2.3.2. It was pointed out that the term $\partial\phi/\partial t$ is not zero for bodies in steady translational motion if the term is defined in the space-fixed coordinate system. The fluid velocity squared term has an effect on sinkage and the hull girder loads at forward speed but the significance is not great compared with the effects due to the other terms in Bernoulli's equation. In calm water, the other terms are the hydrostatic pressure and the pressures due to the terms φ and $-\mathbf{U}\cdot\nabla\phi$. The potential function φ is zero if the body is on pure constant translational motion in calm water. At constant forward velocity U_0, the component $-U_0\,\partial\phi/\partial x$ induces mean shift in the heave force and, for this reason, the term has an effect on the sinkage of the ship and further on the steady hull girder loads. It should be noted that the pressure terms in Bernoulli's equation in this work are defined in the space-fixed coordinate system and not with respect to a moving frame. In the moving coordinate system, the pressure equation has been derived by, for example, Milne-Thomson (1968, p. 89, 3-61). The linearized pressure equation with steady pressure terms formulated in the moving coordinate system at the forward speed of ships has been presented by, for example, Kim (2005).

In regular waves, the time domain method generally gives good predictions for the motions and hull girder loads compared with the model test results. The calculated predictions are better at zero speed than at forward speed. The body nonlinear solution also gives better results than the body linear solution at forward

speed. The time domain method can predict the differences between sagging and hogging bending moments and shear forces.

The body linear solution overestimates motions and loads at forward speed. The body nonlinear solution gives improved predictions. In the body nonlinear solution, the exact body boundary condition is used and the instantaneous floating position of the ship is updated at every time step. Thus, the coupling of the actual floating position of the body geometry and the steady flow is taken into account in the body nonlinear solution. In the body linear solution, this is only taken into account on the mean wetted surface of the hull.

A large part of the stern is also above the mean water level in the body linear solution. As the floating position is not updated in the body linear solution, this part is not included in the solution. However, the flat bottom stern can induce an additional damping effect that is not taken into account in the body linear solution. Furthermore, the calculated vertical accelerations are higher at the bow compared with the model test results. Hence, it is possible for the ship model to pitch about an axis that is farther astern in the calculation than in the model tests. Hence, the heave at the centre of gravity of the ship is greater with the same pitch angle. This can be partly explained by the overestimated heave in the calculation at forward speed.

At forward speed, the free surface elevation around the ship is a combination of the steady and unsteady wave patterns, in addition to the incoming waves. The wave formation due to the steady and unsteady flow at the stern of the ship can have an effect on the calculated predictions at forward speed. In the model tests at forward speed, the stern was always at least partly in the waves because of the ship motions and the free surface elevation at the stern. The actual free surface elevation is not taken into account in the calculation method because the linear free surface boundary condition is satisfied at the mean water level. The calculations show that ignoring the fluid velocity squared term $0.5|\nabla\Phi|^2$ in Bernoulli's equation improves the predictions for the motions and loads. Ignoring the term in Bernoulli's equation is consistent with the linear free surface boundary condition. It is possible that the fluid velocity squared term gives an inaccurate prediction for the motions and loads because of the fluid flow at the stern and the large motions, at the same time. The rapid changes in the wetted surface of the flat bottom stern can have an effect on the solution accuracy. The free surface elevation at the stern has an effect on the flow and the method does not take into account the actual free surface elevation at the stern. Hence, the calculated solution may give an incorrect prediction for the fluid flow, especially for the steady flow at the

stern. However, further studies are needed to investigate the effect of the steady and unsteady flow and the wave formation at the flat bottom stern.

In the body nonlinear solution, the floating position of the ship is updated at every time step, and the exact body boundary condition is satisfied on the actual wetted surface below $z = 0$. Hence, the time domain method can predict the nonlinearities that arise from the changes in the hull geometry when the ship is oscillating at the free surface. The bow of the ship model entered the waves and the pressures acting on the bow increased the sagging loads. At zero speed, the relative motion induced rapid changes in the wetted surface area of the flat bottom stern, increasing the nonlinearities. The harmonic analysis shows that the relative contribution of the zero-order harmonic component, i.e. the mean, has a greater effect on the differences between the sagging and hogging loads than the higher order harmonic components. A large part of the mean of the harmonic components is also explained by the steady part at low wave amplitudes. At higher wave amplitudes, the steady contribution is small, and the largest contribution in the differences of the sagging and hogging loads is due to the ship motions in waves. Nevertheless, the results from regular waves do not include the effects due to the sum and difference frequencies, i.e. the excitation forces and moments from other frequencies than the encountered wave frequency. The irregular wave results include the nonlinear effects due to the sum and difference frequencies. The contribution of the sum and difference effects on nonlinearities of loads in irregular waves was not studied in this work. However, the harmonic analysis showed that the contributions of the higher order harmonic components are relatively small, and it can be assumed that the major part in nonlinearities occurs at the encountered wave frequencies, and the sum frequency effects are small.

In the model tests at forward speed, it was observed that the stern was not out of the waves at small wave amplitudes. At the highest wave amplitude in the tests, the emergence of the stern was still moderate and at least part of the flat bottom stern was in the waves. However, at zero speed and high wave amplitudes, the stern impacts occurred when the flat bottom stern entered the waves. The impacts at the flat bottom stern can influence the sagging loads in the model test results. However, at forward speed, the submergence of the bow into the waves has a greater effect on the differences between the sagging and hogging loads than the zero-speed stern impacts. Based on the model test results, the effect of the impacts was small on the rigid hull girder loads. However, the stern impacts at zero speed can induce dynamic responses on the hull girder. In this work, the hull girder is assumed to be rigid and the dynamics of the hull girder is not taken into account. Further studies are needed to include the wave impact loads in the calcu-

lation method, and investigations should be carried out to study the effect of wave impact loads on hull girder loads and dynamic responses.

Furthermore, the highest wave height in the regular wave tests is perhaps too high for the calculation method at forward speed Fn = 0.25. The wave height is perhaps also too high for the ship because a large part of the bottom of the bow rises out of the waves. In heavy weather, the ship will reduce the speed if there are excessive ship motions. The bow emergence out of the waves and the deck wetness could also have increased the uncertainties in the model test results.

In irregular head waves, the comparisons between the calculated and model test results are presented at zero and forward speeds. The results are given for sea states at which the significant wave heights are H_s = 9 m and H_s = 5 m at zero and forward speeds, respectively. The comparisons are presented as statistical values, peak distributions of response amplitudes and response spectra. In the peak distributions, the differences in the sagging and hogging shear force and the bending moment are clear. The ratio of sagging and hogging is also greater at forward speed than at zero speed. The irregular wave results are in line with the regular wave results at zero and forward speeds. In irregular waves, heave and pitch are well predicted with the time domain method. At zero speed, the bending moment is well predicted, but there are differences in shear force predictions. At forward speed, the calculation gives rather good predictions for the shear force, but the bending moment is underestimated.

In the model tests, the crests of the irregular waves were higher than the absolute values of the troughs, especially in the sea state H_s = 5 m where the tests at forward speed were carried out. This can have an effect on the comparison between the model test and the calculation results. One reason for the asymmetric wave profile could be the capability of the wave-maker to generate sinusoidal waves in the model basin (Mikkola, 2006). However, the calculation method is based on the linear wave theory, and higher order waves are not taken into account. The nonlinearities in waves will increase if the wave heights increase and the waves are becoming steeper. Hence, the wave profile can include higher order components that increase the wave crests, and the troughs become smoother. Higher order wave theories in the calculation method should be investigated starting from, for example, a second-order wave theory. Thus, the effects of the higher order waves on the hull girder loads could be further studied.

Short-term extreme value predictions are given for the shear force and the bending moment at two sea states: H_s = 5 m and H_s = 9 m. The extreme value predictions are based on the Weibull distribution. The extreme values are given as the

most probable extreme values in three-hour sea states. The ratios between the most probable extreme values of the sagging and hogging bending moments are greater at forward speed than at zero speed. Based on the calculation, the ratios of the sagging and hogging bending moment are 1.6 and 1.9 at zero and forward speeds, respectively. Furthermore, based on the model tests, the ratios of the sagging and hogging bending moment are 1.5 and 1.6 at zero and forward speeds, respectively. At zero speed, the calculated prediction is close to the model test result. The differences in the calculated and model test ratios are mainly due to the underestimated loads in the hogging condition. At forward speed, the relative motions at the bow are greater and, for this reason, the nonlinear effects due to the changes in the hull geometry during water entry and exit are also greater. This increases the nonlinearities in the hull girder loads. At zero speed, the flat bottom stern enters the waves, which increase the sagging shear force and bending moment. However, the hydrodynamic loads at the bow due to the forward speed induce greater differences into the sagging and hogging loads than the loads due to the stern at zero speed.

It should be noted that the predictions of the extreme values are based on only two speeds at two sea states, and different results will be obtained in other conditions. The ratios between calculated sagging and hogging moments and shear forces may be different. Furthermore, to obtain the extreme design values for the hull girder loads, several sea states should be included in the analyses. The loads, especially those at different wave periods in higher waves, should be investigated. Moreover, the confidence of the stochastic predictions depends on the duration of the sea state. The confidence of the predictions can be improved using a longer duration of sea states in the calculation and model tests.

The nonlinear time domain method is time-consuming if it is applied to predict extreme values of responses in several different operating and environmental conditions. Linear frequency domain methods are still important to define the extreme values and design sea states for different responses. The number of sea states in which the time domain calculation should be carried out can be reduced by means of the linear predictions. The linear methods can also be applied to determine the critical wave episodes where the nonlinear time domain analyses can be performed to obtain time histories for the nonlinear extreme values.

In this work, the calculation results are only presented in head seas. Model test results are also available for the RoPax ship in oblique waves at zero speed. The developed time domain method includes all of the six degrees of freedom at arbitrary heading angles. However, the verification and validation of the calculation method in oblique waves are missing. Hence, verification and validation in

oblique waves should be performed so that the developed time domain method can be applied to different kinds of wave load predictions in structural analyses.

6. Conclusions

In this work, wave loads of ships were studied by applying a numerical method and experimental results. The aim of the work was to increase understanding of wave loads for modern ship types and to develop a reliable and practical calculation method for wave loads in regular and irregular waves that can be applied to ship-wave interaction problems in structural analyses.

In this work, a time domain calculation method for linear and nonlinear hydrodynamic loads of floating bodies in waves is presented. The perturbation velocity potential is solved using source distributions on the body surface in the constant panel method. The source distributions are represented by means of the transient Green function. The time derivative of the velocity potential in Bernoulli's equation is solved using an acceleration potential method. In the acceleration potential method, a potential function is solved with a similar source formulation to that of the perturbation velocity potential. The acceleration potential method gives a reliable and stable solution for the hydrodynamic pressure. The calculated results show that the time domain method can be applied to ship-wave interaction problems to obtain linear and nonlinear wave loads in the wave frequency range.

The memory part of the transient Green function is solved by a numerical integration applying an adaptive Gauss-Kronrod quadrature formula. Comparisons with the series and asymptotic solutions show that the numerical integration is accurate but time-consuming. In the time domain calculation, the values of the memory part of the transient Green function are determined from the pre-calculated solutions. The pre-calculated solutions are presented as a finite element approximation of the memory part with correct solutions at the nodal points. Using the pre-calculated values of the memory part, the computational time is reduced considerably.

The verification of the method is presented for a hemisphere and cones, and Wigley hull forms are used in the validation. For the hemisphere, the time domain

method gives similar results for the heave added mass and damping coefficients as an analytical solution. For two cones with different deadrise angles, linear heave radiation forces were determined by applying two simple solutions in addition to the time domain method. The two simple solutions were based on the added mass and damping coefficients, and the impulse response function of the cones in forced heave motions. It has been proved that the time domain method gives the same results as the two simple solutions. The nonlinear effects of heave radiation force were also investigated. It is shown that the nonlinearity in the heave radiation force of the cones is significant compared with the linear predictions. For the Wigley hull form, the comparison between the existing experimental results and the time domain method shows good agreement of added mass damping coefficients, exciting forces and moments, and the heave and pitch motions. The calculated sinkage and wave-making resistance coefficients of the Wigley resistance hull form in calm water are also close to the experimental results.

In this work, model test results for a roll-on roll-off passenger ship are presented. The model test results are given for the ship motions, vertical shear forces at fore ship, and vertical bending moments at midship in regular and irregular head waves at zero and forward speeds. The time domain method was applied to predict responses and the calculated predictions were compared with the model test results. In addition to the tests in waves, model tests were carried out in calm water to study the steady flow effects on responses.

In calm water, the model test results show that the steady bending moment and shear force increase if the forward speed increases. The calculated results are in good agreement with the model test results but the uncertainty of the calculated predictions increases if the forward speed exceeds $Fn = 0.20$. For the model test ship, the steady hull girder loads are in the order of 10% of the still water loads at forward speed $Fn = 0.25$. The contribution of the steady bending moment is significant in the differences of the sagging and hogging bending moments in low wave amplitudes but the contribution decreases when the wave amplitude increases.

The model test results show that differences between the sagging and hogging shear force and the bending moment are significant. The nonlinearities are greater at forward speed than at zero speed. The time domain method can predict the nonlinearities in the sagging and hogging shear forces and bending moments in regular and irregular waves. In the body nonlinear solution, the floating position of the ship is updated at every time step and the exact body boundary condition is satisfied on the actual wetted surface. Thus, the time domain method can predict

the nonlinearities that arise from the changes in hull geometry when the ship is oscillating in waves.

The acceleration potential method gives a reliable and stable solution for hydrodynamic forces and moments. Moreover, the acceleration potential method gives consistent predictions in body linear and nonlinear solutions for heave radiation-diffraction forces. However, the applied backward difference method gives clearly different results, and the predictions for the model test ship include uncertainty in the body nonlinear solution if the ship has forward speed and the motions are large. The acceleration potential and backward difference methods give similar predictions for hydrodynamic forces and moments with the body linear solution.

In regular waves at zero speed, the time domain method gives good prediction for the motions and hull girder loads compared with the model test results. At forward speed, the body nonlinear solution gives better predictions than the body linear solution. In the body nonlinear solution, the instantaneous floating position of the ship is updated at every time step and the coupling of the actual body geometry and the steady flow are taken into account. In the body linear solution, the floating position of the ship is not updated and the steady flow is only calculated on the mean wetted surface of the hull.

Furthermore, the free surface elevation around the ship is a combination of the steady and unsteady wave patterns due to the ship's motions, in addition to the incoming waves. However, the velocity potential is only solved up to the undisturbed mean water level. The actual free surface elevation is not taken into account in the time domain method. The free surface boundary condition is linearized at the mean water level. In the linear form of the free surface condition, the fluid velocity squared term does not appear because it is a higher order term. The calculation shows that ignoring the fluid velocity squared term in Bernoulli's equation improves the predictions for the responses. Ignoring the term in Bernoulli's equation is consistent with the linear free surface boundary condition.

In irregular waves, the calculated heave and pitch motions are in close agreement with the model test results, comparing the peak distributions, response spectra and statistical values. At zero speed, the time domain method gives good predictions for the bending moment, but the shear force deviates from the model test results. At forward speed, the calculated shear force is close to the model test results but the bending moment is underestimated. The short-term extreme values were also predicted for the shear forces and bending moments in short-term sea states. The extreme values were determined using the time histories from the model tests and from the calculation. Based on the model test results, the ratios of

the extreme values between the sagging and hogging shear force and bending moment vary from 1.4 to 1.6.

Further studies are needed to investigate the effect of the steady and unsteady flows and waves at the flat bottom stern. Moreover, the time domain method should be further improved to develop the solution of the acceleration potential method. The acceleration potential can be decoupled to the memory and impulsive parts and only the impulsive part has to be solved with the panel method. Further studies are also needed to include the impact loads in the time domain method and to investigate the effect of the impact loads on hull girder loads and dynamic responses. The calculation method should also be verified and validated in oblique waves.

References

Abramowitz, M. and Stegun, I. A. (1972). *Handbook of Mathematical Functions with Formulas, Graphs and Mathematical Tables*. Dover. ISBN 0-486-61272-4.

Ahmed, T. M., Du, S. X., Hudson, D. A., Kingsland, P. W. and Temarel, P. (2005). Improvement of seakeeping prediction method for high speed vessels with transom stern. *International Conference on Fast Sea Transportation, FAST'2005*, St. Petersburg, Russia.

Baarholm, G. S. and Moan, T. (2001). Application of Contour Line Method to Estimate Extreme Ship Hull Loads Considering Operational Restrictions. *Journal of Ship Research* **45:3**, 228-240.

Bandyk, P. J. and Beck, R. F. (2011). The acceleration potential in fluid-body interaction problems. *Journal of Engineering Mathematics* **70**, 147-163.

Batchelor, G. K. (1967). *An introduction to fluid dynamics*. Cambridge University Press. ISBN 978-0-521-66396-0.

Beck, R. and Reed, A. (2000). Modern seakeeping computations for ships. *Proc. 23rd Symposium on Naval Hydrodynamics*, Office of Naval Research ONR.

Bingham, H. B., Korsmeyer, F. T., Newman, J. N. and Osborne, G. E. (1994). The simulation of ship motions. *6th International Conference on Numerical Ship Hydrodynamics*, 561-579.

Brard, R. (1972). The representation of a given ship form by singularity distributions when the boundary condition on the free surface is linearized. *Journal of Ship Research* **16:1**, 79-92.

Chang, M. (1977). Computations of three-dimensional ship motions with forward speed. *The Proc. Second Int. Conf. on Numerical Ship Hydrodynamics*, 124-135.

Chuang, J. M., Qiu, W. and Peng, H. (2007). On the evaluation of time-domain Green function. *Ocean Engineering* **34**, 962-969.

Clement, A. H. (1998). An ordinary differential equation for the Green function of time-domain free-surface hydrodynamics. *Journal of Engineering Mathematics* **33**, 291-217.

Cummins, W. E. (1962). The impulse response function and ship motions. *Schiffstechnik* **9:47**, 101-109.

Dai, Y. Z. and Wu, G. X. (2008). Time domain computation of large amplitude body motion with the mixed source formulation. *8th International Conference on Hydrodynamics*, Nantes.

Datta, R., Rodrigues, J. M. and Guedes Soares, C. (2011). Study of the motions of fishing vessels by a time domain panel method. *Ocean Engineering* **38**, 782-792.

Derrick, W. R. and Grossman, S. I. (1982). *Elementary Differential Equations with Applications*. Addison-Wesley, 2nd edition.

Doctors, L. J., Day, A. H. and Clelland, D. (2008). Unsteady effects during resistance tests on ship model in a towing tank. *Journal of Ship Research* **52:4**, 263-273.

Drummen, I., Wu, M. K. and Moan, T. (2009). Experimental and numerical study of containership responses in severe head seas. *Marine Structures* **22**, 172-193.

Duan, W. and Dai, Y. (1999). Time-domain calculation of hydrodynamic forces on ships with large flare (Part 1: Two-dimensional case and Part 2: Three-dimensional case). *International Shipbuilding Progress*, **46:446**, 209-233.

Elangovan, M., Iwashita, H., Saito, H. and Ito, A. (2008). Seakeeping estimations of fast ships with transom stern. *Journal of the Japan Society of Naval Architects and Ocean Engineers* **7**, 195-206.

Faltinsen, O. M. (1990). *Sea loads on ships and offshore structures*. Cambridge University Press. ISBN 0 521 37285 2.

Ferrant, P. (1991). A coupled time and frequency approach for nonlinear radiation. *18th Symposium on Naval Hydrodynamics*, 67-83.

Finkelstein, A. B. (1957). The initial value problem for transient water waves. *Communications on Pure and Applied Mathematics*, **10**: 511-522.

Fonesca, N. and Guedes Soares, C. (1998). Time-domain analysis of large-amplitude vertical ship motions and wave loads. *Journal of Ship Research* **42:2**, 139-153.

Greco, M. (2001). *A Two-dimensional Study of Green-Water Loading*. Ph. D. Thesis. Department of Marine Hydrodynamics Faculty of Marine Technology, Norwegian University of Science and Technology, Trondheim, Norway.

Guevel, P. and Bougis, J. (1982). Ship-motions with forward speed in infinite depth. *International Shipbuilding Progress* **29:332**, 103-117.

GWS. (1986). *Global wave statistics*. Edited by Hogben, N., Dacunha, N. M. C. and Olliver, G. F., British Maritime Technology Limited (BMT). Published by Unwin Brothers Limited. ISBN 0 946653 38 0.

Hess, J. L. and Smith, A. M. O. (1962). *Calculation of non-lifting potential flow about arbitrary three-dimensional bodies*. Douglas Aircraft Co., Inc. Aircraft Division, Report No. E.S. 40622.

Huang, Y. and Sclavounos, P. (1998). Nonlinear ship motions. *Journal of Ship Research* **42:2**, 120-130.

Hulme, A. (1982). The wave forces acting on a floating hemisphere undergoing forced periodic oscillations. *Journal of Fluid Mechanics* **121**, 443-463.

IACS. (2001). Standard wave data. IACS Recommendation No. 34, 2001.

IACS. (2010). Longitudinal strength of ships. IACS UR S11, Rev. 7. Nov. 2010.

Inglis, R. B. and Price, W. G. (1982). A three dimensional ship motion theory: Calculation of wave loading and response with forward speed. *Trans. RINA* **124**, 141-157.

Isaacson, E. and Keller, H. B. (1966). *Analysis of numerical methods*. Dover Publications, Inc., New York. ISBN 0-486-68029-0.

ITTC. (1984). *17th International Towing Tank Conference, Proceedings Vol. 1*. Göteborg, Sweden.

ITTC. (2002). The Specialist Committee on Waves. Final Report and Recommendations to the 23rd ITTC. *23rd International Towing Tank Conference, Proceedings of the 23rd ITTC – Volume II*.

Iwashita, H. (1997). Numerical seakeeping calculations based on the 3-D Green function method. *Ship Technology Research* **44**, 111-132.

Iwashita, H. and Ohkusu, M. (1989). Hydrodynamic forces on ship moving with forward speed in waves. *Journal of Society of Naval Architects of Japan* **166**.

John, F. (1950). On the motion of floating bodies. II. Simple harmonic motions. *Communication on Pure and Applied Mathematics* **3**, 45-101.

Journee, J. M. J. (1992). *Experiments and calculations on four Wigley hullforms*. TU Delft, MEMT 21.

Jensen, J. J. (2009). Stochastic procedures for extreme wave load predictions – wave bending moment in ships. *Marine Structures*, **22**:**2**, 194-208.

Jensen, J. J., Beck, R. F., Du, S., Faltinsen, O. M., Fonseca, N., Rizzuto, E., Stredulinsky, D. and Watanabe, I. (2000). *Special Task Committee VI.1, Extreme Hull Girder Loading*. 14th International Ship and Offshore Structures Congress (ISSC) 2000, Nagasaki, Japan.

Jensen, J. J., Pedersen, P. T., Shi, B., Wang, S., Petricic, M. and Mansour, A. (2008). Wave induced extreme hull girder loads on containerships. *Trans. SNAME* **116**, 128-152.

Kang, C.-G. and Gong, L.-Y. (1990). A numerical solution method for three-dimensional nonlinear free surface problems. *Proc. 18th Symposium on Naval Hydrodynamics*, 427-438.

Kataoka, S., Sueyoshi, A., Arihama, K., Iwashita, H. and Takaki, M. (2002). A study on body non-linear effects on ship motions. *Trans. of the West-Japan Society of Naval Architects* **104**, 111-120 (in Japanese).

Kataoka, S. and Iwashita, H. (2004). Estimations of hydrodynamic forces acting on ships advancing in the calm water and waves by a time-domain hybrid method. *Journal of the Society of Naval Architects of Japan* **196**, 123-138 (in Japanese).

Kim, B. (2005). Some consideration on forward-speed seakeeping calculations in frequency domain. *Int. Journal of Offshore and Polar Engineering* **15**:**3**, 189-197.

King, B. K., Beck, R. F. and Magee, A. R. (1989). Seakeeping calculations with forward speed using time-domain analysis. *17th Symposium on Naval Hydrodynamics*, 577-596.

Koo, W and Kim, M.-H. (2004). Freely floating-body simulation by a 2D fully nonlinear numerical wave tank. *Ocean Engineering* **31**, 2011-2056.

Kukkanen T. and Mikkola T. P. J. (2004). Fatigue assessment by spectral approach for the ISSC comparative study of the hatch cover bearing pad. *Marine Structures* **17**, 75-90.

Kukkanen, T. (2009). *Summary report of the project: Nonlinear wave loads of ships*. VTT Research report, VTT-R-02391-09. Available at: http://www.vtt.fi/inf/julkaisut/muut/2009/VTT-R-02391-09.pdf

Kukkanen, T. (2010). Wave load predictions for marine structures. *Journal of structural mechanics* **43:3**, 150-166.

Lamb, H. (1932). *Hydrodynamics*. Dover, New York, 6th edition. ISBN 0-486-60256-7.

Lee, C.-H., Newman, J. N. and Zhu, X. (1996). An extended boundary integral equation method for the removal of irregular frequency effect. *International Journal for Numerical Methods in Fluids* **23**, 637-660.

Lee, C.-H. and Sclavounos, P. D. (1989). Removing the irregular frequencies from integral equations in wave-body interactions. *Journal of Fluid Mechanics* **207**, 393-418.

Liapis, S. and Beck, R. (1985). Seakeeping computations using time-domain analysis. *Proceedings of the fourth international conference on numerical ship hydrodynamics*, 34-54.

Lin, W.-M. and Yue, D. (1991). Numerical solution for large-amplitude ship motions in the time domain. *18th Symposium on Naval Hydrodynamics*, 41-66.

Magee, A. R. and Beck, R. F. (1989). Vectorized computations of the time-domain Green function. *The 4th International Workshop on Water Waves and Floating Bodies*, Norway.

Matusiak, J. (2000). Two-stage approach to determination of non-linear motions of ship in waves. *4th Osaka Collouqium on Seakeeping Performance of Ships*, Osaka, Japan.

Matusiak, J. (2001). *Introduction to ship wave making resistance*. Helsinki University of Technology, Ship Laboratory M-227 (in Finnish).

Mei, C. C. (1992). *The applied dynamics of ocean surface waves*. Advanced series on ocean engineering; v. 1. World Scientific Publishing.

Mikkola, T. (2006). Time accurate simulation of a plunger type wave maker using unstructured finite volume solver with surface tracking. *26th Symposium on Naval Hydrodynamics*.

Milne-Thomson, L. M. (1968). *Theoretical hydrodynamics*. Dover Publications (1996). ISBN 0-486-68970-0.

Newman, J. N. (1977). *Marine Hydrodynamics*. The MIT Press, 8th printing. ISBN 0-262-14026-8.

Newman, J. N. (1978). The theory of ship motions. *Advances in Applied Mechanics* **18**, 221-283.

Newman, J. N. (1986). Distributions of sources and normal dipoles over a quadrilateral panel. *Journal of Engineering Mathematics* **20:2**, 113-126.

Newman, J. N. (1992). Approximation of free-surface Green functions. *Wave Asymptotics*. Cambridge University Press, 107-135.

Ochi, M. K. (1990). *Applied probability and stochastic processes in engineering and physical sciences*. A Wiley-Interscience Publication, John Wiley & sons. ISBN 0-471-85742-4.

Ogilvie, T. F. (1964). Recent progress toward understanding and prediction of ship motions. *5th Symposium on Naval Hydrodynamics*, 3-126.

Pawlowski, J. (1992). A nonlinear theory of ship motions in waves. *Proc. 19th Symposium on Naval Hydrodynamics*, 33-57.

Piessens, R., de Doncker-Kapenga, E., Uberhuber, C. W., and Kahaner, D. K. (1983). *QUADPACK*: *A subroutine package for automatic integration.* Springer Verlag. ISBN 978-3-540-12553-2. *QUADPACK* subroutines available at: http://www.netlib.org/ [Accessed on 30 April 2008].

Press, W. H., Teukolsky, S. A., Vetterling, W. T. and Flannery, B. P. (1997). *Numerical Recipes in Fortran 77: The Art of Scientific Computing* (Vol. 1 of Fortran Numerical Recipes, 2nd ed.). Press Syndicate of the University of Cambridge. ISBN 0-521-43064-X.

Price, W. G. and Bishop, R. E. D. (1974). *Probabilistic theory of ship dynamics*. Chapman and Hall Ltd. ISBN 0 412 12430 0.

Sagrilo, L. V. S., Naess, A. and Doria, A. S. (2011). On the long-term response of marine structures. *Applied Ocean Research* **33**, 208-214.

Salonen, E.-M. (1999). *Dynamiikka I & II*. Otatieto, Finland (in Finnish).

Sclavounos P. D, Nakos, D. E. and Huang, Y. (1993). Seakeeping and wave induced loads on ships with flare by Rankine panel method. *The Proc. Sixth Int. Conf. on Numerical Ship Hydrodynamics*, Iowa, USA.

Sen, D. (2002). Time-domain computation of large amplitude 3D ship motions with forward speed. *Ocean Engineering* **29**, 973-1002.

Song, M.-J., Kim, K.-H. and Kim, Y. (2011). Numerical analysis and validation of weakly nonlinear ship motions and structural loads on a modern containership. *Ocean Engineering* **38**, 77-87.

Stoker, J. J. (1958). *Water waves*. John Wiley & Sons Inc., reprinted 1992. ISBN 0-471-57034-6.

Tanizawa, K. (1995). A nonlinear simulation method of 3-D body motions in waves (1st report). Formulation with the Acceleration Potential. *Journal of the society of Naval Architects of Japan* **178**, 179-191.

Vinje, T. and Brevig, P. (1981). Nonlinear ship motions. *The Proc. 3rd Int. Conf. on Numerical Ship Hydrodynamics*, 257-268.

Wagner, H. (1932). Über Stoß- und Gleitvorgänge an der Oberfläche von Flüssigkeiten. *ZAMM – Journal of Applied Mathematics and Mechanics/Zeitschrift für Angewandte Mathematik und Mechanik*, **12**: 193-215.

Wang, L. and Moan, T. (2004). Probabilistic analysis of nonlinear wave loads on ships using Weibull generalized Pareto, and Gamma distributions. *Journal of Ship Research* **48: 3**, 202-217.

Weems, K. M., Lin, W. M., Zhang, S. and Treakle, T. (2000). Time Domain Prediction for Motions and Loads of Ships and Marine Structures in Large Seas Using a Mixed-Singularity Formulation. *Proceedings of the Fourth Osaka Colloquium on Seakeeping Performance of Ships (OC2000)*, Osaka, Japan, 272-280.

Wehausen, J. V. and Laitone, E. V. (1960). *Surface waves*. Encyclopedia of Physics, Volume IX, Fluid Dynamics III. Springer-Verlag. 446-778.

Wehausen, J. V. (1964). Effect of the initial acceleration upon the wave resistance of ship models. *Journal of the Ship Research* **7:3**, 38-50.

Wehausen, J. V. (1971). The motion of floating bodies. *Annual Review of Fluid Mechanics* **3**, 237-268.

Weymouth, G. D., Wilson, R. V. and Stern, F. (2005). RANS computational fluid dynamics predictions of pitch and heave ship motions in head seas. *Journal of Ship Research* **49:2**, 80-97.

Winterstein, S. R. (1988). Nonlinear vibration models for extremes and fatigue. *Journal of Engineering Mechanics* **113**:**10**, 1772-1790.

von Karman, T. (1929). The impact of seaplane floats during landing. Technical Notes, NACA, No. 321.

Wu, G. X. and Eatock Taylor, R. (1996). Transient motion of a floating body in steep water waves. *The 11th International Workshop on Water Waves and Floating Bodies*, Germany.

Wu, G. X. (1998). Hydrodynamic force on a rigid body during impact with liquid. *Journal of Fluids and Structures* **12**, 549-559.

Wu, M. K. and Moan, T. (1996). Linear and nonlinear hydroelastic analysis of highspeed vessels. *Journal of Ship Research* **40:2**, 149-163.

Wu, M. K. and Moan, T. (2005). Efficient calculation of wave-induced ship responses considering structural dynamic effects. *Applied Ocean Research* **27**, 81-96.

Wu, M. K. and Moan, T. (2006). Statistical analysis of wave-induced extreme nonlinear load effects using time-domain simulation. *Applied Ocean Research* **28**, 386-397.

Zhang, X., Bandyk, P. and Beck, R. F. (2010). Time-domain simulations of radiation and diffraction forces. *Journal of Ship Research* **54:2**, 79-94.

Zhu, S., Wu, M. K. and Moan, T. (2011). Experimental and numerical study of wave-induced load effects of open ships in oblique seas. *Journal of Ship Research* **55:2**, 100-123.

Zienkiewicz, O. C. (1971). *The finite element method in engineering science*. McGraw-Hill, London.

Series title and number
VTT Science 15

Title	**Numerical and experimental studies of nonlinear wave loads of ships**
Author(s)	Timo Kukkanen
Abstract	Extreme wave loads have to be defined in the ultimate strength assessment of ship structures. Nonlinearities in extreme wave loads can be significant in high waves. Numerical and experimental studies of nonlinear wave loads are presented in this work. A nonlinear time domain method has been developed and the fundamentals of the method are given. The method is based on the source formulation expressed by means of the transient three-dimensional Green function. The exact body boundary condition is satisfied on the instantaneous floating position of the body. The free surface boundary condition is linear. The time derivative of the velocity potential in Bernoulli's equation is solved with a similar source formulation to that of the perturbation velocity potential. The verification of the method is presented for a hemisphere and cones. Wigley hull forms are used to validate the calculation method in regular head waves and calm water. Model tests of a roll-on roll-off passenger ship with a flat bottom stern have been carried out. Model test results of ship motions, vertical shear forces and bending moments in regular and irregular head waves and calm water are given. The nonlinearities in ship motions and hull girder loads are investigated using the calculation method and the model test results. The nonlinearities in the hull girder loads have been found to be significant. The calculation method is used to predict rigid hull girder loads for the model test ship. It is shown that the time domain calculation method can be applied to ship-wave interaction problems to predict the nonlinear wave loads.
ISBN, ISSN	ISBN 978-951-38-7932-7 (soft back ed.) ISSN 2242-119X (soft back ed.) ISBN 978-951-38-7933-4 (URL: http://www.vtt.fi/publications/index.jsp) ISSN 2242-1203 (URL: http://www.vtt.fi/publications/index.jsp)
Date	September 2012
Language	English, Finnish abstract
Pages	219 p.
Keywords	wave loads, nonlinear loads, numerical methods, model tests, ship strength
Publisher	VTT Technical Research Centre of Finland P.O. Box 1000, FI-02044 VTT, Finland, Tel. +358 20 722 111

Julkaisun sarja ja numero
VTT Science 15

Nimeke	**Laskennallinen ja kokeellinen tutkimus laivojen epälineaarisista aaltokuormista**
Tekijä(t)	Timo Kukkanen
Tiivistelmä	Aaltokuormat on määritettävä arvioitaessa laivojen äärilujuutta. Epälineaarisuudet aaltokuormissa voivat olla merkittäviä kovassa merenkäynnissä. Työssä on tutkittu numeerisesti ja kokeellisesti epälineaarisia aaltokuormia. Työssä on kehitetty aikatason laskentamenetelmä vasteiden määrittämiseksi aallokossa. Menetelmä perustuu nopeuspotentiaalien ratkaisuun lähdejakautumien avulla rungon pinnalla. Lähdejakautumat on esitetty kolmiulotteisen ajasta riippuvan Greenin funktion avulla. Rungon pinnalla toteutetaan tarkka runkopinnanreunaehto. Vapaanpinnan-reunaehto on linearisoitu. Paineen Bernoullin yhtälössä esiintyvä nopeuspotentiaalin aikaderivaatta ratkaistaan samalla lähdejakautumien ratkaisumenetelmällä kuin häiriönopeuspotentiaalin ratkaisu. Laskentamenetelmä on verifioitu puolipallon ja kartion avulla. Wigley-runkomuotoja on käytetty laskentamenetelmän validoinnissa tyynessä vedessä sekä säännöllisessä vasta-aallokossa eri nopeuksilla. Työssä esitetään mallikoe tulokset tasapohjaperän omaavalle ro-pax-alukselle. Mallikokeissa mitattiin aluksen liikkeet ja kiihtyvyydet sekä laivapalkin leikkausvoimat ja taivutusmomentit. Kokeet tehtiin tyynessä vedessä eri nopeuksilla sekä säännöllisessä ja epäsäännöllisessä vasta-aallokossa nollanopeudella ja nopeudella eteenpäin. Epälineaarisuuksia liikkeissä ja kuormissa tutkittiin kehitetyn laskentamenetelmän avulla sekä mallikokeiden tuloksiin perustuen. Tulosten perusteella havaittiin, että epälineaarisuudet ovat merkittäviä mallikoelaivalla. Laskentamenetelmän avulla määritettiin mallikoelaivalle laivapalkin voimat ja momentit. Laskentamenetelmän todetaan soveltuvan hyvin nesterakenne-vuorovaikutusongelmiin ennustettaessa laivojen aaltokuormia.
ISBN, ISSN	ISBN 978-951-38-7932-7 (nid.) ISSN 2242-119X (nid.) ISBN 978-951-38-7933-4 (URL: http://www.vtt.fi/publications/index.jsp) ISSN 2242-1203 (URL: http://www.vtt.fi/publications/index.jsp)
Julkaisuaika	Syyskuu 2012
Kieli	Englanti, suomenkielinen tiivistelmä
Sivumäärä	219 s.
Avainsanat	wave loads, nonlinear loads, numerical methods, model tests, ship strength
Julkaisija	VTT PL 1000, 02044 VTT, Puh. +358 20 722 111

Numerical and experimental studies of nonlinear wave loads of ships

The prediction of wave loads is an important subject in the structural safety of ships. Extreme wave loads have to be defined in the ultimate strength assessment of the ship hull. In severe seas, nonlinearities in wave loads have to be taken into account.

This publication discusses hydrodynamic loads of ships in waves and considers, especially, nonlinear wave loads. Nonlinearities in wave loads are studied with numerical methods and using experimental results. Model tests have been carried out to gain an insight into nonlinearities in hull girder loads and to obtain validation data for a calculation method. A time domain method has been developed and applied to ship-wave interaction problems in regular and irregular waves.

ISBN 978-951-38-7932-7 (soft back ed.)
ISBN 978-951-38-7933-4 (URL: http://www.vtt.fi/publications/index.jsp)
ISSN 2242-119X (soft back ed.)
ISSN 2242-1203 (URL: http://www.vtt.fi/publications/index.jsp)